

# Background Reduction Techniques for the GERDA Experiment

Dissertation

zur

Erlangung der naturwissenschaftlichen Doktorwürde  
(Dr. sc. nat.)

vorgelegt der

Mathematisch-naturwissenschaftlichen Fakultät

der

Universität Zürich

von

Manuel Walter

aus

Deutschland

Promotionskomitee

Prof. Dr. Laura Baudis (Vorsitz)

Prof. Dr. Ueli Straumann

Prof. Dr. Marc Schumann

Zürich 2015



## Abstract

Major questions of modern physics, such as the matter-antimatter asymmetry, the mass of neutrinos and its nature, can be answered by the neutrinoless double beta decay (Chapter 1). The GERDA experiment is searching for this decay in  $^{76}\text{Ge}$ . In Phase I a limit of  $T_{1/2} > 2.1 \cdot 10^{25}$  yr (90% C.L.) was set on the half-life of this decay and a sensitivity of  $1.4 \cdot 10^{26}$  yr is expected for Phase II (Chapter 2). Reducing the background by one order of magnitude is a major goal of the current upgrade, approached by an active liquid argon veto, enhanced pulse shape discrimination capabilities and a reduction of background sources.

In GERDA, germanium detectors are directly immersed into liquid argon. Background events are rejected by their energy deposition in argon, which results in the production of vacuum UV light. It is converted to blue light, detectable with conventional PMTs. The conversion is performed by TPB-coated Tetratex, a component strongly influencing the efficiency of the veto system and developed within the framework of this thesis (Chapter 3). A liquid argon setup was built especially for this purpose. The coated reflector foil was optimised for its light yield, cryogenic stability and radiopurity, achieving a light yield  $3.15 \pm 0.16$  times higher than with uncoated VM2000.

A setup was developed to measure emanation rates down to  $10^{-13}$  mbar l/s individually for different chemical components (Chapter 4), with a mass spectrometer as central unit. The system was employed to measure emanation rates from TPB-coated Tetratex, which were found to be  $( < 317, < 47, 11.1, 12 ) \cdot 10^{-12}$  mbar l/s of the dominant components  $\text{CO}_2$ ,  $\text{N}_2 + \text{CO}$ ,  $\text{H}_2\text{O}$  and the solvent dichloromethane, respectively, after pumping for  $\sim 1300$  min.

Pulse shape discrimination is applied to both semi-coaxial and broad energy germanium (BEGe) detectors deployed in GERDA in order to select signal like events. An alternative multivariate analysis was developed for the former type employing a Support Vector Machine (Chapter 5). Its parameters were optimised by comparing the event classification with a simulation, resulting in a successful signal selection.

The pulse shape discrimination efficiency of both detector types is dependent on the level of electronic noise. An advanced digital noise filter based on wavelet transformations was thus implemented in the official GERDA analysis software (Chapter 6). The parameters were optimised on the background rejection efficiency of BEGe-type detectors, which yielded an improvement by 4% on a measurement with low noise. This filter is also a very useful tool for other applications, such as the pulse shape discrimination with semi-coaxial detectors, enhancing the energy resolution and studies of low energy events.

The calibration source insertion system was upgraded as well (Chapter 7). It was equipped with new, reliable end switch activation pins and 10 m long stainless steel bands and extended by a new parking indicator and shutter alarm system.

These contributions help the GERDA experiment to achieve its goals for Phase II.



## Zusammenfassung

Einige der wichtigsten Fragen der modernen Physik, wie die Materie-Antimaterie-Assymmetrie, die Masse und die Natur der Neutrinos können durch den neutrinolosen doppelten Betazerfall beantwortet werden (Kapitel 1). Das GERDA Experiment sucht nach diesem in  $^{76}\text{Ge}$  und hat in Phase I eine untere Grenze von  $T_{1/2} > 2.1 \cdot 10^{25}$  yr auf die Halbwertszeit gesetzt. In Phase II wird eine Sensitivität von  $T_{1/2} \approx 1.4 \cdot 10^{26}$  yr erwartet, wofür eine Reduzierung des Untergrunds um eine Größenordnung notwendig ist. Dies wird durch eine Instrumentierung des flüssigen Argons, eine verbesserte Pulsformanalyse und Verringerung bekannter Untergrundquellen erreicht (Kapitel 2).

Die Germaniumdetektoren in GERDA sind von flüssigem Argon umgeben, in welchem durch Untergrundereignisse Vakuum-UV Licht erzeugt wird, welches mit TPB beschichtetem Tetratex zu blauem Licht konvertiert und von konventionellen photomultiplier tubes detektiert wird. Untergrundereignisse können auf diese Weise diskriminiert werden. Die beschichtete Folie beeinflusst die Effizienz maßgeblich und wurde im Rahmen dieser Dissertation mit Hilfe eines speziell dafür entworfenen Flüssigargonaufbaus entwickelt (Kapitel 3). Die Lichtausbeute, kryogene Stabilität und radioaktive Reinheit wurden optimiert und eine  $3.15 \pm 0.16$  mal höhere Lichtausbeute erzielt, als mit unbeschichtetem VM2000.

Des Weiteren wurde ein Aufbau entwickelt, mit welchem die chemische Zusammensetzung von ausgasenden Substanzen und deren Raten bis zu einem Wert von  $10^{-13}$  mbar l/s gemessen werden können (Kapitel 4). Mit diesem wurden sehr niedrige Raten für TPB beschichtetes Tetratex gefunden. Das Herzstück der Anlage ist ein Massenspektrometer.

Signalereignisse werden für beide in GERDA verwendeten Detektorarten durch Pulsformanalysen ausgewählt. Für halbkoaxiale Detektoren wurde eine alternative multivariante Analyse entwickelt. Diese verwendet eine Support Vector Machine (Kapitel 5) deren Parameter durch den Vergleich mit einer Simulation optimiert wurden. Mit dieser Methode wurde die Selektion von Signalereignissen erfolgreich durchgeführt.

Die Effizienz der Pulsformanalysen hängt von der Höhe des elektronischen Rauschens ab. Ein flexibler digitaler Filter, basierend auf Wavelet Transformationen, wurde in die offizielle GERDA Software implementiert. Dessen Parameter wurden über die Untergrundunterdrückungseffizienz von BEGe-Typ Detektoren optimiert, welche in einer Messung mit wenig Rauschen um 4 % verbessert (Kapitel 6) wurde. Der Filter ist auch für viele andere Anwendungen ein sehr nützliches Instrument, z.B. für die Pulsformanalyse mit halbkoaxialen Detektoren, eine Verbesserung der Energieauflösung sowie potentielle Analysen welche Ereignisse mit kleinen Energien verwenden.

Das System zur Einführung von Kalibrierungsquellen wurde mit einem neuen, verlässlichen Endschalteraktivierungspin, einem 10 m langen Stahlband und einem zusätzlichen Parkpositionsindikator- und Alarmsystem aufgerüstet (Kapitel 7).

Die im Rahmen dieser Arbeit durchgeführten Entwicklungen tragen dazu bei, die Ziele für Phase II zu erreichen.



# Contents

<b>1</b>	<b>Introduction</b>	<b>8</b>
1.1	Neutrinos . . . . .	9
1.2	Double Beta Decay . . . . .	12
1.2.1	Experimental Signature of the Neutrinoless Double Beta Decay	14
1.3	Status of Current Neutrinoless Double Beta Decay Experiments . .	16
<b>2</b>	<b>The GERDA Experiment</b>	<b>18</b>
2.1	Phase I Hardware and Data Acquisition . . . . .	20
2.2	Background Sources and Event Topologies . . . . .	23
2.3	Detector Types and Pulse Shape Discrimination . . . . .	25
2.4	Phase I Results . . . . .	26
2.5	Upgrades for Phase II . . . . .	26
2.5.1	Procurement of High Purity BEGe Type Detectors . . . . .	28
2.5.2	Liquid Argon Veto System . . . . .	28
<b>3</b>	<b>Development of Efficient Wavelength-Shifting Reflector Foils for Liquid Argon Scintillators</b>	<b>31</b>
3.1	Description of Reflector Foils and Coatings . . . . .	32
3.1.1	Properties of the Reflector Foils . . . . .	32
3.1.2	Coating Technique . . . . .	33
3.1.3	Optical Properties and Thickness of Applied Coatings . . . .	34
3.1.4	Summary of Available Coating-Reflector Combinations . . . .	41
3.2	Mechanical and Cryogenic Stability . . . . .	41
3.3	Fluorescence Spectra for an Excitation Wavelength of 260 nm . . .	43
3.4	Scintillation Process in Gaseous and Liquid Argon . . . . .	46
3.5	Experimental Argon Setup . . . . .	47
3.5.1	Cooling System . . . . .	51
3.5.2	Liquid Argon Level Measurements . . . . .	54
3.5.3	Remote Monitor . . . . .	59
3.5.4	Data Acquisition . . . . .	61
3.6	Analysis Methods . . . . .	62

## CONTENTS

---

3.6.1	PMT Calibration . . . . .	62
3.6.2	Determination of the Triplet Lifetime . . . . .	66
3.6.3	Selection of Alpha Events . . . . .	69
3.6.4	Determination of the Light Yield . . . . .	71
3.7	Reflector Installation and Measurement Procedure . . . . .	73
3.8	Results . . . . .	75
3.8.1	Characterisation of the PMT R11065-10 . . . . .	76
3.8.2	Optimising the TPB Coating Thickness on Tetratex . . . . .	83
3.8.3	Relative Light Yield of Coatings With Commercial Scintillators . . . . .	86
3.8.4	Light Yield Measurements in Liquid Argon . . . . .	87
3.8.5	Long-Term Stability in Gaseous Argon, Liquid Argon and Air . . . . .	90
3.8.6	Delayed Fluorescence from TPB and from VM2000 . . . . .	97
3.8.7	Discussion of Uncertainties . . . . .	98
3.9	Comparison of Results and Methods . . . . .	100
3.10	Radiopurity of TPB Coated Tetratex . . . . .	101
3.11	Installation of TPB Coated Tetratex in the Liquid Argon Veto . . . . .	104
3.12	Coatings of Transparent Nylon . . . . .	107
3.13	Conclusions and Outlook . . . . .	111
<b>4</b>	<b>Emanation Rate Measurement System</b>	<b>113</b>
4.1	Hardware Description . . . . .	114
4.2	Measurement and Loading Procedures . . . . .	116
4.2.1	Solid Samples . . . . .	116
4.2.2	Gaseous Samples . . . . .	118
4.3	Data Acquisition . . . . .	119
4.4	Analysis Procedure and Software . . . . .	121
4.4.1	Reading of Mass Spectra . . . . .	121
4.4.2	Analysis of Mass Spectra . . . . .	121
4.5	Commissioning and Characterisation . . . . .	123
4.5.1	Blank Chamber Emanation Rates . . . . .	124
4.5.2	Electron Multiplier Gain Calibration . . . . .	126
4.5.3	Verification of Measurement and Analysis Procedures . . . . .	127
4.6	Measured Samples . . . . .	130
4.6.1	Emanation from PTFE after Different Cleaning Procedures . . . . .	131
4.6.2	Emanation from TPB Coated Tetratex for GERDA . . . . .	134
4.7	Conclusions and Outlook . . . . .	141
<b>5</b>	<b>Pulse Shape Discrimination for Semi-Coaxial Detectors Employing a Support Vector Machine</b>	<b>143</b>
5.1	Function Principle of a Support Vector Machine . . . . .	144

## CONTENTS

---

5.2	Selection of Training Datasets and Input Variables . . . . .	145
5.3	Parameter Optimisation . . . . .	147
5.3.1	Selection of Single Site Events in a Simulation . . . . .	148
5.3.2	Parameter Scan . . . . .	149
5.4	Application to GERDA Phase I Data . . . . .	155
5.4.1	Comparison to Other Pulse Shape Discrimination Methods . . . . .	162
5.5	Conclusions and Outlook . . . . .	162
<b>6</b>	<b>Electronic Noise Reduction Employing Wavelet Transformations</b>	<b>164</b>
6.1	Pulse Shape Discrimination Principle with BEGe-Type Detectors . . . . .	164
6.2	Introduction to Wavelet Transformations . . . . .	166
6.3	Implementation into the GERDA Analysis Software . . . . .	167
6.4	Demonstration of the Effects of Different Cutting Options . . . . .	171
6.5	Application to the Pulse Shape Discrimination with BEGe-Type Detectors . . . . .	171
6.6	Conclusions and Outlook . . . . .	177
<b>7</b>	<b>The GERDA Phase II Calibration System</b>	<b>178</b>
7.1	Modification of the End Switch Activation Pin . . . . .	178
7.2	Configuration and Calibration of the Absolute Encoder . . . . .	180
7.3	Position Measurement Validation with a 10 m Long Steel Band . . . . .	181
7.4	Source Absorber Oscillation Tests at 9.5 m . . . . .	183
7.5	Installations at LNGS for GERDA Phase II . . . . .	185
7.6	Shutter Alarm and Parking Indicator System . . . . .	187
7.6.1	Exception Handling . . . . .	188
7.7	Conclusions and Outlook . . . . .	189
<b>8</b>	<b>Final Conclusions and Outlook</b>	<b>191</b>
<b>9</b>	<b>Acknowledgements</b>	<b>195</b>

# List of Figures

1.1	Feynman diagram of the (neutrinoless) double beta decay . . . . .	13
1.2	Energy level arrangement responsible for the double beta decay . . .	13
1.3	Allowed range for the effective electron neutrino Majorana mass . . .	15
1.4	Experimental signature of the neutrinoless double beta decay . . . .	15
2.1	LNGS underground area, overview . . . . .	19
2.2	Schematic view of the GERDA experiment . . . . .	22
2.3	Event topologies in GERDA . . . . .	24
2.4	Phase I energy spectrum . . . . .	24
2.5	Measured events and background model at the region of interest . .	25
2.6	Weighting potential for different detector geometries . . . . .	26
2.7	Simulated pulse shapes of single site events in different detector types	27
2.8	Final Phase I spectrum in the region of interest . . . . .	27
2.9	The liquid Ar veto system . . . . .	30
3.1	Drawing of the dip-coating tool . . . . .	34
3.2	Pictures of coatings with TPB and Makrolon on VM2000 . . . . .	36
3.3	Pictures of PS+TPB coatings on VM2000 and copper . . . . .	38
3.4	Pictures of TPB-coated Tetratex . . . . .	39
3.5	Picture of a cracked PS + TPB coating on VM2000 . . . . .	43
3.6	Fluorescence spectra for an excitation wavelength of 260 nm . . . .	44
3.7	Ar scintillation process . . . . .	47
3.8	Schematic of the liquid Ar setup . . . . .	49
3.9	$^{241}\text{Am}$ source spectrum . . . . .	50
3.10	Cooling system block diagram . . . . .	52
3.11	Pressure in cryostat during liquid Ar measurements . . . . .	53
3.12	Drawing of the capacitive level meter . . . . .	55
3.13	Calibration of the capacitive level meter . . . . .	57
3.14	PT100 temperature reading during cool down . . . . .	59
3.15	Monitor of the PMT voltage and current . . . . .	60
3.16	PMT gain determination from single photoelectron spectra . . . . .	63

## LIST OF FIGURES

---

3.17	Histogram of the statistical uncertainty on the PMT gain . . . . .	64
3.18	Ar scintillation pulses with fit to the triplet component . . . . .	66
3.19	Event-based Ar triplet lifetime determination, fit range optimisation	67
3.20	Mean trace, fit with the sum of two exponential decays . . . . .	68
3.21	Component ratio versus integrated pulse height in liquid and gas Ar	70
3.22	Light yield determination and its statistical fluctuations . . . . .	71
3.23	Pictures of the active volume surrounded by a coated reflector foil .	74
3.24	PMT R11065 quantum efficiency and radiant sensitivity . . . . .	76
3.25	PMT base circuit diagram . . . . .	78
3.26	PMT afterpulses at room temperature . . . . .	79
3.27	PMT afterpulses in gaseous and liquid Ar scintillation light . . . . .	80
3.28	PMT trace spoiled by light produced inside the PMT . . . . .	82
3.29	Evolution of the PMT gain at 1500 V . . . . .	83
3.30	Thickness optimisation of TPB coatings on Tetratex . . . . .	84
3.31	Alpha peak position for commercial scintillator coatings in Ar gas .	87
3.32	Alpha peak position for selected coatings in liquid Ar . . . . .	89
3.33	PMT gain during the long-term measurement of coated Tetratex . .	92
3.34	Anticorrelation of gain and relative light yield . . . . .	92
3.35	Long-term stability of TPB-coated Tetratex in liquid Ar . . . . .	93
3.36	Confirmation of the long-term stability employing Ar gas . . . . .	94
3.37	Simulated electric field in the Ar setup . . . . .	96
3.38	Delayed fluorescence from TPB and VM2000 . . . . .	97
3.39	$\gamma$ -spectrum of contaminations in TPB-coated Tetratex . . . . .	102
3.40	Hole pattern of GERDA shrouds for Tetratex fixation . . . . .	104
3.41	Tetratex fixation tests on copper foil . . . . .	105
3.42	Tetratex fixation tests on dummy shrouds . . . . .	106
3.43	Transportation box and Tetratex installed in shroud . . . . .	108
3.44	Light yield with uncoated nylon . . . . .	109
3.45	Picture of nylon coated with Makrolon+TPB . . . . .	110
4.1	Schematic diagram of the emanation rate measurement system . . .	115
4.2	Pressure monitor during sample loading . . . . .	120
4.3	Picture of the emanation system . . . . .	125
4.4	Mass spectrum in the blank emanation chamber . . . . .	126
4.5	Partial pressures for electron multiplier calibration . . . . .	127
4.6	Electron multiplier gain curve . . . . .	128
4.7	Effect of ion gauge on partial pressures . . . . .	130
4.8	Pump-down curve of ethanol cleaned PTFE . . . . .	133
4.9	CO <sub>2</sub> emanation rates of PTFE samples cleaned with ethanol . . . .	135
4.10	Blank chamber emanation measurement for Tetratex . . . . .	136
4.11	Mass spectrum of TPB-coated Tetratex . . . . .	138

## LIST OF FIGURES

---

4.12	Reference mass spectra of $C_2H_4$ , $C_4H_8$ , $CH_2Cl$ and $C_{20}H_{41}Cl$ . . . .	139
4.13	Mass spectra and partial pressure of coated Tetratex emanation . .	140
5.1	Effect of the $C$ and the $\gamma$ parameter on the decision boundary . . .	145
5.2	Mean trace of multi site and single site events . . . . .	147
5.3	Normalised standard deviation of the centre of energy in simulation	148
5.4	Simulated spectrum with single site event selection, strong cut. . .	149
5.5	Simulated spectrum with single site event selection, accepting x-rays	150
5.6	Overview of spectra obtained with different SVM parameter values	151
5.7	Discrepancy of measurement and simulation for different parameters	152
5.8	Classification in measurement and simulation for optimal parameters	154
5.9	Classifier for the long calibration measurement . . . . .	155
5.10	Classified calibration spectra during Phase I . . . . .	156
5.11	Classification of Phase I data, normal threshold . . . . .	158
5.12	Classification of Phase I data, low threshold . . . . .	159
6.1	Principle of pulse shape discrimination with BEGe detectors . . . .	165
6.2	A/E versus energy, no denoising . . . . .	166
6.3	Principle of a wavelet decomposition . . . . .	167
6.4	Different Daubechies scaling and wavelet functions . . . . .	168
6.5	Wavelet transformed waveform . . . . .	169
6.6	Effect of different denoising options . . . . .	172
6.7	Electronic noise level in GERDA and in a vacuum cryostat . . . . .	173
6.8	A/E versus energy, wavelet denoised, soft threshold . . . . .	174
6.9	A/E versus energy, wavelet denoised, smooth threshold . . . . .	175
6.10	Parameter scan with Daubechies 20 wavelets . . . . .	176
6.11	A/E versus energy after optimised wavelet denoising . . . . .	176
7.1	Schematic view of the GERDA calibration system . . . . .	179
7.2	Picture of absorber with new end switch activation pin . . . . .	179
7.3	Calibration curve for the absolute encoder . . . . .	181
7.4	Long-term test of the absolute encoder position . . . . .	182
7.5	Picture of arrangement for absorber oscillation tests . . . . .	184
7.6	Calibration curves of the systems installed for GERDA Phase II . . .	186
7.7	Picture of the shutter alarm and parking indicator system . . . . .	188

# List of Tables

2.1	Characteristic values of GERDA Phases . . . . .	21
3.1	Mechanical, optical and cryogenic properties of coated reflector foils	42
3.2	Filling levels and volumes in the Ar setup . . . . .	58
3.3	Systematic uncertainties on the PMT gain determination . . . . .	65
3.4	Fit range dependence of the triplet lifetime determination . . . . .	69
3.5	TPB coating thicknesses optimisation on Tetratex . . . . .	84
3.6	Summary of light yield measurement uncertainties . . . . .	100
3.7	Radioactive trace contaminations of TPB-coated Tetratex . . . . .	103
3.8	Summary of light yield measurements . . . . .	112
4.1	Blank chamber emanation rates . . . . .	124
4.2	Emanation measurement verification with a known gas sample . . .	129
4.3	Emanation rates of differently cleaned PTFE samples . . . . .	134
4.4	Emanation rates of TPB-coated Tetratex . . . . .	141
5.1	Comparison of pulse shape discrimination methods, coaxial detectors	160
7.1	Verification of the incremental encoder position measurement . . . .	183
7.2	Measured oscillation amplitudes and times of a source absorber . .	185

# Chapter 1

## Introduction

Studying the properties of the neutrino is one of the most active fields in particle physics today. Its first postulation is closely related to the discovery of radioactivity by Antoine Henri Becquerel, who observed in 1896 that uranium salts darken photography plates in the absence of light. In 1898 Ernest Rutherford distinguished two types of radiation by its penetration depth, alpha and beta particles. Paul Villard discovered in 1900 a third type of radiation with an even larger penetration depth, which is not deflected in magnetic fields. This was the discovery of gamma radiation.

In 1903 Ernest Rutherford and Frederick Soddy identified the conversion of elements by beta decay as source of the beta radiation. Maurice Goldhaber and Gertrude Scharff-Goldhaber discovered in 1948 that beta radiation is the emittance of electrons. It was expected to have a constant energy for a given isotope. In the years 1911 to 1914 it was, however, discovered that they are emitted with a continuous energy spectrum. Given the fixed energy difference between the mother and daughter nucleus, this decay would violate energy conservation. A third neutral particle was thus suggested by Wolfgang Pauli in 1930 to be emitted in this decay. This particle was later called neutrino ( $\nu$ ). It was first discovered in 1956 by the reaction [1]

$$\bar{\nu} + p \rightarrow e^+ + n. \quad (1.1)$$

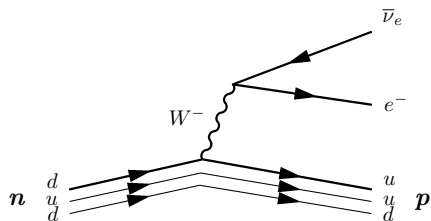
The detection medium was a cadmium loaded organic liquid scintillator. The detector was placed close to a nuclear reactor, which produces electron antineutrinos. Reaction 1.1 is identified by two coincident signatures: two 511 keV gammas from electron positron annihilation and gamma particles radiated by a cadmium atom due to the capture of the neutron.

The neutron  $n$ , another particle taking part in the beta decay, was discovered by James Chadwick in 1932. This finding led to the understanding of the compositeness of atomic nuclei with the constituents protons  $p$  and neutrons. In 1933 Enrico Fermi proposed a theory to explain the beta decay as the decay of a neutron

into a proton, electron and (anti)neutrino in one vertex [2]. The coupling constant of this interaction is weak compared to coupling constants of electromagnetic and strong interactions. This was the first description of a new type of interaction, the so-called weak interaction.

Besides protons and neutrons a large number of hadrons were discovered in the 1960s. Baryons could be successfully described by the symmetry group  $SU(3)$ . The interpretation of Murray Gell-Mann [3] and George Zweig [4] in 1964 suggested that three different quarks exist and all baryons are different combinations of those. These are the up, down and strange quarks. This hypothesis was subsequently confirmed in 1968 by deep inelastic electron nucleon scattering, clearly showing substructures of protons [5].

The previously mentioned theory of weak interactions by Enrico Fermi was also employed to describe weak decays of other particles. It was further developed by Sheldon Lee Glashow [6], Abdus Salam [7] and Steven Weinberg [8] in the 1960s. This resulted in a theory predicting the  $W^-$ ,  $W^+$  and  $Z^0$  bosons with correct masses. In 1983 they were subsequently discovered in  $p\bar{p}$  collisions at CERN. With this knowledge the full beta decay of a neutron into a proton could be understood as a down quark  $d$  of the neutron decaying to an up quark  $u$  emitting a  $W^-$ . The  $W^-$  decays into an electron  $e^-$  and an electron antineutrino  $\bar{\nu}_e$ . The full decay expressed in a Feynman diagram is



## 1.1 Neutrinos

The neutrino is a particle which is particularly difficult to study. The reason thereof is the absence of both electromagnetic and strong charge. An early experiment exploring the nature of the neutrino was performed by Raymond Davis in 1955. It used the idea of Bruno Pontecorvo to detect neutrinos by the reaction

$$\bar{\nu} + {}^{37}\text{Cl} \rightarrow {}^{37}\text{Ar} + e^- \quad (1.2)$$

The experiment employed 41001 of carbon tetrachloride to search for this reaction [9]. Antineutrinos were supplied by a nuclear reactor in Brookhaven. This experiment did not discover reaction 1.2, which suggests a difference between the incoming antineutrino and the neutrino required to produce  ${}^{37}\text{Ar}$  and an electron.

In 1958 it was discovered that neutrinos are left handed. The measurement employs the capture of a K-shell electron by  $^{152}\text{Eu}$ . The europium nucleus has a spin of 0 and the excited daughter  $^{152}\text{Sm}^*$  a spin of 1. The spin of both the emitted neutrino and the captured electron (without orbital angular momentum) must hence point in the opposite direction than the spin of the  $^{152}\text{Sm}^*$  nucleus. The momentum of the recoiling  $^{152}\text{Sm}$  points in the opposite direction than the momentum of the neutrino, since only two particles are in the final state. The direction of the spin of  $^{152}\text{Sm}^*$  was measured through the deexcitation photon. This was performed selecting photons emitted in the direction of the momentum of  $^{152}\text{Sm}^*$ . It was found that the spin of the gammas points anti-parallel to their momentum [10] and thus also in the opposite direction of the momentum of  $^{152}\text{Sm}^*$ . The same is the case for the neutrino. This means that neutrinos are left handed or, equivalently, have negative helicity. In contrast, antineutrinos are right handed. The different helicities would uniquely distinguish the neutrino from the antineutrino, if they were massless. This will be addressed later on.

The presence of a second neutrino flavour was discovered in 1962 [11]. The experiment employed a muon beam, which was produced by the decay of pions. These muons were stopped by an iron shield. The resulting muon neutrino beam was directed to a sparking chamber. There the appearance of muons, but not of electrons, was detected. The conclusion can be drawn that there is a difference between neutrinos produced in the beta decay and neutrinos produced in the muon decay. Hence two flavours of neutrinos do exist.

The Homestake solar neutrino experiment (running from 1970 until 1994) measured the electron neutrino flux by the reaction



The derived flux is approximately 1/3 of the flux expected from solar models [12]. This solar neutrino problem was confirmed by several other experiments such as GALLEX [13] and SAGE [14]. The Kamiokande experiment was able to measure the direction of the neutrinos in 1996 in addition to the flux [15] by elastic scattering of electron neutrinos on electrons. The electrons produce Cherenkov light in a tank containing 3 kt of ultra pure water. The direction of the emitted light allows to reconstruct the direction of the incoming neutrino. This additional information on their direction confirmed the sun as source of the neutrinos.

An experiment permitting more advanced studies of solar neutrinos is the Sudbury Neutrino Observatory (SNO) [16]. It employs heavy water as detection material. This provides these three processes for the neutrinos to interact



Reaction 1.4 is sensitive to electron neutrinos only. The other two methods are sensitive to any neutrino flavour, while the cross section of reaction 1.6 is enhanced for electron neutrinos compared to other neutrinos. Measuring the rates of those three reactions independently allows to determine the total neutrino flux as well as the electron neutrino flux. This revealed in 2002 that the total flux is indeed consistent with expectations from solar models, but the flux of electron neutrinos is reduced. These observations can be explained by neutrino oscillations.

Neutrino oscillations were already predicted by Bruno Pontecorvo in 1957 [17] and 1967 [18]. They occur because the flavour eigenstates  $|\mu_\alpha\rangle$  participating in interactions are different from the mass eigenstates  $|\mu_i\rangle$ . The relation between mass and flavour eigenstates can be described by the Pontecorvo-Maki-Nakagawa-Sakata (PMNS) mixing matrix, which was introduced in 1962 [19] and applied to neutrino oscillations in 1969 [20]. Three distinct neutrino flavours and three distinct mass eigenstates are assumed. The matrix is valid for neutrinos being Dirac particles [21]. It is parametrised by three mixing angles  $\theta_{12}$ ,  $\theta_{13}$  and  $\theta_{23}$  and the CP violating Dirac phase  $\delta_{CP}$

$$\begin{bmatrix} \nu_e \\ \nu_\mu \\ \nu_\tau \end{bmatrix} = \begin{bmatrix} c_{12}c_{13} & s_{12}c_{13} & s_{13}e^{-i\delta_{CP}} \\ -s_{12}c_{23} - c_{12}s_{23}s_{13}e^{i\delta_{CP}} & c_{12}c_{23} - s_{12}s_{23}s_{13}e^{i\delta_{CP}} & s_{23}c_{13} \\ s_{12}s_{23} - c_{12}c_{23}s_{13}e^{i\delta_{CP}} & -c_{12}s_{23} - s_{12}c_{23}s_{13}e^{i\delta_{CP}} & c_{23}c_{13} \end{bmatrix} \begin{bmatrix} \nu_1 \\ \nu_2 \\ \nu_3 \end{bmatrix} \quad (1.7)$$

where  $s_{ij}$  and  $c_{ij}$  are  $\sin\theta_{ij}$  and  $\cos\theta_{ij}$ , respectively. Mass eigenstates can be propagated as a superposition of plain waves. Oscillations occur because of the different propagation resulting from different mass eigenvalues. An observation of neutrino oscillations does in return imply different, non zero, mass eigenvalues. The probability for an oscillation of the original flavour state  $|\nu_\beta\rangle$  after a distance  $L$  into the flavour state  $|\nu_\alpha\rangle$  can be expressed as

$$P(\nu_\beta \rightarrow \nu_\alpha) = |\langle \nu_\alpha | \nu_\beta(L) \rangle|^2, \quad (1.8)$$

with  $|\nu_\beta(L)\rangle$  the state  $|\nu_\beta\rangle$  propagated to  $L$  from its origin. It is a function of squared mass differences, of  $s_{ij}^2$ ,  $c_{ij}^2$  and  $\delta_{CP}$ , depending on the oscillation in question.

The different angles and squared mass differences ( $\Delta m_{13}^2$  and  $\Delta m_{12}^2$ ) have been calculated from the results of various oscillation experiments. The current values are  $|\Delta m_{13}^2| = 2.5 \cdot 10^{-3} \text{ eV}^2$  and  $\Delta m_{21}^2 = 7.5 \cdot 10^{-5} \text{ eV}^2$  [22]. The absolute mass scale can, however, not be derived from oscillations. The eigenvalues of the mass states 1 and 2 are similar and well separated from the mass state 3. The current results allow for three different scenarios. One scenario is called normal hierarchy. In this case  $m_1$  is small compared to  $\Delta m_{13}$  and the mass eigenvalues are ordered as  $m_1 < m_2 \ll m_3$ . A second scenario is the inverted hierarchy where  $m_3 \ll m_1 < m_2$ . The third scenario is called quasi-degenerated hierarchy, where the mass differences are small compared to the mass of the neutrinos.

The fact that neutrinos do have mass implies that there is a component with the opposite handedness. This gives rise to the long standing question of whether there is a distinction between neutrinos and antineutrinos, besides their handedness. Neutrinos and antineutrinos would be two distinct particles if they were of Dirac nature [21] or identical if they were of Majorana nature [23]. The presence of a non-vanishing mass does imply the existence of processes which do violate the conservation of the total lepton number in the latter case. One such process is the neutrinoless double beta decay. It is described in more detail in Section 1.2. A violation of the total lepton number could in return aid to explain the observed excess of matter over antimatter through a process called leptogenesis [24, 25].

Describing neutrinos as Majorana instead of Dirac particles results in two additional Majorana phases  $\alpha_{21}$  and  $\alpha_{31}$  in the neutrino mixing [26]. The PMNS mixing matrix in Equation 1.7 has to be extended by multiplying

$$\begin{bmatrix} 1 & 0 & 0 \\ 0 & e^{i\frac{\alpha_{21}}{2}} & 0 \\ 0 & 0 & e^{i\frac{\alpha_{31}}{2}} \end{bmatrix} \quad (1.9)$$

from the right [27, 28]. Note that the Majorana phases can produce CP violation in addition to the phase  $\delta_{CP}$ [29].

## 1.2 Double Beta Decay

The pairing energy lowers the energy levels of nuclei with an even number of neutrons and protons compared to isobar odd-odd nuclei. Such an arrangement of energy levels is shown in Figure 1.2 on the example of isobars with a mass of 76 amu. A single beta decay is thus energetically forbidden for some nuclei in contrast to two simultaneous beta decays. The difference in the number of protons between such isobars is always two. If the higher energy state has more protons than the lower state, the nucleus can undergo double beta plus decay, single electron capture with a simultaneous beta plus decay or double electron capture. If the higher energy state has more neutrons it can undergo double beta decay. These neutrino accompanied decays are standard model processes. The double beta decay was first described by Maria Goeppert-Mayer in 1935 [30]. It can be expressed by the Feynman diagram shown in Figure 1.1 on the left and has been observed for several isotopes:  $^{48}\text{Ca}$ ,  $^{76}\text{Ge}$ ,  $^{82}\text{Se}$ ,  $^{96}\text{Zr}$ ,  $^{100}\text{Mo}$ ,  $^{116}\text{Cd}$ ,  $^{128}\text{Te}$ ,  $^{130}\text{Te}$ ,  $^{150}\text{Nd}$ ,  $^{238}\text{U}$ ,  $^{130}\text{Ba}$  and  $^{136}\text{Xe}$  [22]. The half-lives of these decays are in the range of  $(10^{18} - 10^{24})$  yr. The one for  $^{76}\text{Ge}$  is  $1.9_{-0.10}^{+0.14} \cdot 10^{21}$  yr [31].

The double beta decay might also occur without the emission of neutrinos (see e.g. [33]). A likely mechanism for such a neutrinoless double beta decay would be an exchange of a light Majorana neutrino, which is shown in the Feynman

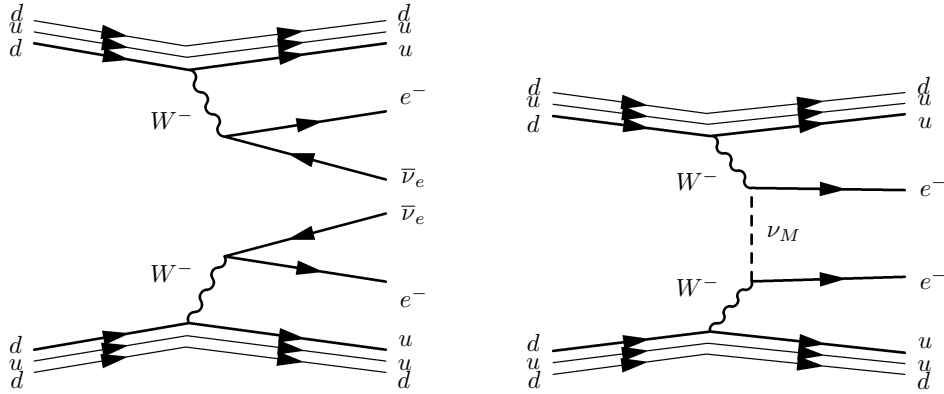


**Figure 1.1:** Left: Feynman diagram for the two neutrino double beta decay. Right: Feynman diagram for the neutrinoless double beta decay, mediated by the exchange of a light Majorana neutrino.

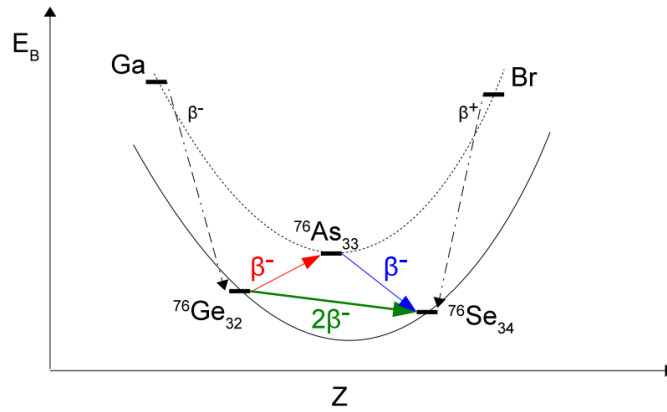


**Figure 1.2:** Energy levels of isobar even-even nuclei lie on a lower parabola than energy levels of isobar odd-odd nuclei. Figure from [32].

diagram in Figure 1.1 on the right. The decay has already been described in 1939 by Wendell H. Furry [34]. A calculation of the half-life was also provided in his work. The value was, however, by orders of magnitude too large because parity violation was not yet known at that time. With the current knowledge and assuming the exchange of a light Majorana neutrino as the dominating process we can calculate the decay rate as

$$\left(T_{1/2}^{0\nu}\right)^{-1} = G^{0\nu}(Q, Z) \left|M^{0\nu}\right|^2 \langle m_{ee} \rangle^2, \quad (1.10)$$

with  $G^{0\nu}(Q, Z)$  the phase space integral,  $M^{0\nu}$  the nuclear matrix element and  $\langle m_{ee} \rangle^2$  the effective electron neutrino Majorana mass.  $M^{0\nu}$  does not contain neutrino mixing parameters. This expression is derived e.g. in appendix B of [28]. The calculation of the nuclear matrix elements contains large uncertainties. The effective electron neutrino Majorana mass is given as

$$\langle m_{ee} \rangle = \sum_i U_{ei}^2 m_i = c_{12}^2 c_{13}^2 m_1 + s_{12}^2 c_{13}^2 e^{i\alpha_{21}} m_2 + s_{13}^2 e^{i(\alpha_{31} - 2\delta_{cp})} m_3 \quad (1.11)$$

with  $U_{ei}$  the PMNS mixing matrix extended by the Majorana phases and  $m_i$  the mass eigenvalues of  $\nu_i$ . The Majorana phases and absolute values of  $m_i$  are unknown. All other values, however, have been measured. This is sufficient to constrain the values of  $\langle m_{ee} \rangle$  as a function of the lightest neutrino mass. The  $2\sigma$  band of allowed values for is shown in Figure 1.3. Measuring the half-life of the neutrinoless double beta decay corresponds to a measurement of  $\langle m_{ee} \rangle$  by Equation 1.10. This provides additional information on the values of the parameters in Equation 1.11. Such a measurement can also distinguish between normal and quasi-degenerated hierarchy. If  $\langle m_{ee} \rangle$  has a value consistent with the inverted hierarchy it cannot be distinguished from the quasi degenerated hierarchy.

### 1.2.1 Experimental Signature of the Neutrinoless Double Beta Decay

The double beta decay is measured by the energy deposition of the two emitted electrons, on the other hand the two anti neutrinos leave a detector without any energy deposition. The result is a continuous energy spectrum for the neutrino accompanied double beta decay. However, if this decay occurs without an emission of neutrinos, the full energy of the decay will be carried by the electrons. This results in a peak at the Q-value of the decay. Such a peak is the signature searched for by current experiments. An energy spectrum as expected for a present neutrinoless double beta decay signal is shown in Figure 1.4 for  $^{76}\text{Ge}$ . This decay has a Q-value of 2039 keV.

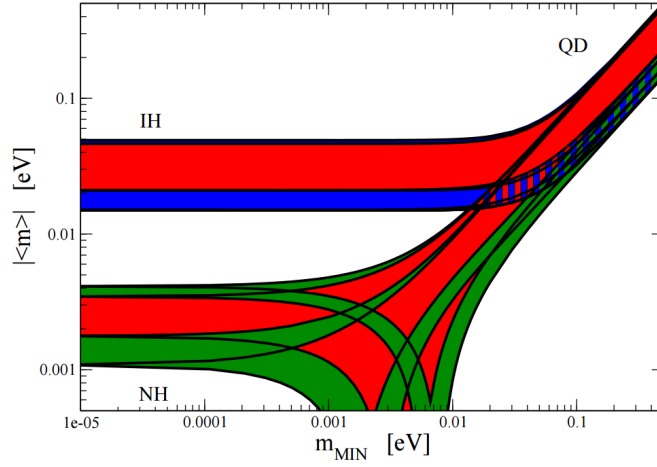


**Figure 1.3:**  $2\sigma$  band of the effective electron neutrino Majorana mass as a function of the lightest neutrino mass for normal (NH), inverted (IH) and quasi-degenerated (QD) hierarchy. Red regions correspond to parameter values of the Majorana phases which lead to CP violation. Figure from [22].

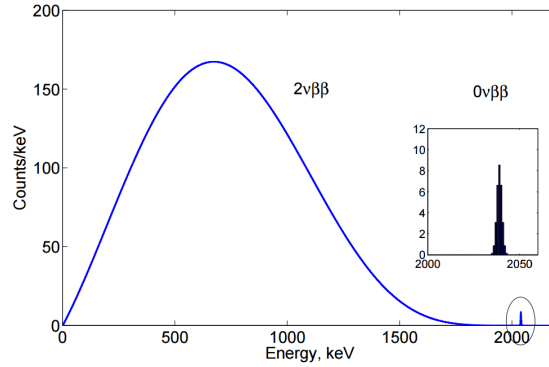


**Figure 1.4:** Energy spectrum of the two electrons emitted by the double beta decay of  $^{76}\text{Ge}$ . The neutrino accompanied case results in a continuous spectrum. The neutrinoless decay would result in a peak at the Q-value of the decay at 2039 keV. Figure from [35].

### 1.3 Status of Current Neutrinoless Double Beta Decay Experiments

This section provides an overview over the most sensitive, recently conducted and current neutrinoless double beta decay experiments. The respective plans for the near future are also summarised. The GERDA experiment will be discussed separately in Chapter 2.

The CUORE experiment employs  $\text{TeO}_2$  bolometers to search for the neutrinoless double beta decay of  $^{130}\text{Te}$  [36, 37]. The Q-value of this decay is  $(2527.518 \pm 0.013)$  keV [38]. Their bolometer crystals are cooled to  $\sim 10$  mK. An energy deposition in a crystal is measured by the produced heat with a neutron-transmutation-doped germanium thermistor. CUORE is running in a staged approach. CUORE-0 finished in March 2015 with a total exposure of 9.8 kg yr of  $^{130}\text{Te}$  [39]. A previous stage called CUORICINO collected 19.75 kg yr of exposure [40]. Combining both stages results in a limit on the half-life of  $T_{1/2} > 4.0 \cdot 10^{24}$  yr. This corresponds to a limit on the effective Majorana neutrino mass of  $< (0.27 - 0.76)$  eV [41]. The full scale CUORE experiment is expected to start data taking in summer 2015 [42]. It is planned to have 206 kg of  $^{130}\text{Te}$ .

The KamLAND-zen experiment searches for the neutrinoless double beta decay in  $^{136}\text{Xe}$ . The Q-value of this decay is  $(2457.83 \pm 37)$  keV [43]. It consists of a 13 t xenon loaded liquid scintillator submerged into 1 kton of liquid scintillator [44]. The fiducial volume contains  $(125 \pm 7)$  kg of  $^{136}\text{Xe}$  [45]. An energy deposition produces scintillation light which is measured with PMTs. KamLAND-zen acquired an exposure of 89.5 kg yr until May 2014. They have set a limit of  $T_{1/2} > 2.6 \cdot 10^{25}$  yr on the half-life of the neutrinoless double beta decay in  $^{136}\text{Xe}$ . This corresponds to a limit on the effective Majorana neutrino mass of  $< (0.14 - 0.28)$  eV [46]. KamLAND-zen is continuing to take data. It is planned to upgrade the experiment in the near future in order to double the mass of  $^{136}\text{Xe}$ .

EXO-200 is a time projection chamber with 200 kg of liquid xenon enriched to 80.6 % of  $^{136}\text{Xe}$ . Both, the charge and the scintillation light are recorded. The charge is collected by wires and the light is detected with large area avalanche photodiodes [47]. EXO-200 acquired an exposure of 100 kg yr of  $^{136}\text{Xe}$  in the period from September 2011 till September 2013. It has set a limit of  $T_{1/2} > 1.1 \cdot 10^{25}$  yr on the half-life of the neutrinoless double beta decay of  $^{136}\text{Xe}$ . This corresponds to a limit on the effective Majorana neutrino mass of  $< (0.19 - 0.45)$  eV [41]. The EXO collaboration now improved their photo sensor electronics and made modifications to lower their background. It is planned to acquire data in this upgraded configuration [48] for two years.

The Majorana-demonstrator employs point contact germanium diodes enriched in  $^{76}\text{Ge}$  with a Q-value of  $(2039.061 \pm 0.007)$  keV [49]. These will be installed in

two ultra pure copper cryostats. A prototype module has been running for one year starting in summer 2014. The first cryostat is currently under commissioning and the second one is being assembled. The Majorana-demonstrator has a total mass of 29 kg of  $^{76}\text{Ge}$ . It searches for the neutrinoless double beta decay and serves as a demonstrator for a scalable technology to construct a future ton scale experiment based on germanium [50].

## Chapter 2

# The GERDA Experiment

The GERDA experiment is located in the Laboratori Nazionali del Gran Sasso (LNGS) of the Istituto Nazionale di Fisica Nucleare (INFN). It is in the centre of Italy near the town of L'Aquila, approximately 100 km north east of Rome. LNGS is the worlds largest underground laboratory. It was built to host experiments which require a strong shielding from cosmic radiation. The laboratory is situated inside the Gran Sasso mountain with a rock overburden of 1400 m. This is corresponding to 3400 meter water equivalent, reducing the flux of muons by a factor of one million and the flux of neutrons by one thousand, compared to the surface [51]. The remaining neutron flux is dominated by natural radioactive contaminations in the limestone. The experimental area is accessed through a highway tunnel. The laboratory consists of three halls hosting several experiments and smaller service tunnels. Each hall is approximately 100 m long and 18 m high. The GERDA experiment is situated in hall A. An overview map including current experiments is shown in Figure 2.1.

GERDA is an international collaboration with approximately one hundred members from sixteen institutions. It is run by an international collaboration of sixteen institutions in Europe. The experiment is searching for the neutrinoless double beta decay of  $^{76}\text{Ge}$ . This decay has a Q-value of  $(2039.061 \pm 0.007)$  keV [49]. The decay is detected employing germanium detectors with an excellent energy resolution. Searching for the decay in  $^{76}\text{Ge}$  allows to employ the same material as source and detector. The two electrons emitted by the decay deposit their energy by the creation of electron-hole pairs in the detector. This results in a charge signal proportional to the deposited energy. There is no deterioration of the energy resolution by inactive material between the source and detector. The experimental signature has been explained in Section 1.2.1. A high resolution is important to distinguish a potential signal from background peaks and to reduce the number of background events in the signal region. It is furthermore relevant to avoid leakage of neutrino accompanied double beta decay events in the neutrinoless region. This

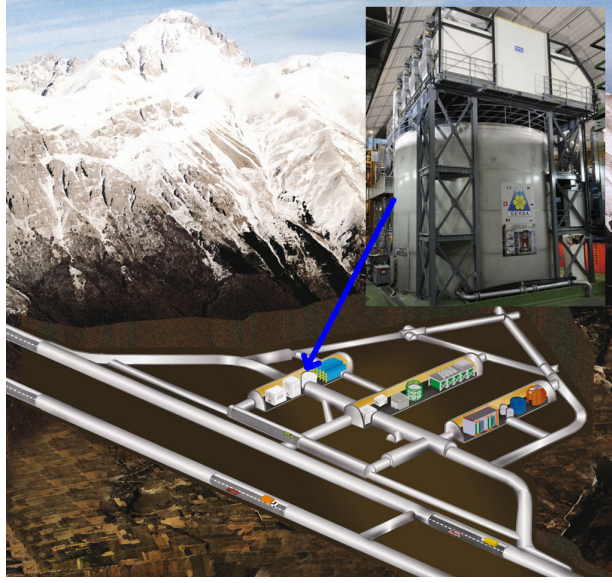


**Figure 2.1:** Overview of the LNGS underground laboratory showing the location of GERDA, the highway tunnels, the three experimental halls and connecting service tunnels. Graphic adapted from [52].

is however relevant only in case of a much lower energy resolution.

The measurement time  $t$  (years) of neutrinoless double beta decay experiments is very small compared to the half-time  $T_{1/2}$  ( $> 10^{25}$ yr) of a potential neutrinoless double beta decay. The exponential decay can thus be expanded by a Taylor series and cut after the linear term yielding a very good approximation. The number of decayed events  $N_d$  for an original number of atoms  $N_0$  is hence

$$N_d = N_0 \frac{t \cdot \ln(2)}{T_{1/2}}. \quad (2.1)$$

The number of originally present  $^{76}\text{Ge}$  atoms in a material of mass  $m$  with an enrichment fraction of  $f_{76}$  is given as

$$N_0 = \frac{N_A \cdot m}{M_{76}} \cdot f_{76}, \quad (2.2)$$

with  $N_A$  the Avogadro's constant and  $M_{76}$  the molar mass of  $^{76}\text{Ge}$ . The actual number of measured signal events is then given as

$$S = \frac{t \cdot \ln(2)}{T_{1/2}} \frac{N_A \cdot m}{M_{76}} \cdot f_{76} \cdot f_{av} \cdot \epsilon_{fep} \cdot \epsilon_{psd}, \quad (2.3)$$

with  $f_{av}$  the fraction of the active volume,  $\epsilon_{fep}$  the fraction of events depositing their entire energy in the active volume (part of the energy of an event can be lost by bremsstrahlung leaving the active volume) and  $\epsilon_{psd}$  the signal acceptance of a potential pulse shape discrimination method. This equation is showing the linear dependence of the sensitivity on  $T_{1/2}$  when running the experiment in quasi background free conditions. In the presence of background, it is only providing the number of signal events and the sensitivity has to be calculated differently.

Assuming a flat distribution of the background in the region of interest (ROI), the total number of background events  $B$  in an energy window  $\Delta E$  can be expressed as

$$B = BI \cdot \Delta E \cdot t \cdot m, \quad (2.4)$$

with  $BI$  the background index in cts/(keV kg yr). The significance  $n_\sigma$  of a potential signal, in number of standard deviations, can be approximated as

$$n_\sigma = \frac{S}{\sqrt{B}}, \quad (2.5)$$

assuming, that the number of events are distributed according to Poisson distributions. The approximation is more exact for larger number of events. Combining Equation 2.3, 2.4 and 2.5 the sensitivity is given as

$$T_{1/2} = \sqrt{\frac{m \cdot t}{BI \cdot \Delta E}} \cdot \frac{N_A \cdot \ln(2)}{M_{76} \cdot n_\sigma} \cdot f_{76} \cdot f_{av} \cdot \epsilon_{fep} \cdot \epsilon_{psd}. \quad (2.6)$$

Hence, the sensitivity does scale with the square root of the exposure in the presence of background. It scales linearly in the absence of background. A large effort is thus made by GERDA to run in the background free regime.

GERDA is following a staged approach. Phase I was running from November 2011 until May 2013 reaching a total exposure of 21.6 kg yr and a BI of  $10^{-2}$  cts/(keV kg yr). In Phase I existing detectors of the former International Germanium Experiment (IGEX) [53] and Heidelberg-Moscow (HdM) [54] experiment were refurbished and deployed. Phase II is aiming for an exposure of 100 kg yr and a background index of  $10^{-3}$  cts/(keV kg yr). This is achieved employing additional germanium detectors with improved energy resolution and pulse shape discrimination properties, a reduction of known background sources and an additional liquid argon veto system. More details are provided in the following sections. An overview over the two phases is provided in Table 2.1.

## 2.1 Phase I Hardware and Data Acquisition

The Phase I, semi-coaxial high purity germanium detectors have a total mass of 18 kg and are enriched to (86-88)% of  $^{76}\text{Ge}$ . They were arranged in an array

	Mass [kg]	BI [cts/(keV kg yr)]	Exposure [kg yr]	Expected $T_{1/2}^{0\nu}$ sensitivity [yr]
Phase I	18	$10^{-2}$	21.6	$2.4 \cdot 10^{25}$
Phase II	35	$10^{-3}$	100	$1.4 \cdot 10^{26}$

**Table 2.1:** Enriched detector mass, background index, exposure and sensitivity of GERDA Phase I (November 2011 – May 2013) and Phase II (expected).

of four strings and directly immersed into a 5.5 m high cryostat with a total of 64 m<sup>3</sup> of liquid argon. The array is surrounded by a 3 m high copper cylinder with a diameter of 0.75 m. It is installed to prevent radon emanating from the cryostat from reaching the detectors by convection. An additional copper cylinder is installed around each detector string to reduce the amount of <sup>42</sup>K ions from drifting to the surface of the detectors. <sup>42</sup>K is a beta emitter with an end point of 3524 keV. It is one of the major contributions to the background at the ROI. It originates from <sup>42</sup>Ar which is naturally present in argon gas. The liquid argon serves as coolant and shielding against neutrons and  $\gamma$  rays from surrounding materials like the cryostat. A mock-up of the experiment is shown in Figure 2.2. The cryostat is surrounded by a 8.5 m high tank, filled with 590 m<sup>3</sup> of ultra pure water. The water is supplied by the Borexino purification plant [55]. The water tank is equipped with PMTs and serves as Cherenkov detector to veto cosmic muons and associated radiation. It additionally absorbs neutrons and  $\gamma$  rays e.g. from surrounding rock. A glove box for detector installation and a lock system to lift and lower the detector array into the cryostat is installed on top of the water tank. Both are situated inside a clean room. The clean room roof is covered by plastic scintillators to veto muons passing through the neck of the cryostat. These are not detected by the water Cherenkov veto system. Weekly or bi-weekly calibrations of the germanium detectors are performed employing <sup>228</sup>Th sources. These are lowered into the cryostat by a system developed and operated by the University of Zurich. It was designed, built and tested in the framework of the PhD theses of Michael Tarka and Francis Froborg [32, 56, 57]. I was participating in the installation and operations for Phase I and upgrading the system for Phase II. This is described more detailed in Chapter 7. Further information about the Phase I hardware can be found in [58].

During data acquisition, raw events were stored in a disk area not accessible to the collaboration. All events with an energy outside the range  $Q_{\beta\beta} \pm 20$  keV were automatically transferred to a location accessible to the collaboration. The first 18.5 kg yr of this dataset were employed to model the background as described in Section 2.2 and in [59] and to develop pulse shape discrimination methods as described in Section 2.3 and in [60]. The data was unblinded in two steps. First,

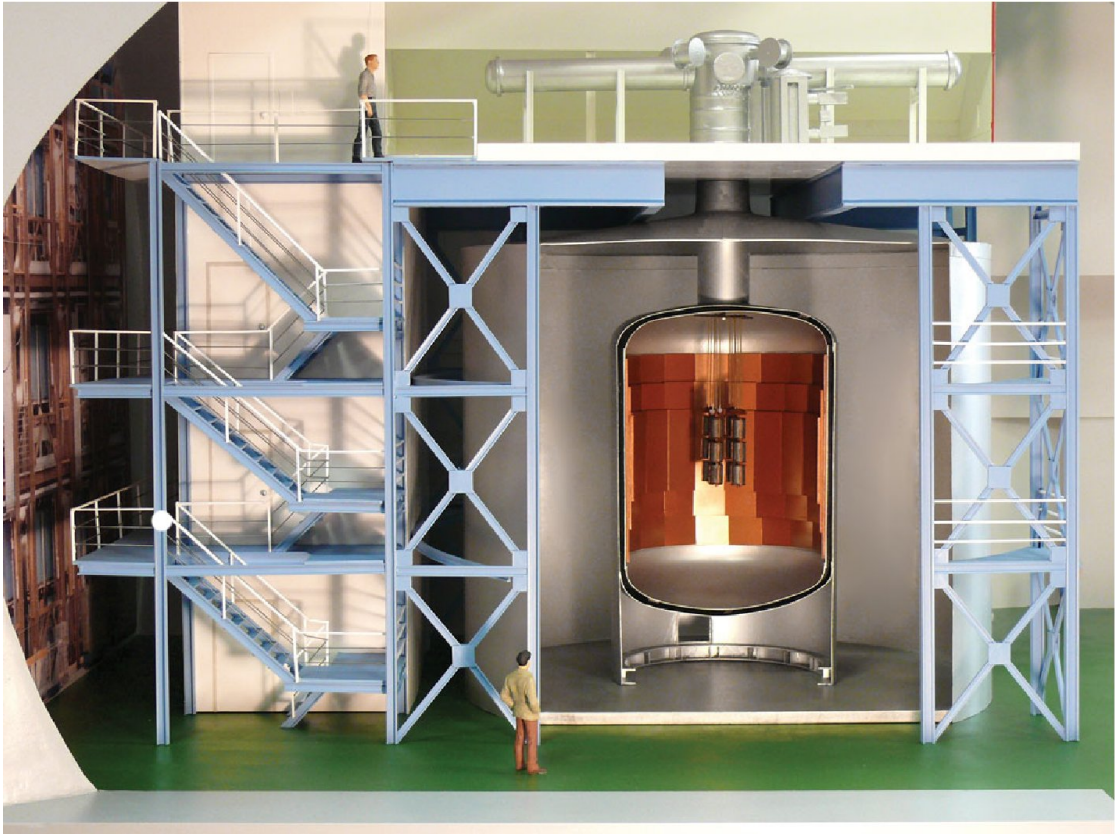


**Figure 2.2:** Schematic view of the GERDA experiment. Bare high purity germanium diodes are directly immersed in liquid argon. The germanium detectors are arranged in strings (enlarged in this figure for better visibility) and placed in the centre of the cryostat. This is surrounded by a water Cherenkov detector to veto cosmic muons. A clean room and an additional plastic scintillator muon veto are situated on top of the water tank. Figure from internal GERDA resources.

the central  $\pm 5$  keV were kept blind and events in the unblinded side bands were compared to the background model. The analysis methods and background model were frozen after this point. Second, the data was fully unblinded and the analysis applied. The results are described in Section 2.4 and published in [61].

## 2.2 Background Sources and Event Topologies

Double beta decay events mostly occur in the detector bulk with the two emitted electrons depositing their full energy in the close vicinity of the decay location. Such events are called single site events (SSE). The background in GERDA originates from different locations and isotopes resulting in different event topologies. These are depicted in Figure 2.3. The outermost, so-called “dead layer“, of the germanium detectors is not active. The inner p+ readout contact is however sufficiently thin to be penetrated by alpha particles originating from decays, e.g. of  $^{210}\text{Po}$  or  $^{226}\text{Ra}$ , on the surface or in the close vicinity. The energy spectrum of those events is a peak slightly below the nominal alpha energy with a long tail extending down to the ROI. Hence, they do contribute to the background at  $Q_{\beta\beta}$ . The n+ high-voltage contact is too thick to be penetrated by alpha particles. Beta particles, e.g. from  $^{39}\text{Ar}$  and  $^{42}\text{K}$  do however penetrate this dead layer.

A large fraction of gamma events, e.g. from the uranium or thorium decay chain, with an energy deposition in the ROI, interact at multiple locations. The interaction points can be in the same detector, in several detectors or in the liquid argon. These so-called multi site events (MSEs) can also be caused by a  $^{60}\text{Co}$  beta decay, which is followed by two gamma decays. Events depositing energy in several detectors are therefore discarded.

Background sources from previously known contaminations and contributions clearly visible in the background spectrum were included in the so-called “Minimum Model“. This model was developed based on 18.5 kg yr of exposure acquired until May 2013. The spectrum measured with the semi-coaxial detectors in this period is shown in Figure 2.4. The spectra resulting from each individual background contribution were simulated and fit to the measured background spectrum in the range of 570–7500 keV. The model is consistent with the data within the statistical uncertainty in this energy range. The measured spectrum around the ROI is shown in Figure 2.5. The 15 keV side bands are unblinded and  $Q_{\beta\beta} \pm 5$  keV is blinded in this Figure. The Minimal Model and its individual contributions are also shown. An important result is, that a flat background is expected at  $Q_{\beta\beta}$ . The model predicts a background index of  $18.5 \cdot 10^{-3}$  cts/(kg keV yr). This is consistent with an interpolation of a flat background in range of  $Q_{\beta\beta} \pm 100$  keV excluding known gamma peaks at 2104 keV ( $^{208}\text{Tl}$  single escape peak) and 2119 keV ( $^{214}\text{Bi}$ ). Further details about the background in Phase I are provided in [59].

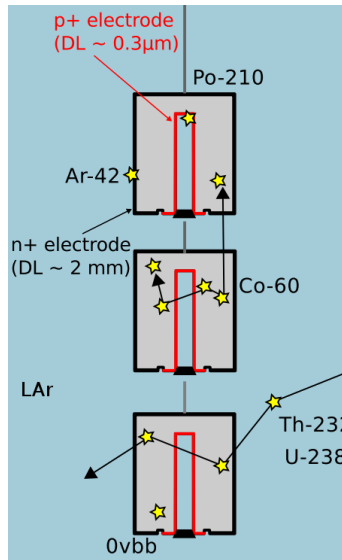


**Figure 2.3:** Schematic view of a detector string. Illustrated are typical event topologies for background events as observed in GERDA. The event marked with 0vbb is a typical signal event depositing its energy at one location in the detector bulk. The red p+ electrode is the signal readout and the black n+ electrode the high voltage contact. Figure from [62].

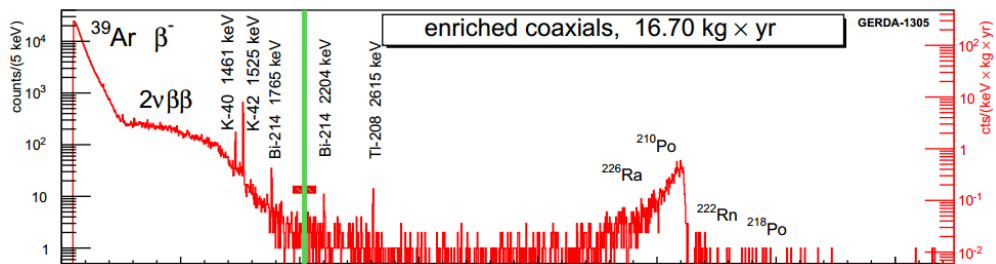


**Figure 2.4:** Energy spectrum acquired in Phase I until May 2013 by the enriched semi-coaxial detectors. The blinded ROI is marked by the green bar. Figure from [59].

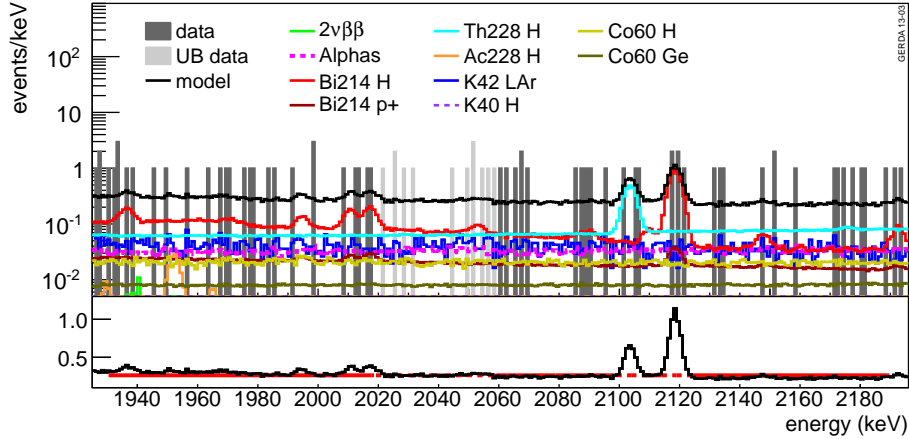


**Figure 2.5:** Measured events around  $Q_{\beta\beta}$  with blinded ROI. Superimposed is the minimal background model and the individual components in this model [59]. H stands for contaminations in the detector holders, Ge in the detector bulk, p+ on the readout contact and LAr for liquid argon close to the detector surface. The p+ readout contact is also the location of the alpha events. Figure from [59].

## 2.3 Detector Types and Pulse Shape Discrimination

GERDA is using custom produced BEGe-type detectors additionally to the previously mentioned semi-coaxial detectors. Both have the high voltage contact on the outer n+ surface. The semi-coaxial detectors have the p+ readout contact in a borehole of the detector (left in Figure 2.6). The BEGe-type detectors are shorter and have a readout pad on one face of the detector (right in Figure 2.6). This results in different distributions of the weighting potential, which is a measure of the amount of charge induced on the readout electrode by a probe charge at the respective location.

SSEs occurring in the bulk of a semi-coaxial detector result in very different pulse shapes, depending on the location of the energy deposition. Such pulse shapes, simulated in the framework of the PhD thesis of Matteo Agostini [63] are shown in Figure 2.7 on the left. This makes a distinction of single and multi site events difficult. GERDA employed in Phase I an artificial neural network to perform this task [60]. An additional method investigated in the framework of this thesis employs a support vector machine. This is described in detail in Chapter 5. On the other hand, for BEGe-type detectors, SSEs in the bulk result in very similar pulse shapes independent of the interaction site. This results in significantly increased

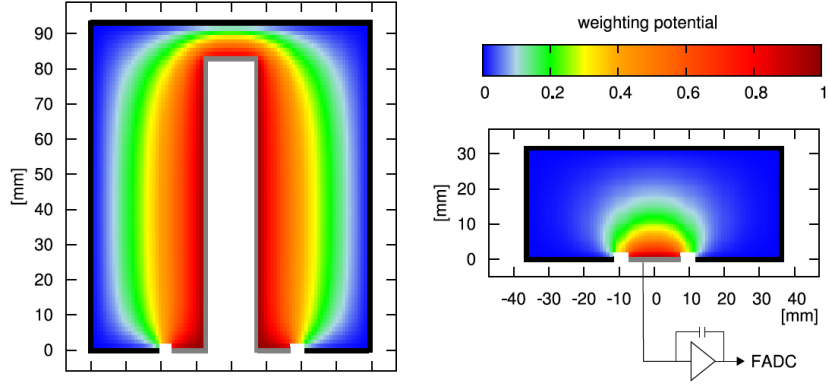


**Figure 2.6:** Weighting potential in a cut through the rotation symmetry axis of a semi-coaxial (left) and BEGe (right) type detector. Figure from [60].

pulse shape discrimination capabilities. The method for BEGe-type detectors is described more detailed in Chapter 6.

## 2.4 Phase I Results

The unblinded energy spectrum at the ROI is shown in Figure 2.8 for the full Phase I data set of 21.6 kg yr. Filled and empty histograms correspond to events accepted or rejected by pulse shape discrimination, respectively. A profile likelihood analysis lead to a best fit of zero events from the neutrinoless double beta decay. This results in a 90% C.L. lower limit of  $> 2.1 \cdot 10^{25}$  yr [61] on its half-life. It disfavours the long standing claim of signal observation [64] with high probability. Combining the results with the former HdM [54] experiment and IGEX [53] yields a limit of  $> 3 \cdot 10^{25}$  yr. This corresponds to a limit on the effective electron neutrino Majorana mass of  $< 0.2 - 0.4$  eV, depending on the employed calculations of the nuclear matrix element. Further details are described in [61].

## 2.5 Upgrades for Phase II

Reducing the background index by one order of magnitude and collecting five times the exposure compared to Phase I requires several upgrades. This includes an improvement of the preamplifiers and detector contacting to reduce electronic noise. Additionally new, lower activity holders were developed employing plates made of silicon. The Phase I radioactive calibration sources were replaced by custom made low neutron flux sources developed in the framework of a PhD thesis at

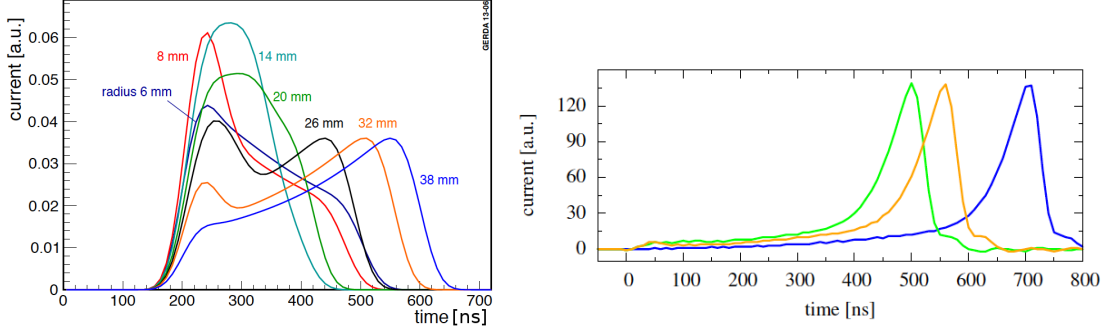


**Figure 2.7:** Simulated current pulses of single site events for different interaction locations. Left: semi-coaxial Phase I detectors. The borehole is at a radius of 6 mm and the outer n+ readout electrode at 38 mm. All interactions were simulated at the same longitudinal position. Superpositions are hardly distinguishable from single site events. Figure from [60]. Right: BEGe-type Phase II detectors. Superpositions are well distinguishable from SSEs. Figure from [63].

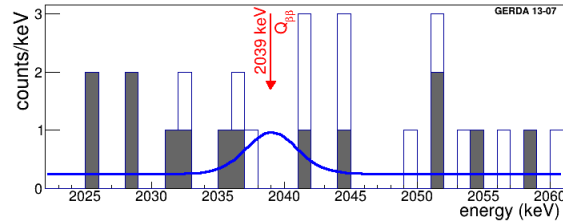


**Figure 2.8:** All events in the ROI for the GERDA Phase I data (21.6 kg yr) after unblinding. Filled and empty histograms correspond to events accepted or rejected by pulse shape discrimination, respectively. The spectrum superimposed in blue corresponds to our limit on the half-life of the neutrinoless double beta decay of  $> 2.1 \cdot 10^{25}$  yr at 90% C.L.. Figure from internal GERDA resources.

the University of Zurich [32]. Upgrades were also applied to the calibration system responsible for the positioning of the calibration sources. These are described more detailed in Chapter 7. The procurement of new BEGe-type detectors and the installation of a liquid argon veto system are described in the following. Further information about upgrades for Phase II is provided in [65].

### 2.5.1 Procurement of High Purity BEGe Type Detectors

Thirty new high purity BEGe-type detectors with a total mass of approximately 20 kg were procured. These detectors have significantly enhanced pulse shape discrimination capabilities compared to the semi-coaxial type (compare to Section 2.3). The germanium was enriched to approximately 86 % in  $^{76}\text{Ge}$  in the form of  $\text{GeF}_4$  employing gas centrifuges at Svetlana department of the company "Production Association Electrochemical Plant" in Zelenogorsk in Russia [66].  $\text{GeF}_4$  was oxidized and transported to PPM Pure Metals GmbH [67] in Langelsheim in Germany where it was transformed to metallic germanium and purified by zone-refinement. The material was then shipped to Canberra Industries Inc. [68] in Oak Ridge in the USA to pull crystals with a final purity of 12N (1 impurity atom per  $10^{12}$  germanium atoms). These crystals were cut into slices and shipped to Canberra Semiconductors N.V. [69] in Olen in Belgium. There, BEGe detectors were produced from those slices. The exposure of the material to cosmic rays was minimized to reduce activation of the germanium. The material was therefore stored underground near by the respective production sites, whenever not in use. It has been ensured by on-site shifts of GERDA members. I was participating in the shift duties, for the crystal production in Oak Ridge, USA. Any material was placed in a shielding container for longer transportations. Further information on the material procurement, diode production and detector characterisation is provided in [70].

### 2.5.2 Liquid Argon Veto System

A large fraction of background events are in coincidence with an energy deposition in liquid argon, either by Compton scattering or due to a coincident emission of a gamma ray. Such an energy deposition in liquid argon results in the production of scintillation light with a wavelength of 128 nm. This vacuum ultra violet (VUV) light is shifted to blue light by a wavelength shifting coating containing Tetraphenyl-butadiene (TPB). It is then detected by (vacuum) photomultiplier tubes (PMTs) and silicon photomultipliers (SiPMs). The full liquid argon veto system, shown in Figure 2.9, is a hybrid of several components. Each detector string is surrounded by a Nylon cylinder brush coated on both sides with a solution of TPB and polystyrene. These Nylon cylinders are transparent to visible

light. A contribution to the development of this coating was made in the framework of this thesis and is described more detailed in Section 3.12. The top and bottom part of the veto consist of an array of nine and three PMTs respectively as well as a copper cylinder lined with dip-coated Tetratex. This wavelength shifting reflector foil was developed, tested, produced and installed in GERDA in the framework of this thesis. It is described in detail in Chapter 3. The PMTs have a diameter of 3" and are of type R11065-20 mod from Hamamatsu [71]. Their windows are coated with a solution of polystyrene and TPB. A curtain of optical fibres of type BCF-91A evaporatively coated with TPB is surrounding the full detector array. The fibres are read out by SiPMs situated at the connection ring of the top lined copper and the central fibre cylinder. Employing fibres increases the active volume of the veto system beyond its diameter, which is limited by the diameter of the cryostat neck.

A large part of the veto system has already been deployed and proved its functionality. Preliminary measurements with this system showed a suppression factor of  $\sim 45$  for a  $^{228}\text{Th}$  source. Some modifications are currently applied to the system. This is expected to slightly improve the suppression factor. A test background run is conducted with five detector strings to get a first estimation of the effective suppression factor.

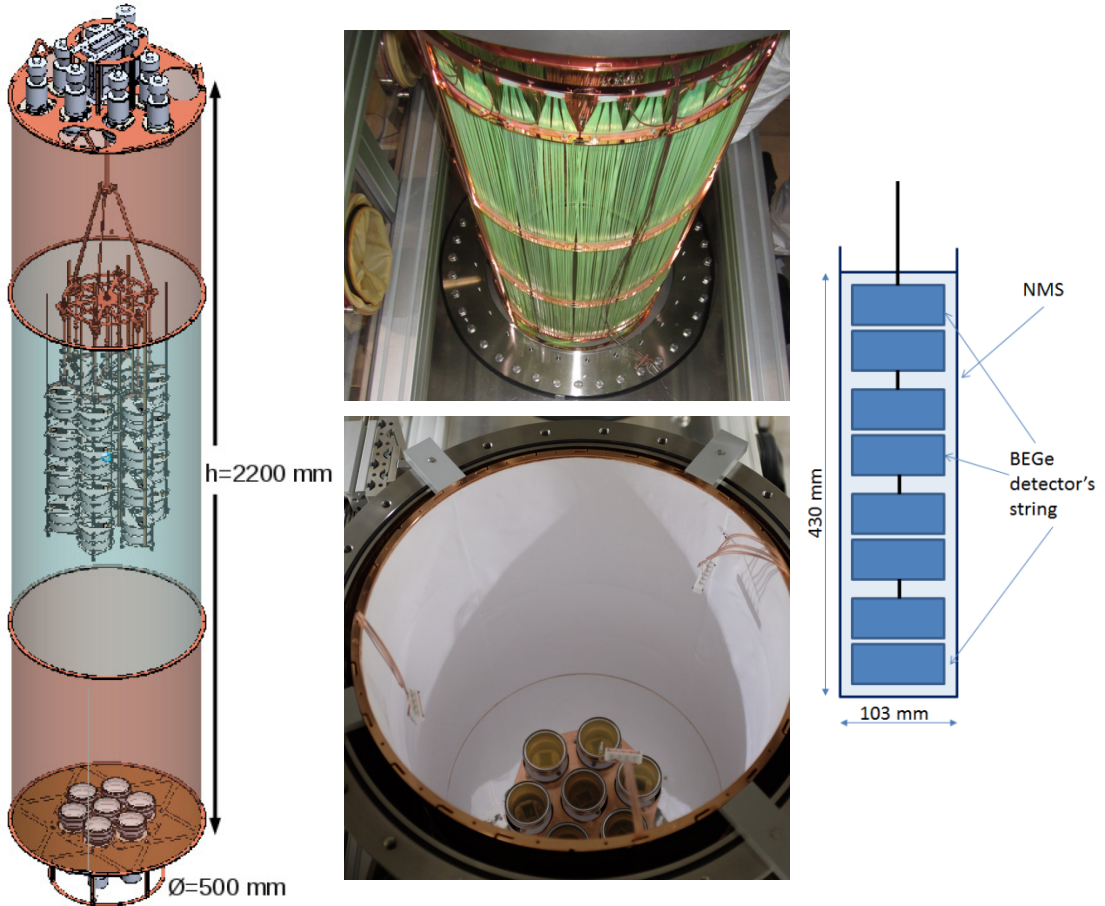


**Figure 2.9:** Left: drawing of the liquid argon veto system surrounding the detector array. It consists of a top and a bottom copper cylinder lined with TPB coated Tetratex and equipped with PMTs, as well as a central cylinder made of TPB coated optical fibres read out by SiPMs. Images from the liquid argon instrumentation group of GERDA.

## Chapter 3

# Development of Efficient Wavelength-Shifting Reflector Foils for Liquid Argon Scintillators

Liquid argon is used as a scintillator in several present rare event search experiments, such as GERDA [72], ArDM [73], DarkSide [74], DEAP [75] and ICARUS [76] and is a likely candidate for upcoming experiments. The liquid argon veto system of GERDA (described in Section 2.5.2) is an important part of the upgrade to Phase II [65], responsible for approximately one third of the background reduction.

Argon scintillation light has a wavelength of 128 nm which is below the transmittance of quartz which is a commonly used window material of light detection devices, such as the photomultiplier tubes (PMTs) employed in GERDA. Converting the light to longer wavelength overcomes this issue. The conversion is typically mediated by molecules excited by the VUV light. The excited molecule then decays through a cascade typically including one decay emitting visible light. A typical substance of this type is Tetraphenyl-Butadiene (TPB). Its emission maximum is at a wavelength of approximately 430 nm for an excitation with 260 nm light. This is shown in Section 3.3.

The coated reflector installed as part of the liquid argon veto system of GERDA is an outcome of the developments presented in this chapter. The focus is set on the production of square-meter-scale wavelength shifting reflectors with long-term stability in liquid argon, a high light yield and low radioactivity. The rejection efficiency of the liquid argon veto depends strongly on its light yield (compare [77] in chapter 4.4.5 and 4.1.3). Its optimisation is thus of high importance. The light yield of different coating and reflector combinations was therefore measured in liquid and gaseous argon in a setup developed especially for this purpose. It

provides conditions almost identical to those in large scale experiments. Many of these coatings are transparent to visible light. This allows a direct transfer of the results to applications where transmitted light is detected instead of reflected light, e.g. PMTs. Earlier developments for LArGe [78] and long-term stability issues observed therein were the starting point of this work.

## 3.1 Description of Reflector Foils and Coatings

All investigated coatings were applied onto one of the following three different materials, VM2000 Radiant Mirror foil from 3M [79], Tetratex crystal wrap from the Donaldson [80] or copper foil. The mechanical and optical properties of these foils and the applied coatings are described in this section, as well as the coating technique.

### 3.1.1 Properties of the Reflector Foils

VM2000 is a highly specular reflective multilayer polyester film with a thickness of  $110\ \mu\text{m}$ . It is very similar or possibly identical to Vikuiti<sup>TM</sup> Enhanced Specular Reflector(ESR) [81]. The reflectivity of the latter is given by the manufacturer as  $> 98\%$ . Immersion and moderate bending in liquid nitrogen does not cause any visible change to the foil. The inspection was also performed under an optical microscope. The foil is flexible to moderate bending and keeps permanent kinks if bent strongly. It is stiff in the longitudinal direction and resistive against moderate scratching with e.g. the finger nail, but not with sharp steel pieces. It is delivered with glue on its back side, which is removed prior to coating using acetone in order to exclude potential influence on the light yield by dissolved glue. VM2000 is fluorescent by itself with the emission maximum at a wavelength of approximately  $420\ \text{nm}$ . The emission spectrum for an excitation wavelength of  $260\ \text{nm}$  is shown in Figure 3.6.

Tetratex is a diffuse and highly reflective foil made of expanded PTFE. This fabric looks bright white and very flexible both to bending and stretching. This makes it very easy to be used to cover complex surfaces. The stretch is partly elastic and partly plastic (see also Section 3.11). Immersion and moderate bending in liquid nitrogen does not cause any visible change to the foil. This includes inspection under an optical microscope. Kinks and scratches result in reduced thickness at the location of the kink or scratch, which reduces the reflectivity at those locations. The susceptibility to both scratches and kinks is moderate and can be avoided by careful handling. The area covered by a kink or scratch is furthermore typically negligible compared to the area of the reflector. The reduction of the reflectivity is hence also negligible. The mechanical stability is

not noticeably reduced by scratches or kinks.

Foils with thicknesses of 38, 76, 127 and 254  $\mu\text{m}$  were tested. A thickness of 254  $\mu\text{m}$  was chosen for further developments because of the following considerations. This thickness has a reflectivity of approximately 95 % [81] at the emission wavelength of TPB of  $\sim 430$  nm. A part of the remaining 5 % is transmitted. This thickness is very resistant against ripping, which is important for the installation. Thicker or multiple layers of this thickness are not considered in order to minimise the amount of material to be installed in GERDA, reducing potential radioactive background. Thinner layers possess lower reflectivity and get deformed easily. Deformation reduces the reflectivity and potentially damages the coating.

The coating test on copper are relevant as it is a known low radioactivity material commonly employed for many components in various low background experiments. Coating copper parts which are illuminated by UV light can improve the light yield of such systems. Copper is quickly forming a dark oxide layer which was removed before the application of coatings by treating it in an acetic acid bath for 15 min and subsequent wiping with fuzz-free wipes wetted by acetone.

### 3.1.2 Coating Technique

All coatings developed in the framework of this thesis are produced by pulling the respective reflector foil at an angle of approximately  $45^\circ$  through a solution containing the fluorescent substance of interest. For this purpose, a tool was developed consisting of a bath holding the solution and two turning cylinders to guide the reflector. A CAD model of this tool is shown in Figure 3.1. The foil is fed above the small cylinder and pushed down into the bath by the big cylinder. The front side of the coated foil is facing downwards and does not get in contact with any surface after leaving the bath. After pulling a foil through the bath it is laid flat on its back side until the coating has dried. This takes from several second up to approximately 1 min depending on the used solvent and reflector foil. This coating process is well suitable for sheets with a size on the order of  $1\text{ m}^2$ .

The solution to coat a reflector foil is prepared dissolving a fluorescent substance, for some coatings together with a polymer to increase the mechanical stability. The polymer can additionally be active and transfer energy from absorbed photons radiatively and non-radiatively to the fluorescent substance. The latter eventually emits the shifted light [82, 83]. TPB is the key fluorescent substance in most of the coatings described in this chapter.

Several solvents were tested for their ability to dissolve TPB. All solvents were of p.a. grade. No or very little solubility was observed in ethanol, isopropyl alcohol and ethylene glycol. A clear solubility, however, with a saturation concentration below 30 g/l was observed for diethyl ether, toluene, acetone and butyl acetate. The saturation concentration was quantitatively determined

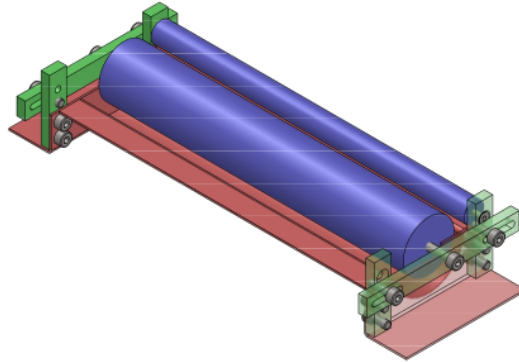


**Figure 3.1:** Tool developed for dip-coating. The foil to be coated is inserted between the two rolls and pulled through a bath below the thick roll containing the fluorescent substance. The face of the foil is pointing downwards.

for for dichloromethane, methyltetrahydrofuran and tetrahydrofuran, respectively with values of  $\sim 46$  g/l,  $\sim 16$  g/l and  $\gtrsim 30$  g/l, respectively. Dichloromethane was used as the standard, solvent for TPB-based wavelength shifter because of the good solubility of TPB and low vapour pressure. The latter assures a short drying time which is important to reduce the amount of dust getting in contact with the wet coating, which otherwise attaches to the reflector. This should be avoided as it is a potential radioactive and impurity emanating contamination. Dichloromethane does furthermore slightly dissolve VM2000, which is expected to result in an increased adherence of coatings. Tetrahydrofuran was considered as a more environmentally friendly alternative to dichloromethane. A solution of TPB in tetrahydrofuran is however yellowish in contrary to the other solutions which are clear. This might be a hint for a potential light yield reduction. This is confirmed by a measurement in gaseous argon presented at the end of Section 3.8.2.

### 3.1.3 Optical Properties and Thickness of Applied Coatings

This section describes the optical appearance of all investigated coating-reflector combinations. This includes the uniformity, as well as optical inspections employing a microscope, both under visible and UV light.

#### Coatings Containing TPB and Makrolon on VM2000

Dip-coating VM2000 with a solution containing only TPB results in very non-uniform depositions and low adherence. TPB can however be embedded into a polymer matrix of e.g. Makrolon to improve uniformity and adherence. The

material Makrolon was chosen because of the following known properties: high mechanical stability, hardness, resistivity to impact force and low temperatures. It was dissolved together with TPB in dichloromethane with a ratio of 20, 40, 60 and 80 % per weight of Makrolon. The total amount of both substances adds up to concentration of 31.3 g/l of dichloromethane in all four solutions. These were applied onto VM2000. In order to obtain uniform coatings it is important to continuously pull the sample through the solution at medium speed ( $\sim 3$  cm/s). Any non-continuity or a different pulling speed results in clearly non-uniform coatings. The larger the fraction of Makrolon the more uniform is the resulting coating. The resulting coated samples look “milky” (Figure 3.2 top left). The origin of this appearance are many small bubbles of different size in the coating layer, visible through an optical microscope (Figure 3.2 top right). They are present for coatings containing up to 60 % of Makrolon and also present for coatings on copper. This excludes the possibility that the bubbles originate from gases formed by the VM2000 in contact with dichloromethane. The “milky” appearance is not present right after the sample left the bath, but develops while the sample is drying. This suggests that the bubbles are gaseous dichloromethane getting trapped when the outer part of the coating layer dries faster than the inner part. Small air bubbles sticking to the surface from the beginning are unlikely given the just described observations. Adding more solvent to the solution, which results in a thinner coating, significantly decreases the number of bubbles per area and increases their diameter. A smaller number of bubbles in thinner coatings is consistent with the proposed mechanism producing the bubbles. The appearance under UV light (Figure 3.2 bottom left) is very similar to the appearance under visible light. Micro crystals are visible for a concentration of 80 % TPB and 20 % Makrolon (Figure 3.2 bottom right). These are most likely crystals of pure TPB not embedded into the polymer matrix. Coatings with this ratio appear significantly more white, which is caused by a larger fraction of diffusively reflected light.

The thickness of each coating was determined measuring the weight of small reflector samples before and after coating. With the coating tool described above and shown in Figure 3.1 it is however not possible to avoid an undefined amount of coating being also deposited on the backside of the reflector foil. Coatings to measure the thickness were therefore produced by dipping a sample vertically into a bath and pulling it out slowly (also vertically). A drop usually forming at the lower end of the sample is removed by a tissue. Pulling vertically instead of under an angle of  $45^\circ$  is assumed to result in a similar coating thickness as obtained using the coating tool. From five measurements for VM2000 with 80 % Makrolon and 20 % TPB, a thickness of  $0.082$  mg/cm<sup>2</sup> was obtained with a standard deviation of  $\pm 10$  %.

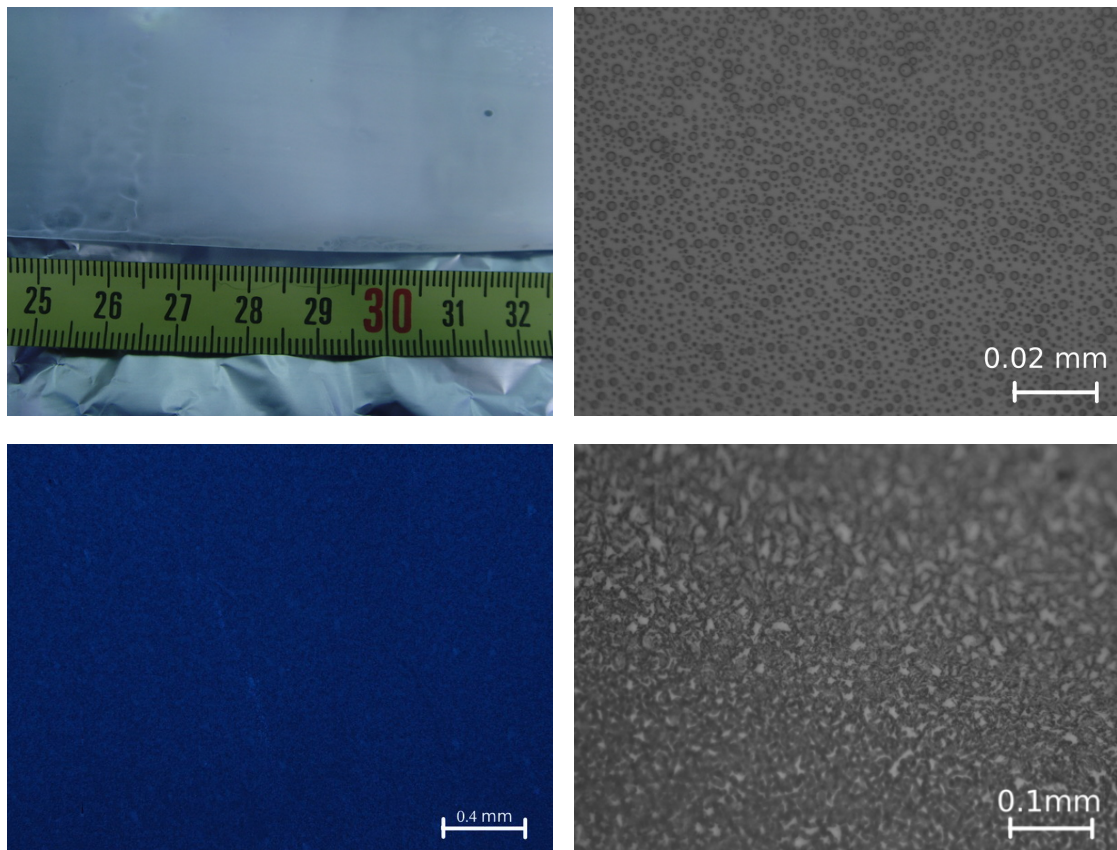


**Figure 3.2:** Coatings containing TPB and Makrolon. Top left: typical “milky” appearance of coatings containing up to 60% of TPB. Top right: microscopic bubbles are the origin of the “milky” appearance. Bottom left: the coatings have the same appearance under UV light. Bottom right: typical micro crystals present in coatings with 80% TPB and 20% Makrolon.

### Coatings Containing TPB and Polystyrene on VM2000

A different coating in which TPB is embedded in a polymer matrix is obtained dissolving 3 g/l of TPB together with 30 g/l of polystyrene (PS) in Toluene. This was found to be a good coating for liquid argon scintillation light in [84] and is currently used in LArGe [78]. It was kindly provided by the MPIK Heidelberg. Coatings with PS and TPB on VM2000 are completely clear (Figure 3.3 top left) and appear uniform, both under UV and visible light. Small non-uniformities are observed employing an optical microscope. It is however difficult to see the coating at all if there are no scratches, as shown in Figure 3.3 on the top right. Four samples of VM2000 were used to determine the thickness as described in the previous section. The mean thickness is  $0.073 \text{ mg/cm}^2$  with a variation of  $\pm 15\%$ . One additional sample of VM2000 was coated without prior removal of the glue on the backside in order to investigate possible effects of glue residuals on the stability and light yield. Illuminating reflector foils coated with TPB and PS with UV light results in bright blue edges. This is caused by light undergoing total reflection inside the coating layer, which can escape at the edges due to a larger incidence angle. This coating was also applied to copper. Here it also appears completely transparent (Figure 3.3 bottom left). Employing an optical microscope there is only the structure of the copper visible (Figure 3.3 bottom right). This microscopically uneven surface most likely increases the adherence of the coating.

### TPB Coatings on Tetratex

The fabric nature of Tetratex causes the solution to be soaked up quickly. This results in coating to be deposited on both sides of the foil as well as inside the foil. Due to this property it is possible to coat Tetratex with a solution containing only TPB and the solvent. Tetratex sheets shrink while the solution is drying and become curly (Figure 3.4 top left). The length of the sides of the sheets is reduced by  $\sim 40\%$ . This can be avoided by fixing it to a PTFE sheet, e.g. by staples (Figure 3.4 top right). The PTFE and staples were cleaned with ethanol in an ultrasonic bath. These sheets become very flat after drying. They look perfectly white under visible light, both by eye and employing an optical microscope (Figure 3.4). Under UV light there are small spots visible which are more bright than the rest. These spots have a size in the range of  $\sim 0.1$  to 1 mm. The spot size is varying from coating to coating even for the same concentration of TPB in the solution. The area covered by these spots increases with the concentration of TPB in the solution. A picture of a coating with a thickness of  $0.73 \text{ mg/cm}^2$  is shown in the bottom right in Figure 3.4. A sample employing Tetrahydrofuran as solvent instead of dichloromethane resulted in an identical appearance.

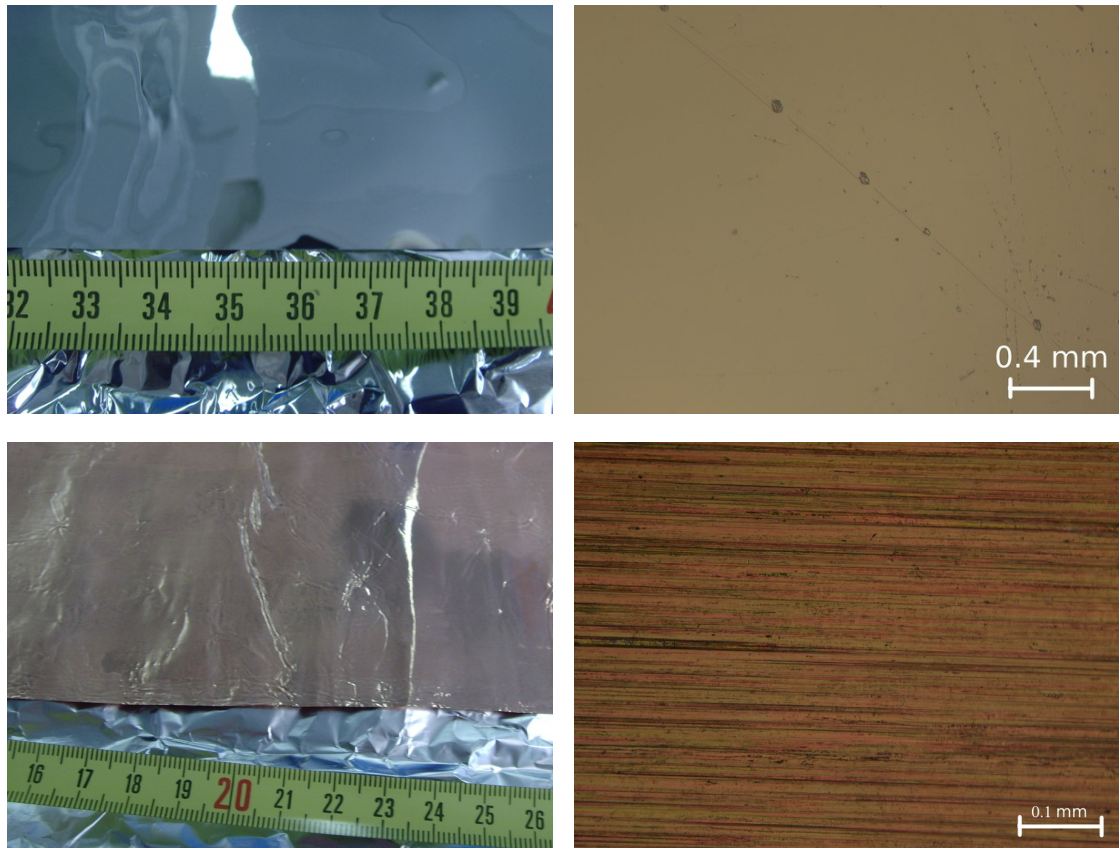


**Figure 3.3:** Coatings with a PS and TPB mixture. Top left: completely clear coating of VM2000. Top right: microscope picture of coating on VM2000 which becomes visible due to the presence of scratches. Bottom left: coated copper foil. Bottom right: same copper foil under the microscope revealing the surface structure of the copper.

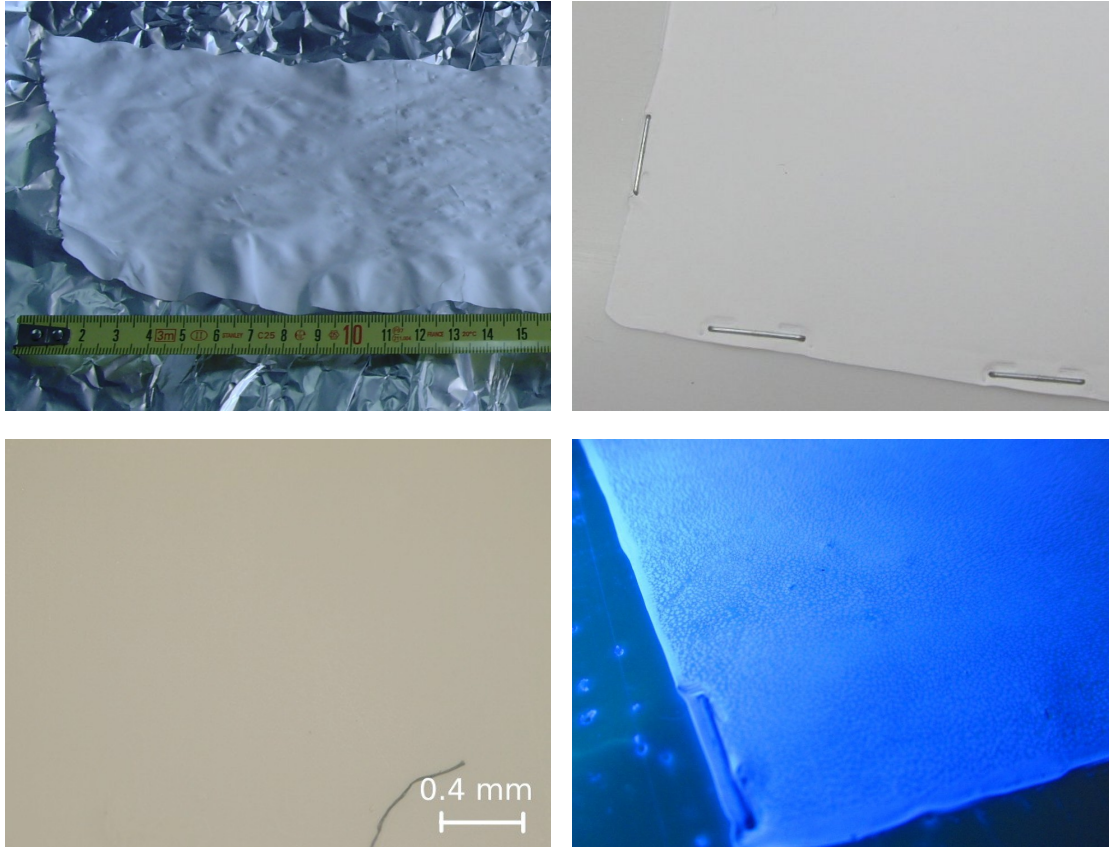


**Figure 3.4:** Tetratex coated with pure TPB. Top left: Tetratex sheet shrinks while the solution is drying and gets curly. Top right: coated Tetratex which was stapled onto a PTFE sheet to prevent shrinking. It is perfectly white under day light. Bottom left: there is no structure visible even with the microscope. The dark line on the bottom right corner of this photograph is a dust particle used to focus the microscope. Bottom right: many spots visible under UV light with sizes in the range of  $\sim 0.1$  to  $1$  mm which are brighter than the rest.

Additionally, a sample of Tetratex was coated with a solution containing 40 % Makrolon and 60 % TPB . This coating looks very similar to coatings containing TPB only but does not possess speckles. The thickness of all coatings on Tetratex was determined on samples which were coated employing the previously described coating tool. It is given as weight of TPB per sheet size and not, as in the case of VM2000 or copper, per surface area. The reason is that the coating is not deposited as layer of coating on both sides of the Tetratex as for the other foils, but rather on the PTFE fibres in the entire depth of the Tetratex. The deposited amount of TPB can be chosen from 0 to 1.18 mg/cm<sup>2</sup> by different concentrations of TPB in the solution. The thickness of these coatings was reproducible within  $\pm 3\%$ . This uncertainty is assumed for the thickness of all TPB coatings on Tetratex.

### **VM2000 Coated with Organic Scintillators**

Commercial plastic scintillators are also good candidates for an efficient wavelength shifter due to the similarity of the scintillation process to the wavelength-shifting process. In scintillators, ionising particles excite atoms or molecules which decay with the emission of light with a wavelength corresponding to an energy below the lowest excitation energy. A photon with an energy above the lowest excitation energy gets absorbed and re-emitted with the same wavelength of the scintillation light. Investigated were plastic scintillators of type UPS-923A, BCF-10 and BC 408. This was performed in a second coating campaign. The scintillators were dissolved in Toluene with a concentration of 33 g/l and coated onto VM2000. All of them result in coatings which look identical to those with PS and TPB. This includes the trapping of part of the shifted light in the coating layer and its release at the edges. The thicknesses of these coatings are 0.16 mg/cm<sup>2</sup>, 0.26 mg/cm<sup>2</sup> and 0.25 mg/cm<sup>2</sup>, respectively. Each thickness was measured from three samples and found to vary by approximately 10 %.

### **VM2000 and Tetratex Evaporatively Coated with TPB**

Two samples which had been evaporatively coated with TPB were also investigated. A Tetratex sample prepared as described in [85] and a VM2000 sample prepared as described in [86]. These were kindly provided by the respective groups. For the apparatus used for the first sample, a capability to coat reflector sheets with up to 120 × 25 cm<sup>2</sup> is reported. For the latter a maximum size of  $\sim 45 \times 45$  cm is estimated from the information provided in their publication. Both samples are diffusively reflecting and white, without visible structures, both by eye and employing an optical microscope. The appearance of both samples is similar to Tetratex dip-coated with pure TPB. They are also uniform under UV light, in contrary to the dip-coated Tetratex. The TPB layer is thick enough for both samples that

the reflective and fluorescent properties are dominated by the TPB. These properties are hence expected to be identical to those described in [85]. It is therefore sufficient to measure the light yield of one of the two samples and compare the mechanical properties of the two.

### 3.1.4 Summary of Available Coating-Reflector Combinations

Summarising, the following coatings applied to VM2000 are investigated: VM2000 dip-coated with TPB + Makrolon in various ratios, polystyrene + TPB with a ratio of 10:1, UPS-923 A, BCF-10, BC 408, evaporatively coated with pure TPB and uncoated. Coatings applied to Tetratex: dip-coated with pure TPB in various thicknesses, with 40 % Makrolon + 60 % TPB and evaporatively pure TPB. Furthermore a de-oxidized copper foil was coated with 60 % TPB + 40 % Makrolon and polystyrene + TPB with a ratio of 10:1.

## 3.2 Mechanical and Cryogenic Stability

Several mechanical tests were performed with a sample of each type of the previously described coating-reflector combinations. Tests include bending, blowing of air, wiping and scratching. One of the three categories, “no damage”, “minor damage” and “significant damage” was assigned to each sample for each of the tests. Bending was applied with a radius of approximately 1 cm. Blowing onto the sample was performed with pressurised air from an air pistol at a strength comparable to strong blowing by a human. Wiping was done with the finger tip in a Vinyl glove applying moderate pressure. Scratching was done with a sharp edge of a stainless steel plate applying moderate pressure. The mechanical stress expected when handling a reflector foil for installation with normal care corresponds to the wipe test. Wiping over Tetratex dip-coated with pure TPB, as well as over VM2000 evaporatively coated with TPB, results in small amounts of TPB on the glove visible using UV light. It does not leave observable traces on the foil itself, both under UV and visible light, for this reason are these samples categorised as “minor damage” for wiping. The results of the mechanical stability tests together with characteristic sample properties are presented in Table 3.1. UPS-923 A, BCF-10, BC 408 and coatings of PS with TPB have very similar mechanical properties and are therefore reported in the same column. The mechanical properties of the coatings are similar for deposition on copper and VM2000.

The cryogenic stability was tested on a sample of each coating, except of UPS-923 A, BCF-10 and BC 408. These were not considered due to lower light yield compared to other coatings (see also Section 3.8.3). Each sample was cycled 10

CHAPTER 3. DEVELOPMENT OF EFFICIENT WAVELENGTH-SHIFTING  
REFLECTOR FOILS FOR LIQUID ARGON SCINTILLATORS

---

reflector	Tetratex		VM2000 / copper			
characteristic	elastic, fabric		stiff, multilayer / plastically deforming			
coating	dip	evap.	evap.	Mak. $\geq 40\%$	Mak. 20%	PS 91%
reflectivity	diffuse	diffuse	diffuse	$\sim$ specular	$\sim$ diffuse	specular
bending	+	+	+	+	+	+
blowing	+	-	+	+	+	+
wiping	o	-	o	+	-	+
scratching	-	-	-	-	-	-
cryogenic	+	+	+	+	+	o

**Table 3.1:** Summary of primary mechanical and optical properties of coatings and reflector foils, as well as results from mechanical stability tests. All coatings contain TPB, the type and fraction of admixture is given if applicable. Mak. is used as an abbreviation for Makrolon. Coatings with PS-923 A, BCF-10 and BC 408 were not tested for cryogenic stability. They possess similar properties as PS+TPB coatings otherwise and are therefore not listed separately. Categories are as following: “+” for no observed damage, “o” minor damage and “-” significant damage.

times between liquid nitrogen and room temperature, bent inside liquid nitrogen and stored in liquid nitrogen for 72 days afterwards. All samples were then inspected for cracks or detached pieces employing an optical microscope. The only sample showing a difference after this procedure is PS + TPB coated on VM2000. Cracks developed in this coating already after the first immersion into liquid nitrogen without bending, preferably at sub-mm to mm scale locations having a thicker coating, due to imperfection of the coating method. Such cracks are shown in Figure 3.5. They are barely visible with the naked eye showing the importance of inspection under an optical microscope. A further deterioration was not observed in the course of the test procedure. The development of cracks during the first immersion was confirmed employing further samples of the same coating. The coating spoiled with glue from VM2000 showed the same behaviour. Cracks were not observed in coatings of PS + TPB on copper. It is however possible that they have been missed because of the surface structure of copper, which strongly dominating the picture under the optical microscope. The mechanical tests previously described were repeated after the cryogenic stability test. All samples showed the same properties as before.

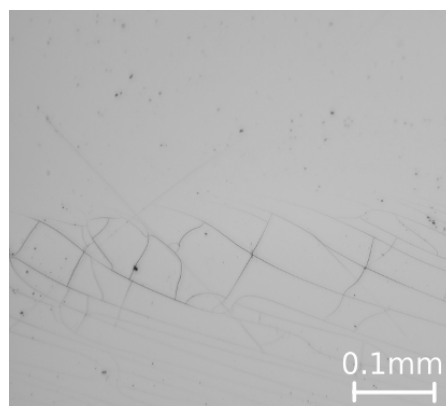


**Figure 3.5:** Picture of cracked PS + TPB coating on VM2000 after immersion in liquid nitrogen.

### 3.3 Fluorescence Spectra for an Excitation Wavelength of 260 nm

A preselection of coated samples was performed based on emission spectra measured with a fluorescence spectrometer of type Cary Eclipse from the Varian company [87] at the MPIK Heidelberg. The device automatically corrects for its spectral sensitivity and is regularly calibrated by the producer. The emission spectra of all types of coatings described in Section 3.1 except of the commercial scintillators have been measured. In order to investigate the uniformity, measurements were performed at 2 to 6 different locations on the samples. The commercial scintillators were not measured since they were coated in a later campaign. The fluorescence spectrometer employs a monochromator to select a specific excitation wavelength from a continuous spectrum. Samples were installed at an angle prohibiting specular reflectance into the spectrum analyser to reduce background from excitation light in the sample emission spectra. A peak at twice the emission wavelength is nevertheless observed in all spectra. It originates from unshifted 260 nm light diffusively reflected by the sample. It is observed at seemingly 520 nm as the diffraction angle of 520 nm is equal to the second order diffraction angle of 260 nm. The excitation wavelength was chosen to be 260 nm as it is the lowest wavelength where light with twice the wavelength is not present in a relevant part of the emission spectra of the coated samples. Typical spectra of the measured samples are shown in Figure 3.6. The area under the peak at 520 nm ( $= 2 \times 260$  nm) is a measure of the diffuse reflectivity of the sample and not related to the shifting efficiency. A large peak at 520 nm as observed for dip-coated Tetratex does hence mean a large diffuse component of the reflectivity (diffuse reflector). A small peak on the other hand means a small diffuse component as for uncoated VM2000. The fluorescence

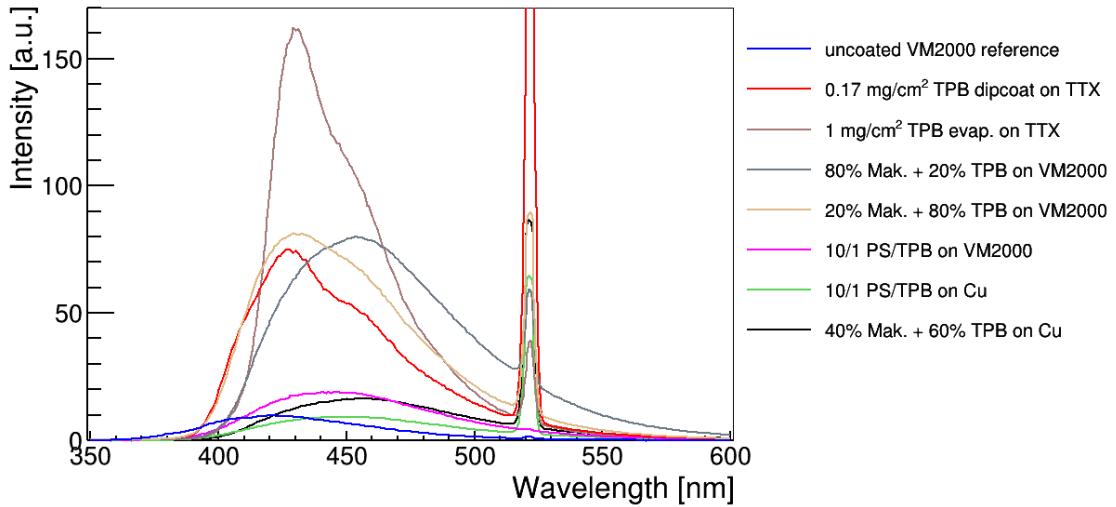


**Figure 3.6:** Typical fluorescence spectra of coated reflector foils using an excitation wavelength of 260 nm. A larger area corresponds to a larger light yield for the given excitation wavelength. The peak at 520 nm originates from unshifted, diffusively reflected light of 260 nm and is a measure for the diffusivity of the sample. It is not related to the light yield.

efficiency is related to the integral over the entire spectrum subtracted by the integral of the peak at 520 nm. Uncoated VM2000 (blue lines in Figure 3.6) was used as reference in order to monitor the time stability of the measurement apparatus, as well as the reproducibility of the measurements. The maximum amplitudes of VM2000 spectra vary by approximately  $\pm 10\%$  around the mean value. This is the approximate uncertainty on the fluorescence spectrometer measurements.

The highest light yield is observed for TPB evaporatively deposited on Tetratex (dark brown line in Figure 3.6). For the given thickness of the coating of  $1 \text{ mg/cm}^2$  it is expected to be strongly dominated by the properties of TPB, independent of the used substrate, as mentioned in Section 3.1. Fluctuations in the amplitude of the fluorescence spectra measured at different locations on this sample are below the fluctuations of the reference VM2000, which shows the uniformity of its light yield.

Coatings of Tetratex applied by wet dipping with  $0.17 \text{ g/cm}^2$  (red line in Figure 3.6) result in a wider spectrum of similar shape. The integral and hence efficiency is smaller compared to the evaporatively coated sample. The wider spectrum might be caused by interactions of TPB molecules with the PTFE of Tetratex. This might be more visible than in the evaporatively coated sample due to the thinner TPB layer. Another possibility is that some TPB molecules

might have been chemically changed either by dissolving in dichloromethane or by evaporation. Fluctuations in the amplitude of the fluorescence spectra measured with this sample are similar to the reference VM2000. This shows the uniformity of its light yield. The thickness of the TPB on the evaporatively coated sample is much larger. This is suggesting a thickness dependence of the light yield which is further investigated in Section 3.8.2.

All coatings with TPB + Makrolon on VM2000 have a similar integrated intensity. Makrolon ratios of 60 and 80 % have additionally the same spectral shape. Representatively shown is the spectrum for 80 % Makrolon + 20 % TPB (gray line in Figure 3.6) and 20 % Makrolon + 80 % TPB (light brown line in Figure 3.6). Fluctuations in the amplitude of the fluorescence spectra measured at different locations on the sample with 80 % Makrolon + 20 % TPB are below the fluctuations of the reference VM2000. Fluctuations increase with increasing TPB concentration up to approximately 20 %. This confirms the observed non-uniform appearance of these ratios as described in Section 3.1.3. Coatings with high Makrolon content show a clearly different spectral shape with the maximum at longer wavelengths compared to pure TPB. This shows that Makrolon either lowers the emission energy of photons emitted by TPB by modifying its energy levels or emits the light itself. The spectral shape of coatings with 80 % TPB and 20 % Makrolon is similar to that of pure TPB with a small enhancement in intensity at longer wavelengths for the former. Tetratex coated with 40 % Makrolon and 60 % TPB possess the same integral and a similar spectral shape as VM2000 samples with the same coating.

Coatings with PS + TPB on VM2000 show an efficiency about twice of uncoated VM2000 but significantly lower than all previously described samples. Fluctuations in the amplitude of the fluorescence spectra measured at different locations on this sample are similar to the fluctuations of the reference VM2000. This shows the uniformity of its light yield. A VM2000 sample coated with PS + TPB, which had been spoiled with glue from the back side of the VM2000, shows about 20 % less efficiency. This is not very significant but a hint that the glue slightly reduces the light yield. It should hence not get in contact with coating solutions. The obtained fluorescence spectra are compatible in shape and height relative to those presented in [84].

Coatings on copper possess a significantly reduced efficiency compared to the same coatings on VM2000, which shows the importance of the reflector itself. PS + TPB on copper (green lines in Figure 3.6) has an efficiency which is similar to uncoated VM2000. The efficiency of Makrolon + TPB on copper is approximately twice as high. Fluctuations in the amplitude of the fluorescence spectra measured at different locations on these samples are about 20 %. This is twice as high as fluctuations of the reference VM2000 and suggests a stronger non-uniformity

compared to the PS + TPB coating on VM2000. These results are still important despite the relatively low light yield because they are showing the potential to significantly improve the light yield when detector components are present which can not be covered by reflector foils but can be coated with a wavelength shifter.

These measurements show that a thick coating of TPB on Tetratex will likely have the highest light yield among the measured samples. The second highest efficiency was observed for coatings with Makrolon + TPB. 80 %Makrolon + 20 % TPB is favoured amongst the different measured compositions due to the highest uniformity, while the light yield is the same. Coatings of Makrolon + TPB on copper resulted in approximately twice as much light emitted as for uncoated VM2000.

### 3.4 Scintillation Process in Gaseous and Liquid Argon

The scintillation light of argon has a wavelength of 128 nm. This is significantly shorter than the 260 nm of the fluorescence spectrometer. The light yield and emission spectra of coated reflector foils can be different for different wavelengths. It is therefore necessary to confirm the results at the excitation wavelength of interest. A special setup was built for this purpose. It allows to additionally study possible effects of argon gas and liquid argon ( $\sim 87$  K) both on the stability and light yield. The measured light yield in liquid argon might be slightly different compared to gaseous argon because of the following reasons. A change in temperature has been observed to cause a slight change in the emission spectrum of TPB [86]. The reflector does additionally undergo thermal contraction and the refractive index is different for liquid and gaseous argon. The latter results in changed refraction and reflection properties at the 'wavelength shifter' - argon and argon - 'light detection device' surfaces. A difference might be observed in particular for coatings acting as light guide for shifted light, as e.g. PS + TPB on VM2000.

The argon scintillation light is produced in the following process. Ionising particles in liquid or gaseous argon excite or ionise argon atoms. Those interact with other argon atoms and form neutral and ionised excited  $\text{Ar}_2$  dimers, also called excimers. Ions eventually neutralise with free electrons and the neutral excimers decay, emitting light with a wavelength of 128 nm. This process was described by [88] and is depicted in Figure 3.7. The energy of a 128 nm photon is below the lowest excitation energy of argon atoms, thus argon is transparent to this light and acts as a scintillator.

The excimers are produced either in a singlet or a triplet state with very distinct lifetimes but the same wavelength. The lifetimes are approximately 7 and

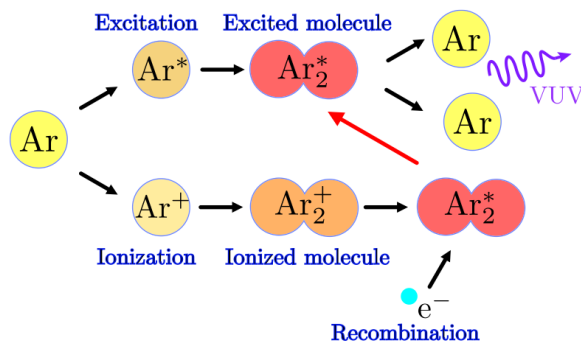


**Figure 3.7:** Illustration of the scintillation process in argon. Figure from [89].

1600 ns [90] in liquid argon. The observed decay time of the light pulse in gaseous argon is different. For the singlet component it is dominated by the excimer formation time for pressures below approximately 10 bar [91] where the (pressure-independent) decay time of the molecular state starts to dominate. The formation time is decreasing with increasing gas pressure [91]. In the same reference it is shown that the decay time of the light pulse from the triplet lifetime is pressure-independent with a value of ( $\sim 3200 \pm 300$ ) ns. This shows that the formation time is negligible compared to the (pressure-independent) decay time of the triplet state.

Impurities reduce the light yield and the lifetime, primarily of the triplet component [92]. Non-radiative deexcitations through collisions with impurities are the origin of both reductions. This provides the possibility to monitor the reduction in light yield due to impurities, by monitoring the triplet lifetime. This is an important property exploited in the measurements presented in this chapter. A reduction of the light emitted by the singlet component is relevant only for large impurity concentrations or setups in which VUV photons have to travel meter-scale distances before getting shifted. In the latter case VUV photons can get absorbed by these impurities.

### 3.5 Experimental Argon Setup

The argon setup is designed to measure scintillation light emitted by liquid or gaseous argon. A drawing of the setup is shown in Figure 3.8. Argon gas with a purity of 99.9999% (6.0) is filled from a gas bottle. Liquid nitrogen can be employed to condensate the argon gas on a copper cooling coil. The cooling power is regulated by the flow rate of evaporated nitrogen at the output side of this coil. The flow was initially controlled by a manual needle valve integrated into a flow meter. This was later replaced by an electronically driven regulating valve. The control is performed by a PID controller module using as input the pressure

inside the cryostat (further details are provided in Section 3.5.1). The liquid level is measured employing a capacitive level meter. The filling level is additionally verified by two PT100 resistance thermometers inside the chamber, located at the bottom of the cryostat and just above the PMT face. Further details about the level determination are provided in Section 3.5.2. The system can be evacuated by a turbo molecular pump.

Scintillation light is produced by 5486 keV alpha particles from a 30 Bq  $^{241}\text{Am}$  source exciting gaseous or liquid argon. It is installed in the centre of an aluminium disk confining the active volume from the bottom. The produced 128 nm scintillation light is then shifted to longer wavelength by a surrounding reflector foil forming a cylindrical shell (blue in the right drawing of Figure 3.23). The shifted light is detected with a 3 inch low radioactivity PMT of type R11065-10 from the Hamamatsu company [71] (see also Section 3.8.1), closing the top part of the active volume together with an aluminium and a PTFE ring. The active volume contains approximately 0.73 l which corresponds to 1.3 kg of liquid argon. The PTFE ring has four holes spread uniformly in the circular direction. These holes permit gas bubbles in liquid argon to escape in order to avoid a pocket of argon gas in front of the PMT window. A liquid-to-gas transition would reflect a fraction of the light resulting in a reduced light detection by the PMT. The downward facing PMT is held by an additional conical PTFE ring preventing it from floating in liquid argon. This PTFE ring is pushed down by four metal springs ensuring sufficient force applied to the PMT irrespective of thermal contraction. The reflector foil is the only system component which is coated by a wavelength shifter. As a result scintillation light hitting the PMT directly, the aluminium parts or the alpha source is reflected with low probability or absorbed without production of any PMT signal. A thick PTFE filler is placed between the cryostat wall and the active volume when operating in liquid to reduce the argon consumption. It is removed for measurements in gaseous argon to minimise the amount of emanated impurities, such as air and humidity trapped in the pores of the PTFE. The influence of these impurities when operating in liquid is much lower compared to operation in gas due to the significantly larger amount of argon in the chamber ( $\rho_{\text{liquid}} \approx 787 \cdot \rho_{\text{gas}}$ ) and a reduced mobility of impurity molecules at lower temperature.

The  $^{241}\text{Am}$  source was custom made for this setup by Dr. R. Dressler and Dr. I. Usoltsev at the Paul Scherrer Institut (PSI) [93]. The Am is deposited by molecular plating onto a round 25  $\mu\text{m}$  thick stainless steel substrate with 15 mm in diameter. The energy spectrum of the alpha particles emitted from the source is shown in Figure 3.9. It has been measured at PSI using a Canberra PIPS detector with 19 keV energy resolution. The source was tested for cryogenic stability cycling 10 times between liquid nitrogen and room temperature. The activity of the source

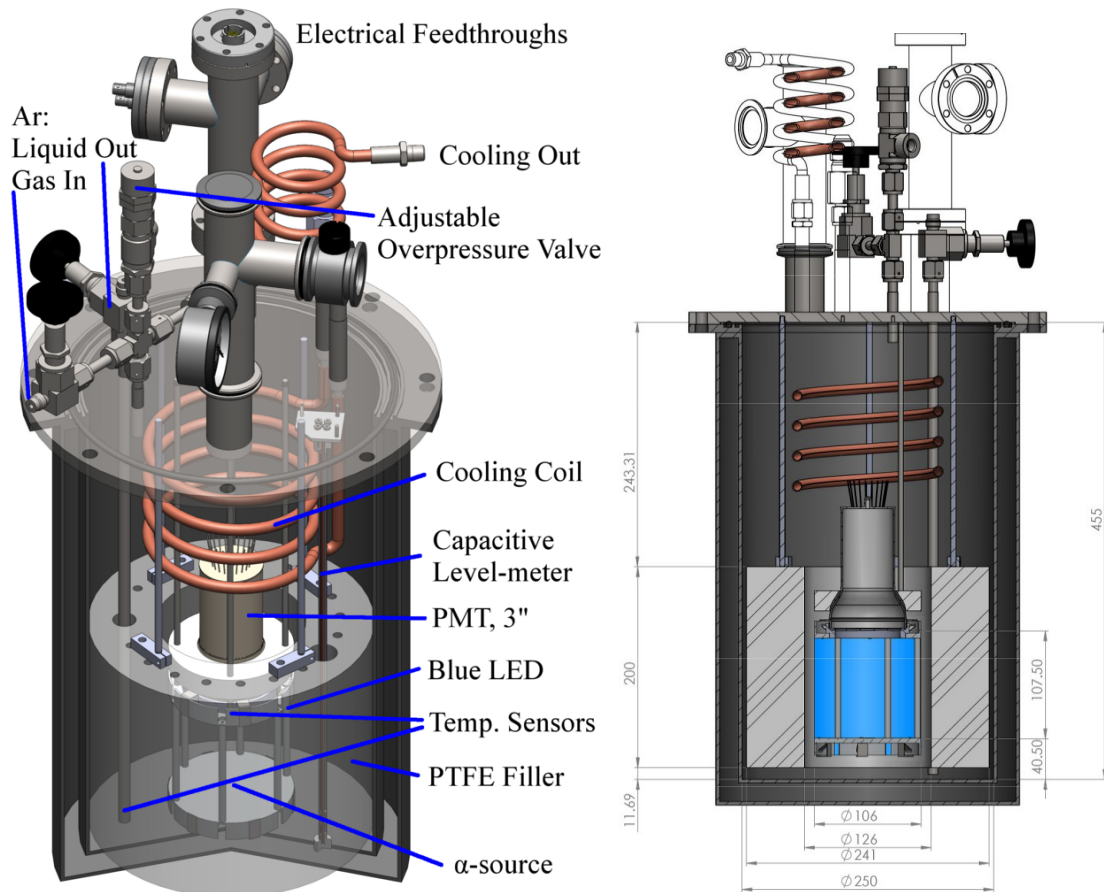


**Figure 3.8:** Schematic figure of the setup to measure the light yield in liquid argon obtained with different coated reflector foils. The setup is equipped with a 3 inch PMT of type R11065-10, an  $^{241}\text{Am}$  source, a capacitive level meter and a pressure controlled automatic cooling system. The position of the coated reflector is illustrated in blue in the right drawing. Dimensions are in mm.

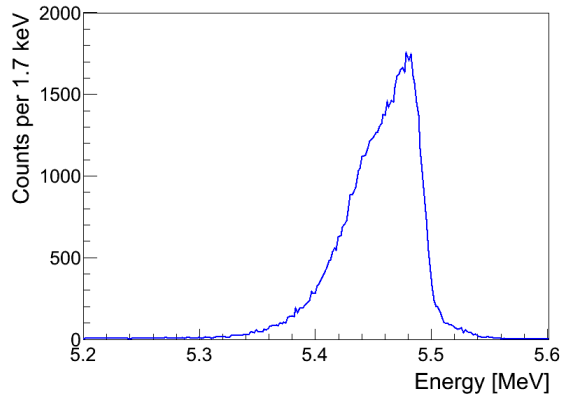


**Figure 3.9:** Alpha spectrum emitted by the  $^{241}\text{Am}$  source, recorded with a Canberra PIPS detector (active area  $600\text{ mm}^2$ ) during 15 min [94].

was measured for 15 min before and after this cycling employing the characteristic gamma line at 59.5 keV. The number of background-subtracted counts in this peak was 3496 and 3532, respectively. These values agree within statistical fluctuations. The source is further described in [94].

The setup is equipped with a mechanical analog pressure sensor with an operational range from a few mbar to approximately 3 bar absolute pressure. It is providing a gas independent pressure reading, which is important in particular for measurements in gaseous argon. Furthermore, the setup is equipped with an electronic gauge consisting of a cold cathode ion gauge for low vacuum pressures and a Pirani gauge operating up to ambient pressure. An adjustable overpressure valve set to open at 1.2 bar overpressure is protecting the dewar and PMT from damage.

Electrical connections are realised employing feedthroughs on three CF40 flanges. One feedthrough is housing two BNC connections, the second two SHV connections and the third a 19 pin MIL-C-26482 connector. These connectors are situated on the air side. One BNC is connected on the vacuum side to a  $50\ \Omega$  coaxial cable with PTFE dielectric and no outer insulation. This type of cable was chosen because of expected low emanation rates and stability in cryogenic environments. All other cables inside the chamber are of this type except of the high voltage cable. The ground and high voltage are connected inside the chamber by two separate PTFE-insulated cables without shielding. The signal and the high voltage cable are both soldered directly to the PMT base where the grounds of the two are directly connected. Both grounds are additionally connected to the chamber at the respective feedthrough.

The PMT base is made of PTFE populated by standard electrical components.

These have been arranged maximising the distance between blank metal parts in order to minimise the risk of electric discharges in argon gas. Sharp edges are avoided to eliminate strong electric fields which could trigger discharges. The high voltage pin at the base was wrapped with PTFE tape for additional insulation. A PTFE tube was put around the high voltage pin on the inside of the SHV feedthrough to prevent electrical discharges at this location, which is always in gaseous argon during measurements. The second BNC and SHV are spare to provide flexibility for upgrades or other uses of the setup.

The 19 pin MIL-C-26482 feedthrough is connected to several components. This includes the two PT100 temperature sensors, which occupy two pins each. The PT100 are read out by a bench-top digital multimeter with two channels. It directly converts the measured, temperature dependent resistivity into a temperature reading. A LED, which is installed inside the top corner of the active volume is connected with two further pins on the vacuum side. On the air side it is connected to an arbitrary pulse generator. The LED is wrapped with PTFE tape for attenuation and diffusion of the light. Three more pins are connected to the capacitive level meter which is described in more detail in Section 3.5.2.

The top flange of the chamber is additionally connected to the ground of the electronics rack by a separate grounding cable of large cross section. The rack is housing a power supply of type N1470 and an ADC of type V1720 from CAEN [95], both employed for the PMT.

The inner side of the cryostat body, as well as the PMT were cleaned with fuzz-free wipes wetted with ethanol. All other surfaces which get in contact with the argon are cleaned with ethanol in an ultrasonic bath. This includes the PTFE filler, cables and the PMT base.

### 3.5.1 Cooling System

Liquid nitrogen has a boiling point of  $\sim 77$  K which makes it a suitable coolant for liquid argon with a boiling temperature of  $\sim 87$  K. Liquid nitrogen is filled from a dewar by an insulated tube into a copper cooling coil, situated inside the upper half of the main cryostat volume. The cooling coil is fed through the top flange by a double wall tube to reduce thermal conductance to the top flange. An additional copper coil is connected on the output side, outside the cryostat to evaporate remaining liquid nitrogen. The cooling power is regulated by the flow of nitrogen gas on the output side. This was initially realised by a manual valve integrated into a mechanical flow meter of type VAF-G1-10M-1-0 from Swagelok [96] with a measurement range of 120 to 1200 stdl/h. The flow can however be increased significantly above this value, which was exploited to obtain fast cooldowns. The argon filling speed was then limited by the aperture of the pressure reducer at the argon gas bottle. A nitrogen flow of approximately 1050 stdl/min is sufficient

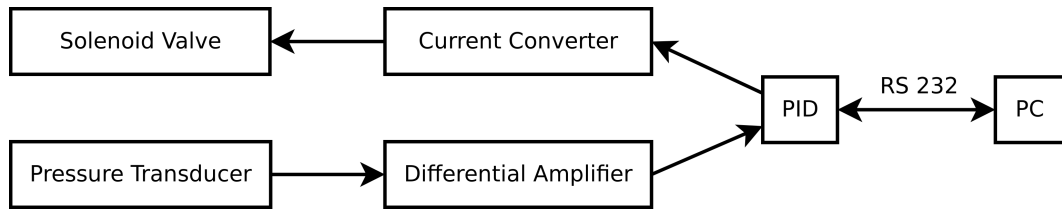


**Figure 3.10:** Block diagram of the automatic cooling system. PID controller is regulating the liquid nitrogen flow by a solenoid valve using the chamber pressure as control variable.

to maintain a constant pressure when filling is completed. It has to be slightly adjusted every few minutes, once stable conditions are reached. A sinter block is installed at the outlet of the flow meter to reduce noise caused by streaming nitrogen.

The manual valve was later replaced by a PID-controlled system, permitting long-term operations without the need of a person regularly adjusting the cooling power. A block diagram of this automatic cooling system is shown in Figure 3.10. The pressure in the cryostat is measured by a pressure transducer of type PX302-100AV from OMEGA Engineering Inc. [97]. It can operate in the range from 0 to 6.9 bar delivering a differential output voltage in the range of 0–100 mV, which is proportional to the pressure. The signal is converted to an absolute voltage (relative to ground) in the range of 0–10 V by a custom made differential amplifier. This is read out and displayed by a PID controller of type ESM-4450 from EMKO Electronics [98]. The pressure reading is calibrated by a two point calibration at 0 mbar and at ambient pressure. The PID controller is additionally driving the differential amplifier with 24 VDC. The latter provides 10 VDC to the pressure transducer. The PID controller is furthermore equipped with a module of type EMO-430 providing a current in the range of 0–20 mA. This control signal is shifted up by a custom made current converter, to a range of 0–200 mA, which is required by the solenoid valve. The converter is powered by a wall wart and the solenoid valve by the PID controller.

The controller can be set through its front panel or a software provided by the company running on a PC. The communication between the PC and the controller is carried out employing the RS 232 standard. The program is further more used to display and save the pressure reading, as well as the solenoid valve control signal. Remote control of the PC and hence the PID controller is permitted by the software Chrome Remote Desktop from Google.

The liquid nitrogen is delivered to the system from pressurised dewars containing 160 l. One such dewar lasts for approximately three days permitting to run over

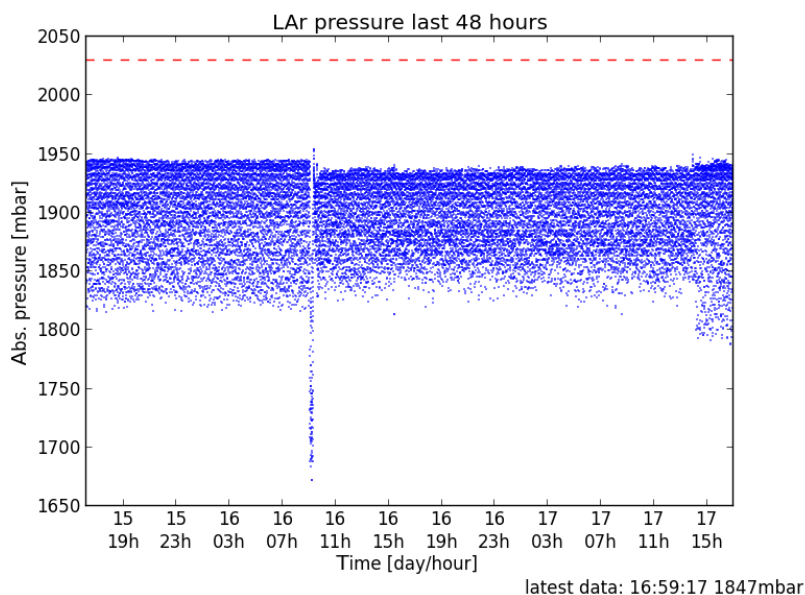


**Figure 3.11:** Absolute pressure reading in the cryostat of the argon setup while cooling with a PID-controlled system. The spike at approximately 9 am of the 16<sup>th</sup> is caused by the changing of a dewar, supplying the liquid nitrogen. The dashed orange line corresponds to the alarm threshold.

night and during the weekend, without the need of personal on-site presence. The level of liquid nitrogen is monitored remotely as described in Section 3.5.3. In order to change a liquid nitrogen dewar, it has to be disconnected from the insulated tube. The connection has to be heated up to room temperature beforehand. This operation results in an interruption of the cooling system for approximately 5 min. The system is beforehand cooled down to a pressure approximately 250 mbar lower than the operating pressure, in order to avoid exceeding this value. The development of the pressure during a measurement in liquid is shown in Figure 3.11. The spike at approximately 9 am of the 16<sup>th</sup> is caused by replacing the liquid nitrogen dewar.

The weight of the proportional (P), integral (I) and differential (D) contribution to the control signal for the solenoid valve were tuned manually. The pressure was stable within approximately  $\pm 60$  mbar. Nitrogen in the filling tube is partly liquid and partly gaseous. As a result an undetermined fraction of liquid nitrogen, with a much higher cooling power than gaseous nitrogen enters into the cooling coil when the solenoid valve opens. This unpredictability of the cooling power is driving the fluctuations. These are on the other hand not expected to have any effect on the

measurement of the light yield, as it is pressure-independent in liquid argon.

The nitrogen used for cooling is released into the laboratory room which might be a problem for people if the fresh air supply is not sufficient. Therefore the fraction of the volume  $r_N$  of the laboratory taken up by the nitrogen gas evaporated within one day was estimated based on a consumption of 160 l of liquid nitrogen in three days:

$$r_N = \frac{V_{NG}}{V_{Lab}} = \frac{\frac{\rho_{LN}}{\rho_{GN}} \cdot V_{LN}}{V_{Lab}} \approx 20 \%. \quad (3.1)$$

Hence approximately 20% of the volume of the lab is replaced by nitrogen from the cooling system per day when running with liquid argon. This is expected to be well compensated by the room ventilation. The nitrogen flow is significantly higher during cooldown, potentially lowering the oxygen fraction in the room by a notable amount. It is therefore recommended to open a window during this operation.

### 3.5.2 Liquid Argon Level Measurements

The liquid argon level is measured by two PT100 sensors, as well as a capacitive level meter. The level meter is a cylindrical capacitor with an empty volume of the dielectric. The inner electrode is a copper wire with a diameter of  $d_i = 1.2$  mm, while the outer electrode is made of a stainless steel pipe with an inner diameter of  $d_o = 6$  mm. Both are held and insulated from each other by PTFE end caps. A drawing of the level meter is shown in Figure 3.12. The capacity  $C(L)$  of such a geometry of 403 mm length  $L$  is given by

$$C(L) = \frac{2\pi\epsilon_r\epsilon_0 L}{\ln(d_o/d_i)} = 14\text{pF}, \quad (3.2)$$

where  $\epsilon_0$  and  $\epsilon_r$  are the vacuum and relative permittivity, respectively. The outer electrode has a slit along almost the full length of the level meter. This is allowing liquid argon to fill the space between the two electrodes with rising liquid level. The filling causes a change of the capacity due to the different relative permittivity of liquid (1.5 [99]) compared to gaseous argon (1). The capacity  $C(l)$  of a level meter filled with liquid argon up to  $l$  is the sum of the capacities of a capacitor with length  $l$  and  $\epsilon_r = 1.5$  and one with length  $L-l$  and  $\epsilon_r = 1$ :

$$C(l) = \frac{2\pi\epsilon_0}{\ln(d_o/d_i)}(\epsilon_r l + L - l) = \frac{2\pi\epsilon_0 l(\epsilon_r - 1)}{\ln(d_o/d_i)} + C(L). \quad (3.3)$$

The level is hence proportional to the current capacity of the level meter minus a constant offset. Three PTFE pieces with a height of 3 mm each were inserted into the level meter at known positions filling out the volume between the two

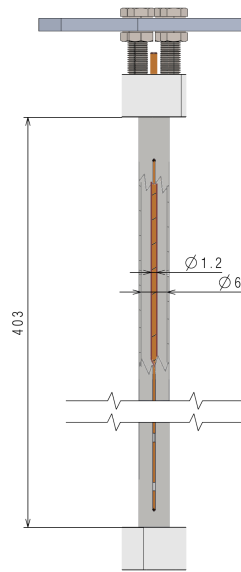


**Figure 3.12:** Drawing of the cylindrical capacitive level meter with a slit in the outer electrode. The slit permits liquid argon to fill the space between the two electrodes according to the filling level in the cryostat. In the bottom part of the slit are two small PTFE pieces acting as dielectric at their positions. These are used to calibrate the level reading. Dimensions are in mm.

electrodes at the respective location. They are used to calibrate the level measurement exploiting the fact that plateaus are expected at capacities corresponding to the levels of these PTFE pieces when filling the chamber.

Each of the two electrodes is connected by the core of a coaxial cable to a separate pin on the 19-pin feedthrough, both on the air and vacuum side. The shielding of both cables is connected to each other at the level meter, the vacuum and air side of the feedthrough, as well as on the readout board. The vacuum and air side shieldings are connected through one pin of the 19-pin feedthrough. This connection scheme was chosen to minimise the stray capacity of the cables.

The readout is performed using a Universal Transducer Interface (UTI) chip on an evaluation board. Both are from the company Smartec [100]. It was installed in a metal case to reduce electronic pick up noise. The coaxial cables coming from the liquid argon chamber are connected to the board using SMA (SubMiniature version A) connectors. The UTI chip can be run in different modes and the board has to be populated with resistors and capacitors correspondingly. Selected was “Mode 4” as named in the UTI manual version 3.0. In this configuration three capacities are measured. The maximum allowed capacity in this mode is 300 pF. The measurement values are of arbitrary units and need to be converted if a value

in the unit Farad is desired to be obtained. The conversion can be performed by a readout software when connection of the three slots is performed in the following way. One slot is connected to the level meter measuring  $C_M$ , one to a reference capacitor with  $C_R = 33$  pF and one left empty measuring  $C_0$ . The empty slot provides a measurement of the offset. The capacity of the level meter  $C_L$  (including stray capacities of the cabling) is then calculated as

$$C_L = \frac{C_M - C_0}{C_R - C_0} \cdot 33 \text{ pF}. \quad (3.4)$$

The UTI board is providing a RS232 interface for communication with a PC. The measured values are requested, displayed and written to an ASCII file by a Python script running on this PC. The data from the ASCII file is then plotted using a ROOT [101] script. It can be viewed remotely employing the software Chrome Remote Desktop from Google. The typical evolution of the capacity while cooling the chamber down and filling it with liquid argon is shown in Figure 3.13 on the left. The fluctuations (noise) in the measured capacities of this run are particularly low compared to other runs, revealing features in its evolution. The changes in capacity between 10:30 and 11:40 are attributed to thermal contraction of various level meter components. Changes in argon gas pressure can not be the origin of these variations as the relative permittivity of gaseous argon is much to close to 1 to change the capacity. The sudden rise at 11:44 is most likely the time when the liquid argon level exceeds the lower end of the slit in the outer electrode of the level meter and suddenly fills the lower part of it. The short steep rise at 11:48 might be caused by the bottom aluminium plate holding the alpha source, which is filling additional volume. The three small plateaus at 11:54, 12:00 and 12:06 are probably the three PTFE pieces in the level meter installed for calibration. These are not visible in most other measurements due to larger fluctuations in the capacity reading. The measured capacity is  $\sim 50\%$  larger than calculated. However, the calculated value does not take into account stray capacities of the cabling, hence these can well account for the larger measured value.

The calibration of the level meter is done based on five different levels. The first level is the bottom of the level meter, which is 25 mm above the bottom of the dewar. The minimum in capacity at approximately 11:38 is taken to correspond to this level. The beginning of the slit corresponds to a level of 38 mm and the bottom of the three PTFE pieces to 53, 77 and 112 mm, respectively. The volume occupied by the PTFE pieces does not get filled with liquid argon, which was taken into account. The fifth level is the top of the PTFE filler at 203 mm. These calibration points are shown together with a linear fit in Figure 3.13. The uncertainties on the read capacity is  $\pm 0.02$  pF. The uncertainty on the relative distance of the various calibration levels is 2 mm. The fitted curve is strongly inconsistent with the measured values, given these uncertainties. The distance of the components

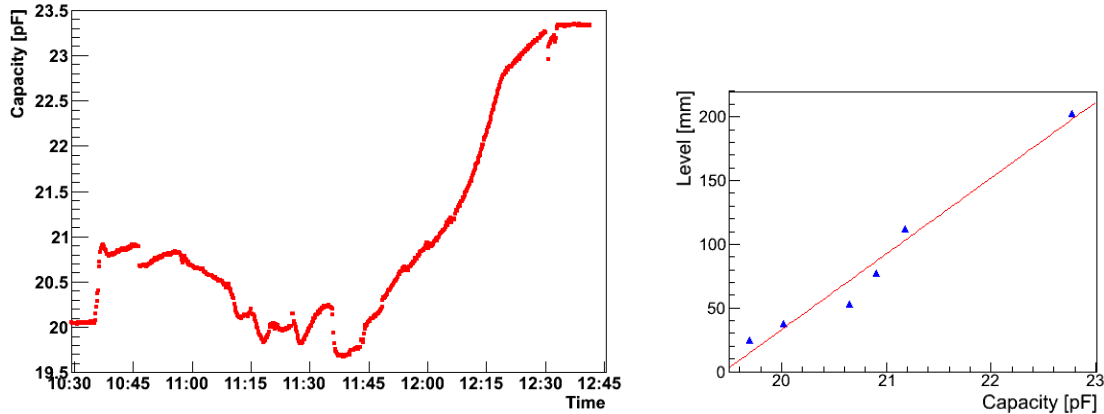


**Figure 3.13:** Left: typical capacity evolution of the level meter during cool down. It is fluctuating until liquid argon starts to enter the level meter at 11:44. From this point on, the capacity is rising with the level. Right: calibration points of the level meter with large discrepancy from a linear behaviour. Uncertainties on the measured values are similar to the marker size.

from the bottom of the cryostat is known with an uncertainty larger than  $\pm 2$  mm due to an imprecise knowledge of the shape of the bottom of the cryostat. If this value is measured wrong, it would cause an identical shift of all level. This shift corresponds to an offset of the fitted polynomial in Figure 3.13 and has no effect on the bad description. The capacity at the minimum just before filling is fluctuating by  $\pm 0.2$  pF for different fillings. The significant changes in capacity before the liquid level is rising are not understood in detail. For these reasons the level determined by the level meter is merely considered to be indicative. A method based on the amount of filled argon was therefore chosen as the primary method for the level determination. This method is described in the following.

A certain volume of liquid argon corresponds to a certain filling level. For light yield measurements it is not necessary to know the exact level. The only requirement is that the PMT face is completely immersed in liquid argon. It is therefore sufficient to know the volume required to reach this level. For this determination, liquid nitrogen was filled into the setup up to some specific levels. Reaching these levels is determined by eye, opening a KF flange on top of the cryostat. The volume of the liquid nitrogen was calculated by its weight (density = 0.81 kg/l), measured by placing the setup on a balance. This volume can then be used to calculate the amount of argon gas filled from a gas bottle, which corresponds to the same volume and the same filling level. Argon gas at room temperature has a density per bar pressure of  $\rho_{\text{gas}}/\text{bar} = 0.00178$  kg/(1 bar). The amount of liquid

CHAPTER 3. DEVELOPMENT OF EFFICIENT WAVELENGTH-SHIFTING  
REFLECTOR FOILS FOR LIQUID ARGON SCINTILLATORS

---

Level	Weight LN <sub>2</sub> [kg]	V <sub>liquid</sub> [l]	V <sub>Solidworks</sub> [l]	Δp [bar]
PMT face	2.7	3.3	2.7	52.5
PTFE filler top	3.3	4.1	3.7	64.2
PMT top	5.4	6.7	6.7	105.0
base top	7	8.6		136.1

**Table 3.2:** The volume required to reach a certain filling level is determined by the weight of filled liquid nitrogen and compared to the volume determined from Solid Works. The measured volume is furthermore used to calculate the pressure difference in a 50l argon gas bottle resulting from the condensation of the respective amount of liquid argon.

argon ΔV<sub>l</sub> filled from a bottle of volume V<sub>g</sub> which is causing a pressure change of Δp in the bottle can hence be calculated as

$$V_l = \frac{pV_g\rho_{\text{gas}}}{\text{bar}\rho_{\text{liquid}}}, \quad (3.5)$$

with ρ<sub>liquid</sub> = 1.4 kg/l the density of liquid argon. Assumed is a constant temperature. Positions, measured weight, calculated volume and corresponding pressure difference in a 50l gas bottle are provided in Table 3.2. The level when liquid argon touches the PMT face could not be seen properly and has a large uncertainty, all other levels were clearly visible. The volume calculated by the technical drawing program Solid Works is also provided for three different levels.

The volume determined with liquid nitrogen and Solid Works for the level “PMT top” are equal. The measurement for the level “PTFE filler top” is ~10 % larger than calculated by Solid Works. It has to be ensured that the liquid level is at least above the PMT face to avoid reflections of light at the liquid-gas surface, which would reduce the amount of light detected by the PMT. Therefore filling 60 bar was chosen as the standard procedure which is expected to provide a sufficiently large safety margin. This allows three fillings from one argon bottle. The filling level was verified by eye, opening a KF flange in the top part of the cryostat at the end of the respective measurements and was always found to be just below the top face of the PTFE filler. Impurities introduced by this procedure are irrelevant for consecutive measurements, as the KF flange is warm and argon gas is flowing out of the opened port. This prevents the formation of ice and the setup has to be opened anyway for the installation of the next sample.

The PT100 sensor just above the PMT face is used for level verification while filling. The temperature measured by a PT100 sensor drops suddenly by approximately 30 K when the liquid level reaches the sensor and stays at this temperature. An example of the temperature development during one cool down is shown for both sensors in Figure 3.14. The intermediate decreases in temperature of the top

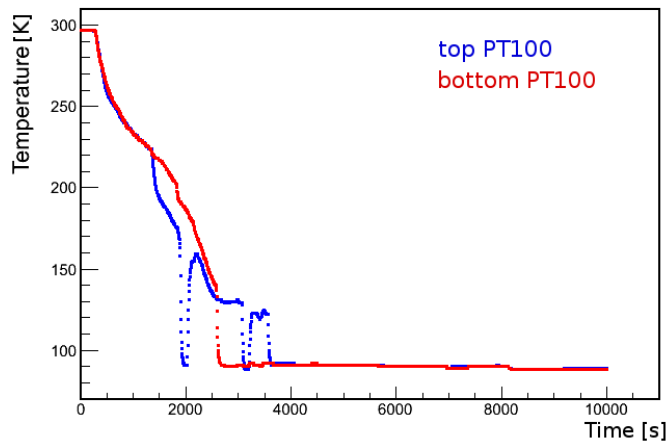


**Figure 3.14:** Evolution of the temperature during cool down and filling of the liquid argon setup. The top sensor is installed right above the PMT face indicating a sufficient filling level. The bottom sensor is installed at the bottom of the cryostat indicating the presence of liquid argon in the setup.

PT100 are attributed to liquid argon drops falling onto the sensor. The temperature difference between the top and bottom sensor is smaller than 0.8 K when both sensors are in the liquid. This behaviour was observed for all fillings and is considered to be a reliable verification for a sufficient filling level. The temperature reading can be accessed remotely employing the software Chrome Remote Desktop from Google.

### 3.5.3 Remote Monitor

A remote monitor is set up displaying all parameters relevant for stable operation. Of those, the pressure in the cryostat, the PMT filling level of the liquid nitrogen dewar feeding the cooling coil, the PMT high voltage and current are displayed on a slow control homepage common for the whole working group. It furthermore displays the number, date and time of the most recent run. This is realised using an existing software infrastructure which was adopted to the requirements for this setup and described in detail in the following. The pressure reading of the chamber is written to file by the PID controller software. It is automatically plotted for the last 48 and 168 h by a python script using matplotlib [102]. The plot is then transferred to a web server. If the pressure exceeds 2030 mbar absolute pressure an alarm SMS is automatically sent by the python script to several members of the working group. This allows for 5 to 10 min to react before the pressure

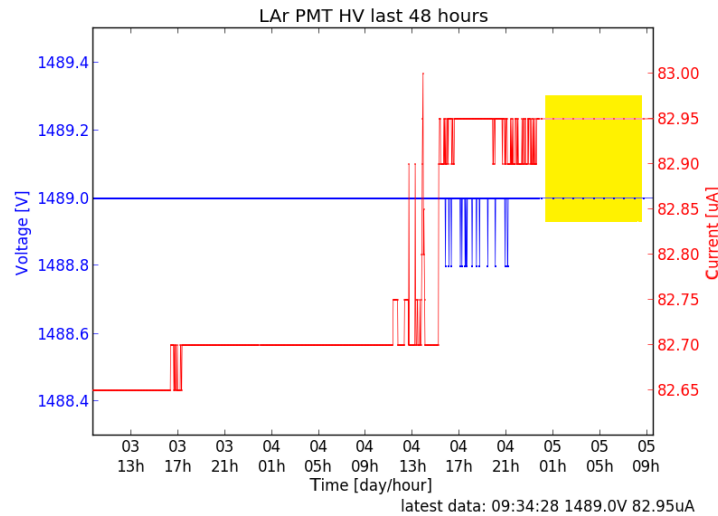


**Figure 3.15:** PMT voltage and current monitor. A communication loss to the high voltage module can be seen by large spacing of measurement points in time, as in the marked yellow region.

reaches 2200 mbar at which the overpressure valve opens and potentially introduces impurities. A danger of damaging any system component is not present in any case. The filling level of the liquid nitrogen dewar is monitored using a webcam with an integrated light directed towards an analog level meter. The webcam image is saved periodically by the program WebCamImageSave from NirSoft [103] and transferred to a web server by the script making the pressure plots.

The power supply of type N1470 from CAEN, which is providing the necessary voltage for the PMT, is connected to a PC by a USB port allowing to monitor the PMT voltage and current. Both values are plotted by a python script and transferred to the web server. A connection failure can be observed by significantly larger spacing of measurement points in time. An example plot of the high voltage and current monitor with a connection failure marked in yellow is shown on the right in Figure 3.15. The power supply allows to set a maximum supply current, which was set to a value of  $120 \mu\text{A}$ . A higher current is occurring only in case of a failure, e.g. an electrical discharge. The power supply turns the voltage off in this case. It can be restarted remotely employing the software Chrome Remote Desktop from Google. The latter is also used to access the temperature readings of the PT100 sensors in the chamber, the level meter, as well as the PID controller including its parameters and setpoints. It can furthermore be used to restart any of the other scripts.

### 3.5.4 Data Acquisition

The PMT (current) pulses are recorded using a 250 MHz analog to digital converter (ADC) with 12 bit resolution of type V1720 from CAEN [95]. The gain of the PMT is sufficiently large in order to record the signals without prior amplification. The ADC has an input range of 2 V peak to peak. Data from and to the ADC board are transferred through an optical fibre connected to a PC by a PCI board from CAEN. Data analysis is performed offline employing separate programs.

Settings of the ADC board are made by two configuration files read by the program which is also performing the data acquisition. It was already existing and adopted to the specific needs of this setup. A new data file format was therefore implemented saving the trace in a double array and the length of the trace in an integer. These are integrated into a ROOT [101] tree structure and stored as a ROOT file format, which provides data compression. A shell script was written which is starting the data acquisition automatically after a certain time and for a total number of events which can be set. It can further be set to start a new measurement periodically e.g. every 2 h. It automatically determines the next unused run number which will be assigned to the next measurement. This is done scanning the folder names in the location where the traces are stored.

The ADC can be set to trigger internally with a constant threshold. This threshold was set to a value above the height of single photoelectrons to avoid triggering on single electrons emitted thermally from the PMT photocathode (dark counts). The ADC resolution of 12 bit corresponds to 4096 samples. The offset is chosen such that the baseline is at approximately 3950 ADC counts in order to have a large range for the negative PMT pulses with some space for baseline fluctuations. The length of recorded traces was set to 2048 samples and the number of samples recorded before the trigger to 410. The pre-trigger samples are employed to calculate the baseline and noise level. This results in a mean peak position in time of recorded alpha events at approximately sample 414, hence recording

$$n_{\tau_2} \frac{(4096 - 414) \cdot 4\text{ns}}{3200\text{ns}} = 9.2 \quad (3.6)$$

number of decay times of the triplet component in case of pure liquid and  $n_{\tau_1} = 4.6$  in case of pure gaseous argon. This corresponds to a fraction of  $e^{-9.2} = 1.0 \cdot 10^{-4}$  and 1 %, respectively, of light from the triplet component to be missed. The amount of light missed from the much shorter singlet components is orders of magnitudes smaller and hence totally negligible. Worse argon purity reduces the fraction of missed light further. The total amount of light reconstructed from one event is hence underestimated by less than 1 % using these ADC settings.

## 3.6 Analysis Methods

The analysis of recorded PMT traces is performed in several steps. In a first step, basic quantities of each individual event are extracted from recorded traces. This is performed employing a modified version of an analysis software originally developed for the ArDM [73] experiment. The parameters for the determination of those quantities are set in a configuration file. The determination of quantities relevant for the measurements presented in this chapter are described in the following, together with the principle of the further analysis. Programs and macros of the further analysis were developed in the framework of this thesis. The latter are described in detail subsequently.

The time range for baseline calculations was chosen to be 10 to 400 samples after the beginning of the trace. The software calculates the mean of the baseline, subtracts the baseline and then calculates its root mean square (RMS) for each event. After a first iteration all samples above three times the baseline RMS are removed. Calculations of baseline parameters and subtraction are then repeated. This procedure removes signals possibly present in the baseline. The negative PMT trace is then inverted before the calculation of other quantities.

The inverted trace is used to determine the Maximum signal amplitude, called “peak value” and its position in time, called “peak time  $t_p$ ”. The integral is calculated separately for the singlet component and the full trace. The latter corresponds to the energy of the event. The singlet component is taken to be the integral in the range  $[t_p - 20 \text{ ns}, t_p + 30 \text{ ns}]$ . The total integral is calculated from  $t_p - 20 \text{ ns}$  to 10 ns before the end of the trace. A further integration method, which is used to calibrate the PMT, is described in Section 3.6.1. This PMT calibration is performed in a second step. It allows to convert the integral from time integrated ADC counts to number of photoelectrons (pe). The number of photoelectrons detected for 5486 keV alpha events is then employed to calculate the light yield of a given coating-reflector combination at a given argon purity.

### 3.6.1 PMT Calibration

The PMT gain is calibrated directly from light yield measurement traces, not from dedicated calibration runs, allowing to continuously monitor potential changes. This is realised employing a peak finding algorithm operating in the following way: When the recorded trace exceeds two standard deviations of the pedestal, the time range gets classified as a peak. The integral of a peak is then calculated summing up all samples above threshold plus one sample before and after. The integral of all individual peaks is then plotted into a histogram. The large number of single photoelectron events present in the triplet components results in single photoelectron spectra with high statistics, if the argon purity is high. The lower the

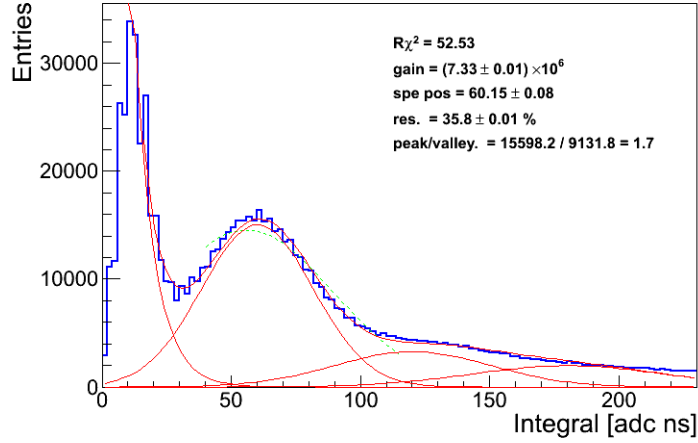


**Figure 3.16:** Single photoelectron spectrum at a PMT voltage of 1500 V obtained from 10000 liquid argon scintillation pulses using a peak finding algorithm. Superimposed is a fit with the sum of an exponential decay, describing the noise and three Gauss distributions to describe single, double and triple photoelectron events.

purity the worse the electronic noise event to single photoelectron event ratio. The obtained histogram is then fit with the sum of an exponential function to describe the noise component and three Gaussian functions for 1, 2 and 3 photoelectrons. The mean and standard deviation of these are fixed relative to each other. This is realised employing only one  $\mu$  and  $\sigma$  in the fit. The mean and sigma of the three Gaussian distributions are then given as  $1\mu$ ,  $2\mu$  and  $3\mu$  and  $\sigma$ ,  $\sigma \cdot \sqrt{2}$  and  $\sigma \cdot \sqrt{3}$ , respectively. This takes into account the statistically expected correlation. A typical fit to a single photoelectron spectrum obtained from a measurement in liquid argon is shown in Figure 3.16.

The PMT gain  $g$  is then calculated from  $\mu$  converting ADC ns into charge collected at the readout and then into an amplification factor. An ADC count corresponds to a certain voltage which is simply the ratio of the input range (here 2 V) to the resolution (here 12 bit). The voltage at the ADC originates from a current flowing over two  $50\ \Omega$  resistors in parallel. One connecting the anode of the PMT to ground at the base and one in the ADC. The integral over one pulse corresponds hence to the total charge arriving at the readout anode. For a pulse originating from a single photoelectron, this value divided by the charge of one electron  $e$  is the gain of the PMT:

$$g = \mu \cdot \frac{2\text{ V}}{2^{12}} \cdot \frac{1}{\frac{50\ \Omega}{2} \cdot 250\ \text{MHz} \cdot e} \quad (3.7)$$

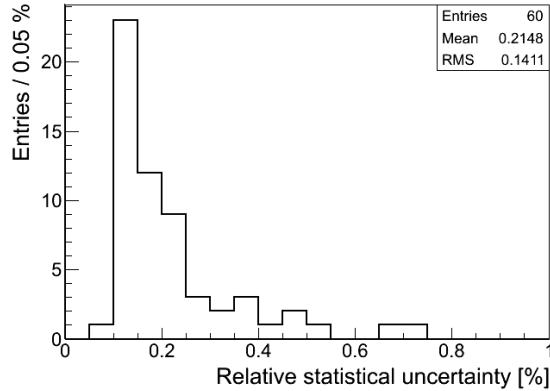


**Figure 3.17:** Histogram of relative statistical uncertainties of the PMT gain determined from 60 independent measurements at 1500 V.

The fit was done employing the ROOT framework. It provides directly the statistical uncertainty on the gain for each fit. The relative uncertainty of 60 independent gain measurements of a PMT at a voltage of 1500 V is plotted in Figure 3.17. 90% of the cases have an uncertainty below 0.4 %, which is taken as the statistical uncertainty for all gain measurements.

Systematic uncertainties were studied using a measurement of uncoated VM2000 in liquid argon. This was performed varying several parameters: the threshold of the peak finding algorithm, the fit range, binning and the fit function. When varying the fit function, also the fit range was changed in order to select the range in the spectrum within which the respective fit function represents the majority of events. The resulting mean single photoelectron (SPE) integrals in ADC ns are shown in Table 3.6.1. These are used to calculate the respective relative fluctuations (also provided in the table). The mean of SPE integral obtained by the standard procedure (2 ADC ns/bin,  $2\sigma$  threshold, exponential plus three Gauss distributions, fit range 15 – 250 ADC ns) is included for each calculation of the fluctuations. exp is written as abbreviation for an exponential function and G for a Gaussian function.

The total systematic uncertainty can be obtained adding these variation quadratically. This is assuming that these variations are representative for the respective systematic uncertainties and independent from each other. The total systematic uncertainty of the method is hence estimated to be 1.74 %. Combined with the statistical uncertainty of 0.4 % one obtains a total uncertainty of 1.8 % for the PMT calibration. It is dominated by the choice of the fit function and threshold of the peak finding algorithm.

	SPE mean
standard parameters	<b>75.51</b>
1.5 $\sigma$ threshold	76.75
3 $\sigma$ threshold	77.11
4 $\sigma$ threshold	77.21
5 $\sigma$ threshold	77.25
relative fluctuation [%]	<b>0.95</b>
range 15 – 300 (ADC ns)	76.37
range 10 – 250 (ADC ns)	75.41
range 20 – 250 (ADC ns)	76.04
range 15 – 200 (ADC ns)	75.48
relative fluctuation [%]	<b>0.56</b>
4 (ADC ns) per bin	75.45
1 (ADC ns) per bin	75.75
0.5 (ADC ns) per bin	75.77
8 (ADC ns) per bin	75.74
relative fluctuation [%]	<b>0.20</b>
G, range 40 – 120	77.57
exp + G, range 15 – 120	77.64
exp + G + G, range 15 – 200	76.34
exp + G + G + G + G, range 15 – 350	75.67
relative fluctuation [%]	<b>1.33</b>

**Table 3.3:** Study of systematic uncertainties on the PMT gain determination by variations of the mean of the SPE peak (in ADC ns) determined employing various the peak finding thresholds, fit ranges, binnings and fit functions. G is written as abbreviation for a Gaussian and exp for an exponential function. The respective standard deviation divided by the average SPE mean is provided for each parameter.

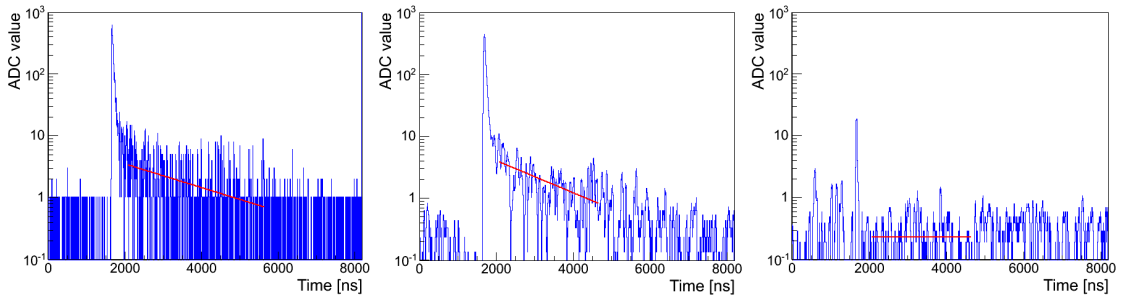


**Figure 3.18:** Traces of events with an exponential fit to the triplet component in a measurement of uncoated VM2000 in liquid argon. Left: typical alpha event with a decent description of the triplet decay. Center: same event with the previous application of a 40 ns (10 sample) moving window average. Right: typical low energy ( $\lesssim 50$  pe) event resulting in a wrong fit.

### 3.6.2 Determination of the Triplet Lifetime

The triplet lifetime is determined in two ways. Once on an event-by-event bases and once based on mean traces. The former is determined in the first level analysis software. The software was therefore modified to perform a maximum likelihood fit to the triplet component of each event. The resulting decay time is then saved into the standard ROOT tree which also contains all other first level quantities. An option was implemented to choose the number of traces superimposed by the corresponding fit which are saved as an image file, to verify proper functioning. Three example traces with the respective fit from a measurement of uncoated VM2000 in liquid argon are shown in Figure 3.18. The left one is an alpha event with 697 pe. The fit is decently describing the triplet component. On the right is an event with a total integral of 23 pe. The fit is obviously not describing the exponential decay of the triplet component. This is typical for events with less than  $\sim 50$  pe. These low energy events are therefore not considered. The triplet lifetime determined from the event-based fit, is shown in Figure 3.19 on the left. The histogram includes all events with an integral larger than 50 pe. The shape was empirically found to fit well with a Landau distribution. This function was therefore used to determine the most probable value (MPV).

The mean and MPV of triplet lifetime distributions were used to study systematic effects of the event-based determination method. The fit range is one possible source of systematic bias. The range is set relative to the “peak time“ of each event. The start is always kept at 400 ns after the peak time and the end was chosen to be 2000, 2500, 3000 or 4000 ns after the peak time. Additionally, the effects of a moving window average (MWA) of width 40 and 200 ns (10 and 50 samples),

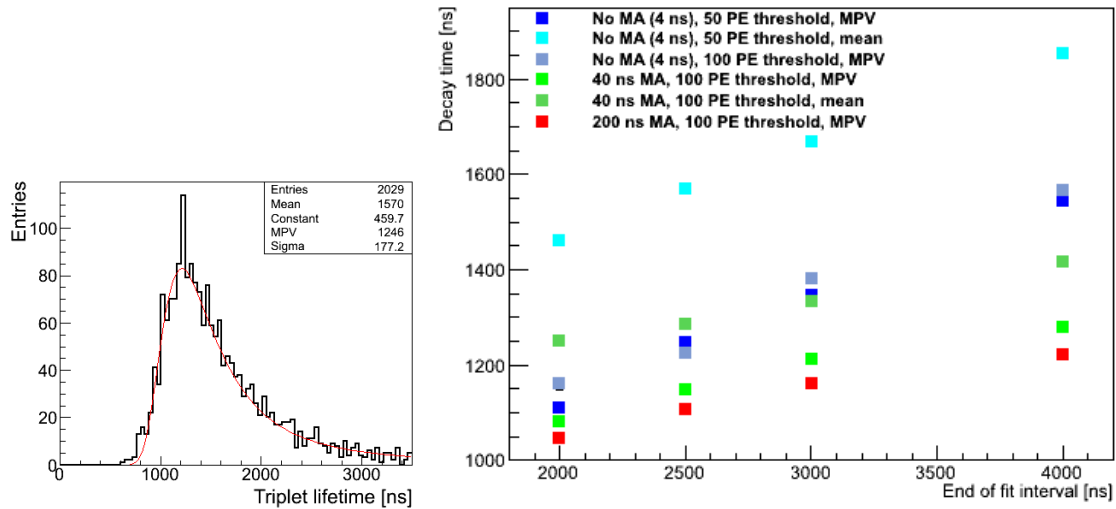


**Figure 3.19:** Left: distribution of triplet lifetime determined by an event-based fit in the range 400 to 2500 ns after the peak time. The histogram contains all events above 50 pe from originally 3000 events. Right: the determined triplet lifetime is strongly dependent on the chosen value of the parameters.

as well as increasing the threshold from 50 to 100 pe were studied. The resulting values obtained from the same data are shown in Figure 3.19 on the right. A strong dependence on the endpoint of the fit range is observed independent of the other parameters. The threshold has only a minor effect. Using the MPV instead of the mean results in a lower triplet lifetime, as expected based on the shape of the distribution. Increasing the MWA window decreases the determined triplet lifetime and slightly reduces the dependence on the end of the fit range. Based on the described observations a fit range of 400 to 3000 ns after the peak time and a 40 ns MWA window were chosen. The most probable triplet lifetime obtained with these parameters is similar to the one obtained with the method described below. The event-based method is however not considered to be reliable, because of the observed strong dependence on the chosen parameters. It is nevertheless useful to identify changes in the purity in the course of a measurement. This is performed plotting the event-based triplet lifetime as function of the event number for all events above 50 pe.

The purity determination of argon is performed by the determination of the triplet lifetime. To compare different light yield measurements it is crucial to have a reliable triplet lifetime. Therefore a second method was investigated performing a fit of an exponential to a mean trace. The fit routine employs a maximum likelihood method. The mean trace is calculated from 1000 consecutive events removing events with an integral of less than 50 pe. A fit with two exponential

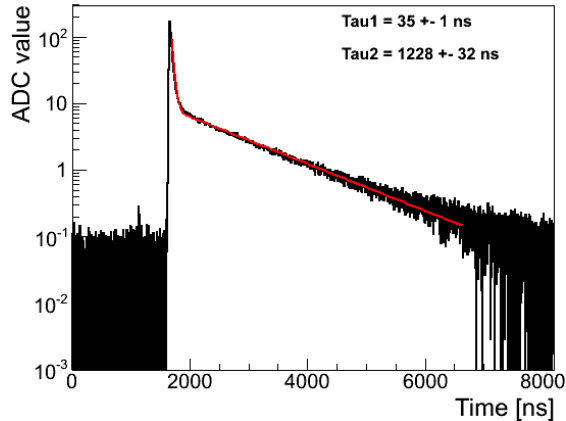


**Figure 3.20:** Very good description of the falling side of a mean pulse by two exponential decays (red line). Here from a measurement of uncoated VM2000 in liquid argon. The obtained decay times of the fast and slow component are named in the Figure with Tau1 and Tau2. Uncertainties as calculated by the fit routine.

functions, one for the singlet and one for the triplet component provides a good description of this mean trace. Such a fit superimposed to a mean trace is shown in Figure 3.20. A slight discrepancy is observed in the transition region between the singlet and triplet component, as well as at the end of the trace in case of TPB coatings. Both are attributed to delayed emission from the wavelength shifter. More details about the latter are provided in Section 3.8.6.

The very good description of the falling side of the pulse gives a high confidence on a determination based on a fit with an exponential decay. The triplet lifetime is therefore determined fitting the pulse with one exponential decay in a range which is dominated by the triplet component, after the intermediate component. This is the case more than 350 ns after the peak time. The systematic uncertainty originating from the fit range was determined using different start and stop values. These and the resulting triplet lifetime are provided in Table 3.6.2. The standard deviation of these triplet lifetimes is 18 ns. This is assumed to correspond to the systematic uncertainty of this method. Using a range of 400 to 4000 ns after the peak is resulting in a triplet lifetime close to the mean from all ranges. This was chosen as standard range.

10 000 events are typically taken for one measurement allowing for the determination of 10 independent triplet lifetime values from mean traces. The fluctuation of these is on average  $\sim 9$  ns for measurements in liquid argon. This is taken as the statistical uncertainty. Combining this quadratically with the previously estimated systematic uncertainty one obtains a total uncertainty of  $\sim 20$  ns for the triplet lifetime in measurements in liquid argon. The fluctuations for different sets

Fit range start	Fit range end	Triplet lifetime
400	3000	1214
400	4000	1241
400	5000	1269
350	4000	1236
450	4000	1246
500	4000	1249

**Table 3.4:** Different triplet lifetimes obtained from the same mean when varying the fit range of one exponential function. The fit range given relative to the peak time.

of events within the same measurement in gaseous argon are typically in the range of 20 to 60 ns and hence dominating over the systematic uncertainty from the fit range. The fluctuations within the respective measurements are therefore used as an estimate for the uncertainty in gas measurements.

An event-based fit method was found to be suitable to constantly monitor the triplet lifetime but does not allow an accurate determination. An exponential fit to a mean trace was on the other hand found to provide a reliable value. The latter is used to compare different light yield measurements.

### 3.6.3 Selection of Alpha Events

The ratio of light in the fast component divided by the total amount of light is called component ratio. This ratio is smaller for light originating from electron traces compared to nuclei traces due to different ionisation densities [104]. This property is exploited to distinguish background gamma events from signal alpha events. The former deposit energy in argon by recoiling electrons. The separation efficiency is 100% at alpha energies of the americium source and becomes worse at lower energies. Gamma events are only visible in measurements with liquid argon in contrary to measurements in gaseous argon due to a higher interaction probability at higher densities. The component ratio versus energy for a measurement of TPB-coated Tetratex in liquid argon is shown in Figure 3.21 on the left. The gamma ray band contains also muon events, which deposit energy in a range extending far beyond the alpha particles and saturate the ADC. Both, ambient background gamma events, as well as muon events are visible only because of the low activity of the alpha source of  $\sim 30\text{Bq}$ . The contamination of background events at energies of the alpha particles is expected to be negligible. They are nevertheless removed for liquid measurements by a cut on the component ratio, which is visualised by the dark orange line in Figure 3.21 on the left. This is performed because of the easy and efficient method to remove any potential influ-

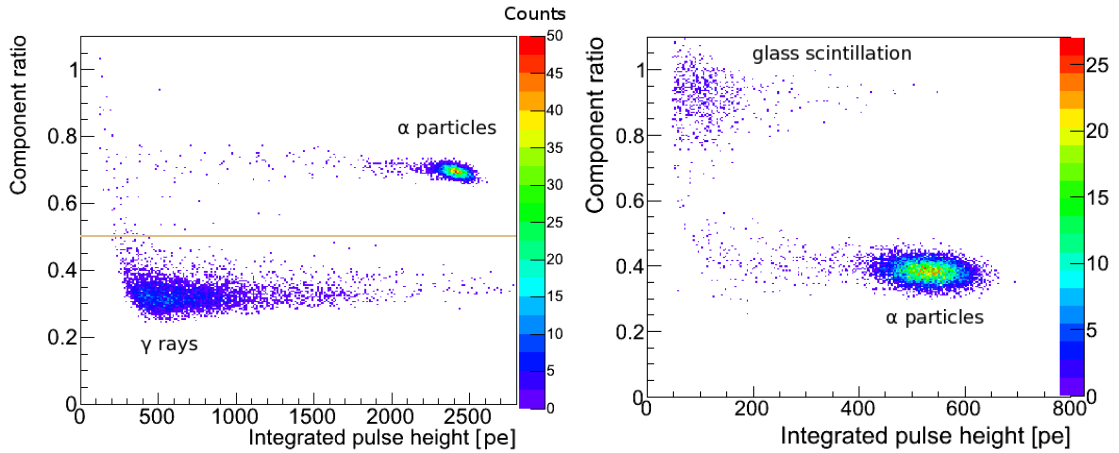


**Figure 3.21:** Component ratio versus integrated pulse height for a measurement of TPB-coated Tetratex. Left: in liquid argon at a purity corresponding to a triplet lifetime of  $\sim 1352$  ns. Alpha events have a larger component ratio than electron recoils from gamma events, resulting in a good separation of background and signal. Right: in gaseous argon at a purity corresponding to a triplet lifetime of  $\sim 2653$  ns.

ence of background events. The component ratio of alpha events increases with decreasing purity due to the stronger quenching of the triplet component. It is  $\sim 0.7$  for the for the measurement in Figure 3.21. The value of the cut was chosen to allow fluctuations in the component ratio without removing alpha events. The cut threshold was checked for each run.

The component ratio for alpha events in gaseous argon is smaller compared to liquid argon. It is  $\sim 0.4$  for the measurement of TPB-coated Tetratex in gaseous argon, as shown in Figure 3.21 on the right. The triplet lifetime in this measurement was 2964 ns. The selection of alpha event in gaseous argon is performed based on the energy only without any application of a component ratio cut. This is sufficient as the fraction of background events present at the alpha peak is even smaller than in measurements in liquid argon. The accumulation of events around a component ratio of  $\sim 0.9$  is most likely scintillation of the quartz window of the PMT excited by background gamma rays [105] or Cherenkov light [106]. The light is produced by recoiling electrons in the quartz window from ambient radioactivity and muons passing through the window. These events are also observed in measurements in liquid argon but less dominant because of a much higher rate of background gamma events.

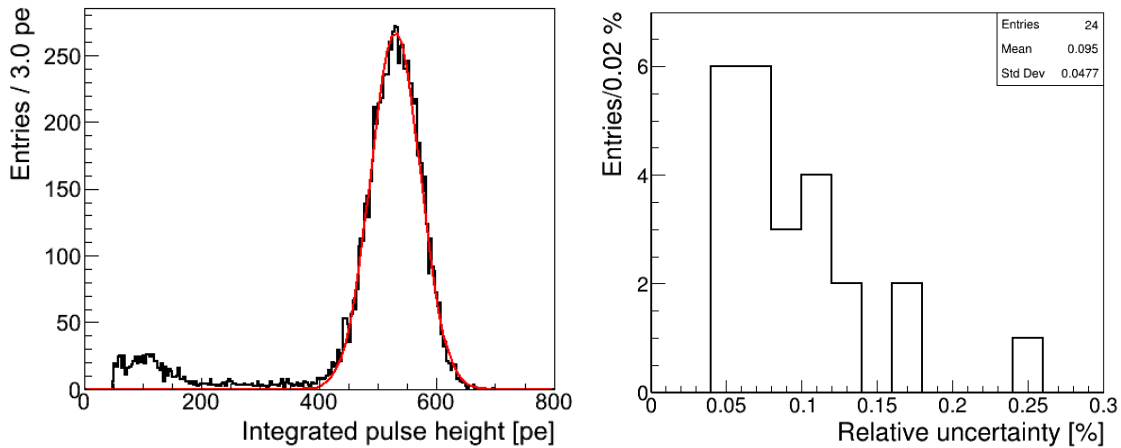


**Figure 3.22:** Left: integrated pulse height spectrum in black of a measurement of TPB coated Tetratex in gaseous argon without applied component ratio cut. Superimposed in red is a Gaussian distribution, which is fit to the spectrum to determine the mean number of photoelectrons per alpha event. Right: distribution of relative statistical uncertainty on the mean of 24 independent measurements.

### 3.6.4 Determination of the Light Yield

The light yield obtained with a certain wavelength-shifting reflector foil is determined by the average number of photoelectrons detected for an alpha particle from the  $^{241}\text{Am}$  source. This number is determined for measurements in liquid and gaseous argon by fitting the alpha spectrum with a Gaussian distribution. The mean obtained from the fit corresponds to the average number of photoelectrons detected by the PMT for one alpha event. The spectrum and fit for a measurement of Tetratex coated with  $0.49 \text{ mg TPB/cm}^2$  is shown in Figure 3.22 on the left. The fits are performed using the ROOT internal  $\chi^2$  method. Alpha events are selected as described in the previous section.

The fit routine also calculates the statistical uncertainty on the Gaussian mean value. This was used to calculate the relative uncertainty on the mean value in 24 different light yield measurements. The distribution of these is shown in Figure 3.22 on the right. In 90% of the cases this uncertainty is smaller than 0.15%, which is negligible compared to the uncertainty of the gain determination. A variation in the gain does cause a variation in the determined light yield. The size of the variation of the latter is directly proportional to the former. The uncertainty on the light yield is hence dominated by the uncertainty of the PMT calibration. A summary of uncertainties is given in Section 3.8.7.

### Purity Independent Method

Maintaining a constant argon purity for all individual measurements and over the course of longer runs is very difficult. A special method was therefore developed to compare different measurements in good approximation independent from the argon purity in the respective measurement. This can be achieved comparing the measured light yield to the light yield of a reference sample at the same triplet lifetime. The light yield of the reference sample must therefore be known at all purities present in any other measurement. This is achieved measuring a sample at several triplet lifetimes interpolating intermediate lifetimes and extrapolating lifetimes outside the measured range.

The presented measurements, uncoated VM2000 was selected as reference. It is the most robust wavelength-shifting reflector foil at hand and expected to be the least sensitive one to mechanical damage or ageing. In a first step, the light yield (in mean number of photoelectrons for  $^{241}\text{Am}$  alpha events) was measured for VM2000 for several argon purities. The obtained triplet-life-time-dependent light yield was then fit with a linear function allowing to interpolate and extrapolate the VM2000 light yield to any triplet lifetime. This linear function can be employed to calculate the relative (to VM2000) light yield of any other measurement at the triplet lifetime of that measurement. This is in a good approximation a purity-independent measure of the light yield and is used to compare different wavelength shifter in liquid and gaseous argon. The reason for this quantity to be purity-independent is explained in detail in the following. The influence of wavelength shifting by impurities [107] is also discussed. The measurement results obtained with this method are presented in Section 3.8.3 and 3.8.4.

The rate of photons emitted by decaying excimers  $N_\gamma$  can be approximated by the sum of two exponential decays

$$N_\gamma = Ae^{-\frac{t}{\tau_1}} + Be^{-\frac{t}{\tau_2}}, \quad (3.8)$$

where the first term represents the singlet and the second the triplet state with decay times  $\tau_1$  and  $\tau_2$ , respectively. The height of the emitted light pulse at  $t=0$  is independent of the purity in contrary to the integral with a value of  $A \cdot \tau_1 + B \cdot \tau_2$ . The decay time of non-radiative deexcitations by impurities is much larger than the singlet lifetime, but smaller than the triplet lifetime for the presented measurements. The total amount of light is hence proportional to the measured triplet decay time  $\tau_2$  plus a constant assuming no wavelength shifting by impurities. This results in the amount of detected light  $L_d$  of

$$L_d(WLS) = (A\tau_1 + B\tau_2) \cdot \epsilon_{WLS}, \quad (3.9)$$

with  $\epsilon_{WLS}$  an effective efficiency containing the conversion, light collection and PMT sensitivity. The relative light yield  $L_r$  of a wavelength shifter is then the

ratio:

$$L_r = \frac{L_D(WLS)}{L_D(VM2000)} = \frac{\epsilon_{WLS}}{\epsilon_{VM2000}} \quad (3.10)$$

and hence independent of the purity (the measured alpha peak position at a measured  $\tau_2$  is compared to the alpha peak position of VM2000 extrapolated to the same  $\tau_2$ ).

If there are impurities which shift light additionally to the coated reflector foil one has to extend the formula for  $L_d$  with a term for the light absorbed by impurities. If the light is absorbed with a probability  $P_i$  and detected with an effective efficiency  $\epsilon_i$  containing the conversion and collection efficiency, as well as the PMT sensitivity, Equation 3.9 becomes:

$$L_d(WLS) = (A\tau_1 + B\tau_2)(P_i \cdot \epsilon_i + (1 - P_i)\epsilon_{WLS}). \quad (3.11)$$

$P_i$  depends on the purity and hence on the measure  $\tau_2$  which would result in a non-linear dependence of the alpha peak position as function of  $\tau_2$ . The resulting influence on the relative light yield can be studied looking at the functional form of  $L_r$  in the presence of light-shifting impurities:

$$L_r(WLS) = \frac{P_i\epsilon_i + (1 - P_i)\epsilon_{WLS}}{P_i\epsilon_i + (1 - P_i)\epsilon_{VM2000}}. \quad (3.12)$$

The formula is valid under the assumption that each measurement is dominated by the same impurities. The assumption is justified as our primary source of impurities is air emanating from the pores of PTFE components, mainly the large PTFE filler. For  $P_i \rightarrow 0$  the ratio becomes equal to  $\epsilon_{WLS}/\epsilon_{VM2000}$  and for  $P_i \rightarrow 1$  (all light shifted by impurities) equal to 1. All presented wavelength shifter-reflector combinations have an efficiency higher than the uncoated VM2000 reference. A higher impurity concentration would hence result in an underestimation of the light yield.

A significant contribution from wavelength-shifting impurities would hence be observable in the measurements by a non-linear dependence of the absolute light yield on the triplet lifetime and an underestimation of the relative light yield at low argon purities. Attention is given to the presence of any of these signatures in all measurements.

### 3.7 Reflector Installation and Measurement Procedure

The installation location of the coated reflector foil in the liquid argon setup has been explained in Section 3.5. The top and bottom aluminium pieces of the active

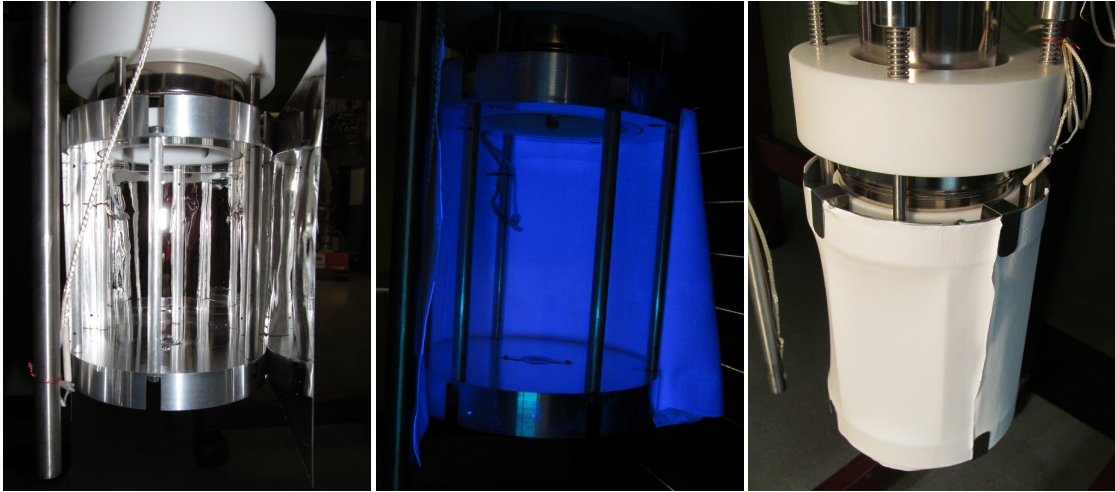


**Figure 3.23:** Left: picture of the active volume while installing VM2000 coated with BCF-10. Visible is, in the top part of the active volume, the PTFE ring on top of which the PMT is sitting. Centre: Tetratex coated with pure TPB during installation and illuminated by UV light. Visible is also the LED inside the rear part of the active volume and the alpha source in the centre of the bottom aluminium disc. Right: fully installed Tetratex coated with pure TPB. The stainless steel clamps which are holding the reflector foil are clearly visible, as well as the PT100 temperature sensors on the right side just below the PTFE holder and on the left bottom, at the end of the tube.

volume have a rim directed outwards and are connected by six aluminium bars equally distributed on their outer edges inside the active volume. The reflector foil is wrapped around this cylinder and clamped to the top and bottom rim by four clamps each. The foils are cut to a length to allow between 5 and 20 mm overlap. It is taken care to minimise gaps between the aluminium and the the reflector, as well as the vertical gap at the overlap of the foil. It was however not always possible to avoid gaps with a width of up to a few mm. Pictures during and after the installation of reflector foils are shown in Figure 3.23 also depicting the active volume. It was tried to install the reflector foils as straight as possible in the vertical direction. There was however usually an inward bending of Tetratex, visible in Figure 3.23 on the right. This is caused by the flexibility of this reflector foil.

The large PTFE filler surrounding the active volume is installed for measurements in liquid argon, which significantly reduces the required amount of argon. After closing the chamber, it is flushed at least three times with gaseous argon reaching a pressure of several hundred mbar and pumped to  $\sim 1$  mbar between each flushing. This procedure is performed to remove impurities such as water.

The chamber is then pumped to a pressure below  $5 \cdot 10^{-5}$  mbar before filling argon for a measurement. The pressure is measured while pumping and by a cold cathode gauge calibrated for air. A test measurement is performed in the beginning of a cool down in case of a liquid argon measurement. This is to save argon in case of insufficient purity or malfunctioning of the PMT. These test measurements are not suitable for the determination of a light yield due to varying pressures during measurements and different temperatures between the measurements. The pressure in the chamber is expected to influence the measured light yield in case of gaseous argon. It was therefore filled to  $(10 \pm 0.2)$  psi =  $(690 \pm 14)$  mbar overpressure for all measurements in gas.

Before starting a measurement, all connections to the 19 pin MIL-C-26482 feedthrough are removed on the air side. This is performed to remove potential sources of electronic noise and background light produced by the LED. It was doubtless observed that the LED emits light when a cable is moved, which is connected to the LED on the air side. The other end of the cable on the air side does not have to be connected. Electromagnetic fields in the room, inducing a voltage when the cable is moved, might be responsible for this effect. The feedthrough is covered by aluminium foil and a plastic cap because it was observed that all three types of electrical feedthroughs at the chamber are not light-tight. The empty BNC connector is covered for the same reason by a  $50 \Omega$  termination cap and the empty SHV connector by an SHV plug with a cable stub.

After measurements in liquid, the argon is removed through a pipe reaching to the bottom of the cryostat. This is performed to shorten the time required for warm up. The chamber is then left to warm up for three days before opening, to avoid water condensation and freezing on the internal components. It is then opened and the reflector foil, as well as the chamber are visually inspected, employing visible and UV light, for potentially detached pieces of the coating.

## 3.8 Results

Several results were obtained with the liquid argon setup and are presented in this section. The results include the characterisation of the PMT, the light yield obtained with different coated reflector foils measured in gaseous and liquid argon, measurements of the long-term stability of TPB-coated Tetratex, an analysis of the time structure of the fluorescence light, as well as light yield measurements of coated transparent nylon.

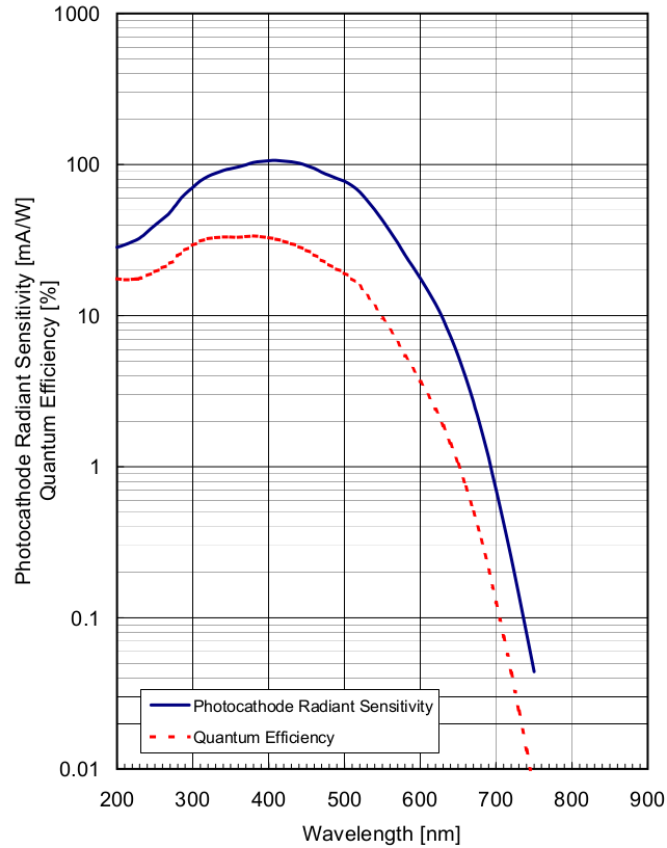


**Figure 3.24:** Photocathode quantum efficiency and radiant sensitivity as a function of the incident wavelength at room temperature. The measurement and figure are provided by Hamamatsu [108] for the PMT installed in the argon setup. Below 200 nm both quantities steeply decrease, according to Hamamatsu. Radiant sensitivity is the cathode current divided by the incident radiation flux in watt.

### 3.8.1 Characterisation of the PMT R11065-10

The 3 inch PMT installed in the argon setup is of type R11065-10 from Hamamatsu [71]. A new version of this type is installed in GERDA (R11065-20 MOD). This twelve dynode PMT was developed for deployment in liquid argon and is the argon version of the Xenon PMT R11410, which differs by the photocathode material. -10 and -21 stand for modified versions of the PMT with reduced radioactive trace contaminations. The choice to employ the same PMT type for the argon setup as for GERDA was made to characterise this PMT additionally to long-term stability tests performed at the MPIK Heidelberg. The maximum quantum efficiency of the PMT used in the argon setup is  $\sim 34\%$  with a plateau in the range of 300 to 400 nm. Its quantum efficiency curve is shown in Figure 3.24.

Properties like linearity and gain are strongly dependent on the electrical circuit connected to the PMT. This circuit is described in the following. The voltage supply for the PMT photocathode and dynodes is realised by a voltage divider board connected to the PMT pins. The ratio of voltages was chosen according to the recommendation in the data sheet provided by the producer. The circuit diagram of this PMT base is shown in Figure 3.25. The same base but with 10 nF capacitors and a 1 k $\Omega$  termination at the readout anode instead of 47 nF and 50  $\Omega$  was tested for linearity in [109]. According to Figure 7.10 therein, a deviation from linearity of less than 5 % is expected for signals below 32500 pe at a gain of  $5 \cdot 10^6$  and at room temperature. Measurements therein showed that the base and not the PMT itself is causing non-linearity. A measurement done by Klaus Jänner from the MPIK-Heidelberg is also presented therein. It shows that the capacity of capacitors employing X7R ceramics, like those used in base for the argon setup, drops by 5 % at liquid argon temperature compared to room temperature. This is well overcompensated mounting 47 nF capacitors instead of 10 nF. A larger capacity increases the linear range if the non linearity is caused by the limited amount of charge available on the dynodes connected to the capacitors, otherwise it does not have any effect. The base used in the Ar setup of this work is hence linear to at least the same number of photoelectrons as the base measured in [109], at the same gain. The linearity limit is anti-proportional to the gain. The gain in the measurements presented here is at most twice as high as in the linearity measurements. The largest observed signals contain approximately 2500 pe. This is well within the linear range, also at liquid argon temperature.

### Afterpulses

PMTs usually produce afterpulses with a PMT specific time delay and probability. Afterpulses are caused by two initial processes, photoelectrons elastically scattered of the first dynode on the one hand and ionised residual gas atoms along the trajectory of photoelectrons on the other hand. In the former case, one of the photoelectrons emitted by the photocathode and accelerated onto the first dynode scatters elastically back from the first dynode. The other electrons undergo the normal amplification process producing the main PMT pulse. The scattered electron is accelerated again onto the first dynode kicking out further electrons which then undergo the normal amplification process producing an afterpulse up to several tens of ns after the initial pulse [110]. The latter type of afterpulses are produced by residual gas ions drifting to the photocathode. Here they kick out several electrons which then undergo the normal amplification process. The ion is produced by primary photoelectrons hitting residual gas atoms in the PMT. Ions of same mass and charge hit the photocathode with only small time deviations irrespective of the position of ionisation. The reason is the distribution of the

CHAPTER 3. DEVELOPMENT OF EFFICIENT WAVELENGTH-SHIFTING  
REFLECTOR FOILS FOR LIQUID ARGON SCINTILLATORS

---

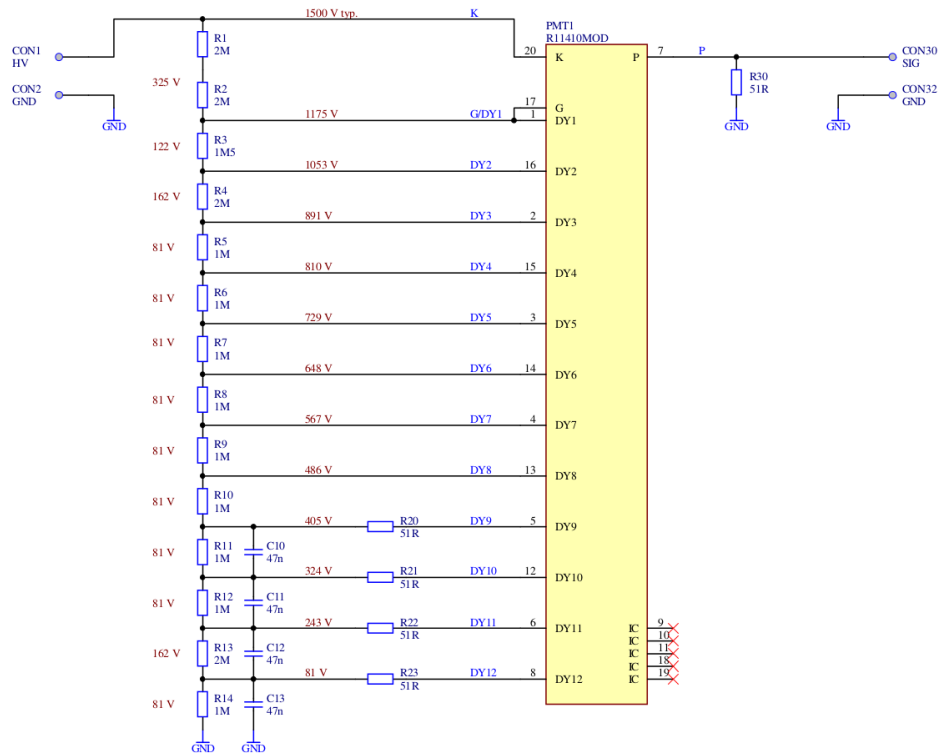


**Figure 3.25:** Circuit diagram of the PMT base as used in the argon setup. Capacitors between the last dynodes provide additional charge. This reduces the voltage decrease between those dynodes caused by large light signals. Resistors between these capacitors and the dynodes damp charge oscillations between the two. The signal output is terminated by  $51\ \Omega$  to avoid reflections. Values of resistors are given in Ohm. 1M5 is read as  $1.5\ \text{M}\Omega$ . Values of capacitors are in Farad.

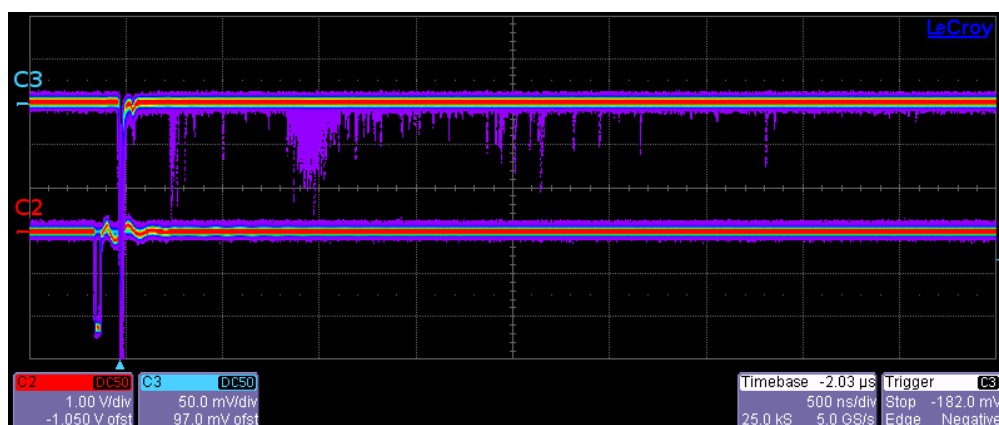


**Figure 3.26:** Oscilloscope screen shot for afterpulse investigations at room temperature. Superimposed are many LED driver signals in C2 and the resulting PMT signals in C3. An accumulation of afterpulses is observed  $\sim 300$  and  $\sim 950$  ns delayed with respect to the initial light pulse.

electric field in the PMT, which causes stronger acceleration of ions further from the photocathode [111]. Ions with different mass and charge hit the photocathode at different times.

The dead time in GERDA caused by the liquid argon veto, is determined by the rate at which light is detected. The dark count rate is irrelevant at liquid argon temperatures. The primary source of light is the beta decay of  $^{39}\text{Ar}$  with a decay rate of  $\sim 1$  Bq/kg [112], [113]. Afterpulses induced by these events would further increase the dead time. They might also disturb diagnostics of background sources performed employing the liquid argon veto. It is therefore beneficial to know the rate and time delay of afterpulses produced by the installed PMT type. Both were measured at room and liquid argon temperature. At room temperature this was performed employing the LED instead of scintillation light in order to avoid afterpulses being covered by light emitted by the triplet component of argon excimers. The LED was driven by a 30 ns square pulse of 2.2 V height. The driver and PMT pulse were plotted employing a digital oscilloscope. Many superimposed PMT pulses are shown in Figure 3.26 (channel C3) together with the LED driver pulse (channel C2). The readout is triggered on a constant threshold on the falling edge of the PMT pulse. A clear accumulation of pulses is observed approximately 300 and 950 ns after the main PMT signal peak. These fit well to the peaks identified in [114] to originate from  $\text{H}_2$  and  $\text{CH}_4$  residuals. For present setting of the driver pulse  $\sim 18\%$  of the events contained at least one afterpulse. The afterpulse rate is strongly dominated by pulses with a delay of  $\sim 950$  ns, which corresponds to  $\text{CH}_4$ . More than one afterpulse was observed in some events.

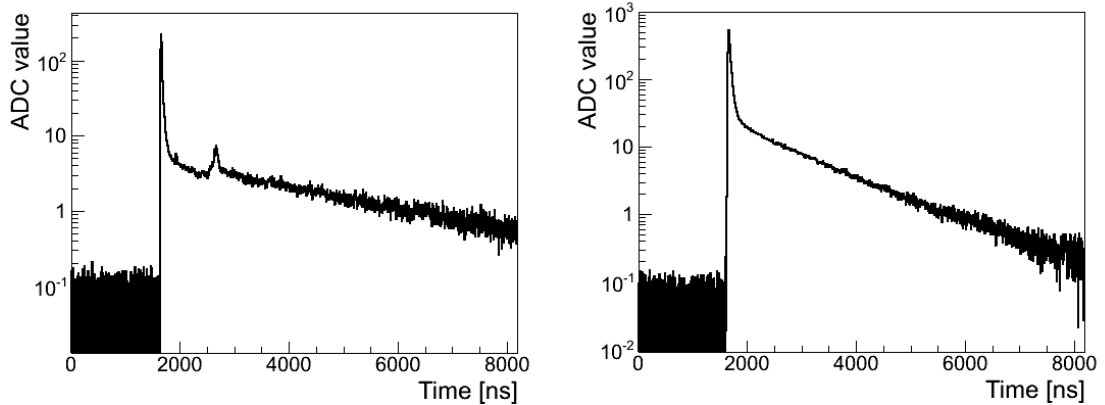


**Figure 3.27:** Left: mean trace of gas argon scintillation pulses at room temperature with clearly visible afterpulse accumulations  $\sim 300$  and  $950$  ns after the light pulse maximum. Right: afterpulses are not visible in the mean trace of liquid argon scintillation pulses.

The ratio of afterpulses caused by different residual gases was found to vary for different PMTs of type R11410 [115] (xenon version of the PMT). Here, the ratio is not determined because of the availability of one PMT only. The peak approximately  $60$  ns after the main peak is present in all events taken with a LED. It is not observed in any mean trace from scintillation pulses in gaseous argon (at room temperature, Figure 3.27 on the left) and liquid argon (Figure 3.27 on the right). This is in contrary to the other two afterpulse accumulations which are visible at room but not at liquid argon temperature. The accumulation at  $60$  ns is therefore most likely not caused by elastically back-scattered electrons but rather by a second light pulse from the LED caused by charge oscillations in the driver signal. This is supported by the fact that the maximum of the first, highest oscillation in the LED driver pulse occurs  $\sim 60$  ns after the main driver pulse.

The false additional pulse area caused by the afterpulses gets cancelled out for measurements of the relative light yield, assuming an average afterpulse rate proportional to the integral of the afterpulse-free signal. Hence, afterpulses do not affect the results of light yield measurements presented in this work. The height of the tail in the mean traces relative to the height of the maximum is similar,  $950$  ns after the maximum, for both cases shown in Figure 3.27. This means that the afterpulse rate is suppressed at liquid argon temperature at least to a rate which would result in a peak at most as high as the height of fluctuations at that time. The height of those fluctuations is approximately  $10\%$  of the signal height. The afterpulse peak height in gaseous argon is however approximately  $170\%$  of the

signal height caused by the triplet component. The absence of a visible afterpulse rate is supporting the model that these afterpulses originate from ionised residual gas molecules rather than surface contaminations on the first dynode. At liquid argon temperature the residual gas molecules get attached to the surfaces in the PMT resulting in a lower residual gas pressure. The observed low limit on the signal area caused by afterpulses in liquid argon is advantageous for the liquid argon veto system of GERDA.

### Internal Discharges

Sometimes the PMT was constantly observing faint light. This light is most likely originating from a faint glow discharge. An argon scintillation pulse spoiled by such background light is shown in Figure 3.28. These were observed in both liquid and gaseous argon measurements. There was no systematic trigger observed for the occurrence of this background light. The intensity was sometimes constant and sometimes increasing or decreasing on the time scale of minutes. It was always starting or disappearing without notable reason. Turning the PMT off and back on did not result in an observable difference. It furthermore appeared in measurements with different PMT voltages but more frequently at higher voltages. The PMT current was sometimes exceeding  $120\mu\text{A}$  which is the set threshold in the power supply to turn the voltage off. Such a case when the PMT gets turned off is called trip. The current without background light is  $\sim 82\mu\text{A}$  at 1500 V. Ramping up the PMTs supply voltage after a trip was usually possible and resulted in similar background light conditions as before the trip. The discharges which are the source of light are most likely occurring inside the PMT body near the stem. This is concluded as the behaviour is not affected by varying the gas pressure between 1 and 2 bar and if the full PMT and base are covered with liquid argon. Liquid argon is a much better insulator than gaseous argon. A discharge on the inside of the high voltage feedthrough is unlikely as an improved insulation at this location did not result in any difference. The hypothesis is further supported by the fact that similar issues were observed by a group at the MPIK Heidelberg, because of which they contacted the producer which confirmed the issue and modified the PMT design accordingly.

### Gain Stability

The gain of the PMT was observed to fluctuate with time. The largest number of measurements were taken at a PMT voltage of 1500 V, spread over a time period of more than one year. The gains determined from these gas and liquid measurements are shown in Figure 3.29. It shows that the fluctuation in gain is not dominated by the temperature of the PMT. This was confirmed measuring the

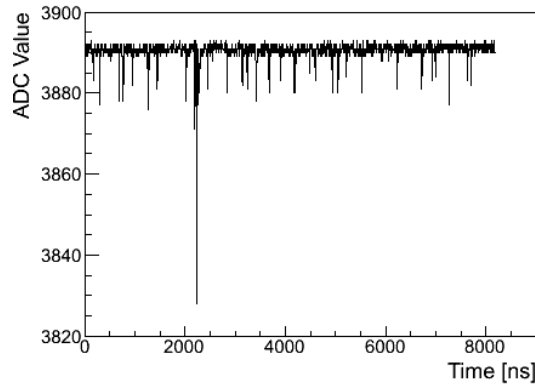


**Figure 3.28:** Background light which is sometimes continuously observed. It is most likely produced inside the rear part of the PMT.

gain before during and after a cool down, which does not show a tendency. The gain seems to vary more at liquid argon temperature than at room temperature. Note that liquid argon covers typically only the lower half of the PMT (PMT window and half of the body). The rest of the PMT, including the base are in gaseous argon close to the cooling coils. The temperature of this part is not known but expected to be close to liquid argon temperature in measurements in liquid argon. A measurement started in May 2013 running for 100 days in which the PMT was constantly kept in liquid argon revealed several sudden gain changes. This is shown in Figure 3.33. The gain was additionally determined at room temperature before and 20 days after the long-term test. It was found to decrease from  $(7.35 \pm 0.13) \cdot 10^6$  to  $(6.91 \pm 0.12) \cdot 10^6$  excluding a self recovery at room temperature with a significance of  $2.4\sigma$ . The correlation between the previously described background light or sparks and changes in gain is not clear. It was observed that a drop in gain was usually preceded by a spark. Sparks were however also observed without a noticeably subsequent gain change. Turning the PMT off and back on does not result in an observable gain change or recovery. The reason for these fluctuations in gain is not clear.

### Summary on the PMT Characterisation

The afterpulse rate of the PMT was found to be negligible at liquid argon temperature. Overall, the PMT was confirmed to be suitable for deployment in GERDA if the new version proves to have a much lower probability to produce background light by internal discharge. This light prohibits to increase the PMT voltage. In combination with the low gain observed in some measurements it was sometimes impossible to determine the gain, given the present electronic noise level. This

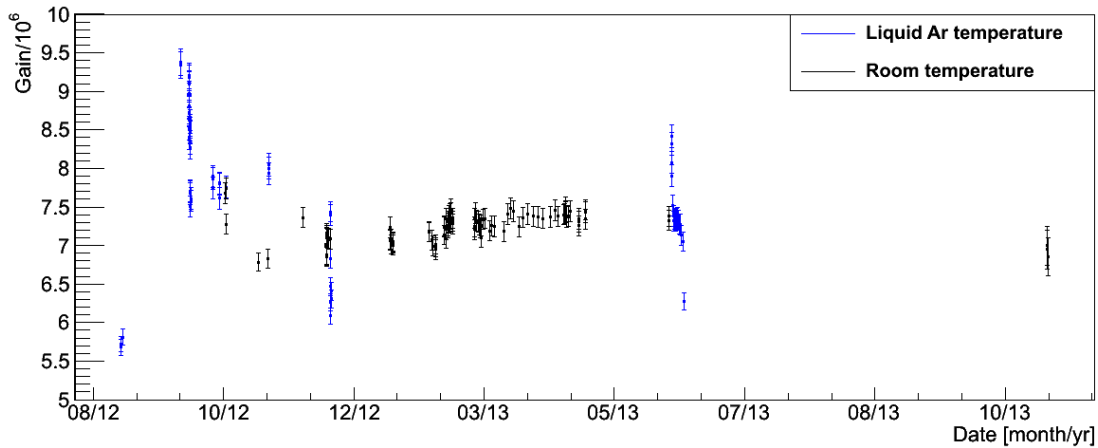


**Figure 3.29:** Measurements taken at room and liquid argon temperature with a PMT voltage of 1500 V showing large fluctuations of the gain.

could be a potential issue for GERDA. Changes in PMT gain occur in time scales of days which can be handled by a continuous gain monitor. This can easily be achieved employing argon scintillation light without dedicated calibration runs as described in Section 3.6.1.

### 3.8.2 Optimising the TPB Coating Thickness on Tetratex

The measurements presented in Section 3.3 indicate a very high light yield for TPB-coated Tetratex and room for improvements with respect to the thickness of the coating. It is therefore optimised measuring the light yield in argon gas for thicknesses in the range of 0.17 to 1.18 mg/cm<sup>2</sup>. The latter corresponds to the saturation concentration of TPB in dichloromethane of  $\sim 4.6$  g/100 ml. The thickness was controlled by the concentration of TPB in the solution. The same coated sample was usually measured twice. The second time it was reinstalled upside down in order to quantify fluctuations originating from systematic uncertainties caused by the installation procedure like the curvature of the reflector foil or a gap. An additional sample was prepared from a separate solution of TPB for a thickness of 0.90 mg/cm<sup>2</sup>. The measured thickness of the first sample was  $(0.91 \pm 0.027)$  mg/cm<sup>2</sup> and the second  $(0.88 \pm 0.027)$  mg/cm<sup>2</sup>. These are combined and presented as a thickness of 0.90 mg/cm<sup>2</sup>. Both are prepared from a solution with the same concentration of TPB and their thickness is consistent within the measurement uncertainty.

The measured alpha peak position as function of triplet lifetime for one measurement of each thickness is shown in Figure 3.30 on the left. Also shown is the

CHAPTER 3. DEVELOPMENT OF EFFICIENT WAVELENGTH-SHIFTING  
REFLECTOR FOILS FOR LIQUID ARGON SCINTILLATORS

---

Thickness [mg/cm <sup>2</sup> ]	0.173	0.40	0.49	0.69	0.83	0.90	1.18
Number of measurements	1	2	2	2	2	3	2
Average relative yield	2.16	2.47	3.33	3.60	3.03	3.62	3.12
Standard deviation	–	0.003	0.025	0.097	0.032	0.207	0.296

**Table 3.5:** Summary of relative light yield measurements for different TPB coating thicknesses on Tetratex.

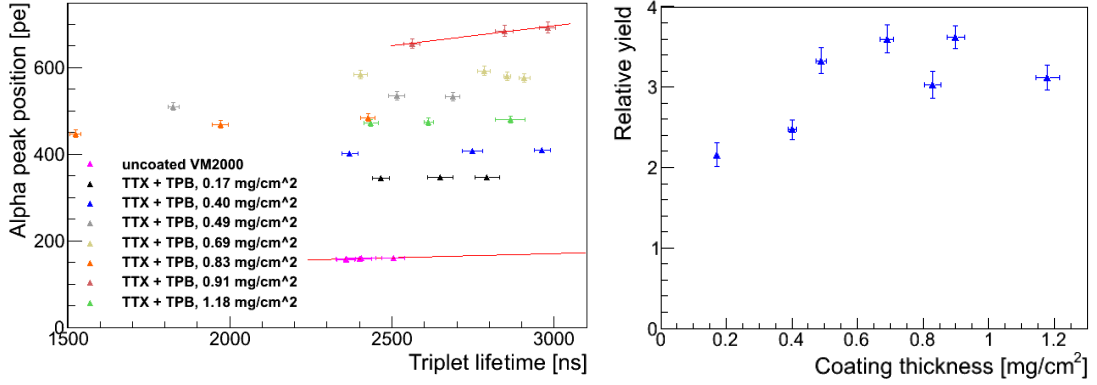


**Figure 3.30:** Tetratex coated with different thicknesses of TPB. Left: alpha peak position as function of the triplet lifetime for different measurements with a linear fit to the reference VM2000 measurement series and a linear fit to the series showing the highest yield. Error bars correspond to 7% as explained in the text. Right: mean relative light yield for different coating thicknesses. Uncertainties include systematic uncertainties. More details are provided in the text.

linear fit to the measurement of uncoated VM2000 which is used as a reference. The thicknesses of the measured samples, the number of measurements performed for the respective thickness, the average relative light yield  $\mu_i$ , as well as the standard deviation  $\sigma_i$  of the relative light yield of the respective thickness are given in Table 3.5. The results are also shown in Figure 3.30 on the right. The mean relative standard deviation  $r$  weighted with the number of measurements  $n_i$  for the respective thickness is

$$r = \sum_i \frac{\sigma_i}{\mu_i} \cdot (n_i - 1) = 7\%. \quad (3.13)$$

This is taken as the uncertainty to compare the relative light yield of different coated samples. If several series of measurements were performed for the same coating thickness (remounted or several coated samples), the uncertainty was divided by the square root of the number of series measured for that thickness.

The highest relative light yield was obtained for coatings with a thickness of

0.90 mg/cm<sup>2</sup>. The relative light yield of the coating with a thickness of 0.83 mg/cm<sup>2</sup> seems too low. It is approximately three standard deviations lower than for the next thinner (0.69 mg/cm<sup>2</sup>) and thicker (0.90 mg/cm<sup>2</sup>) coating. The measurements for this thickness were therefore particularly checked. This includes a visual inspection and comparison of each analysis step described in Section 3.6. No anomalies were found, it is therefore not discarded and considered as an under fluctuation.

The thickness dependence of the relative light yield is small for thicknesses above  $\sim 0.5$  mg/cm<sup>2</sup>. This is an advantageous property for the application of dip-coatings to larger sets of foils. A larger set implies a longer time required for the application of the coating. The solvent dichloromethane in the bath of the coating tool is continuously evaporating during this time. Its volatility results in a relatively fast increase in the TPB concentration and hence an increasing in coating thickness. When reaching the concentration saturation of TPB, flakes form and sometimes attach to the reflector foil to be coated. These flakes can easily fall off later and might harm the experiment. This can be prevented choosing a solution with a concentration significantly below saturation. I suggest a concentration of  $\sim 30$  g/l of TPB in dichloromethane as standard which corresponds to a thickness of  $\sim 0.8$  mg/cm<sup>2</sup>. This thickness is close to the maximal observed light yield and will be used for GERDA. A possible explanation for a reduced light yield at thin coating thicknesses is provided in Section 3.8.6.

The alpha peak position  $\mu_\alpha$  of the series which yielded the highest light yield was extrapolated to the nominal longest triplet lifetime in gas of 3200 ns. This was performed in order to determine the highest nominal light yield in gaseous argon achievable with this setup configuration. The extrapolation was performed fitting the data points with a linear function using the ROOT framework. The fit is shown in Figure 3.30 left. The resulting constant and slope are  $(421 \pm 113)$  pe and  $(0.0917 \pm 0.0405)$  pe/ns, respectively. Uncertainties as provided by the fit routine, which takes into account the uncertainties of the individual points. This is 1.8 % as described in Section 3.8.7 and does not take into account systematic uncertainties of the installation of the foil. The extrapolated alpha peak position is

$$\mu_\alpha(3200 \text{ ns}) = 422 \text{ pe} + 0.0917 \text{ pe/ns} \cdot 3200 \text{ ns} = 715 \pm 7.8 \text{ pe.} \quad (3.14)$$

This corresponds to a light yield for alpha particles of  $(130 \pm 1.4)$  pe/MeV <sub>$\alpha$</sub>  at 5.485 MeV. Note that approximately half of the scintillation light is shining onto the <sup>241</sup>Am source, and not onto the wavelength shifter. This is reducing the light yield with respect to scintillation occurring in the centre of the active volume. The uncertainty  $\sigma_\mu$  was obtained propagating the uncertainties of the constant  $\sigma_c$  and slope  $\sigma_s$  taking into account their correlation through the covariance matrix

element  $C(\sigma_c, \sigma_s)$  (provided by the fit routine):

$$\begin{aligned}\sigma_\mu &= \sqrt{\sigma_c^2 + \sigma_s^2 \tau_2^2 + 2C(\sigma_c, \sigma_s)\tau_2} \\ &= \sqrt{(113 \text{ pe})^2 + (3.2 \mu\text{s})^2 \cdot (0.0405 \text{ pe/ns})^2 - 2 * 4.61 \text{ pe}^2/\text{ns} \cdot 3.2 \mu\text{s}} \quad (3.15) \\ &= 7.8 \text{ pe}.\end{aligned}$$

A sample of Tetratex coated with 3 g/100 ml of TPB in Tetrahydrofuran was additionally prepared (further information about this solvent is provided in Section 3.1.2). This solution resulted in a coating thickness of  $(0.707 \pm 0.023)\mu\text{m}$ . The relative light yield of this coating was measured in gaseous argon and found to be  $2.49 \pm 0.17$ . This is significantly lower than for coatings of similar thickness, which had been produced employing dichloromethane as solvent. Tetrahydrofuran is therefore not further considered.

### 3.8.3 Relative Light Yield of Coatings With Commercial Scintillators

This section presents relative light yield measurements in gaseous argon of the commercial scintillators BCF-10, BC408 and UPS-923A dip coated onto VM2000. Gaseous argon was chosen instead of liquid because of the much faster measurement procedure and smaller argon consumption. Measurements of TPB-coated Tetratex in gaseous argon are described in Section 3.8.2.

The purity of the argon gas in those measurements corresponded to triplet lifetimes in the range of 1500 to 2500 ns. In order to obtain purity independent results the method described in Section 3.6.4 is used. For this method it is necessary to first measure the average number of photoelectrons  $N_\alpha$  produced by alpha events in gaseous argon for uncoated VM2000 at different triplet lifetimes  $\tau_2$ . The measured points were then fit with a linear function. The resulting dependence is

$$N_\alpha = 112 + 0.0194 \cdot \tau_2. \quad (3.16)$$

This is used to determine the relative light yield for each measurement. The triplet lifetimes for the measurements of VM2000 are in a small range compared to the other measurements. The uncertainty introduced by this is still expected to be small compared to other uncertainties. An additional reference measurement series with a larger range was therefore not performed. The measured alpha peak positions as function of the triplet lifetime of all measurements with the commercial scintillators are shown in Figure 3.31. Also shown is the reference measurement series together with the linear fit employed to determine the relative light yield. The measure values of the latter are 1.18, 1.19, 1.20 and 1.20 with an average of  $1.19 \pm 0.08$  for BC408; 1.23, 1.23 and 1.24 with an average of  $1.23 \pm 0.09$  for

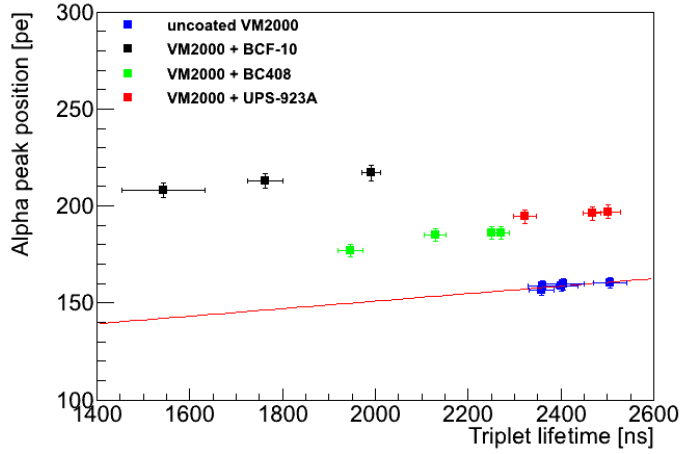


**Figure 3.31:** Alpha peak position measured with commercial scintillators coated unto VM2000 measured in gaseous argon. Also shown the measurement series of uncoated uncoated VM2000 with a linear fit used as reference. Error bars as described in Section 3.8.7.

UPS-923A and 1.46, 1.45 and 1.44 with an average of  $1.45 \pm 0.10$  for BCF-10. The measurements at different triplet lifetimes, of the relative light yield for one coating, result in very similar values. This confirms the validity of the VM2000 reference-function. In combination with the decreasing absolute light yield with decreasing triplet lifetime it also confirms the assumption that the amount of light shifted by impurities is small compared to the light shifted by the respective wavelength shifter.

These measurements show that commercial scintillators can indeed be used as a wavelength shifter for VUV scintillation light. The largest relative light yield was found coating with BCF-10. It yielded an improvement by a factor of  $1.45 \pm 0.10$  compared to uncoated VM2000. The results are compared to other coatings in Section 3.9. The primary source of impurities in gas measurements is expected to be air emanating from pores of the PTFE holder of the PMT. The total amount is estimated to be in the range of approximately 0.01 – 0.5 ppm based on the results of [89].

### 3.8.4 Light Yield Measurements in Liquid Argon

The relative light yields of the best candidate coated reflector foils were measured in liquid argon. These were chosen based on their mechanical properties (Section 3.2) and light yield, measured in argon gas (Section 3.8.2 and 3.8.3) or with the fluorescence spectrometer (Section 3.3). The selected coatings are 10:1 PS:TPB

and 80 % Makrolon + 20 % TPB on VM2000, as well as pure TPB on Tetratex. The light yield of those was measured relative to uncoated VM2000 as described in Section 3.6.4. Tetratex was coated with a concentration of 3.3 g/100 ml of TPB in dichloromethane which resulted in a thickness of  $(0.88 \pm 0.027)$  mg/cm<sup>2</sup>. These samples had been measured in gaseous argon before. Its relative light yield in gas is included in the result presented in Table 3.5 for a thickness of  $(0.90 \pm 0.027)$  mg/cm<sup>2</sup>. VM2000 was measured in liquid argon at several different argon purities. This series of measurements was obtained intentionally spoiling the argon with air between those measurements. The chamber was emptied, warmed up and pumped after the first reference measurement series with VM2000 but not opened. A second series of measurements was then taken. These two were combined and fit with a linear function which is used as reference for other measurements in liquid argon. The mean number of photoelectrons for alpha events detected with VM2000  $N_\alpha$  can then be calculated for any triplet lifetime  $\tau_2$  by

$$N_\alpha = 112.2 \text{ pe} + 0.0194 \text{ pe/ns} \cdot \tau_2. \quad (3.17)$$

These alpha peak position values and the reference linear fit are shown in Figure 3.32. Also shown are the measurements of the other selected coatings. Uncertainties are assumed to be the same as for measurements in argon gas and hence dominated by systematics. The error bars drawn in this figure correspond to 7 % uncertainty as determined in Section 3.8.2. It is the uncertainty relevant to compare different coatings to each other. It was intentionally chosen to plot this uncertainty in contrast to the uncertainty on the alpha peak position of individual measurement points (1.8 %) in order to visualise the significance of the different obtained light yields.

The light yield of the reference VM2000 measurements shows a linear dependence on the triplet lifetime. This confirms the assumption that the amount of light shifted by impurities is small compared to light shifted by the coated reflector foils. It is furthermore confirmed by a measurement performed without wavelength shifter which resulted in an upper limit of  $< 2\%$  of light detected compared to uncoated VM2000. The assumption of purity independence of the relative light yield is hence justified for these measurements.

Amongst the measured samples, Tetratex coated with pure TPB shows the highest relative light yield of  $2.96 \pm 0.21$  and  $3.39 \pm 0.24$  for the two measurements. The average is  $3.15 \pm 0.16$ . This is a large improvement compared to the previous candidate for GERDA, which was VM2000 coated with PS and TPB, with a relative light yield of  $1.5 \pm 0.11$ . VM2000 coated with the optimal ratio of Makrolon and TPB (80 % and 20 %) was found to have the second highest relative light yield of  $2.3 \pm 0.16$ . This is 27 % lower than TPB-coated Tetratex. It is therefore a very good alternative for coatings where transparency to visible light is required, e.g. PMT windows.

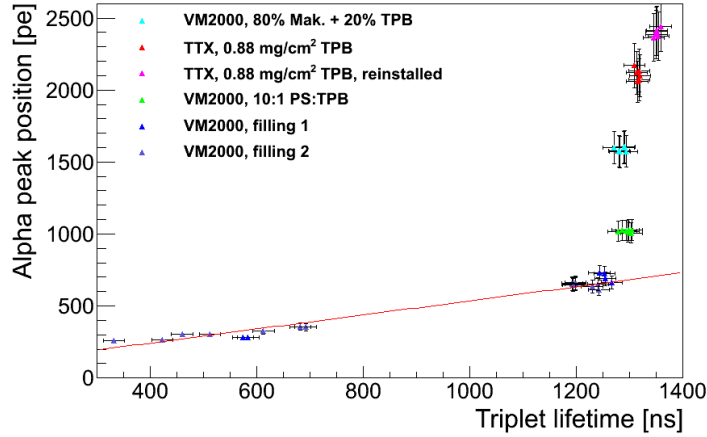


**Figure 3.32:** Alpha peak position for the best candidate coatings on VM2000 and Tetratex measured in liquid argon. Error bars represent the uncertainty to compare the light yield of different coatings as described in Section 3.8.7.

The primary sources of impurities present in those measurements are expected to be initial contaminations in the argon bottle (purity class 6.0) and air emanating from pores of PTFE detector components. An estimation of impurity concentrations is performed based on the results of [116] and [117] assuming a composition similar to air. Therein the triplet lifetime was measured as a function of  $O_2$  and  $N_2$  contamination separately. Their purest argon had a contamination of  $\sim 4 \cdot 10^{-3}$  ppm  $O_2$  and  $\leq 0.5$  ppm  $N_2$  resulting in a triplet lifetime of  $\sim 1200$  ns. This is shorter than in all best candidate measurements of the light yield presented in this chapter. Their upper limit on the initial  $N_2$  contamination of 0.5 ppm  $N_2$  corresponds to  $\sim 0.14$  ppm  $O_2$  under the assumption of air. Such an  $O_2$  contamination resulted in a decrease of the triplet lifetime of  $\sim 150$  ns in their measurements. Such an impurity concentration is hence a very conservative upper limit for the measurements of the best candidates presented in this section.

The decrease in argon purity within one measurement series of TPB-coated Tetratex is too small to make an extrapolation of the absolute light yield to the nominal maximal purity of 1600 ns. It is therefore calculated for the remounted sample at its mean purity of  $(1356 \pm 20)$  ns. Resulting in a mean light yield of  $(2400 \pm 43)$  pe for alpha particles at an energy of 5486 keV. This corresponds to an absolute light yield per MeV of  $(247 \pm 4)$  pe/MeV $_{\alpha}$ . The standard deviation of the triplet lifetime and light yield of those measurements are 4.9 ns and 22 pe, respectively. The light yield of nuclear recoils is reduced compared to electronic recoils, which is called nuclear quenching. The relative scintillation efficiency was measured in liquid argon in the energy range of  $\sim 10$  to

$\sim 250$  keV [118], [119], [120], [121] and found to be flat above  $\sim 50$  keV within that range, as predicted by theory [122], [123]. Assuming the relative scintillation yield of that flat region of  $\sim 0.28$  for the alpha particle at 5486 keV one obtains a light yield for electron recoils of  $\sim 882$  pe/MeV. Note that half of the 128 nm scintillation light falls onto the  $^{241}\text{Am}$  source.

### 3.8.5 Long-Term Stability in Gaseous Argon, Liquid Argon and Air

TPB-coated Tetratex was investigated on its long-term stability. Both the relative light yield and mechanical properties were subject of these studies. The coated reflector was therefore exposed to ambient air for 51 days and immersed in liquid argon for 100 days.

#### Long-Term Stability in Air

TPB-coated Tetratex was investigated on possible effects on its stability and efficiency when being stored in air. Employed was a Tetratex sample dip-coated with 3.3 g/100 ml of TPB in dichloromethane, which resulted in a thickness of  $(0.88 \pm 0.027)$  mg/cm<sup>2</sup>. The coated foil was installed in the argon setup directly after coating and its relative light yield was measured in liquid argon to be  $2.96 \pm 0.21$ . The foil was removed from the setup after this measurement and stored in an open shelf in the laboratory for 51 days. It was wrapped in aluminium foil to avoid direct exposure to light and dust. The packaging does result in a permanent exposure to oxygen and humidity from the air. Afterwards it was reinstalled in the argon setup and the measurement was repeated in liquid argon resulting in a relative light yield of  $3.27 \pm 0.23$ . This corresponds to an increase with a negligible significance of  $\sim 1\sigma$ . The coating was furthermore optically inspected under day and UV light. No deterioration was observed. This measurement shows that the coating is resistant to storage in air on a time scale of at least several months. Both the mechanical stability and the relative light yield did not decrease within 51 days. This significantly simplifies the production, transportation, installation and storage. There are no requirements to keep coated sheets under special atmosphere, which is particularly useful for spare foils.

#### Long-Term Stability in Liquid Argon

The long-term stability in liquid argon was tested with a Tetratex sample dip-coated with 3.3 g/100 ml of TPB in dichloromethane. The coating was prepared from the solution used later to coat the reflector foils to be installed in GERDA. It

resulted in a thickness of  $(0.83 \pm 0.02)$  mg/cm<sup>2</sup>. Its relative efficiency was periodically measured keeping the sample constantly in liquid argon for 100 days. The purity was decreasing during the measurement from an initial triplet lifetime of  $(1260 \pm 20)$  ns to  $(700 \pm 20)$  ns. The initial lifetime corresponds to a contamination of  $< 0.5$  ppm N<sub>2</sub> and  $< 0.14$  ppm O<sub>2</sub> as described in Section 3.8.4. The final triplet lifetime of 700 ns corresponds accordingly to  $\lesssim 1.2$  of O<sub>2</sub> and  $\lesssim 4.4$  of N<sub>2</sub>.

The PMT voltage had to be changed during the long-term measurement, once from 1500 V to 1475 V due to sparking and once from 1475 V to 1490 V to obtain a better separation of the single photoelectron peak from noise. The sparking occurred most likely inside the PMT. This was also described in Section 3.8.1. The worse separation is mainly driven by a decreasing gain and number of single photoelectron events. The latter is caused by the decreasing argon purity, which is reducing the triplet component of the light pulse.

The gain was determined for each measurement as described in Section 3.6.1. Its evolution during these measurements is shown in Figure 3.33 on the top. Shown on the bottom are single photoelectron spectra representative for the respective periods with a constant gain. The single point on day six with a gain of  $6.3 \cdot 10^6$  is at a PMT voltage of 1500 V, like in the previous measurements. This is the largest observed gain change between two consecutive measurements taken at the same PMT voltage. Error bars up to day 25 correspond to the previously found uncertainty of 1.8%. For later measurements the separation of the single photoelectron peak from the noise was worse resulting in a larger uncertainty, which is guessed to be approximately twice as large ( $\sim 3.6\%$ ).

An anti-correlation is observed between gain and relative light yield fluctuations within periods without an obvious gain change. This is visible in Figure 3.34. This demonstrates that the gain change from one run to the next is small compared to the fluctuation originating from the gain determination. Therefore, a mean gain is used for all measurements in periods without a clear gain change. These mean gains are shown by the red lines in Figure 3.33 top and were determined fitting a constant to the respective time range using the fit routine provided by ROOT. This method does additionally prevent a continuously increasing bias by the continuously decreasing fraction of single photoelectrons. Hence, a continuous change in the relative light yield can not be caused by this reason. The uncertainty on the fit parameter provided by the routine was used as uncertainty on the relative light yield of those measurements. It is taking into account the uncertainties provided for each gain measurement but not instrumental uncertainties introduced by the installation of the foil. For some measurements the separation of the single photoelectron peak was insufficient to determine the gain (gaps in figure 3.33). It is assumed that the gain in those measurements is the same as the determined mean for that time period.

## CHAPTER 3. DEVELOPMENT OF EFFICIENT WAVELENGTH-SHIFTING REFLECTOR FOILS FOR LIQUID ARGON SCINTILLATORS

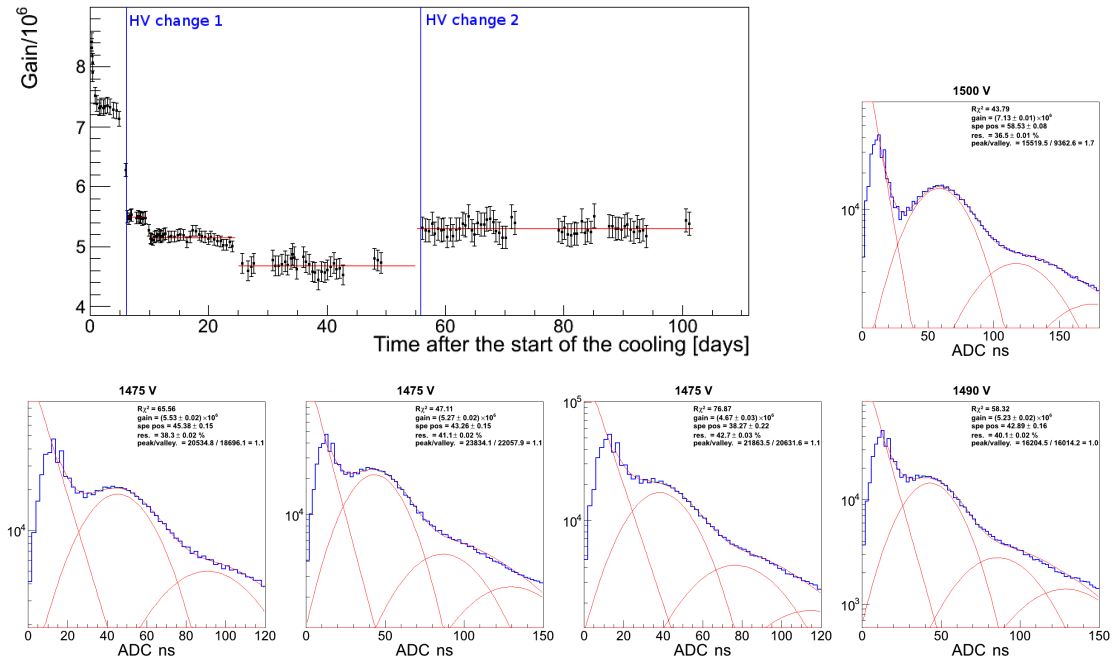


**Figure 3.33:** Top left: gain evolution during the long-term measurement. The mean gain for the last four regions with stable gain was determined by a fit with a constant, which is shown by the red curves. Top right and bottom: single photoelectron spectra typical for the five regions with constant gain.

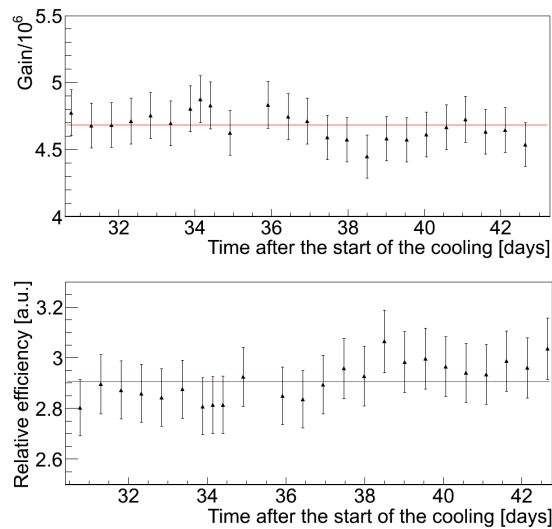


**Figure 3.34:** Deviations of the determined gain from its mean are anti-correlated with deviations of the relative light yield from the mean light yield.

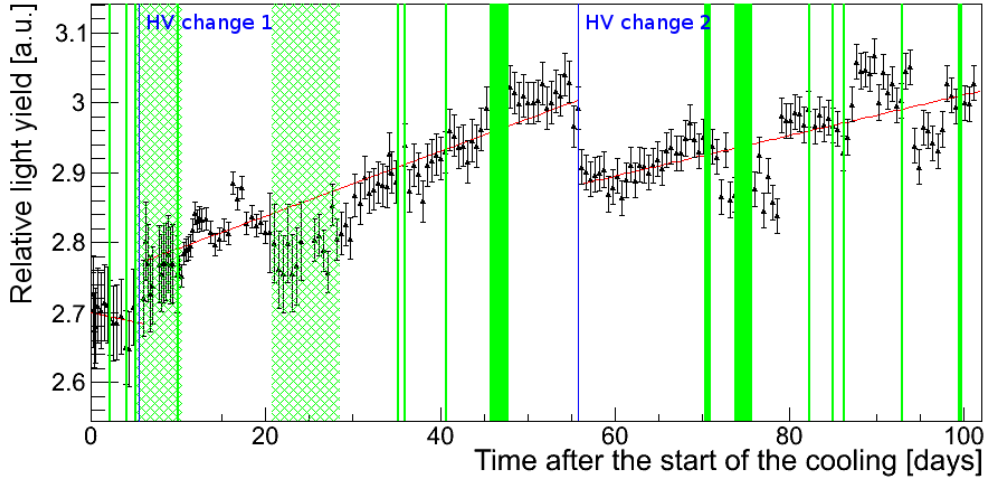


**Figure 3.35:** Relative light yield of Tetratex dip-coated with TPB as a function of time in liquid argon, measured relative to uncoated VM2000. Time periods with 1500 V, 1475 V, 1490 V PMT voltages were fitted separately with a linear function. Error bars as described in Sec. 3.8.

The relative light yields of all measurements within the 100 days are shown in Figure 3.35. The three periods with constant PMT voltage were separately fit with a linear function resulting in an apparent increase of  $(14 \pm 7)\%$  over the period of 100 days. The clusters of events around day 75 and day 95 are showing a light yield more than the uncertainty lower than the linear fit. The gains in those measurements could not be determined and were taken from the average in that region. If the real gain in those measurements was smaller than the used mean it would explain the lower determined light yield for those. A possible explanation was not found for other observed deviations. Error bars reflect the uncertainty on the gain determination but do not include a change in the geometry of the reflector foil. Convection of liquid argon and tension in the foil might lead to changes in the geometry within the 100 days of operation. Therefore an uncertainty of 7% obtained as described in Section 3.8.2 is conservatively assumed for a change over the whole period. The apparent increase is further investigated in the following.

The long-term measurement in liquid argon is complemented by measurements in gas argon carried out before and after. The alpha peak position as function of triplet lifetime for the two series measured in gas is shown in Figure 3.36. Each series was fit with a linear function. Dividing the two functions one obtains an increase of  $(3.9 \pm 7)\%$ . This is in consistency with both, an increasing and a constant light yield. It is an important complimentary confirmation of the stability. Both gas measurement series were taken under the same conditions and impurity

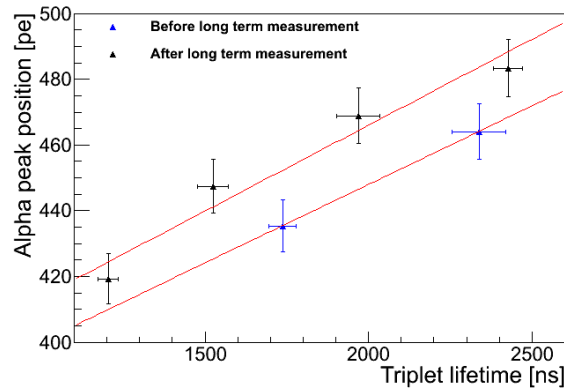


**Figure 3.36:** Comparison of the light yield in gaseous argon before and after the long-term measurement in liquid argon. Both series were fit with a linear function which is employed to evaluate a potential change.

level in contrast to the measurements taken during the liquid argon measurement. The chamber has not been opened between the two measurements in gas. The uncertainty on the change between these two measurement series is conservatively assumed to be similar to measurements with intermediate remounting, as thermal contraction, liquid and gas flow might have changed the geometry of the reflector foil slightly. Several potential reasons for the apparent increase in light yield are discussed in the following.

### Detailed Studies of Measurement Conditions

The relative light yield is expected to be insensitive to changes in purity if the amount of light shifted by impurities is negligible compared to the coated reflector. Otherwise it is expected to decrease with increasing impurity concentration. This was described in detail in Section 3.6.4. It can therefore not explain a rise in efficiency with increasing impurity concentration. Impurities are therefore unlikely to be the origin of the apparent increase.

The PMT photocathode and body are at negative high voltage in contrary to all other metal parts of the setup which are not part of the PMT and grounded, in particular the aluminium plate holding the alpha source. This results in an electric field above the surface of the alpha source. The light yield of liquid argon is dependent on the electric field [124], which is a potential source of influence on the measured light yield of the reflector foils. In particular, a reduction in the electric field strength above the alpha source could result in an increased amount of scintillation light. A reduction can be caused by a change of the PMT voltage or by charge accumulation, e.g. at the PMT window, reflector foil or PTFE holder.

The electric field in the active volume was therefore simulated using the Comsol Multiphysics [125] software. The simulation includes the dewar approximated by a conductive can, the PMT, the PTFE ring where the PMT is sitting on, the aluminium cage which is defining the active volume, the  $25\ \mu\text{m}$  thick  $^{241}\text{Am}$  source, the PTFE filler and liquid argon. Other components are not expected to have a relevant influence on the electric field at the position of scintillation light production and are therefore not included in the model. The distribution of the electric potential obtained from this simulation is shown in Figure 3.37 on the left for the nominal PMT voltage of 1500 V. The alpha particles from the  $^{241}\text{Am}$  source have a range of  $\sim 52\ \mu\text{m}$  in liquid argon. The scintillation light is produced along this track with a larger fraction of light produced at the end of the track. The field strength is therefore evaluated slightly above half of the track length of the alpha particle,  $28\ \mu\text{m}$  above the source. It is shown in Figure 3.37 on the right and has a strength of 1400 V/m. This low electric field and in particular an even lower change in the field is not expected to have an observable effect on the presented results. It hence disfavours charge accumulation as the dominating effect for the apparent light yield increase. The relative light yield did however seem to change slightly when the PMT voltage was changed. The change is not very significant due to the presence of other changes with similar size. If it would be real, it would be in slight tension with the conclusion from the electric field simulation.

In case of saturation of the PMT base, overlinearity [110] would be expected. This would artificially increase larger signals which were present in the beginning of the measurement when the argon purity was higher. Measurements with VM2000 would be less effected due to the smaller light yield. The effect on measurements with VM2000 can therefore be assumed to be negligible compared to Tetratex in this scenario. As a result a seemingly decreasing light yield would be expected with decreasing purity and hence later times in this measurement. This is the exact opposite of what has been observed. This is a confirmation that the PMT base is linear in the range of the measurements and not the cause of the observed apparent increase of the shifting efficiency.

### Conclusions on the Long-Term Stability

An explanation for the apparent increase of  $(14 \pm 7)\%$  was not found. It is unclear if it is a real effect or caused by unknown uncertainties of the measurement or analysis procedure. The results do nevertheless prove the long-term stability of TPB coated Tetratex. This was the main goal of the long-term measurements. The detailed investigations conducted in this context support the reliability of other relative light yield measurements.

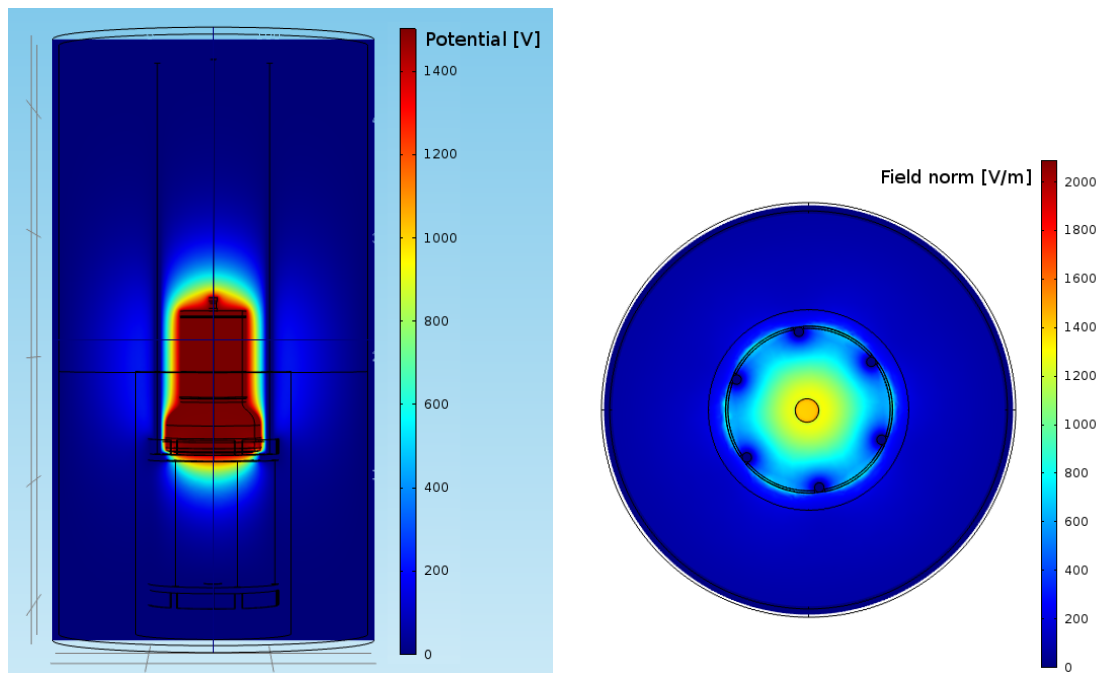


**Figure 3.37:** Left: side view of the electric potential in a cut through the centre of the setup. Right: top view of the norm of the electric field within the range of the alpha particles,  $28 \mu\text{m}$  above the  $^{241}\text{Am}$  source. Plots are produced with the Comsol Multiphysics software package [125] for a PMT voltage of 1500 V.

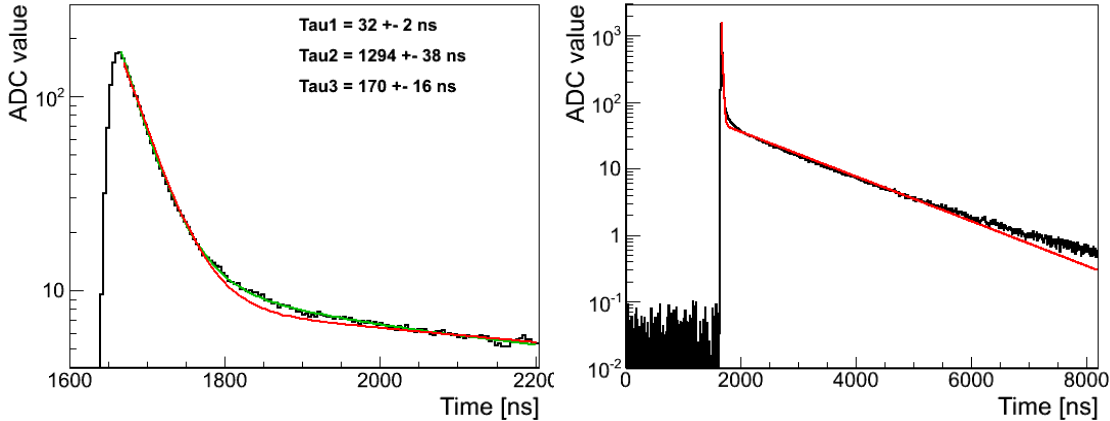


**Figure 3.38:** Mean trace with fit of two and three exponential decays. Left: good/excellent description in a measurement with uncoated VM2000 in liquid argon by two/three exponential decays (red/green line). The obtained decay times of the fast, slow and intermediate component are labeled with Tau1, Tau2 and Tau3, respectively. Uncertainties are as provided by the fit routine. Right: typical mean trace of measurements of coatings containing TPB. An excess of light is visible over a two-exponential model in the transition region between the singlet and triplet component, as well as after the triplet component.

### 3.8.6 Delayed Fluorescence from TPB and from VM2000

Fitting the decay of the mean trace with two exponential functions as already mentioned in Section 3.6.2 does not properly describe the transition region between the singlet and triplet component. Including an intermediate component allows however to accurately fit this region for measurements with uncoated VM2000, as shown in Figure 3.38 on the left. The enhanced signal strength compared to a two component fit is observed in the time range of approximately 120 to 350 ns after the peak. This is not compatible with afterpulses and is therefore interpreted as a third component in the detected light. It originates presumably from a delayed emission of the fluorescence of VM2000 (polyester), excited by light from the singlet component of argon. The argon singlet component has a much larger amplitude than the triplet component resulting in the visibility of the delayed emission from VM2000 on top of the argon triplet component. The decay time of the delayed VM2000 emission obtained from the shown fit is 170 ns. This is small compared to triplet lifetimes in the presented light yield measurements and not expected to have an influence in the time range used for its determination (400 – 4000 ns).

Mean traces from TPB-coated Tetratex, as well as coatings containing TPB on VM2000 show a larger excess over a two decay model in the transition region compared to uncoated VM2000. An additional excess is observed after the triplet

component. It was not possible to obtain stable fit results with a three component decay model, including one exponential for the singlet, one for the triplet and one for an intermediate component. This fact fits well with the non-exponential time structure of a delayed emission from TPB excited by argon scintillation light as described in [126].

Such a delayed emission is expected to result in a decreased value of the component ratio. This was investigated on measurements which have a similar triplet lifetime, which is important as the measured component ratio is also dependent on the triplet lifetime. A decrease is indeed observed for coatings containing TPB compared to other coatings and uncoated VM2000, both for measurements in gaseous and liquid argon. The two thinnest coatings of Tetratex with pure TPB with a thickness of 0.17 and 0.40 mg/cm<sup>2</sup> resulted however in a component ratio similar to coatings not containing TPB. The origin might be interactions of TPB molecules with the PTFE substrate. Molecules situated close to the PTFE surface are covered by less TPB if the coating is thin enough and are hence exposed to the scintillation light. The interactions might influence the excited TPB states possibly resulting in a non-radiative deexcitation and hence the absence of a delayed emission. This could also be the reason for the lower light yield observed with these coating thicknesses (light yield measurements were presented in Section 3.8.2).

### 3.8.7 Discussion of Uncertainties

The determinations of uncertainties of individual analysis steps and estimations of uncertainties based on fluctuations of measurements performed under seemingly identical conditions, were provided in the respective sections. This section is summarising those uncertainties and discussing further uncertainties and their influence on the measured light yield.

After some measurements there was a small slit at the side of the active volume where the reflector foil is overlapping, visible in Figure 3.23 on the right. Light escaping through such a slit is not detected. The width of that slit was always smaller than 5 mm. An estimation of an upper limit on the fraction of light lost through that slit (compared to the absence of a slit) is conducted based on the following assumptions:

- all light hitting this slit is lost,
- each surface is illuminated with equal intensity,
- the reflectivity of aluminium parts for shifted light is 90 %, the reflector 99 % and the PMT 0 %,
- the 5 mm wide and 10 mm high PTFE surface next to the PMT window is neglected,

- the PMT and aluminium absorb 128 nm light,
- the aluminium rods in the active volume are neglected.

The total surface area of the active cylinder is  $53447 \text{ mm}^2$ , of a 5 mm wide slit  $537 \text{ mm}^2$ , of the cylinder mantel  $35798 \text{ mm}^2$ , of the PMT face  $4560 \text{ mm}^2$ , of aluminium on bottom and top  $13\,088 \text{ mm}^2$ . The fraction of 128 nm light lost through the slit (additionally to the 128 nm light always lost by falling onto the PMT or aluminium) is hence  $A_{slit}/A_{mantel} = 0.015$ . The probability  $p_r$  of shifted light getting reflected is:

$$\begin{aligned} p_r &= (0 \cdot A_{PMT} + 0.90 \cdot A_{Al} + 0.99 \cdot (A_{reflector} - A_{slit}) + 0 \cdot A_{slit})/A_{tot} \\ &= (0.9 \cdot 13088 + 0.99 \cdot (35798 - 537))/53477 = 0.87, \end{aligned} \quad (3.18)$$

of which the fraction  $p_r \cdot A_{slit}/A_{tot}$  is lost. The total fraction of light lost through the slit is then given by the sum of the fraction of primary unshifted light lost and the sum over infinite number of reflections  $n$  of the shifted light lost in each reflection

$$\begin{aligned} &A_{slit}/A_{mantel} + (1 - A_{slit}/A_{mantel}) \sum_{n=0}^{\infty} (p_r^n \cdot A_{slit}/A_{tot}) \\ &= 0.015 + 0.985 \sum_{n=0}^{\infty} (0.87^n \cdot 537/53447) = 0.081. \end{aligned} \quad (3.19)$$

This means that the maximum fraction of light which might have been lost through a slit is  $\sim 8\%$ . This upper limit is large compared to uncertainties of the analysis method but too small to explain the average fluctuation of  $\pm 7\%$  as observed in Section 3.8.2 ( $\pm 7\%$  corresponds to a range of  $14\%$ , compared to a range of  $8\%$  obtained by this estimation). This suggests an additional source of uncertainty which might be both a longitudinal bending of the reflector foil and variations in the thickness of the Tetratex possibly caused by stretching or contraction of the foil during installation and storage.

The presence of a delayed fluorescent light emission was shown in Section 3.8.6. Light from the triplet state is dominant over delayed light in the time range used to determine the triplet lifetime in case of high argon purity for all coatings. It is therefore not expected to have a significant impact on the determination of the triplet lifetime in those cases. The long tail of the delayed light emission in case of TPB does however result in an overestimation of the triplet lifetime in measurements with an argon purity corresponding to less  $\lesssim 850 \text{ ns}$ . This results in a purity correction which is too small and hence an underestimation of the light yield. The only measurements with such a low argon purity are the last few data points of the long-term stability measurements of coated Tetratex in

Variable	PMT calibration	$\tau_2$ (sys.)	$\mu_\alpha$	$L_r$ remounted	slit
Uncertainty	$\pm 1.8\%$	$\pm 20$ ns	$\pm 0.15\%$	$\pm 7\%$	$<_{-0}^{+8}\%$

**Table 3.6:** Summary of uncertainties for measurements of the light yield in argon. PMT calibration stands for the combined uncertainty on the single photoelectron position,  $\tau_2$  for the triplet lifetime in liquid argon measurements,  $\mu_\alpha$  for the determination of the alpha peak position not including uncertainties on the PMT calibration, "  $L_r$  remounted " for the empirically determined uncertainty on the measurement of the absolute value of the relative light yield  $L_r$  (in contrast to a comparison of values of  $L_r$  measured without intermediate remounting) and "slit" for the light lost through a slit potentially forming during cool down.

liquid argon. For the latter, a higher light yield than expected was observed. Considering a possible overestimation of the purity in those measurements would result in an even larger increase of light yield with time. The rise can hence not be caused by this and the observed stability of the coating is indeed confirmed. A quantification of this purity and coating dependent uncertainty is difficult. It is furthermore irrelevant for the conclusions drawn from the presented measurement and therefore not further investigated.

The Table 3.6 is summarising all quantified uncertainties. Depending on the results to be compared, different uncertainties are relevant. For comparison of the light yield between measurements where no geometrical change of the reflector foil is possible, the uncertainty on the PMT calibration of  $\pm 1.8\%$  is dominating. This is also the case for the relative light yield, as every individual measurement uses the same reference VM2000 measurement. A change in the reference would hence result in the same relative change for all individual measured light yield values. For a comparison between measurements where a geometrical change of the reflector foil is possible, the uncertainty of  $\pm 7\%$  empirically determined in Section 3.8.2 is relevant. It includes effects originating from mounting and dismounting, such as the curvature of the mounted foils and slits. The curvature influences the solid angle of scintillation light hitting the coated reflector foil and the solid angle of illuminated reflector foil seen by the PMT. Both have an effect on the measured amount of light. For coatings remounted several times, the uncertainty was divided by the square root of the number of mounts.

### 3.9 Comparison of Results and Methods

This sections compares the light yield measurements for different coated reflector foils obtained with different measurement methods. The relative light yield for VM2000 coated with PS + TPB was measured to be  $1.5 \pm 0.1$  in liquid argon.

The maximum intensity of the emitted light in the fluorescence spectrometer was however twice as high as for uncoated VM2000. The different spectral shapes in the latter measurement and the spectral response of the PMT in the argon setup can not explain the observed discrepancy. An even larger discrepancy is measured for coatings with 80 % Makrolon and 20 % TPB, for which an eight times higher amplitude is observed compared to a relative light yield in liquid argon of 2.3. This shows that measurements with a fluorescence spectrometer at an excitation wavelength of 260 nm are not sufficient to predict the coating/reflector foil combination which results in the largest light yield for argon scintillation light and that measurements with argon scintillation light are necessary. The difference is therefore assigned to a lower shifting efficiency or different emission spectrum for argon scintillation light compared to 260 nm light. The results obtained with the fluorescence spectrometer are still expected to provide a valid estimation when comparing the same coating on different reflector foils like VM2000 or copper.

0.90 mg/cm<sup>2</sup> of TPB-coated on Tetratex has been measured to result in a relative light yield in gaseous argon of up to  $3.62 \pm 0.14$  and in liquid argon of  $3.15 \pm 0.16$ , respectively. This is a difference of  $0.47 \pm 0.21$  which corresponds to a significance of  $2.2\sigma$ . It is not clear if this is a real effect or caused by measurement uncertainties. There is no clear physical reason to prefer the one or the other. On the one hand, reflections at the argon/PMT surface are expected to be smaller for the liquid argon compared to gas. The reason is the refractive index of liquid argon which is closer to that of the PMT window. The reflectivity on the reflector argon surface, on the other hand, might be reduced for liquid argon compared argon gas for the same reason. If the observed difference is real it could mean that the latter is true and has a larger effect compared to the former.

In order to compare the results measured in the liquid argon setup to other experiments employing other light detection devices, it is necessary to know the spectral response of PMT. This is was provided in Figure 3.24.

### 3.10 Radiopurity of TPB Coated Tetratex

Traces of radioactive isotopes in Tetratex and TPB have been identified quantitatively employing three complementary techniques: gamma ray spectrometry, inductively coupled plasma mass spectrometry (ICP-MS) and radon emanation.

The gamma ray spectrometry was performed by Francesco Piastra from the University of Zurich employing the low-background high-purity germanium detector facility Gator [127] operated in the underground laboratory of LNGS. Activities of radio-isotope contaminants are determined from the intensities of their most prominent gamma lines taking into account their respective photo-absorption efficiencies. It is determined for each gamma line by a Monte Carlo simulation em-

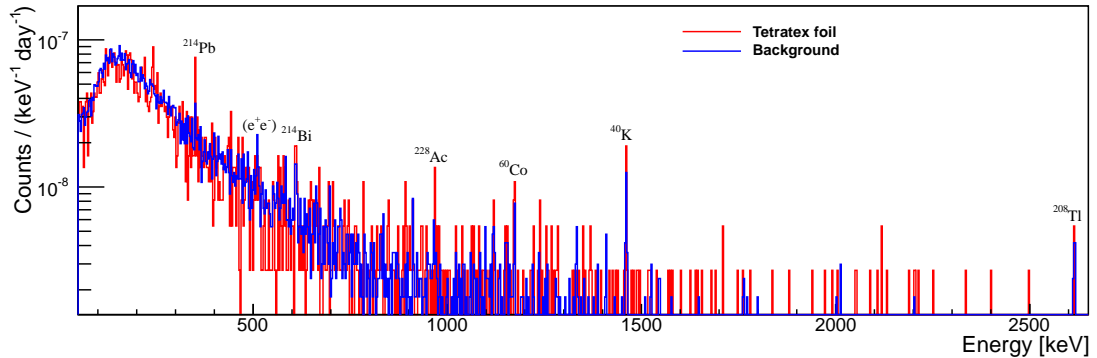


**Figure 3.39:** Spectral count rate of TPB-coated Tetratex (red) superimposed by the Gator background (blue).

ploying a detailed GEANT4 [128] model of the sample and detector. The branching ratios of different gamma lines for each isotope or decay chain are taken into account by the G4RadioactiveDecay class [129].

A complete set of eight full size sheets (as required for GERDA) were coated in the ETH clean room facility “First Lab”. This also served as a test of the coating procedure for the final set to be installed in GERDA. All sheets together have a total weight of 208 g and were measured for 10.5 days in the Gator cavity. Before loading, the foil was folded to a rectangular shape. The resulting dimensions are 10 cm×15 cm and an average height of 4.5 cm. This size is comparable to the size of the Ge detector. The sample was placed on top of the detector’s cryostat a few mm from the sensitive crystal.

The measured gamma ray spectrum of the coated Tetratex is shown in Figure 3.39 (red) and compared to the background (blue). The latter was acquired in a 47.8 days run. For all isotopes of interest the rates of the gamma lines are compatible with background expectations (a detection claim is based on a statistical test with 5% significance level). In Table 3.7 the upper limits at 90% C.L. are reported for each isotope analysed with this technique. The coated Tetratex was placed in a dust tight bag and transported back to the University of Zurich. It is stored there to be quickly available as emergency replacement for sheets installed in GERDA.

ICP-MS measurements were performed by the chemical service of LNGS. A sample of uncoated Tetratex, a sample of scintillation grade TPB from Sigma Aldrich and a sample of Tetratex dip-coated with TPB dissolved in p.a. grade dichloromethane were analysed. The measured blank subtracted concentrations in Tetratex/TPB/coated Tetratex are 0.053/0.016/0.173 ppb for  $^{232}\text{Th}$ , 0.071/0.014/0.123 ppb for  $^{238}\text{U}$ , and 287/137/746 ppb for  $^{40}\text{K}$ . These values converted

CHAPTER 3. DEVELOPMENT OF EFFICIENT WAVELENGTH-SHIFTING  
REFLECTOR FOILS FOR LIQUID ARGON SCINTILLATORS

---

mBq/kg	<sup>238</sup> U	<sup>226</sup> Ra	<sup>228</sup> Ra	<sup>228</sup> Th	<sup>235</sup> U	<sup>40</sup> K	<sup>60</sup> Co	<sup>137</sup> Cs	<sup>232</sup> Th
Gator	<115	<11.6	<15.3	<9.79	<6.68	<54.3	<3.43	<3.58	
coated	1.5					23			0.70
TTX	0.9					9			0.21
TPB	0.17					4			0.06

**Table 3.7:** Summary of radioactive trace contaminations in Tetratex dip-coated with TPB, pure TPB and uncoated Tetratex. Activities in the first line are for TPB-coated Tetratex obtained by gamma ray spectrometry with Gator. The last three lines are results obtained by ICP-MS. "Coated" stands for Tetratex coated with TPB and "TTX" for uncoated Tetratex. Uncertainties on values from ICP-MS measurements are 30 %. Upper limits at 90 % C. L.. <sup>238</sup>U, <sup>226</sup>Ra, <sup>228</sup>Ra, <sup>228</sup>Th and <sup>235</sup>U represent the sub decay chains <sup>238</sup>U-<sup>230</sup>Th, <sup>226</sup>Ra-<sup>206</sup>Pb, <sup>228</sup>Ra-<sup>228</sup>Ac, <sup>228</sup>Th-<sup>208</sup>Pb and <sup>235</sup>U-<sup>207</sup>Pb, respectively.

into activities are provided in Table 3.7 together with the activity limits obtained with Gator.

A further potential radioactive contamination is radon emanating from the wavelength shifter, which can reach the Ge-detectors in GERDA through the liquid argon. They contribute to the background in the ROI by subsequent alpha decays. More details are given in Section 2.2. The emanation rate of <sup>222</sup>Rn was therefore measured by the Max-Planck-Institut für Kernphysik in Heidelberg. 373 g of uncoated Tetratex was loaded into a vacuum chamber, which was pumped, and flushed with radon-depleted helium. This cleaning procedure is resetting the current radon level. Emanating <sup>222</sup>Rn is then accumulated in the vacuum chamber and transferred to proportional counters employing radon-depleted helium gas. The number of radon decays is detected in the proportional counters and converted into a radon emanation rate. An upper limit of 54 μBq/kg was found at 90 % C.L. A more detailed description of the setup and measurement procedure can be found in [130].

The background contribution caused by the measured radioactive trace contaminants on the coated reflector foil was simulated as part of the full liquid argon veto by others in the collaboration. It was found to be well within the requirements for deployment in GERDA Phase II.

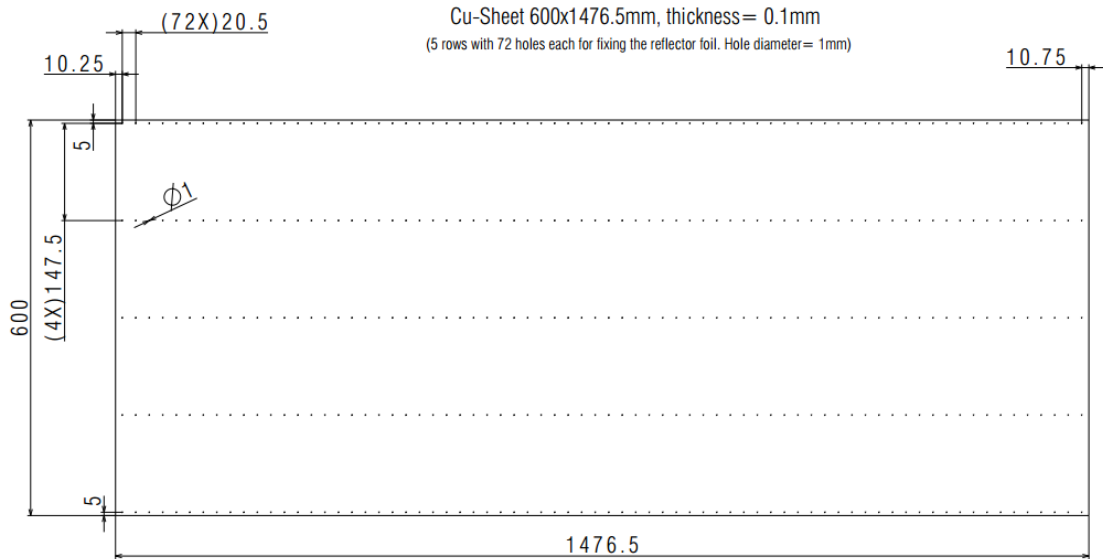


**Figure 3.40:** Drawing of the hole pattern in the mantle of the copper shrouds for the installation of the coated Tetratex reflector in GERDA. Dimensions are in [mm].

### 3.11 Installation of TPB Coated Tetratex in the Liquid Argon Veto

The coated reflector foils will be installed inside two copper cylinders, the so-called "radon shrouds". Each of those has a height of 600 mm and a circumference of 1476.5 mm. The copper has a thickness of 0.1 mm. The Tetratex is available on a roll with a width of 457 mm. It was decided to produce 4 sheets with a length of 64 cm for each cylinder. These are cut to the length of the cylinder and a width of 40 cm to cover the inside of the cylinders with an overlap of 3 cm. The sheets need to be fixed with a method introducing as little radioactivity as possible. It has to withstand long-term operation in liquid argon and multiple deployments without deteriorating the liquid argon purity. A method fulfilling these criteria is stitching the coated foil to the copper cylinders employing 100  $\mu\text{m}$  thick nylon wire. The copper sheets of the cylinder mantle are therefore prepared with an array of holes, 1 mm in diameter. The arrangement of the holes is shown in Figure 3.40. The reliability of this installation technique was intensively tested beforehand and is described in the following.

In a first test holes with a diameter of 1 mm were drilled into a 0.1 mm thick copper foil employing two different methods. Once the copper foil was placed on top of a plastic plate and once between two plastic plates. The former method

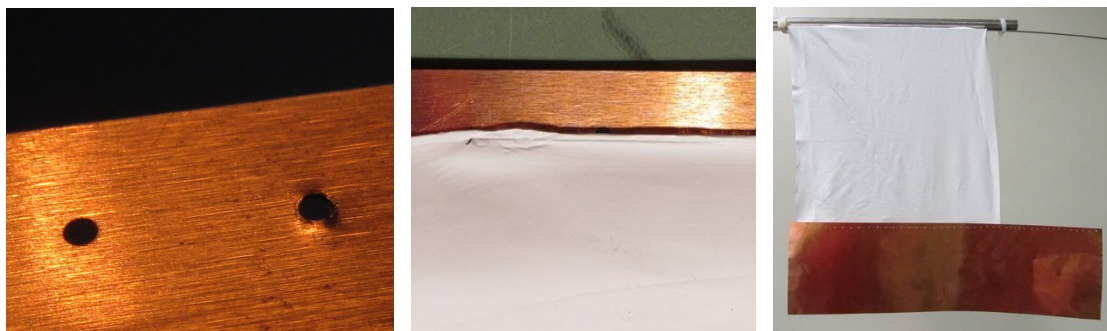


**Figure 3.41:** Left: holes drilled between two plates (left sample) and lying on one plate (right sample). Centre: a stitch with a  $100\ \mu\text{m}$  thick nylon wire to fix Tetratex on a  $100\ \mu\text{m}$  thick copper foil. Right: copper foil hung on Tetratex for a long-term mechanical stress test.

results in holes with rough edges and the latter in smooth edges. This is shown in Figure 3.41 on the left. A nylon wire was put through these holes and closed to a ring by a reef knot. A stability sufficient for installation in GERDA was found for the smooth edges by pulling on the wire until it ripped. The maximum force was significantly reduced in case of rough edges. In the production of the final copper foil it was hence ensured to have smooth edges. A right trapezoid shaped Tetratex sheet with a width of 217 mm and a length of 259 mm on one side and 344 mm on the other side was fixed to a piece of copper foil by stitching. Employed was a  $100\ \mu\text{m}$  thick nylon wire. The distance between the holes is  $\sim 4\ \text{cm}$ . It was then cycled ten times between liquid nitrogen and room temperature. No damage was observed, neither to the foil nor to the nylon wire. The long-term stability to mechanical stress was afterwards tested. The copper sheet with a weight of 37 g was therefore hung onto a rod by the Tetratex foil for 34 days. It was hung in a way resulting in an asymmetric load as shown in Figure 3.41 on the right. It stretched over the course of these days (not instantaneously) by 2 mm on the left and 33 mm on the right. Again no damage is observed, neither at the foil nor at the nylon wire. Leaving the Tetratex one day for relaxing resulted in a net contraction on the left side of 2 mm and a stretch on the right side of 21 mm. This shows that the Tetratex foil stretches partly elastically and partly plastically.

A second test was performed on a  $21 \times 31\ \text{cm}$  piece of a  $100\ \mu\text{m}$  thick copper foil with holes drilled with a horizontal and vertical distance of 4 and 15 cm, respectively. This corresponds to the final scheme but with twice the horizontal distance. It was clamped to a holder forcing its curvature to the same curvature as the GERDA shrouds. An approximately  $9 \times 17\ \text{cm}$  large piece of coated Tetratex and a  $13 \times 30\ \text{cm}$  uncoated piece was fixed to the copper by stitching. This is shown in Figure 3.42 on the left. The small holes along the edges of the coated Tetratex

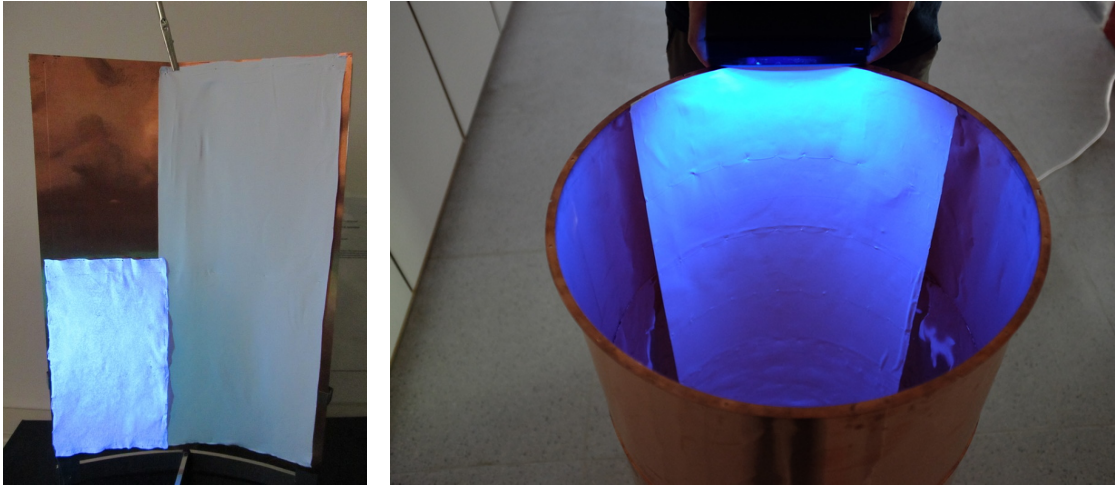


**Figure 3.42:** Left: dummy shroud with a small coated and a larger uncoated piece of Tetratex for fixation stability stress tests in liquid nitrogen. The samples are illuminated by day and UV light. Right: full size sheet of coated Tetratex after test installation in a prototype shroud illuminated by UV light.

are from the prior fixation to a PTFE sheet for coating. It was already slightly curly before stitching it to the copper foil. This dummy shroud was then placed in liquid nitrogen for 11 days and in air for 3 days. Furthermore five cycles between air and liquid nitrogen were performed. Each time it was inserted quickly into the nitrogen causing strong boiling. After these stress tests, air was blown between the Tetratex and the copper foil using an air gun. This was performed such that the Tetratex was clearly pulled away from the copper like a sail. The foil, all stitches and knots survived all these stress tests without any damage or sagging (pocket formation). This is proving a stability by far sufficient for an installation in GERDA.

The maximum distance of the Tetratex and copper after these tests was 3 mm. This distance is taken to define a safety distance for any moving objects to the shroud inner wall of 10 mm. It is meant to avoid any moving object from getting stuck or ripping off the reflector foil. The closest objects to the shroud are the sources holders of the calibration system with a distance of 26 mm. This provides a sufficient safety margin for oscillations of the source holder (see Section 7.4).

The last performed test was the mounting of a  $93 \times 44.5$  cm piece of coated Tetratex into a 90 cm high prototype copper shroud. It is higher than the final shroud with a height of 60 cm. The distance between the holes employed for stitching was 4 cm horizontally and 15 cm vertically. The fixing procedure proved to work well and the coating got no visible damage during installation. This was controlled by eye using a UV lamp. The installed sheet illuminated by a UV lamp

is shown in Figure 3.42 on the right. All stitches were stable but there is a small distance between the nylon wire and the copper caused by the curvature of the copper. Based on this it was decided to reduce the horizontal spacing between holes to 2 cm in order to reduce the likelihood for moving parts to get stuck on a nylon wire. Based on the results from all presented tests it was decided to use this method for installation in GERDA.

For the final production for GERDA a set of ten sheets with a length of 64 cm each was coated with a solution containing 30 g TPB per 1 l of dichloromethane. The production procedure was identical for the foils produced for gamma ray screening. The sheets and solution were prepared in a clean room at the physics institute of University of Zurich and transported in a dust tight box to the ETH clean room facility “First Lab” where they were coated. Each Tetratex sheet is stapled onto a PTFE sheet which is held in the transportation box by frames especially designed and built for this purpose. A drawing of this dust tight box and the frames is shown in Figure 3.43 on the left. The frames ensure to avoid contact of the face of the foil with anything else during transportation. The sheets were transported to LNGS into the GERDA clean room employing the same box. There eight sheets were cut to  $60 \times 40$  cm and installed in the two copper shrouds of the GERDA Phase II PMT veto system. The fixation of the edges of each sheet was backed up by a second nylon wire. One such shroud lined with coated Tetratex is shown in Figure 3.43 on the right. It is also visible on the picture shown Figure 2.9. It was taken after the installation of the bottom PMT array. Two spare sheets are stored at LNGS in the dust tight box together with spare nylon wire in case a replacement would be required.

## 3.12 Coatings of Transparent Nylon

Cylinders made of transparent nylon are used in GERDA to block  $^{42}\text{K}$  from accumulating at the Ge detectors. This isotope is producing background in the ROI. Each cylinder has a diameter of 103 mm and is surrounding one detector string as depicted in Figure 2.9 on the right. These so-called nylon mini-shrouds were developed by the MPIK Heidelberg. Nylon was chosen as material because of two reasons: the Borexino experiment has shown that nylon can be very radio-pure [131] and it is transparent for visible light. The light produced by background events close to the detectors is important for an efficient liquid argon veto. The nylon was therefore investigated on its properties in gaseous and liquid argon. It was furthermore coated with different wavelength shifters. My contribution to these developments are described in the following.

In a first step, nylon foil was placed in front of uncoated VM2000 and installed in the argon setup. A detection of argon scintillation light in this configuration

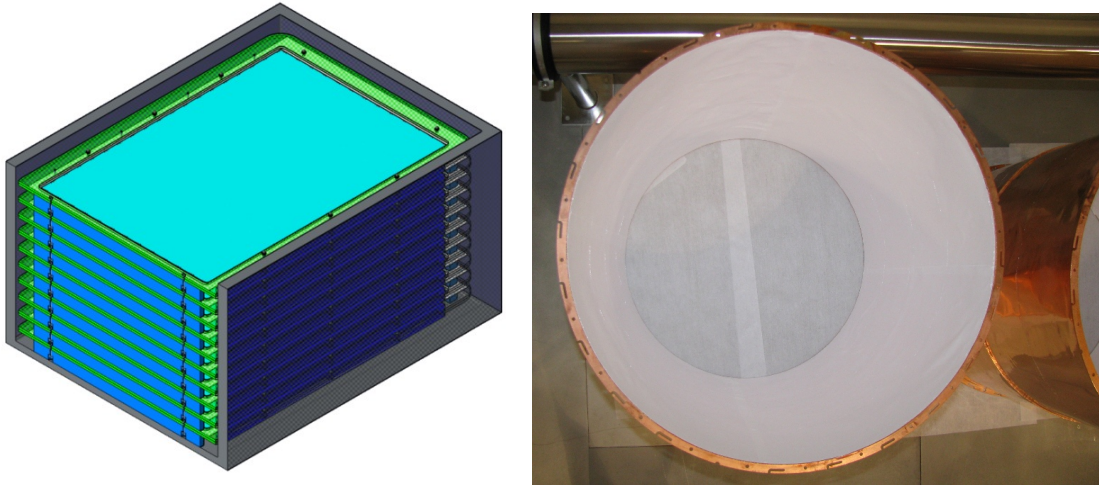


**Figure 3.43:** Left: dust tight transportation box with frames holding the coated reflector foils. Right: GERDA copper shroud lined with coated Tetratex.

would imply one of the two following cases. 128 nm light would either have passed the nylon foil and was shifted by the VM2000 or the nylon would shift this light by itself. The argon setup was evacuated to a pressure of  $4.6 \cdot 10^{-5}$  mbar before it was filled with argon gas to  $\sim 1.7$  bar. The gas purity was observed to quickly decrease resulting a triplet lifetime of  $\sim 240$  ns, 10 min after filling. This low triplet lifetime is caused by emanation from nylon. Another contamination was excluded reinstalling VM2000 without the nylon foil which resulted in a triplet lifetime of 1593 ns, 5 min after filling. The nylon foil was then reinstalled, the chamber pumped for two days and flushed twice with argon gas. This did not result in an observable improvement of the triplet lifetime. Emanation is hence occurring from the nylon bulk rather than its surface.

Following measurements were taken in liquid argon over a time range from  $\sim 1.5$  to  $\sim 3$  h after the start of filling. These measurements resulted in triplet lifetimes of  $(1351 \pm 19)$  ns,  $(1330 \pm 54)$  ns,  $(1327 \pm 27)$  ns and  $(1356 \pm 59)$  ns. These are similar to other measurements without nylon and do not show a rising impurity concentration. The absence of observable contaminations in liquid argon can be explained by two effects. The number of argon atoms is much larger in the same volume of liquid argon compared to gaseous argon, which results in a smaller relative contamination for the same absolute amount of contaminants. The outgassing rate is most likely significantly reduced at liquid argon temperature.

The light yield in these measurements with nylon is so low, that the alpha peak is not clearly visible. The trigger threshold is cutting into the integrated pulse height spectra as shown in Figure 3.44. For this reason the peak position is

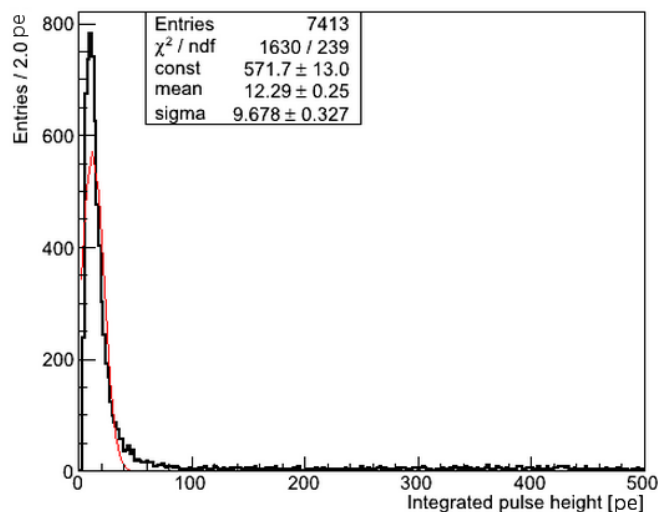


**Figure 3.44:** Integrated pulse height spectrum of alpha events measured with uncoated nylon placed in front of uncoated VM2000. The trigger threshold is cutting into the spectrum, by cutting events with low pulse height. The mean obtained by this fit is taken as conservative upper limit on the light yield.

taken as conservative upper limit on the light yield. The result is a relative light yield of  $< 0.02$  and proves that nylon has to be coated in order to be employed in GERDA. The coating will be applied on the inside, to avoid a dead region of the veto system within the shroud and on the outside, to avoid a reduced veto efficiency near the shrouds.

Several different coatings were applied to nylon using two different coating methods. Painting with a brush on the one hand and dip coating with the coating tool previously described in Section 3.1.2 on the other hand. Coatings applied in a first campaign are 80 % Makrolon with 20 % TPB, 60 % Makrolon with 40 % TPB, pure TPB with a concentration of 3.3 g/100 ml in dichloromethane and PS with TPB in a ratio of 10:1. The uniformity of the coating on the front side of the foil is similar employing brush and dip-coating. A picture of two pieces of nylon coated with 80 % Makrolon and 20 % TPB is shown in Figure 3.45. The left, triangular sample was coated by painting and the right by dip-coating. The back side of dip-coated samples is not covered uniformly. However, brush coating allows to coat both sides independently with the same uniformity. Others within the GERDA collaboration also found out that it is easier to influence the coating thickness employing brush coating compared to dip-coating. Therefore, brush coating was chosen as the method to coat nylon. Similar mechanical stability was obtained for coatings on nylon compared to coatings on VM2000. The uniformity of all samples was a little bit lower on nylon compared to VM2000. Samples illuminated with

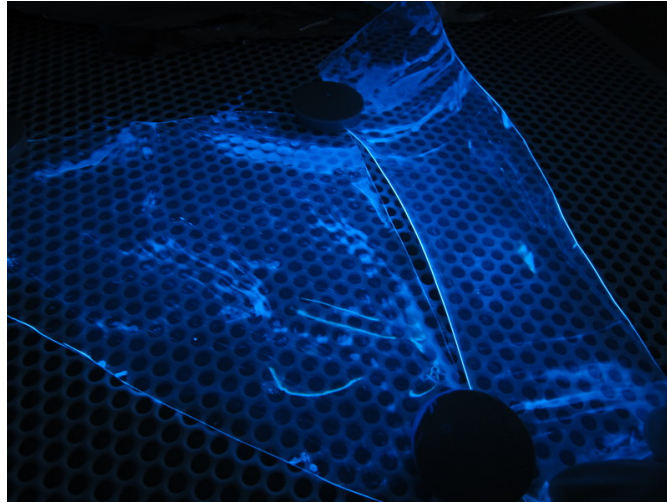


**Figure 3.45:** Two samples of nylon coated with a solution containing 80 % Makrolon and 20 % TPB. The samples are illuminated by a UV lamp. The left, triangular sample was coated by painting and the right by dip-coating. The much brighter edges are visible, showing that shifted light gets guided to the edges of the foils.

a UV lamp look bright on the edges. This light is expected to be shifted light trapped in the nylon foil and guided along the foil.

A nylon foil brush coated from one side with 10:1 PS:TPB was installed in the argon setup with the coating facing inward and in front of an uncoated VM2000. First, a measurement in argon gas was performed. The gas purity was observed to decrease quickly resulting in a triplet lifetime of  $\sim 750$  and  $\sim 650$  ns approximately 5 and 9 min, respectively after filling. This corresponds to a reduced rate of impurities emitted from the sample compared to uncoated nylon. It is nevertheless very high. In subsequent measurements in liquid argon a triplet lifetime of  $(1346 \pm 13)$  ns was obtained from 4 measurements carried out in the time range of 2.5 to 5 h after the start of filling argon. The triplet lifetimes of these measurements of  $(1332 \pm 11)$  ns,  $(1341 \pm 14)$  ns,  $(1355 \pm 18)$  ns,  $(1355 \pm 9)$  ns do not show any hint of deterioration which means a low emanation in liquid argon. The relative light yield of this coating is  $0.43 \pm 0.03$ . This low relative light yield compared to the same coating on VM2000 which yielded  $1.5 \pm 0.1$  is presumably caused by light guided to the edges of the nylon foil. The edges on the top and bottom of the nylon foil are outside the active volume. However, this light guiding might be advantageous for GERDA where the edges will face towards the PMTs, as it might increase the light collection efficiency.

Coated samples were further investigated by the MPIK Heidelberg employing

the same fluorescence spectrometer as described in Section 3.3. The obtained spectral shapes and intensities relative to each other were similar as previously shown for coatings on VM2000. Fluctuations for measurements at different locations on nylon were approximately twice as large, reflecting the reduced uniformity of the coatings. The higher light yield observed for coatings of 80 % Makrolon and 20 % TPB compared to PS + TPB as measured on VM2000 before is confirmed by these measurements. The TPB concentration in the latter coating was increased to 20 % based on these results. It is now showing a similar intensity (within the uncertainty of  $\sim 40\%$ ) of shifted light compared to the coating with 80 % Makrolon and 20 % TPB. Then it was decided by the MPIK Heidelberg to use 80 % PS and 20 % TPB as coating due to more experience with coatings containing PS instead of Makrolon. Further tests with prototypes of coated nylon mini-shrouds had been carried out in LArGe [77] by others in the collaboration. The combined suppression factor of the liquid argon veto pulse shape discrimination and the physical blocking by the nylon mini-shroud were measured therein for  $^{42}\text{K}$ . It was found to be  $\sim 1000$  in the ROI. The suppression factor for  $^{42}\text{K}$  is expected to be similar in GERDA.

### 3.13 Conclusions and Outlook

Several coatings applied to VM2000 and Tetratex were investigated on their mechanical and cryogenic stability. Most of those coatings were produced employing a dip-coating method. This method permits for an easy and cheap production of meter-scale reflector foils. The light yield of these coated reflector foils was optimised in liquid and gaseous argon. A setup was especially developed for this purpose allowing measurements under conditions almost identical to those in GERDA, as well as in other liquid argon experiments. This permits a direct transfer of the presented results to an application in those experiments. The relative light yields of the most relevant measured samples are summarized in Table 3.8. Tetratex dip-coated with pure TPB proved to be the superior coated reflector foil resulting in a light yield in liquid argon  $3.15 \pm 0.16$  times that of uncoated VM2000. It furthermore proved to be insensitive to long-term operation in liquid argon and exposure to air. Its mechanical stability was found to be sufficient for normal handling during installation. It was further investigated on radioactive trace contaminants and found to be within the specifications for GERDA. The emanation rates of this foil are investigated in Section 4 and found to be negligible. Based on the positive results it was decided to be installed in GERDA as part of the liquid argon veto system. A low material installation method was therefore developed and successfully tested. The Tetratex foil was installed in GERDA and is expected to last at least for the full period of Phase II. The background in the region of in-

	TPB on TTX	Mak+TPB	PS+TPB	BC / UPS	BCF-10
GAr	$3.62 \pm 0.14$			$1.2 \pm 0.08$	$1.5 \pm 0.11$
$\tau_2$ (G)	2564 – 2981			1946 – 2501	1543 – 1991
LAr	$3.15 \pm 0.16$	$2.3 \pm 0.16$	$1.5 \pm 0.11$		
$\tau_2$ (L)	1279 – 1319	1271 – 1295	1279 – 1305		

**Table 3.8:** Summary of light yields measured with different coatings relative to uncoated VM2000. Coatings were applied to VM2000 except pure TPB, in which case Tetratex (TTX) was employed. All coatings were applied by dip-coating. The relative light yield of this coating is for the optimal thickness of  $0.9 \text{ mg/cm}^2$ . Mak+TPB stands for 80 % Makrolon and 20 % TPB, PS+TPB for a ratio of 10:1 PS:TPB, G and L for gas and liquid, respectively and  $\tau_2$  for the triplet lifetime observed in the respective measurements. BC / UPS stands for BC408 and UPS-923A which resulted in the same relative light yield. For coatings measured several times the average relative light yield is provided.

terest is expected to be reduced by approximately one order magnitude in Phase II compared to Phase I. The argon veto is contributing  $\sim 1/3$  of this reduction.

Other investigated coatings are relevant for surfaces where covering by a reflector foil is not possible or desired, e.g. the nylon mini-shroud and PMT windows. Amongst the tested coatings, 80 % Makrolon with 20 % TPB resulted in the highest light yield. Applied to VM2000,  $2.3 \pm 0.16$  times higher than uncoated VM2000. This coating proved to be stable to cryogenic temperatures and mechanical stress. The main results presented in this chapter have been published in [94].

The argon setup employs a PMT of type R11065-10. It was characterised and found to occasionally suffer from internal sparking. Other parameters were found to be suitable for GERDA. A new version of this PMT (R11065-20 MOD) is installed in the liquid argon veto system.

The argon setup was furthermore employed for measurements of the light yield of coated nylon. This is employed for the production of mini-shrouds, which prevent  $^{42}\text{K}$  from accumulating at the detectors. The  $^{42}\text{K}$  originates from  $^{42}\text{Ar}$  present in the liquid argon and is a significant background contribution.

The argon setup is readily available for further measurements and is currently employed to characterise new silicon photomultipliers at liquid xenon temperature ( $\sim 165 \text{ K}$ ). An upgrade could be made to obtain more stable pressure conditions close to liquid argon temperature, if required. Constantly removing the gaseous nitrogen from the filling side of the cooling line would most likely be sufficient. The argon setup will be employed in the future to characterise a new PMT, designed for operation in liquid argon.

## Chapter 4

# Emanation Rate Measurement System

Any material is typically emanating different chemical substances, depending on the material and history of that specific components. So do components employed for the constructions of experiments. The emanation can either originate from the surface or bulk. Typical surface contaminations are water from ambient humidity and residual hydrocarbons, e.g. machine oil from the production. Emanation from the bulk is typically enhanced for polymer and porous materials compared to metal parts. This leads to a much higher total emanation rate of the former.

The performance of high and ultra-high vacuum chambers, as well as (liquid) noble gas detectors depends on the emanation rate of all internal components. Different substances are differently harmful depending on the particular application and apparatus. If materials with a potentially high outgassing rate are planned to be installed in a setup, it is crucial to identify the emanating gases and measure their respective rates of emanation.

A system capable of both the identification of the outgassing substance and measuring the respective outgassing rates was developed. It is employing only full-metal components in contact with the inner surface of the system to ensure a very low blank emanation rate. It is furthermore designed to minimise both the influence of all apparatus instruments on the measurement and contaminations of the system when loading or unloading samples. The central component of the system is a mass spectrometer which is part of a residual gas analyser unit (RGA) of type XT200M from the Extorr company [132]. The emanation system is furthermore capable to measure the constituents of gas samples.

The system was built not merely to measure TPB-coated Tetratex for GERDA and PTFE installed in GERDA and XENON1T, but also to support future detector developments. This includes local experiments with liquid and gaseous xenon at the University of Zurich and collaborations in which our group is participating,

such as XENON [133], GERDA and the Darwin [134] consortium.

This chapter presents the developments and measurements performed in the framework of this thesis. It furthermore includes results from work performed in the framework of the Master thesis of Michael Miloradovic [135] under my supervision. These are the verification of measurement procedures, measurements of blank chamber emanation rates, as well as measurements of PTFE pieces cleaned by various methods.

## 4.1 Hardware Description

The system is designed to offer the possibility to isolate and pump the emanation chamber, the RGA and the pressure gauge volumes individually. This allows to minimise contaminations in the loading and unloading procedures, as well as influences of the devices on measurements. The pressure gauge is a combined Bayard-Alpert hot filament (B-A), Piezo and Pirani vacuum gauge. The RGA is a combined B-A and Pirani gauge and a quadrupole mass spectrometer. It can be operated in a mass range of 1-200 amu/q and has a detection limit for partial pressures of  $\sim 10^{-13}$  mbar, due to an optional internal electron multiplier. The device allows to set the scan speed in the range of (0.1 – 1000) samples/s. The scan speed defines the integration time for the charge at each mass point. A smaller scan speed results in a higher accuracy of the measurement, in particular in a lower noise level. A higher scan speed allows for a faster mass spectra acquisition. A sample-by-sample baseline subtraction is activated for all measurements, which significantly improves the sensitivity. The RGA is separated from the emanation volume by a regulating valve of type VML 14 from Hositrad [136], capable to control pressures down to  $1.3 \cdot 10^{-11}$  mbar. The full system is shown by a schematic diagram in Figure 4.1.

The measurement principle of a B-A gauge is important to know in order to correctly understand the behaviour of the emanation system. B-A gauges and cold cathode ionisation gauges ionise the residual gas and measure the ion current, which is proportional to the pressure of a given gas mixture. A B-A gauge uses a hot filament as electron source in contrary to a cold cathode ionisation gauge, where electrons are provided by field emission. The former requires significantly lower voltages (approximately one order of magnitude) between the filament and readout electrode. The energy of residual gas ions are therefore much smaller in the former case, which results in a lower pumping rate of the gauge itself. Therefore a B-A was chosen in order to minimize the influence of the gauge on emanation measurements. Both types of gauges are expected to possess similar emanation rates. Both types are furthermore commonly delivered with a degas function which is evaporating surface contaminations inside the gauge or RGA. The hot filament

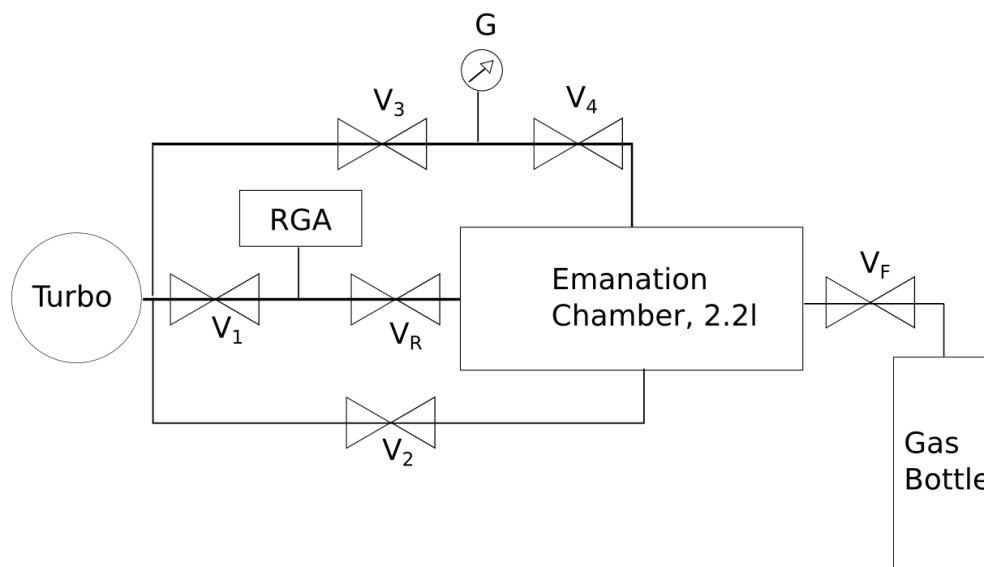


**Figure 4.1:** Schematic diagram of the emanation rate measurement system. The emanation chamber can be loaded with solid samples through a CF100 flange or with gaseous samples through  $V_F$ , an all-metal VCR 1/4" valve.  $V_{1-4}$  are all-metal CF40 angle valves,  $V_R$  is a regulating valve,  $G$  is a composite full-range pressure gauge and RGA is a residual gas analyser consisting of a full range pressure gauge and a mass spectrometer with a built in electron multiplier for enhanced sensitivity. Turbo is a pump stand containing a turbo molecular pump and a membrane pre-pump.

in the RGA is an ion source for both the integrated B-A gauge and the mass spectrometer.

The pressure gauge is of type 390 Micro-Ion ATM from Granville-Phillips [137]. The pressure is displayed at the pressure gauge and can be additionally read out through a RS-232 connection. A LabVIEW program was written to read out and plot the pressure continuously as well as log it in a text file. This program is used to monitor and document the pressure evolution at the pressure gauge during all operations. The RS-232 connection, as well as the control and power supply of the gauge are realised through a 15 pin connector on the pressure gauge. The RS-232 is directly connected to a PC. The other pins are connected to a separate control box custom developed together with the electronics workshop of the University of Zurich. It is driven by a wall power supply and feeds the required power to the pressure gauge. The control box is housing four switches, one for each of the following functions: gauge main power, degas, calibration and ion gauge off (pirani and piezo remain operative). It is furthermore equipped with a BNC connector providing an analog output proportional to the pressure. The analog signal is created by the Granville gauge itself.

Pumping of the system is realised by a turbo molecular pump. It is connected to the system through a CF63 tube which is connecting the three CF40 pumping lines. The larger diameter at the pump increases the pumping cross section of the whole system. The turbo molecular pump can be switched off independently from a membrane pre-pump, allowing to flush the chamber with argon gas in order to remove surface contaminations like water.

## 4.2 Measurement and Loading Procedures

Measurement procedures for solid and gas samples were developed and verified. The resulting recommended procedures are described in detail in this section. The verification is explained in Section 4.5.3. It is not mentioned in the specific steps that all samples and setup components in contact with the vacuum are always handled wearing powder free gloves.

### 4.2.1 Solid Samples

Loading of solid samples is performed in a specific way in order to minimise contaminations of the chamber. Prior to loading a sample, all valves except  $V_4$  are closed. It is kept open to measure the pressure in the emanation chamber. The chamber is then filled with a slight overpressure of argon gas from a gas bottle in order to reduce water contamination of the chamber when opening. After filling,  $V_4$  is closed to reduce contamination of the gauge when the chamber is opened by

the CF100 flange holding  $V_F$ . The samples are placed inside the chamber through this flange. After closing the flange again, the chamber is pumped through  $V_2$  using the membrane roughing pump.  $V_4$  is opened after  $\sim 5$  min which corresponds to a pressure in the emanation chamber of  $\sim 4.5$  mbar. The chamber (including the gauge G) is then flushed three times with  $\sim 300$  mbar argon gas and pumped to  $\sim 4.5$  mbar between each flush. This procedure removes water and other volatile contaminants. After this, the chamber and pressure gauge are pumped by the turbo pump with  $V_2$ ,  $V_3$  and  $V_4$  opened typically for at least one hour before opening  $V_1$  and  $V_R$  at the RGA. The pressure development at the gauge G during such a loading procedure is shown in Figure 4.2 on the left. The vertical steps in the pressure reading are artefacts of switching from the gas type insensitive Piezo to the Pirani gauge. It is caused by a disadvantageous sensitivity of Pirani gauges to such pressure ranges in argon gas. The loading procedure reduces significantly the amount of water and other contaminants reaching the RGA. This is important as the RGA possesses a large surface and a relatively small pumping cross section. The latter originates from its geometry and placement in a CF40 tube.

It is recommended to perform a helium leak check at this point of the procedure. The helium partial pressure can conveniently be measured employing the RGA. The hole system is then pumped until the desired base pressure for an emanation measurement is reached. The composition of the residual gas can be measured continuously and written to disk while pumping. This data can then be utilised to determine the evolution of residual gas constituents, which supports the identification of the source of emanation. The pressure gauge G should be decoupled from the system for emanation measurements closing  $V_4$  and  $V_R$  to achieve the best possible accuracy. The internal electron multiplier can be switched on to obtain a higher sensitivity. In the present setup this emanation is measured for each mass to charge ratio value independently in contrary to measurements with a pressure gauge. This significantly increases the sensitivity of the system, especially for substances with mass peaks which are not on top of the blank chamber background.

Depending whether the emanation rate of the sample is high or low, two different methods are employed for the measurement. The rate of a sample is considered as "high" if the pressure in the chamber reaches the limit of the linear regime of the RGA ( $\sim 5 \cdot 10^{-6}$  mbar within a couple of minutes). In this case the RGA is employed to constantly measuring with the valves  $V_1$ ,  $V_2$  and  $V_R$  fully opened. Then the valve  $V_1$  and  $V_2$  are closed and the pressure rise is directly observed with the mass spectrometer until reaching saturation. In this case the blank emanation rates of the chamber and the pumping rate of the RGA are expected to be negligible and are not taken into account. This method is also referred to as "pressure rise" method.

In case of a low outgassing rate sample, the valves  $V_R$  and  $V_2$  are closed. The sample emanates in this configuration into the chamber without interference with the RGA or pressure gauge. The pressure gauge and the RGA are continuously pumped during emanation. The emanation time must be chosen according to the desired sensitivity.  $\sim 10$  min before reaching the emanation time, the data acquisition with the RGA is started and the valve  $V_1$  closed. The scan speed is typically set to 144 samples/s to obtain sufficient time resolution for the analysis.  $V_R$ , connecting the RGA and the chamber is kept closed for 6 min. This is sufficient to determine the momentary outgassing rate of the RGA and the partial pressures in the RGA  $p_R$  at the time opening  $V_R$ . After opening  $V_R$  a higher or lower pressure  $p_3$  is observed in the RGA depending on the partial pressure of the emanating species in the RGA and chamber volume, which correspond to outgassing rates in the RGA and chamber respectively. Knowing the volume of the chamber  $V_C$ , the RGA  $V_R$  and the duration of emanation, the rate of the emanation chamber plus sample can be determined without bias of emanation from the RGA. The amount of emanated gas  $p_O \cdot V_C$ , assuming constant temperature and the ideal gas equation, is then given as

$$p_O \cdot V_C = (V_R + V_C) \cdot p_3 - V_R \cdot p_R. \quad (4.1)$$

A constant temperature can be assumed due to a negligible heat capacity of the gas at a pressure below  $10^{-5}$  mbar compared to the chamber inner surface. This method is in the following referred to as "accumulation method". It is also used to measure the outgassing rate of the blank system.

An emanation rate measured with this method corresponds to an effective average rate within the emanation time. This corresponds to the actual emanation rate as long as re-adsorption on detector components and the sample is negligible compared to emanation. This is the case for all gases which are not chemically active with the chamber components. The hot filaments of the pressure gauge and the RGA are considered the most critical reaction partners. This assumption is verified in Section 4.5.3. The vapour pressure of the emanating component must additionally be much smaller than the partial pressure of that component. This is usually fulfilled at the operational pressure of the system of  $\lesssim 5 \cdot 10^{-6}$  mbar. Vapour pressures of emanating substances are typically in the range of  $10^{-2}$  to 500 mbar.

## 4.2.2 Gaseous Samples

Gas samples are filled into the chamber through the 1/4" VCR connection of  $V_F$ . After connecting the gas sample container, valve  $V_1$ ,  $V_3$ ,  $V_4$  and  $V_R$  are closed and the turbo molecular pump stopped. Then and  $V_F$  is opened and the turbo pump

is started again. The chamber is pumped including the connection pipe to the gas sample container for at least 30 min before opening  $V_3$  and then  $V_4$ . Opening the valves in this order reduces the amount of emanated gas from G reaching the chamber. The valves  $V_1$  and  $V_R$  are opened earliest when the pressure measured by G is below that measured by the RGA. The RGA pressure is typically dominated by  $\text{CO}_2$  and  $\text{CO}$ , which can be pumped easily. The chamber pressure on the other hand is most likely dominated by  $\text{H}_2\text{O}$  which is much slower to pump, especially from the RGA volume. It is therefore recommended to wait even longer. A helium leak check should be performed after opening  $V_1$  and  $V_R$ .

Before filling a gas sample into the chamber it must be ensured that all partial pressures are sufficiently low. What sufficiently means can be understood in a few lines. First, data acquisition with the RGA is started, the valves  $V_2$ ,  $V_3$  and  $V_R$  are closed and  $\gtrsim 1$  mbar of the gas sample is filled into the chamber. A pressure of 1 mbar is sufficient for the remaining procedure and keeps chamber contributions small. Correction factors for the Pirani gauge of the respective gas sample must be taken into account when reading the pressure. Valve  $V_4$  is closed immediately after filling to minimise contributions from G. The evolution of the pressure at gauge G during such a procedure is shown in Figure 4.2 on the right. The valve  $V_R$  is now opened until the RGA measures a pressure of up to  $\sim 5 \cdot 10^{-6}$  mbar. This is the maximum pressure below saturation, which is resulting in the highest possible sensitivity. Note that  $V_1$  is kept open, continuously pumping the RGA. This configuration allows for approximately six days of measurement until the chamber is empty if 1 mbar of gas was filled into the chamber. The method is referred to in the following as “gas method” and allows for a high accuracy while minimising the effect of the RGA. This permits also to measure the  $\text{O}_2$  content, which would otherwise be removed by the hot filament as further described in Section 4.5.3.

### 4.3 Data Acquisition

The RGA comes with the software “VacuumPlus” running on Microsoft Windows. It is employed for operation and calibration of the RGA and to display the currently scanned spectrum. It has limited trend displaying options for partial pressures. The software does furthermore stream the measured spectra in XML (Extensible Markup Language) syntax to a named pipe which can be written to file employing a further program also provided by the company. Each file can contain several spectra and has a header containing the xml version and an identifier for the encoding of the file content. Every spectrum consists of a spectrum header and subsequently the partial pressures for each mass to charge ratio measured by the mass spectrometer.

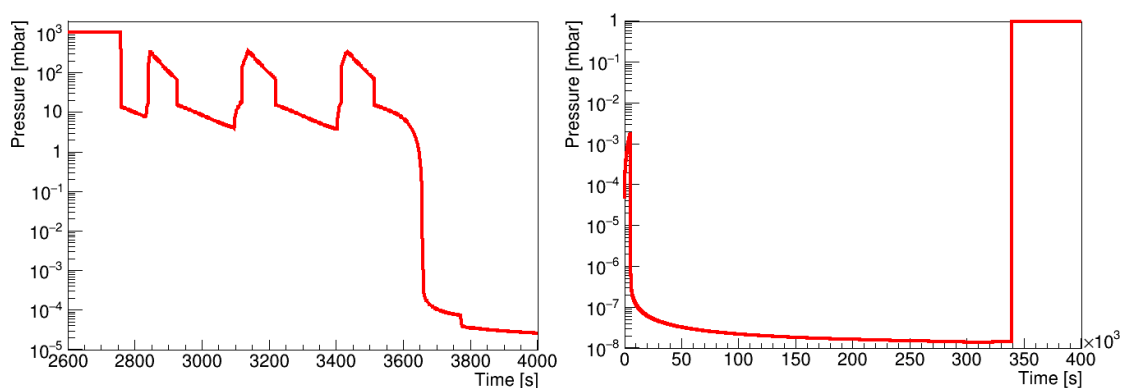


**Figure 4.2:** Left: pressure evolution while loading a solid sample. Ambient pressure in the beginning of the diagram followed by a steep decrease when opening  $V_4$ . The chamber is then flushed three times with Ar gas. The vertical steps are not physical but caused by switching from the gas insensitive Piezo to the gas sensitive Pirani gauge. The fast change at  $\sim 3780$  s is caused by opening  $V_3$ . Right: pressure evolution while connecting and loading a gas sample. The connection tube is pumped through  $V_4$  while G is outgassing with  $V_3$  and  $V_4$  closed for  $\sim 1.5$  h ( $\sim 5400$  s) until they are opened. Following is a pumping period of 4 days at the end of which 1 mbar of gas is filled into the chamber.

## 4.4 Analysis Procedure and Software

A software, written in C++, was developed in the framework of this thesis to read and analyse spectra from the XML files. The program is divided in three parts, a class to hold a spectrum with its respective header information, a xml reader consisting of a set of functions to read data from a xml file into the correct variables of the spectrum class and a part analysing and plotting the mass spectra or partial pressures. The latter part was extended in the framework of the Master thesis of Michael Miloradovic [135]. The function principle and most relevant checks performed by the software are explained in the following.

### 4.4.1 Reading of Mass Spectra

Each spectrum header starts with a "<Data" and each partial pressure measurement with a "<Sample" string. The xml reader starts at the beginning of the files and searches for the next header marker. The numbers following this marker are assumed to correspond to the beginning and end of the scanned mass to charge ratio range, the number of measured pressures per amu, the pressure unit, the pressure reading of the Pirani gauge, the total pressure, a variable indicating the status of the RGA filament and a running spectrum number in the given order. The header ends with a ">". The reader checks if the correct number of values is found before reaching ">" and discards the spectrum otherwise, displaying a warning. In case of correct length, an object of type RgaSpectrum is created with the correct size to hold the following partial pressures. It now searches for the "<Sample" identifier and fills their values to the spectrum until reaching "</Data>" which identifies the end of a spectrum. It now checks if the number of read samples corresponds to the number of samples expected from the header and discards the spectrum otherwise, displaying a warning. The first and last spectrum of a file are typically incomplete, as well as spectra where RGA parameters were changed during their acquisition.

### 4.4.2 Analysis of Mass Spectra

The program is designed to handle spectra with different settings or length within one file. The header information and spectra can be retrieved from the spectrum container class. The function "GetPMbarAtMass(double mass)" is implemented to retrieve the measured partial pressure closest to "mass" converted into mbar, independently from the pressure unit used to save the data. Note, that the amplification of the internal electron multiplier is not taken into account, as the xml files do not contain any information about its status. The partial pressure streamed

by the “VacuumPlus” software is also not corrected for the amplification by the electron multiplier.

A correct calculation of a pressure based on the measured pressure value requires several steps. The mass spectrometer and the B-A gauge measure the pressure in terms of an ion current. Both are using the same hot filament as an ion source, hence measuring the pressure of the same volume. The current and hence pressure reading is dependent on the type of gas. It is calibrated for nitrogen and needs to be scaled for other gases using the so-called relative ionisation gauge sensitivity  $k_r$ . This scaling factor is provided by the manufacturer Extorr [132] for the following gases: air, H<sub>2</sub>O, O<sub>2</sub>, D<sub>2</sub>, H<sub>2</sub>, He, Ar, N<sub>2</sub>, NO, CO, CO<sub>2</sub>, Ne, CH<sub>4</sub>, Kr, Xe, SF<sub>6</sub>. The provided values are expected to suit best for this device and are used for those gases. The value for  $k_r$  of these gases is in the range of 0.13 (for He) to 2.84 (for Xe). A larger value corresponds to a higher sensitivity. The factor varies slightly with the ionisation energy [138], which is 70 eV for the device employed in this work. For other chemical compounds, values provided by [138] (75 eV ionisation energy) are used unless stated differently. Values of compounds given in the RGA manual and therein vary typically by at most 10%. As a conservative assumption 10% was taken as the uncertainty on all relative efficiencies. Values presented by other references differ typically a few percent more than from this reference.

Measuring partial pressures with a mass spectrometer requires additionally the knowledge of the cracking pattern of the molecule of interest. The cracking pattern is caused by the dissociation of molecules during ionisation and double ionisation resulting in peaks at various mass to charge ratios for a gas consisting of only one molecule species. The previously mentioned  $k_r$  is valid for the summed current of all fragments. H<sub>2</sub>O for example results in peaks at amu/q of 18, 17, 16 and 1 with an absolute fraction  $f$  of 0.75, 0.19, 0.02 and 0.05 respectively. These values are dependent on the ionisation energy (70 eV in this work). Patterns are provided by the manual for Ar, CO<sub>2</sub>, He, H<sub>2</sub>, Kr, N<sub>2</sub>, O<sub>2</sub>, and H<sub>2</sub>O. For other compounds, values provided by [139] are used. Values provided therein differ on average by 0.05 from the values provided by the manual. This is taken as the uncertainty on cracking patterns, if not stated differently. Measured mass spectra are typically a superposition of the cracking patterns of several components. The actual partial pressure  $p_x$  of a component  $x$  is determined by taking the uncorrected pressure reading  $p_u$  of a mass to charge ratio dominated by this component and dividing it by the respective fraction in that mass to charge ratio peak and the relative gas sensitivity:

$$p_x = \frac{p_u}{f \cdot k_r}. \quad (4.2)$$

This corresponds to the true total partial pressure of that molecule including its fragments. The program plots automatically the trend of the partial pressures

determined from all spectra in the xml file. The file has to be specified in the command line as the first argument. Components to be drawn can easily be selected in the code. Further components can be added in a simple way, if their cracking pattern and relative ionisation probability is known. The former can be found in [139] for most chemical components. The analysis program does furthermore plot the trend of ratios between several partial pressures. This can be used to distinguish chemical elements with common mass to charge ratio peaks but different cracking pattern. The ratio of amu/q 15 to 16 for example to distinguish methane from atomic oxygen. It can also be employed to identify composed contaminations with a known composition, e.g. air.

The program allows to plot individual selected spectra using the option “-s” followed by the spectrum number. A running number is assigned to each complete spectrum in the file (counting starts with 0). Multiple spectra can be drawn, each time using “-s” followed by the respective spectrum number. Spectra taken with the electron multiplier can be corrected for the mass to charge ratio dependent gain using the option “-sEM” instead of “-s”. Note that the gain is not correct for H and H<sub>2</sub>. More details about the electron multiplier gain are provided in Section 4.5.2. Information about the analysis software is also provided in [135].

## 4.5 Commissioning and Characterisation

This section presents the commissioning of the setup including the characterisation of the internal electron multiplier and a validation of the measurement procedures. The first step after assembling the full system (shown in Figure 4.3) was the determination of the volumes of all separable areas. The volume of the emanation chamber with all valves closed was determined from the technical drawing of the system to be  $V_c = 2.2281$ . The volume in the RGA  $V_r$  enclosed by the valves  $V_1$  and  $V_R$  and the volume in the pressure gauge G enclosed by  $V_3$  and  $V_4$  are then determined measuring the pressure with the Piezo gauge in G (accurate to 3 digits) in the following way. First, all valves were closed except  $V_4$  and the chamber and gauge G were filled with Ar gas to 1000 mbar. After this the gauge was pumped and refilled with gas from the chamber. The pressure reading is now 887 mbar. Using the ideal gas equation this can be used to calculate  $V_G = 0.2841$ . The leak valve is then opened to fill the RGA volume resulting in a pressure of 791 mbar. This is used to calculate  $V_r = 0.3051$ .

The system was pumped for  $\sim 1$  week reaching a pressure of  $\sim 2.6 \cdot 10^{-8}$  mbar and subsequently baked at  $\sim 120^\circ\text{C}$  for four days in order to remove impurities. The degas cycles of the pressure gauge and RGA were run twice right after baking (chamber still hot). These are sequences predefined by the manufacturer to remove surface contaminations within the respective devices. The full system was then

Component	Mean [ $10^{-12}$ mbar l/s]	$\sigma$ [ $10^{-12}$ mbar l/s]
H <sub>2</sub>	144	124
CO <sub>2</sub>	2.6	1.4
N <sub>2</sub> +CO	0.61	0.24
H <sub>2</sub> O	0.73	0.26

**Table 4.1:** Mean and standard deviation ( $\sigma$ ) of nine emanation rate measurements of the blank chamber performed after separate baking of the regulating valve.

left for cool down for 8 hours, which is expected to be sufficient to reach room temperature. The pressure has dropped to  $\sim 6.4 \cdot 10^{-9}$  mbar by this time.

### 4.5.1 Blank Chamber Emanation Rates

Measurements of outgassing rates of the blank chamber after the baking resulted in inconsistent values varying by more than one order of magnitude. The spectra were strongly dominated by a peak at 28 amu/q. This is most likely CO which was then identified to originate from the regulating valve. The location was found heating individual parts with a heat gun while observing the mass spectra measured by the RGA. This valve was therefore baked at  $\sim 200^\circ\text{C}$ , once for 4 hours and once for 11 hours. The opening of the leak valve was varied during baking to ensure pumping of all its surfaces. Fluctuations between subsequently measured emanation rates were significantly smaller. The average rates out of 9 measurements are provided in Table 4.1.

The spectrum of the blank chamber acquired with the electron multiplier at a scan speed of 10 samples/s is shown in Figure 4.4. There are now visible peaks above the acquired mass range of (1–46) amu/q. Present are H<sub>2</sub> (2 amu/q), H<sub>2</sub>O (18 amu/q), CO (28 amu/q), O<sub>2</sub> (32 amu/q), Ar (40 amu/q) and CO<sub>2</sub>(44 amu/q), as well as their fragments and doubly ionised peaks. Additionally visible is a peak at 30 amu which is probably caused by ethane or potentially NO originating from HNO<sub>3</sub> residuals from cleaning of vacuum components by the producer.

The measured emanation rates vary from one measurement to another. This variation is understood to be real and dependent on the history of the chamber. That it is not caused by the measurement or analysis procedure is shown by the results in Sections 4.5.3 and 4.6.1. For samples with emanation rates below approximately one order of magnitude above the blank chamber, it is strongly recommended to perform a blank measurement right before and after the sample and at similar pumping times. Pumping time is the time passed between starting the pump after the chamber had been opened and the time at which the valves are closed to start accumulating the emanating gasses of the chamber or sample.

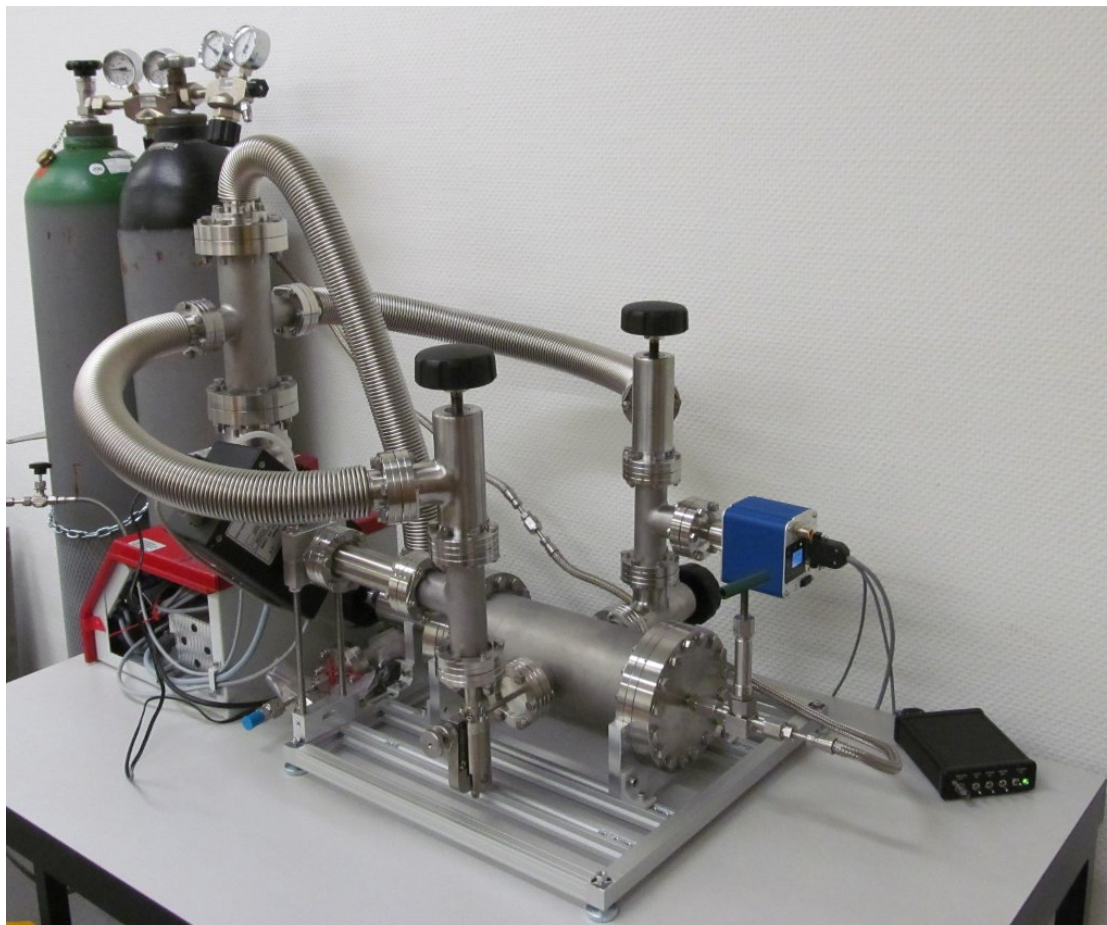


**Figure 4.3:** Picture of the fully assembled emanation measurement system. The vertical chamber is the emanation volume connected on the right side to the pressure gauge G (blue box) and on the left side to the RGA (black box). The flange on the front side is used for sample loading and housing the gas connection. The pump stand (red cover) is situated on the back side and connected by three pump lines.

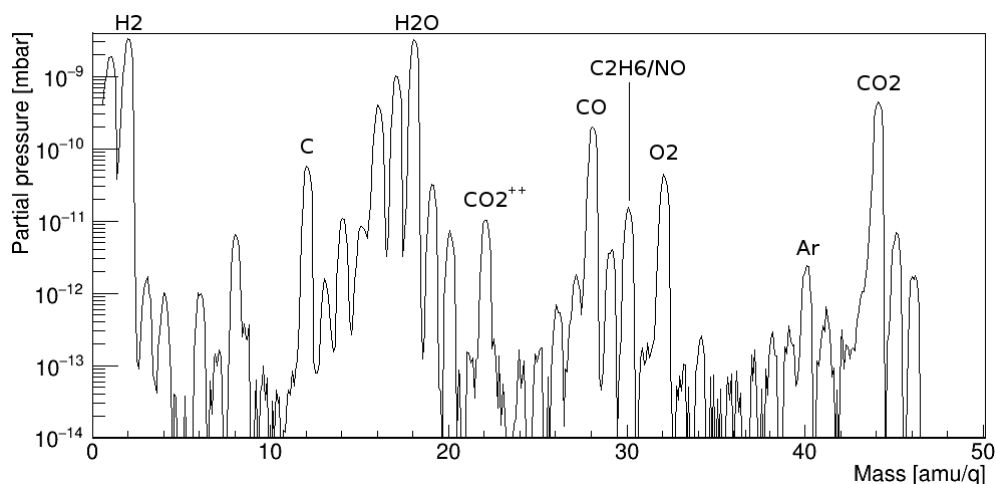


**Figure 4.4:** The mass spectrum of the blank chamber after baking of the regulating valve. It is dominated by  $\text{H}_2$  (2 amu/q),  $\text{H}_2\text{O}$  (18 amu/q),  $\text{CO}$  (28 amu/q) and  $\text{CO}_2$  (44 amu/q). Note that mass spectra are not corrected for different relative ionisation gauge sensitivities.

### 4.5.2 Electron Multiplier Gain Calibration

The mass spectrometer is equipped with an electron multiplier to increase the ultimate sensitivity. The high voltage of the amplifier was factory calibrated to a gain of 1000 for  $\text{N}_2$ . The gain for other gases was determined from two separate measurements, in both cases while pumping. First, spectra of the blank chamber were taken with the electron multiplier turned off. This is providing partial pressure readings for mass to charge ratios of 2, 16, 17, 18, 28 and 44. The multiplier was turned on after several scans and turned off again after a few more scans. The evolution of the partial and total pressure readings during this procedure are shown in Figure 4.5 on the left. A second measurement was taken with a TPB-coated Tetratex sample providing partial pressure readings for mass to charge ratios values of 12, 27, 28, 49, 57 and 84 (an identification of the peaks is provided in Section 4.6.2). The electron multiplier was turned on after a couple of scans but not turned off again. This evolution of the partial pressure readings is shown in Figure 4.5 on the right.

All partial pressures in the on/off state were fit with a constant. The gain was then determined as a function of the mass to charge ratio by dividing the fit values of the “on” state by the fit values of the “off” state. This provides two values for the gain of each mass to charge ratio chosen in the first measurement and one value for each in the second. The pressure was constant during these measurements. All gain values are shown in Figure 4.6 together with an exponential fit to all points

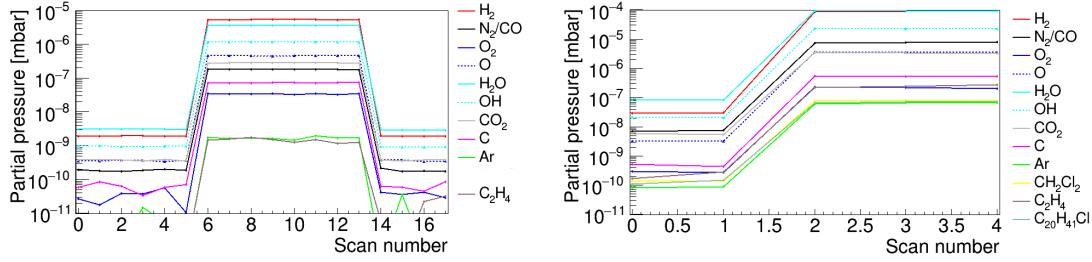


**Figure 4.5:** Evolution of partial pressure readings when turning the electron multiplier on and off. The actual partial pressures are constant for the full period of both plots. Left: empty chamber. Right: chamber loaded with TPB-coated Tetratex.

(red curve) and excluding hydrogen (blue curve). The red curve does not provide a proper description for most of the range. The blue curve does however properly describe the gain for all molecules except of hydrogen. It is therefore employed to describe the gain and has the functional form of

$$g(x) = e^{7.46-0.0210 \cdot x}. \quad (4.3)$$

It is also employed for hydrogen even if the gain observed for hydrogen is obviously not described correctly. This is not a problem as the height of the hydrogen peak is not expected to be used quantitatively in spectra with the electron multiplier turned on. In case it will be used in a specific case, this can be corrected simply scaling the hydrogen value by hand. There are several possible reasons for the observed difference for hydrogen. An exponential function might not be the appropriate functional form, an inverse proportionality to mass to charge ratio, however, does not provide a better description. Another possible explanation is that hydrogen might be released by the electron multiplier during operation.

### 4.5.3 Verification of Measurement and Analysis Procedures

The measurement and subsequent analysis procedures were verified performing measurements on a gas sample with known composition. The gas sample was prepared filling 0.328 mbar of argon with a purity of 6.0 and 0.682 mbar of dry air into the chamber. The pressure values are as indicated by the Pirani gauge of G. They will be corrected for the gas-dependent gauge sensitivity in order to obtain the correct relative contents. These gas samples are used to verify both the gas, as well as the accumulation method. Both were described in Section 4.2. The latter is mimicked filling a small amount of the gas sample through  $V_R$  into the RGA volume with closed  $V_1$ . In the gas sample method a scan speed of

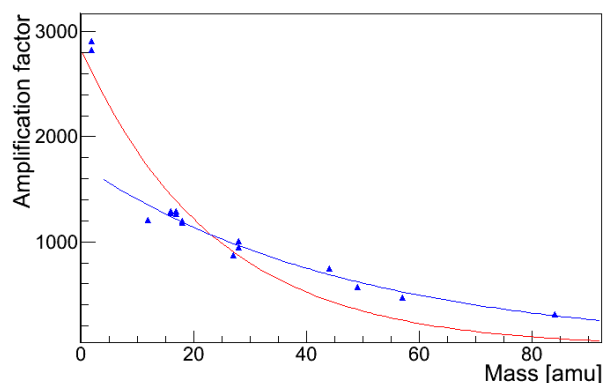


**Figure 4.6:** Gain of the electron multiplier in the mass spectrometer as measured from Figure 4.5, together with a fit of an exponential function including all values (red curve) and excluding molecular hydrogen (blue curve). The latter is used for all presented analysis.

0.1 samples/s was chosen in order to reach the highest possible sensitivity. The acquisition of one spectrum takes  $\sim 5$  h using these settings. For the accumulation method a scan speed of 144 samples/s was chosen to obtain a sufficient time resolution ( $\sim 14$  s/scan). This scan speed is too high to resolve the krypton content of air ( $\sim 1.1$  ppm). The electron multiplier was additionally turned off in this measurement in order to reduce the wear of the RGA in case of accidentally filling a higher pressure into the RGA.

The constituents of the gas in the RGA can not be determined relative to the total pressure reading of the RGA, as its sensitivity is gas type dependent and hence is not a valid reference. All partial pressures were therefore determined relative to  $N_2$ . These ratios were employed to calculate the volume fraction of the respective component relative to the total gas mixture (assuming a correct pressure reading for  $N_2$ ). The fraction obtained with both methods, as well as the expected fraction and relative deviation (difference divided by expected from the  $N_2$  pressure) are presented in Table 4.2.

Measured values agree with the expected values within 13 % on average, except of the  $O_2$  concentration in the accumulation method. The amount of observed oxygen is significantly lower than expected. This is most likely caused by absorption of oxygen chemically reacting with the hot filament. It is further investigated at the end of this section. Assuming no more oxygen in the gas in the RGA one would expect 51.4 % of Ar in the mixture. This would mean a deviation of 6.8 % instead of 20.7 % from the expected value and an average deviation of 9.3 %. This is used as an estimation of the measurement uncertainty for all partial pressures, except

Method	calculation	gas method		accumulation method	
	expected	measured	dev. [%]	measured	dev. [%]
Ar	45.5 %	46.8 %	2.8	54.9 %	20.7 (6.8)
O <sub>2</sub>	11.5 %	9.63 %	16.3	~ 0 %	100
Kr	0.627 ppm	0.699 ppm	11.4	–	–

**Table 4.2:** A gas sample with a known composition was employed to verify the gas and accumulation method. The value 6.8 % for the accumulation method assumes no oxygen, left in the RGA. Dev. is used as abbreviation for deviation.

for oxygen in the accumulation method. The correct detection of the krypton concentration shows the good sensitivity of the system to traces with a concentration on the order of 1 ppm. The exact detection limit depends on the relative ionisation gauge sensitivity and the cracking pattern of the respective trace component. The partial pressure of H<sub>2</sub> was observed to occasionally change in some measurements without obvious reason. It is very reactive and mobile within metal parts. H<sub>2</sub> rates are therefore conservatively assumed to be indicative rather than quantitative.

The hypothesis that the oxygen deficit is caused by the hot filament of an ion gauge was further investigated. Therefore a measurement was performed employing the gas method. The valve V<sub>4</sub> was however kept open constantly in contrary to the standard for this method. The pressure in the chamber was decreasing slowly from a pressure reading above  $\sim 2 \cdot 10^{-2}$  mbar to a lower value. Partial pressures were recorded during the whole process. The Granville pressure gauge activates the hot filament at  $\sim 2 \cdot 10^{-2}$  mbar. The oxygen partial pressure measured by the RGA was decreasing by one order of magnitude at this point (Scan 145 in Figure 4.7). The partial pressure of CO<sub>2</sub> did simultaneously increase by one order of magnitude. The increase was observed within one scan and the decrease within two scans. Hydrogen is additionally increasing from this point on. The time required for one scan is  $\sim 36$  min. The absorption of O<sub>2</sub> in the chamber and emission of CO<sub>2</sub> took hence at most 72 min. This shows that the ion gauge of G absorbed the oxygen and emitted carbon dioxide and hydrogen. The most likely component of the gauge responsible for this effect is the hot filament. The partial pressures of other gases which are not fragments of O<sub>2</sub> or CO<sub>2</sub> were not affected.

The presented characterisation measurements show that gases chemically reactive with metal, like O<sub>2</sub> can only be reliably measured with the gas method and switched off ion gauge G. The emanation rate of O<sub>2</sub> can not be determined with the accumulation method. With the pressure rise method employed for samples with a high outgassing rate, O<sub>2</sub> is expected to be detectable, it might however show a deficit depending on its actual outgassing rate. The partial pressure of

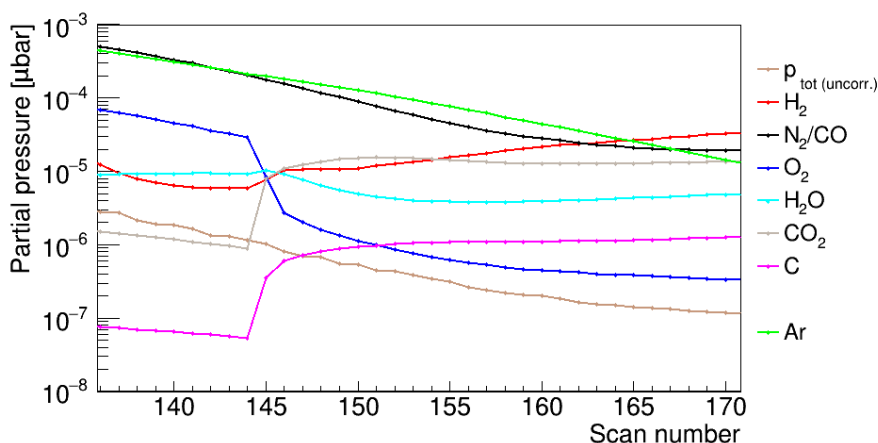


**Figure 4.7:** Evolution of partial pressures measured with the gas method. The Granville gauge was connected to the main chamber during this measurement ( $V_4$  opened). At scan 145 the ion gauge of G turned on, resulting in a sudden decrease of the  $O_2$  partial pressure and an increase of the  $CO_2$  and  $H_2$  partial pressures.

$CO_2$  proved to be increased significantly by the ion gauge of G. It is expected that the ion gauge in the RGA behave similar. Emanation rates of  $CO_2$  from samples must therefore be considered to be upper limits if they are not orders of magnitude above the blank chamber. A cross check of the  $CO_2$  rate is recommended also for higher emanation rates. The otherwise correctly obtained constituents show the reliability of the quantitative determination of relative compositions. For the absolute scale of partial pressure readings it is relied on the correct calibration by the producer (for nitrogen) with the only cross check being the consistent pressure reading of the RGA and G.

## 4.6 Measured Samples

This section describes the measurement of a TPB-coated Tetratex sample and measurements of differently cleaned PTFE blocks. The former sample possesses a low outgassing rate making a detailed blank measurement necessary. It is measured with the accumulation method. The latter possess a high rate and are measured employing the pressure rise method.

### 4.6.1 Emanation from PTFE after Different Cleaning Procedures

PTFE is installed in many cryogenic liquid experiments. In GERDA it is used as insulating spacer in the Ge diode holders and PMT holders, for a funnel guiding the sources through the top PMT array and as dielectric in cables. PTFE is also installed in the liquid argon setup described in Chapter 3. Its filler, PMT holder and cables form the major PTFE pieces in this setup. In XENON1T, the successor of XENON100 [133] it is used as a reflector and for the field shaping rings of the time projection chamber, as dielectric in cables and in PMT holders.

The emanation rate of PTFE was measured employing four PTFE blocks cleaned by different procedures. The procedures themselves have not been developed in the framework of this thesis. The four blocks were cut out of one PTFE plate. The surfaces of all blocks were subsequently milled to guarantee a smooth surface identical for all four pieces. The final dimensions of the blocks are  $(148_{-0}^{+0.1})$  mm by  $(69_{-0}^{+0.1})$  mm by  $(19_{-0}^{+0.1})$  mm which corresponds to a surface of  $286.7\text{ cm}^2$ . The following procedure was employed to clean one sample with acetone and one sample with ethanol:

- Wipe PTFE with Kimwipes and the solvent.
- Wipe a beaker with Kimwipes and solvent.
- Fill the beaker with 850ml of the solvent, insert the PTFE, cover the beaker with Al-foil.
- Place the beaker in an ultrasonic bath and run for 15 min.
- Fill beaker with fresh solvent and flip the sample such that another surface touches the bottom of the beaker, and run in ultrasonic for 10 min.
- Remove PTFE, let the solvent drain from PTFE for 30 s.
- Place the clean sample on an aluminium foil and cover with an aluminium foil (to protect from dust).
- Let it dry for 10 min.
- Flip the sample over and let it dry for other 5 min (use fresh Al-foil).

A second sample was cleaned with ethanol later on, to obtain a cross check of the measurement results. This cleaning procedure does not remove metallic radioactive trace contaminations on sample surfaces. These might be harmful, e.g. in case of the PTFE spacers used in the Ge diode holders in GERDA or the PTFE for the XENON1T time-projection chamber. A procedure developed by GERDA specifically for cleaning these spacers is therefore also tested. The detailed cleaning steps are:

- Immerse the PTFE in acetone and put it for 15 min in an ultrasonic bath.
- Remove the acetone by rinsing the PTFE several times with de-ionized water and additionally treat it in an ultrasonic bath with de-ionized water for 5 min. This is particularly important for the safety as acetone and  $\text{HNO}_3$  can cause explosions when getting in contact with each other!
- Immerse the sample in a 5 % (by mass)  $\text{HNO}_3$  solution.
- Treat the sample for 15 min in an ultrasonic bath with the acid (in a beaker) and leave it there for 1 h and 45 min.
- Rinse it after the acid treatment several times with de-ionized water.
- Place it for other 5 min in an ultrasonic bath with de-ionised water (in a beaker).
- Dry the sample by slightly wiping it with Kimwipes and let it dry other 20 min in air (protected from dust by aluminium foil).

All samples were cleaned at most one day before insertion into the chamber. They were wrapped in aluminium foil and placed in a sealable bag for storage and transportation from the cleaning site to the emanation chamber. Wrapping in aluminium foil was performed before placement inside the bag in order to avoid contaminations by the plastic bag. Such contaminations are observed for the Tetratex sample, presented in the next section. The partial pressures in the chamber were monitored while pumping with the PTFE sample, starting 75 min after the start.  $V_1$  was opened shortly before that, while  $V_R$  remained closed. Such a pump-down curve for the PTFE piece cleaned with ethanol is shown in Figure 4.8. It was acquired over the following  $\sim 19$  h. The ratio of nitrogen to oxygen is as expected for air in the beginning and drifts towards higher oxygen concentrations with time. The ratio of nitrogen to argon on the other hand is shifted towards higher argon concentrations at the beginning and approaches the ratio expected for air. A probable explanation for these observations is given in the following. Air is trapped inside the pores of the PTFE piece and is continuously emanating from the sample. The concentration of argon is higher close to the surface due to the three argon flushes involved in the loading procedure of the sample. However, the argon did not penetrate deep into the bulk of the sample. Its partial pressure in the residual gas is therefore enhanced relative to nitrogen only at the beginning of the pump-down. The primary source of oxygen and nitrogen is expected to be air in the full time range shown in Figure 4.8. The change of the ratio of their partial pressures is assumed to originate from a different mobility of the two gases. The mobility does not have a major effect in the beginning, when gas trapped in pores close to the sample surface is dominating. It becomes more and more relevant when the emanation is dominated by the gas supplied by pores with increasing

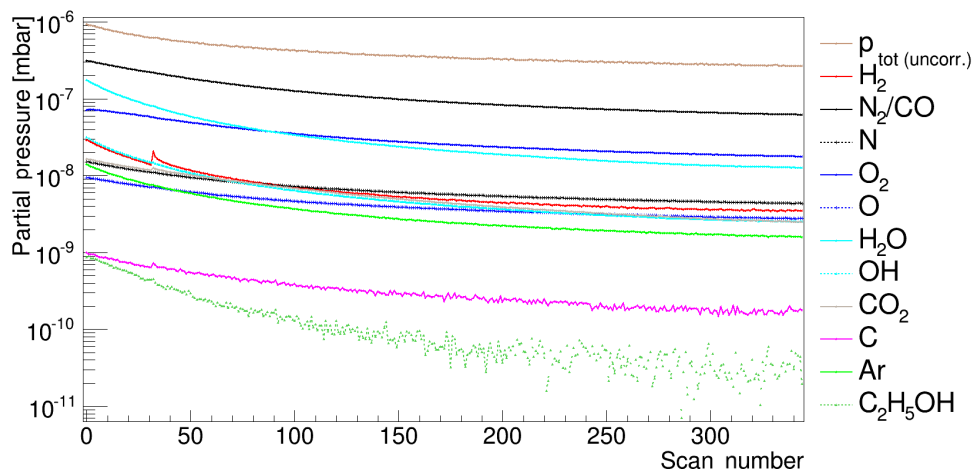


**Figure 4.8:** Evolution of partial pressures during  $\sim 19$  h of pumping of a PTFE sample cleaned with ethanol in an ultrasonic bath. The measurement was started 75 min after the beginning of the pumping.

path length to the sample surface. These observations together with the fact that PTFE is known to be porous and that the samples were stored in air since their production shows that the partial pressure at mass 28 is indeed dominated by nitrogen and not CO. This behaviour was observed for all four samples. The respective solvent used to clean the sample is visible in the mass spectra of all four PTFE samples. This includes acetone and  $\text{HNO}_3$  for the third sample.

The PTFE samples were measured employing the pressure rise method as described in Section 4.2.1. The emanation rate of the blank chamber and RGA are expected to be negligible for those measurements. The rates are determined fitting a linear function to the evolution of the respective partial pressure. The resulting outgassing rates of the most prominent components are provided in Table 4.3. These are obtained at pumping times of  $\sim 3600$  h and  $\sim 5500$  h. The emanation is dominated by  $\text{N}_2$  which exceeds the rate of any other component by at least one order of magnitude and is similar for all three samples. The largest difference for the dominant components is observed for  $\text{CO}_2$ . The sample cleaned with  $\text{HNO}_3$  show the highest emanation rate for this gas amongst the three samples. Its rate is  $\sim 2.3$  times and  $\sim 4.5$  times higher than for the samples cleaned with acetone or ethanol, respectively. The origin of the higher observed emanation rate can be explanation by reactions of residual  $\text{HNO}_3$  and acetone. The products of this reaction are  $\text{CO}_2$ ,  $\text{H}_2\text{O}$ , and  $\text{C}_2\text{H}_3\text{OH}$  (called ethenol or vinyl alcohol). Ethenol has a mass of 44 amu additionally contributing to the increase of the height of this

[mbar·l/s]	Blank	Acetone	HNO <sub>3</sub>		Ethanol
Pumping [min]	various	3600		5590	
Surface [cm <sup>2</sup> ]	—	286.7			
CO <sub>2</sub>	$2.6 \cdot 10^{-12}$	$1.51 \cdot 10^{-8}$	$3.5 \cdot 10^{-8}$	$1.75 \cdot 10^{-8}$	$3.9 \cdot 10^{-9}$
N <sub>2</sub> +CO	$6.1 \cdot 10^{-13}$	$4.6 \cdot 10^{-7}$	$5.4 \cdot 10^{-7}$	$4.9 \cdot 10^{-7}$	$4.4 \cdot 10^{-7}$
O <sub>2</sub>	—	$1.51 \cdot 10^{-8}$	$8.4 \cdot 10^{-9}$	$4.8 \cdot 10^{-9}$	$1.10 \cdot 10^{-8}$
Ar	—	$1.40 \cdot 10^{-8}$	$1.77 \cdot 10^{-8}$	$1.20 \cdot 10^{-8}$	$1.25 \cdot 10^{-8}$

**Table 4.3:** Emanation rates of various PTFE samples after the respective time of pumping. An empty cell means the respective value was not determined. A “—” means the value is either too small to be detected or covered by another substance with a peak at the same mass to charge ratio.

peak. A confirmation of the validity of the CO<sub>2</sub> measurements is given in the next paragraph. The H<sub>2</sub>O emanation rates were not determined as these are expected to depend strongly on the ambient humidity to which the sample was exposed before insertion into the emanation chamber.

The fourth PTFE piece was cleaned with ethanol in the same way as the first sample. This was performed to verify the presented measurements, in particular checking if the observed difference in the CO<sub>2</sub> emanation rate is caused by the different cleaning procedures rather than by uncontrolled conditions. Its emanation rate was therefore measured for several pumping times. This is shown in Figure 4.9. Additionally shown are the rates measured from the first sample for a pumping time of 6970 min and 8300 min. The evolution and height of the rates are consistent for the two samples, which verifies the entire procedure. The  $\sim 4.5$  times higher CO<sub>2</sub> emanation rate for the sample cleaned with HNO<sub>3</sub> is hence a real effect.

#### 4.6.2 Emanation from TPB Coated Tetratex for GERDA

Emanation rates from a sample of TPB-coated Tetratex were measured. This sample was coated together with the wavelength-shifting reflector foils installed in the GERDA liquid Ar veto. The sample is assumed to be representative for the foils installed in GERDA. It is furthermore anticipated to have a low outgassing rate. For such samples it is important to know the rate of the blank chamber as accurately as possible at the time of the sample measurement. Blank rates are therefore measured before and after measuring the sample. Blank and sample measurements were performed for similar pumping times employing the accumulation method as described in Section 4.2.1. The evolution of the partial pressure in the RGA for a blank measurement before the Tetratex sample is shown in Figure 4.10. Such plots were used to determine the outgassing rates according to equation 4.2.1.

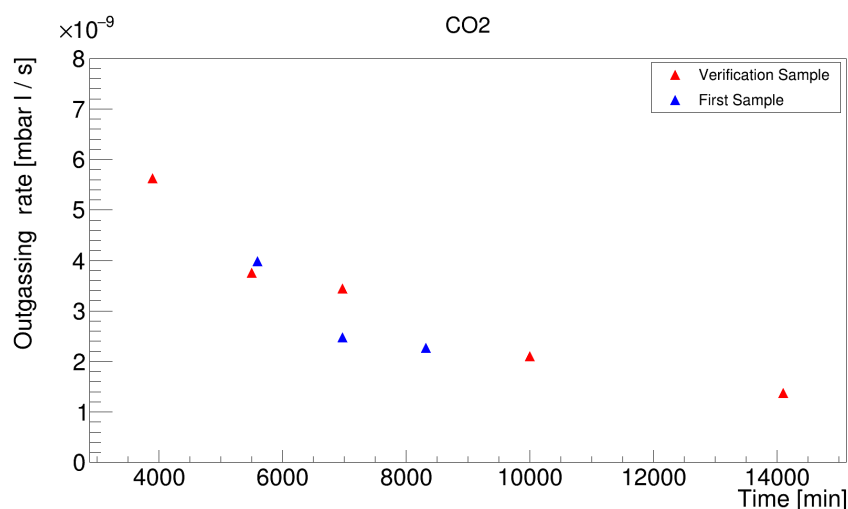


**Figure 4.9:** Emanation rates of  $\text{CO}_2$  from two PTFE samples cleaned with ethanol for different pumping times. The two samples were prepared and measured independently but with the same procedures. The determined rates are consistent with each other.

The partial pressures displayed in the beginning of the plot correspond to pressures in the RGA while pumping, isolated from the emanation chamber. The following time range with rising partial pressures is employed to determine the pressure in the RGA  $p_R$  at the time of opening the regulating valve. It is caused by outgassing of the RGA itself. The scan number corresponding to the opening time is 39. The partial pressures caused by emanation from the RGA at this point were extrapolated, fitting a linear function to the respective graphs. The fit range was chosen individually for each partial pressure depending on the range (just before opening) within which it can be approximated by a linear function. The subsequent time range is used to determine  $p_3$  in a similar way. The blank rates before the measurement of the Tetratex sample are provided in Table 4.4.

A mass spectrum of the blank chamber emanation was additionally acquired before and after measurements with the Tetratex sample. These were taken with activated electron multiplier while pumping the chamber with all valves but  $V_4$  opened. The blank spectrum acquired before the Tetratex measurements is shown in Figure 4.11 together with the Tetratex spectrum. In the blank spectrum  $\text{H}_2$ ,  $\text{H}_2\text{O}$ ,  $\text{CO}$ ,  $\text{Ar}$ ,  $\text{CO}_2$  and a small  $\text{O}_2$  peak are visible additionally to a peak at 30 amu/q which corresponds to the mass of  $\text{NO}$  and ethane. The former is a residual from the  $\text{HNO}_3$ -cleaned PTFE sample measured before. The latter is a common residual gas in vacuum systems. The ratio of the peaks at 15 amu/q and 14 amu/q suggest an additional small contribution of methane.

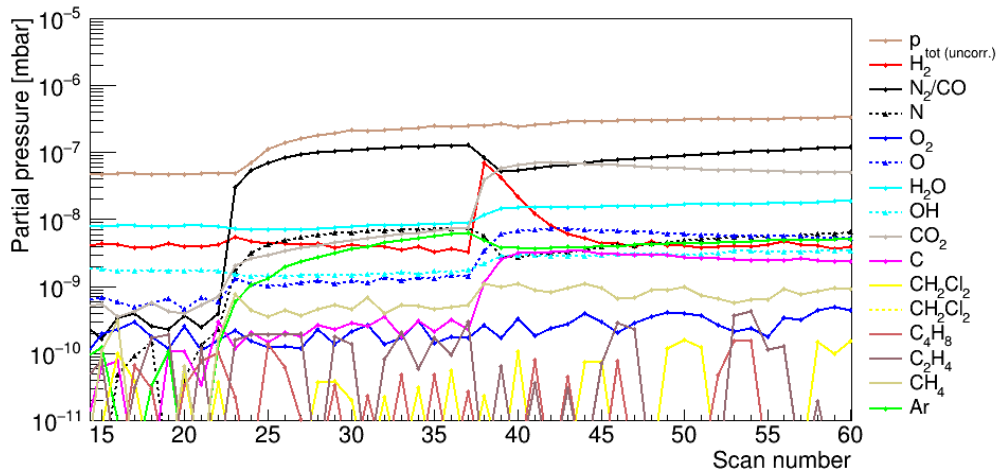


**Figure 4.10:** Evolution of selected partial pressures in the RGA during an emanation measurement of the blank chamber before measurements of TPB-coated Tetratex. First points were acquired while pumping the RGA, isolated from the emanation chamber. The next  $\sim 15$  data points ( $\sim 6$  min) correspond to the emanation of the RGA itself. The following step is caused by fully opening the regulating valve, equalising the partial pressures in the RGA and the chamber. The emanation time was  $\sim 92$  min.

A sample of TPB-coated Tetratex with a size of  $362\text{ cm}^2$  from the wavelength shifting reflector foil installed in the GERDA liquid Ar veto was measured. A mass spectrum of the sample after pumping for 2 h is shown in Figure 4.11. The spectrum was taken with the activated electron multiplier. The emanation of this sample is dominated by  $\text{H}_2\text{O}$ ,  $\text{H}_2$ ,  $\text{N}_2/\text{CO}$  and  $\text{CO}_2$ . Residuals of the solvent dichloromethane, as well as fragments from the polyethylene packaging which was used for transportation of the coated Tetratex are visible with lower intensities. These fragments are ethylene, butene and long polyethylene chains with an attached chlorine atom. Long molecules were probably detached from the polyethylene foil by a reaction with dichloromethane. The spectra of the pure individual components are shown in Figure 4.12 as available from NIST [139]. Chloroicosane ( $\text{C}_{20}\text{H}_{41}\text{Cl}$ ) is taken as a representative for polyethylene chains detached by dichloromethane. Non-chlorinated polyethylene can be distinguished from chlorinated polyethylene chains by the absence of a peak at  $91\text{ amu/q}$  and by the relative height of several other peaks. Furthermore, the presence of  $\text{CH}_3$  (methane) can be derived from the ratio of the peak height at  $15$  to  $14\text{ amu/q}$ . This is a fragment produced by any hydrocarbon and does not necessarily emanate from the sample itself. The abundance of  $\text{CH}_3$  is nevertheless used to calculate an emanation rate of methane corresponding to an upper limit. TPB emanating from the sample would cause peaks with high relative intensities at  $165$  and  $167\text{ amu/q}$ . The absence of visible peaks at those mass to charge ratios is an important observation, showing that TPB is not expected to detach from the reflector foil by evaporation.

The emanation rates of the coated sample were determined in two measurements performed with the accumulation method. For the first measurement the valves of the chamber were closed after  $\sim 1305\text{ min}$  ( $21:45\text{ h}$ ) of pumping and the emanating gases were accumulated for  $62\text{ min}$  before measuring their partial pressures. In a second measurement the sample was pumped for  $\sim 3240\text{ min}$  ( $54\text{ h}$ ) and the accumulation time was  $78\text{ min}$ . Both measurements were taken without electron multiplier to reduce the wear of the mass spectrometer when exposed to higher pressure. The mass spectra for a pumping time of  $\sim 1305\text{ min}$  before and after opening the regulating valve are shown in Figure 4.13 on the top. The bottom of the figure shows the development of partial pressures during the measurement procedure. Visible are the same components as described above except of chlorinated polyethylene chains, which are most likely still present but below the sensitivity with switched off electron multiplier. A detection limit of  $5 \cdot 10^{-10}\text{ mbar}$  is estimated and employed to calculate an upper limit of their emanation rate. The peak at  $28\text{ amu/q}$  shows a delayed rise, which is an indication that this rise is not due to gas entering through the regulating valve but due to  $\text{CO}$  released by the RGA induced by the other gases. The measured rates for Tetratex are provided in

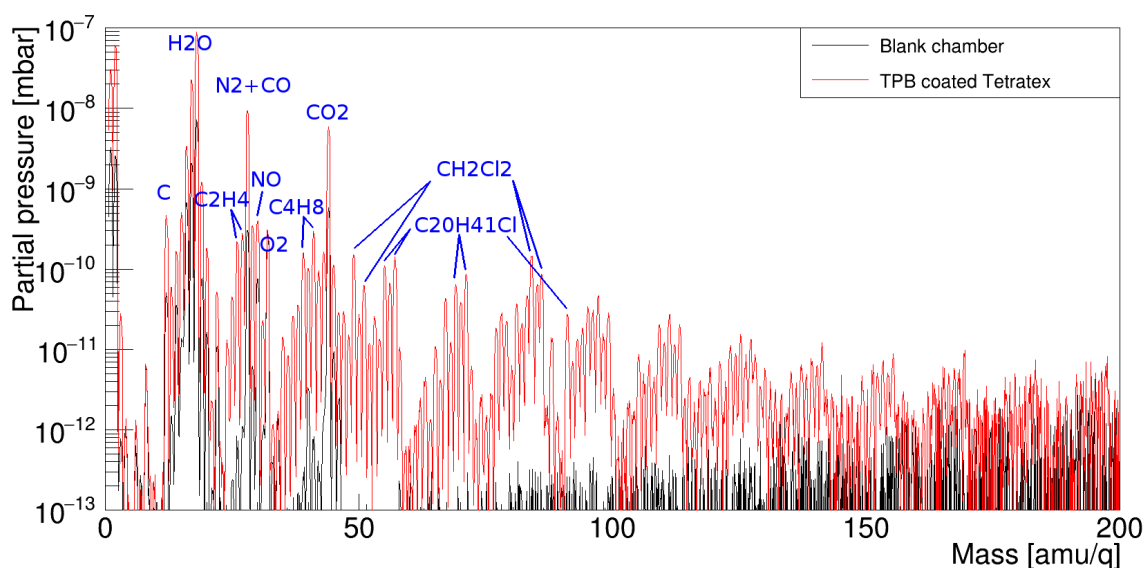


**Figure 4.11:** Mass spectrum of gas emanated from TPB-coated Tetratex at a pumping time of 2 h. The most prominent mass to charge ratio peaks are labelled with the chemical substances dominating those peaks.

Table 4.4. Blank rates are not subtracted for values provided therein. The relative ion gauge sensitivity for Dichloromethane was taken from [140].

The blank measurements performed after the coated Tetratex show residuals of ethylene, butene, and polyethylene chloride (with electron multiplier turned on only) after pumping for  $\sim 2$  h in addition to the components observed before measuring Tetratex. Dichloromethane is not visible anymore. The blank rates after the Tetratex sample are also provided in Table 4.4.

Upper limits are provided for undetected components, different values originate from different accumulation times. The emanation rates of  $\text{CO}_2$ , CO and dichloromethane from Tetratex were additionally determined for pumping times of 4689 and 8686 min to investigate their evolution. Dichloromethane is emanating with a rate continuously decreasing with the pumping times. This is expected but in contrast to the emanation of  $\text{CO}_2$  and CO. Partial pressure readings for CO and  $\text{CO}_2$  while pumping do however show a continuous decrease. This behaviour suggests that there is an additional source of CO and  $\text{CO}_2$  during the emanation measurements and the values should therefore be treated as upper limits. An emanation of  $\text{CO}_2$  from an ion gauge was previously described at the end of Section 4.5.3. Further candidate sources for both molecules are valves (when opening or closing) and a release in the RGA triggered by incoming gas of other species.

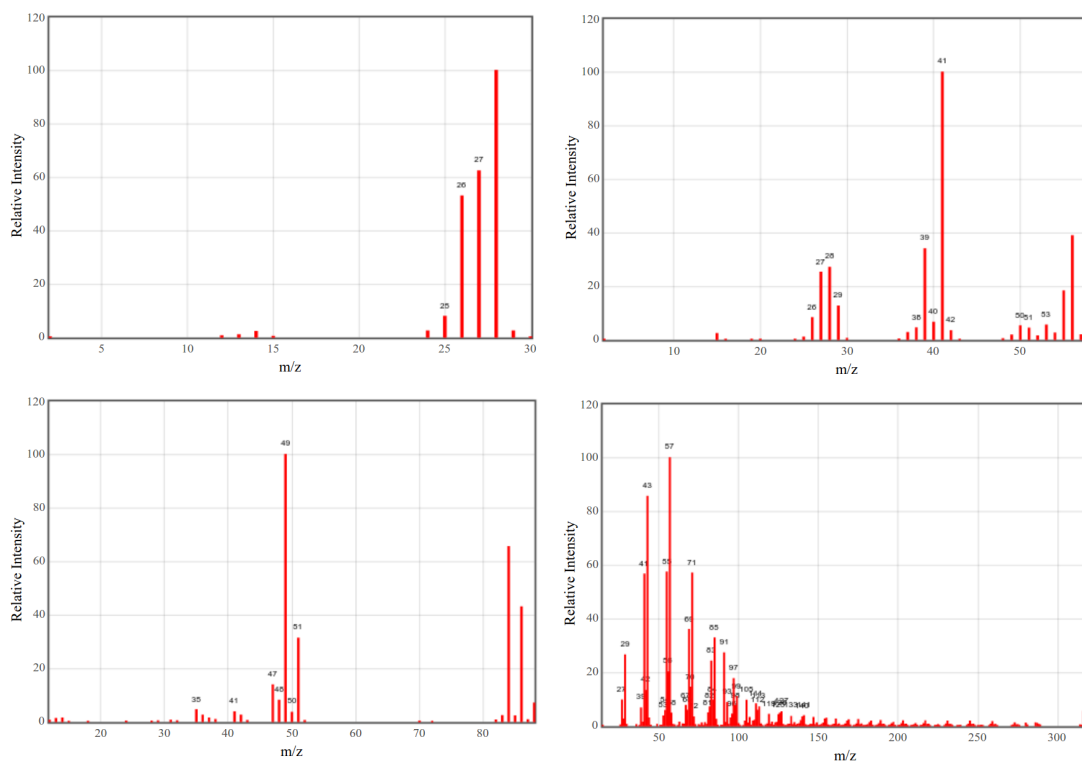


**Figure 4.12:** Individual mass spectra taken from [139] for ethylene (C<sub>2</sub>H<sub>4</sub>), butene (C<sub>4</sub>H<sub>8</sub>), dichloromethane (CH<sub>2</sub>Cl) and chloroeicosane (C<sub>20</sub>H<sub>41</sub>Cl). These are constituents of the mass spectrum of the TPB-coated Tetratex sample. The latter molecule is representative for polyethylene chains of different length which got chlorinated by dichloromethane.

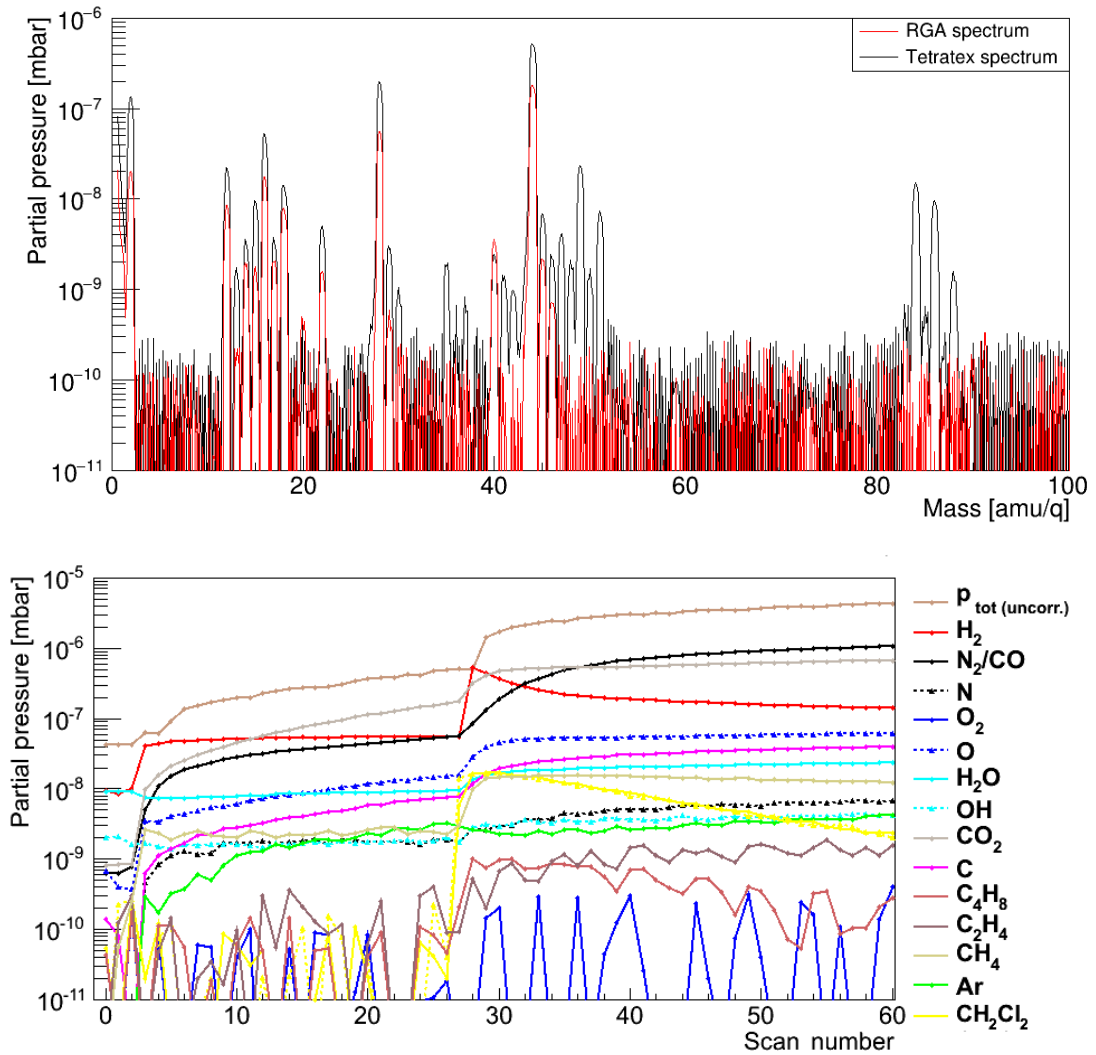


**Figure 4.13:** Emanated gases from TPB-coated Tetratex at a pumping time of  $\sim 1305$  min. Top: mass spectrum before (scan 26 in red) and after (scan 30 in black) opening the regulating valve. The emanated gases were accumulated for 62 min. Bottom: evolution of the partial pressures during this measurement.

[ $10^{-12}$ mbar·l/s]	Blank before	TPB-coated Tetratex				Blank after
Pumping [min]	1317	1304	3244	4689	8686	1320
CO <sub>2</sub>	34	< 317	< 408	< 434	< 189	97
N <sub>2</sub> +CO	15.9	< 47	< 216	< 117	< 52	13.0
H <sub>2</sub> O	6.3	11.1	6.8			3.9
Ar	1.24	1.09	0.39			1.04
CH <sub>2</sub> Cl <sub>2</sub>	< 0.23	12.0	9.2	8.7	7.0	< 0.16
C <sub>2</sub> H <sub>4</sub>	< 0.23	0.50	0.61			< 0.16
C <sub>4</sub> H <sub>8</sub>	< 0.23	1.31	0.48			< 0.16
C <sub>2</sub> nH <sub>4</sub> nCl	< 0.23	< 0.34	< 0.27	< 0.30	< 0.17	< 0.16

**Table 4.4:** Emanation rates of a TPB-coated Tetratex sample with a size of  $361.6\text{ cm}^2$  after different pumping times, as well as rates of the blank chamber before and after the measurement. Blank rates are not subtracted from rates for Tetratex.

The total emanation rate of the Tetratex sample is approximately one order of magnitude higher than the emanation rate of the blank chamber. This is a very good result and its emanation rate will be even lower at liquid argon temperature. The main emanating components in descending order are CO<sub>2</sub>, CO, CH<sub>2</sub>Cl<sub>2</sub> and H<sub>2</sub>O, while rates of the first two are upper limits. The contribution of Tetratex to the total emanation rate of all components in GERDA is expected to be negligible based on these results.

## 4.7 Conclusions and Outlook

A mass-resolved emanation rate measurement system was designed, built and commissioned at the University of Zurich. The system is employed to identify the constituents of emanating gases by a mass spectrometer with a range of 1–200 amu/q. A software was developed to read, analyse and display mass spectra, as well as the evolution of partial pressures during pump-down and emanation measurements. A gas sample with known composition was employed to successfully verify the quantitative analysis procedure with a sensitivity to trace components below 1 ppm. It also shows the capability to identify traces in gas samples down to this concentration. Emanation rates of the blank chamber were measured to be as low as ( $\sim 144, 2.6, 0.61$  and  $0.73$ )  $\cdot 10^{-12}$  mbar l/s for the dominating components H<sub>2</sub>, CO<sub>2</sub>, CO and H<sub>2</sub>O, respectively. The sensitivity of the system to emanation rates is  $\sim 1 \cdot 10^{-13}$  mbar l/s, depending on the emanating component. The uncertainty on measured rates was estimated to be  $\sim 10\%$ .

The system was successfully employed to measure a TPB-coated Tetratex sample from the GERDA liquid argon veto system. It was found to possess excellent emanation rates well suitable for deployment in GERDA. The dominant rates after a pumping time of  $\sim 1300$  min are ( $< 317$ ,  $< 47$ ,  $11.1$ ,  $12$ )  $\cdot 10^{-12}$  mbar l/s for  $\text{CO}_2$ ,  $\text{N}_2+\text{CO}$ ,  $\text{H}_2\text{O}$  and the solvent dichloromethane, respectively. Emanation from PTFE cleaned with acetone, ethanol or acetone and nitric acid was additionally measured. All samples were found to be dominated by similarly high rates of nitrogen with a value of  $\sim 5 \cdot 10^{-7}$  mbar l/s after a pumping time of  $\sim 3600$  min. Significantly different emanation rates were observed for  $\text{CO}_2$ . The sample cleaned with nitric acid showed a rate of  $\sim 3.5 \cdot 10^{-8}$  mbar l/s,  $\sim 4.5$  or  $\sim 2.3$  times higher compared to samples cleaned with ethanol or acetone, respectively. Based on these results it is recommended to use ethanol as the standard cleaning procedure unless removal of metallic surface contaminations is crucial. In that case cleaning with nitric acid is required.

The emanation rate measurement system is available and ready for measurements of further samples. The analysis software is written and commented to be easily understandable by anyone with C++ knowledge.

## Chapter 5

# Pulse Shape Discrimination for Semi-Coaxial Detectors Employing a Support Vector Machine

In GERDA Phase I, 87.5% of the exposure was acquired with semi-coaxial germanium detectors and 12.5% with BEGe-type detectors. Approximately 15 kg of semi-coaxial germanium detectors and 20 kg of BEGe-type detectors will be installed in Phase II. The former type was hence providing the major part of the Phase I exposure and is expected to provide a significant fraction in Phase II. The discrimination power between signal-like single site events (SSEs) and multi site event (MSE) background is however significantly worse for this type of detector. A single variable cut was found to be insufficient to separate the two classes of events. A multivariate pulse shape discrimination (PSD) method is therefore required. Machine learning algorithms are suitable tools to perform such analyses. A promising candidate amongst the available algorithms is the so-called Support Vector Machine (SVM). The optimisation of its parameters employing GERDA calibration measurements and its application to GERDA physics data are presented in this Chapter.

The developments are performed employing the semi-coaxial detector ANG2 with a mass of 2833 g. This is the largest amongst all enriched GERDA detectors with highest exposure. It was chosen to obtain the highest statistics. It was furthermore stably operated at 3500 V over the full period of Phase I. The methods developed with this detector can be applied to all other detectors.

## 5.1 Function Principle of a Support Vector Machine

An SVM assigns a value to each event, representing the class of this event. This so-called classifier was chosen to have a negative value for events classified as multi site and a positive value for events classified as single site. The classifier is calculated based on a set of variables representing this event. The set is treated as vector  $\vec{x}$  in a space with  $n$  dimensions, which is corresponding to the number of variables. The classification is performed finding a hyperplane in this  $n$  dimensional space separating the two classes of events. The distance  $y$  of each event is the classifier for that event and is calculated as

$$y = \langle \vec{w}, \vec{x} \rangle + b, \quad (5.1)$$

with the vector  $\vec{w}$  and constant  $b$  to be determined in a process called learning. Note, the distance of events on one side of the plane has the opposite sign than for events on the other side. The learning algorithm is searching for the vector  $\vec{w}$  and constant  $b$  maximising the distance of all events to this decision boundary. This learning is performed employing events with a known classification. It defines  $\vec{w}$  and  $b$  uniquely besides a constant factor, which is fixed by an additional condition: the absolute value of the distance of the closest points to the decision boundary is 1. This is called a hard-margin SVM and the band of the decision boundary  $\pm 1$  is called margin. Events at the edge of the margin obtain a higher weight for the determination of  $\vec{w}$  and  $b$ , compared to events with a larger distance. This type of SVM furthermore requires clean training samples which are not available in our application. This can be handled by a soft-margin SVM, in which the normalisation is replaced by a penalty system. It allows misclassification and events within the margin by assigning a penalty to each such event, depending on its distance to the margin boundary of its class. The sum of penalties gets weighted with the factor  $C$  and is minimised simultaneously to maximising the distance to the decision boundary of all other events. The effect on the decision boundary of the parameter  $C$  is illustrated in Figure 5.1 on the left. Large values of  $C$  result in a behaviour similar to a hard margin SVM.

In order to obtain a non-linear separation of the two event classes, the scalar product  $\langle , \rangle$  is replaced by a so-called kernel function. In the work presented in this chapter a Gaussian kernel function with the mathematical form

$$e^{-\gamma \|\vec{w} - \vec{x}\|^2} \quad (5.2)$$

is employed. It is elsewhere also referred to as “radial basis function” kernel. The parameter  $\gamma$  defines the allowed bending of the decision boundary. The effect of

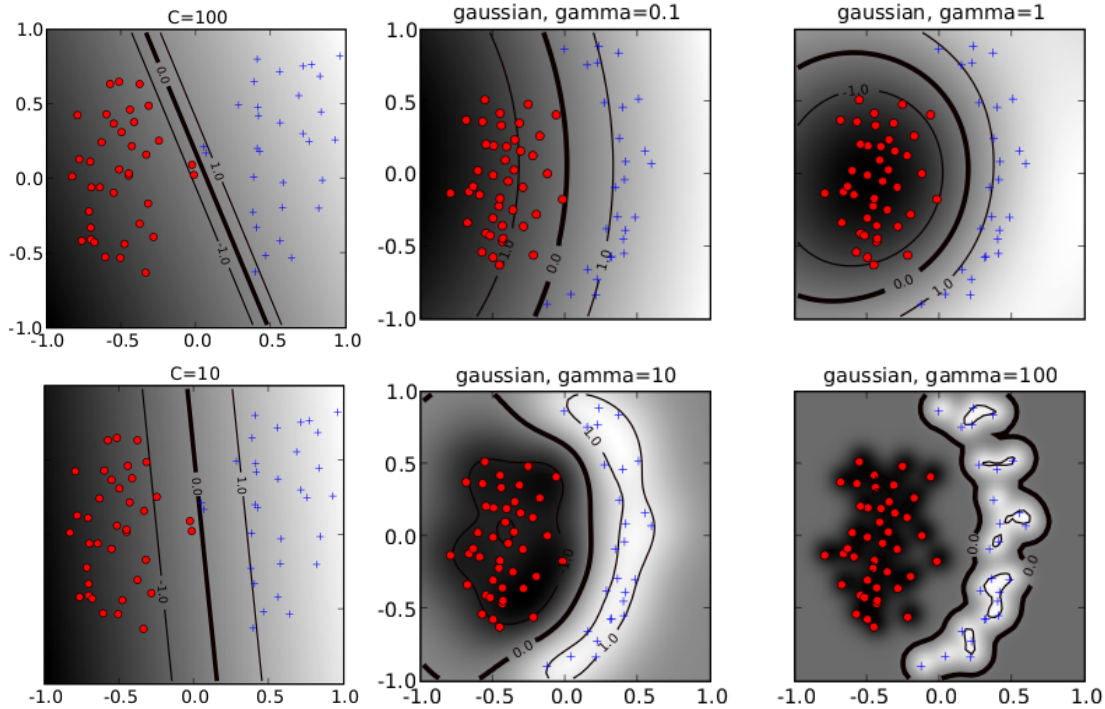


**Figure 5.1:** Two plots on the left: illustration of decision boundaries obtained for different values of  $C$ . The optimal parameter set depends on the application. Plots in the centre and on the right: illustration of decision boundaries obtained for different values of  $\gamma$ . A Gaussian kernel function was employed in all cases. A larger value of  $\gamma$  results in a finer decision boundary. Smaller values are less sensitive to overfitting. All plots in this figure are from [141].

different values of this parameter is illustrated in Figure 5.1 on the right and in the centre.  $\gamma$  must be provided as input to the learning procedure and its value has to be optimised manually together with the value of  $C$ . Further information about SVMs is provided e.g. in [141]. The implementation of an SVM employed in this chapter is called SVM<sup>light</sup> and is optimised for large datasets as described in [142].

## 5.2 Selection of Training Datasets and Input Variables

Training an SVM requires a data set of events with known classification (single site or multi site). These are available in calibration measurements acquired with  $^{228}\text{Th}$  sources. A proxy for SSEs is provided by the 1592.5 keV double escape peak

(DEP) of  $^{208}\text{Tl}$ . Events in this peak originate from 2614.5 keV gamma rays which did undergo pair production. The positron and electron get stopped and deposit their kinetic energy within a few hundred  $\mu\text{m}$  by the production of electron-hole pairs. The positron eventually annihilates with an electron producing two 511 keV photons. These two photons can escape the detector without further interaction, resulting in a total energy deposition of 1592.5 keV. The nearby full energy peak (FEP) at 1620.74 keV from  $^{212}\text{Bi}$  is employed as a proxy for MSE. It contains primarily events which underwent pair productions and both 511 keV events did deposit their energy in the detector.

The selection is performed based on the energy in a window of the respective peak position  $\pm 3$  keV. The contamination by events from the respective other class (MSEs in the SSE sample and the other way round) is discussed in Section 5.3.1. Note that DEP events are preferably located in the corners of the detectors. The two 511 keV gamma rays have a larger escape probability at those locations, while FEP does not show such a geometrical preference. Employing the DEP as SSE proxy can lead to a bias towards a volume selection. An other SSE proxy is however not available in calibration data. This is further discussed in Section 5.5.

The number of events in peaks employed for the energy calibration is much larger than the number of events in the DEP. Normal calibration measurements contain hence to little statistics in the DEP and a long calibration measurement was taken in particular for the development of pulse shape analysis (PSA) methods. It was acquired in the beginning of Phase I and is employed for the developments presented in this chapter. The mean trace of all events in the DEP (3631 counts) of this data is shown in Figure 5.2 together with the mean trace of all events in the FEP (4278 counts). A difference is visible between the two. Each trace was scaled by the uncalibrated energy of the event prior to the calculation of the mean traces. The energy is determined employing a digital semi-Gaussian [143] shaping algorithm. It is available in the GERDA analysis software GELATIO [144] and was also employed for the energy reconstruction in GERDA Phase I.

The scaled ADC values of the charge pulse have been chosen as input variables for the SVM. The time window was chosen identical to the one in Figure 5.2. This set of variables was selected as it is expected to contain the maximal amount of information. Each trace is scaled by the energy to avoid a selection based on the pulse height. The uncalibrated energy was chosen over the calibrated, as it is expected to partly cancel out drifts in the electronic readout chain. The time window is fixed relative to the trigger position calculated by the GELATIO module GEMDTrigger. It corresponds to the first sample which exceeds three standard deviations of the baseline. The module saves only trigger positions for which the signal stayed above threshold for at least 40  $\mu\text{s}$  (4000 samples). In all cases data quality cuts are applied. Noisy events are rejected by a cut on the baseline standard

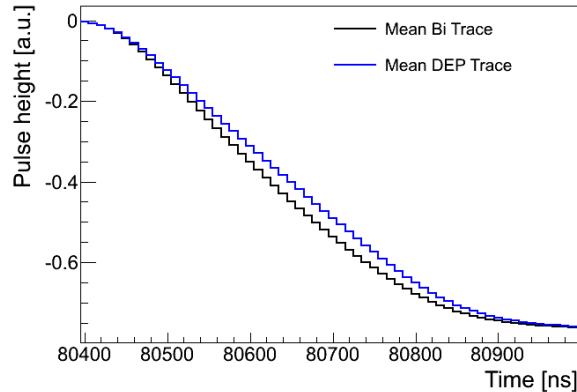


**Figure 5.2:** Mean trace of events in the 1621 keV FEP from  $^{212}\text{Bi}$  (black line) and the 1592 keV DEP from  $^{208}\text{Tl}$  (blue line). Shown is the time window employed for the PSA.

deviation. Pile-up events are rejected by a cut on the number of triggers found within one trace, the position of the trigger and the baseline slope.

### 5.3 Parameter Optimisation

The optimisation of the parameters  $C$  and  $\gamma$  was performed comparing SSE spectra obtained from Monte Carlo (MC) simulations with SSE spectra obtained from the classification by the SVM. The first step for the optimisation was therefore to simulate the long calibration measurement. This was performed employing the Geant4 [128] based MC simulation software MaGe [145]. The relevant, high energy part of the calibration spectrum is given by the decays of  $^{212}\text{Bi}$  and  $^{208}\text{Tl}$ . Other isotopes were not simulated in order to minimise computation time. In total  $1.2 \cdot 10^9$  primary events were generated. The energy resolution as a function of energy is available for each GERDA calibration measurement, described by a square root function plus a constant. The energy of each event was convoluted with a Gaussian distribution with a width defined according to the square root function. A single site event selection for simulated data was then defined and employed to produce SSE spectra. These were then employed to compare with the classification by the SVM.

The zero position in the MaGe coordinate system relative to the SIS position was determined in the framework of the PhD thesis of Andrea Kirsch [146] and corresponds to  $(5200 \pm 40)$  mm for the Phase I configuration. In MaGe the z-axis is directed upwards, while the z-axis of the SIS is pointing downwards. The SIS source positions of the long calibration measurement were 5400 mm, 5600 mm and

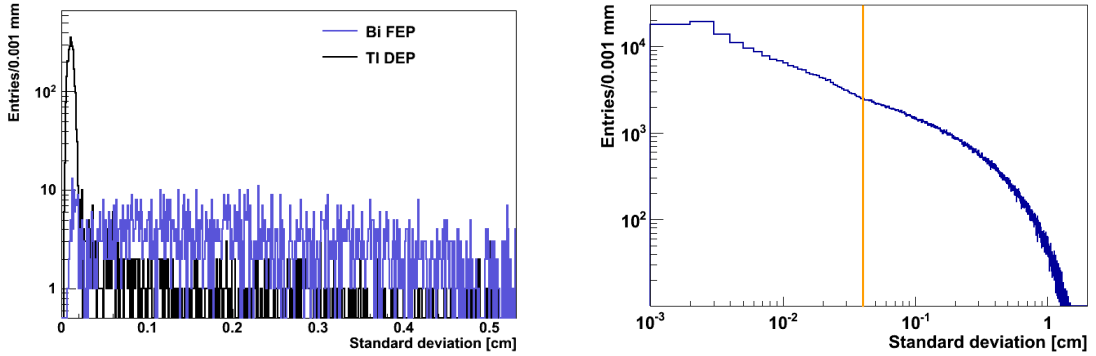


**Figure 5.3:** Standard deviation of the centre of energy in the simulation of the long calibration. Left: calculated for events in the DEP at 1593 keV superimposed by events in the 1621 keV FEP. Right: calculated for events in spectrum. The SSE cut threshold of 0.04 mm is illustrated by the orange line.

5600 mm for S1, S2 and S3 respectively. They do hence correspond to -200 mm, -400 mm and -400 mm in MaGe.

### 5.3.1 Selection of Single Site Events in a Simulation

The first step in the analysis of the MC simulation was to define a SSE cut. The hit positions and hit energies were employed for this purpose. First, the centre of energy is calculated. This is performed by weighting all hit positions with the respective energy deposition. The standard deviation of this variable is then calculated and normalised by the total energy deposition in this detector. The distribution of the normalised standard deviation of the centre of energy is shown in Figure 5.3. The events in the DEP show a clear enhancement in the region below 0.02 mm. The maximal distance of hits in those events is typically several hundred  $\mu\text{m}$ . It is given by the range of the electron-positron pair. Applying a cut at this value results in the energy spectra shown in Figure 5.4.

A cut threshold of 0.02 mm does however reject events with secondary x-rays, which originate from bremsstrahlung produced by the electron-positron pairs and from recombination of knocked-out binding electrons. The fraction of events with additional x-rays increases with increasing energy. It is hence higher at the Q-value of the double beta decay (2039 keV) than at the energy of the DEP (1593 keV). Events with a standard deviation of the centre of energy in the range of 0.02 mm – 0.04 mm are typically events with a secondary x-ray. They have a spot of energy deposition within several hundred  $\mu\text{m}$ , caused by the electron-positron pair, and an energy deposition by a secondary x-ray several mm away. Events just above this energy are typically multiple Compton scattering events. The distribution of

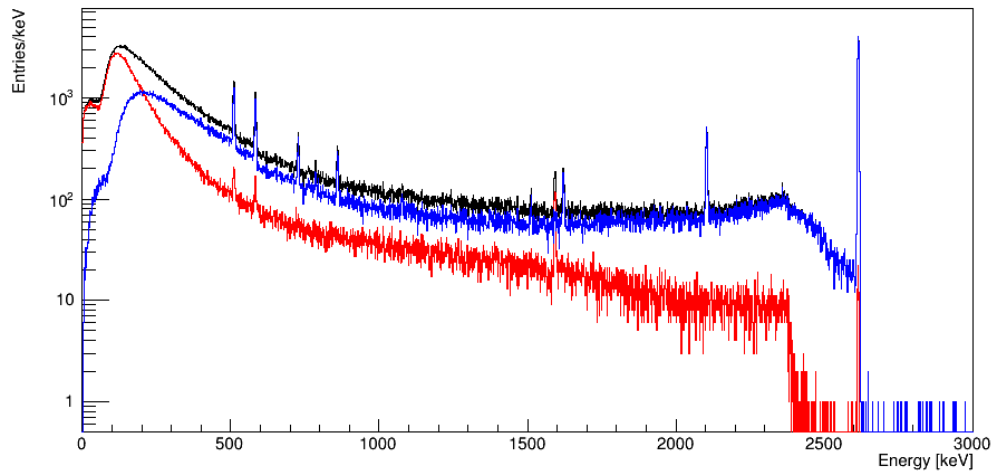


**Figure 5.4:** Simulated spectrum of the long calibration measurement (black line). Superimposed is the single (red) and multi (blue) site content. Events are categorised applying a cut of 0.02 mm on the standard deviation of the centre of energy.

the centre of energy for all events in the simulated long calibration shows a slight kink at the value of 0.04 mm. This is suggesting a change of process producing the dominating fraction of events in the respective regions. The cut threshold employed for the production of the reference SSE and MSE distributions is thus chosen as 0.04 mm. The resulting spectra are shown in Figure 5.5. The cut does strongly reject high energy FEPs as well as events above the Compton edge of the 2614.5 keV peak of  $^{208}\text{Tl}$ . These are dominantly MSE. It does also keep most events in the DEP and at very low energies. Both are SSE dominated.

### 5.3.2 Parameter Scan

The SSE spectrum obtained from the simulation is compared with the SSE spectra obtained by classification with the SVM in order to optimise the parameters  $C$  and  $\gamma$ . The range of  $3 \cdot 10^{-3}$  to  $3 \cdot 10^6$  and  $3 \cdot 10^{-6}$  to 30, respectively, was first scanned with a step size of a factor of 10. The SVM was trained with each doublet of parameter values and then applied to the full spectrum of the long calibration data. Parameter combinations which are not expected to yield a meaningful result are not tested. This was decided based on the spectra obtained from neighbouring parameter sets.

Oscillations are observed in the energy spectra of some parameter combinations, in particular for high values of  $\gamma$ . These oscillations are interpreted to be caused by overfitting, when the algorithm finds decision boundaries selecting small groups of events or individual events. The observation that overfitting occurs more likely for

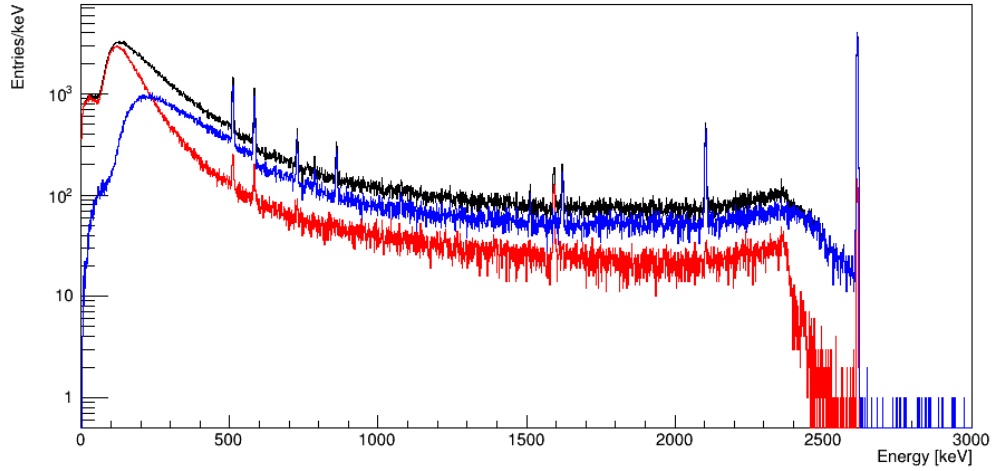


**Figure 5.5:** Simulated spectrum of the long calibration measurement (black line). Superimposed is the single (red) and multi (blue) site content. Events are categorised applying a cut of 0.04 mm on the standard deviation of the centre of energy. This includes events with secondary x-rays in the single site category.

larger values of  $\gamma$  is in accordance with the expectation (compare also Figure 5.1). For some parameter sets the SVM is clearly not capable to separate the two classes of events and classifies all of them as MSE. An overview of the obtained SSE and MSE event spectra of this rough scan is shown in Figure 5.6. Not plotted are spectra for  $\gamma = 30$  because of space constraints. Those look similar to spectra with  $\gamma = 3$  but with larger amplitudes for the oscillations.

The SSE spectra obtained with the SVM were compared to the SSE spectrum from the MC simulation. This was performed scaling the simulated spectrum to the same number of events as the measured calibration spectrum. The energy range employed for scaling is (1200–2800) keV. The SSE spectra from the measurement are then subtracted by the scaled SSE spectrum from simulation. The integral of this differential spectrum is then calculated in the energy range of (1200–2800) keV. Its value is shown as a function of  $C$  and  $\gamma$  in Figure 5.7. The total number of events in this energy range is 465084 in the full spectrum (MSE + SSE, both in data and scaled MC).

For most parameter sets, the number of SSEs in the data is larger than in the scaled MC simulation. The SVM is hence classifying too many events as single-site. There is a large range of the two parameters for which the integrated difference varies only slightly. Employing a parameter set on this plateau is expected to yield more robust results. A slight shift of the plateau for a specific data set could cause false rejection in case of choosing a parameter set close to a steep drop or false acceptance in case of a step rise. A false rejection might suppress

## CHAPTER 5. PULSE SHAPE DISCRIMINATION FOR SEMI-COAXIAL DETECTORS EMPLOYING A SUPPORT VECTOR MACHINE

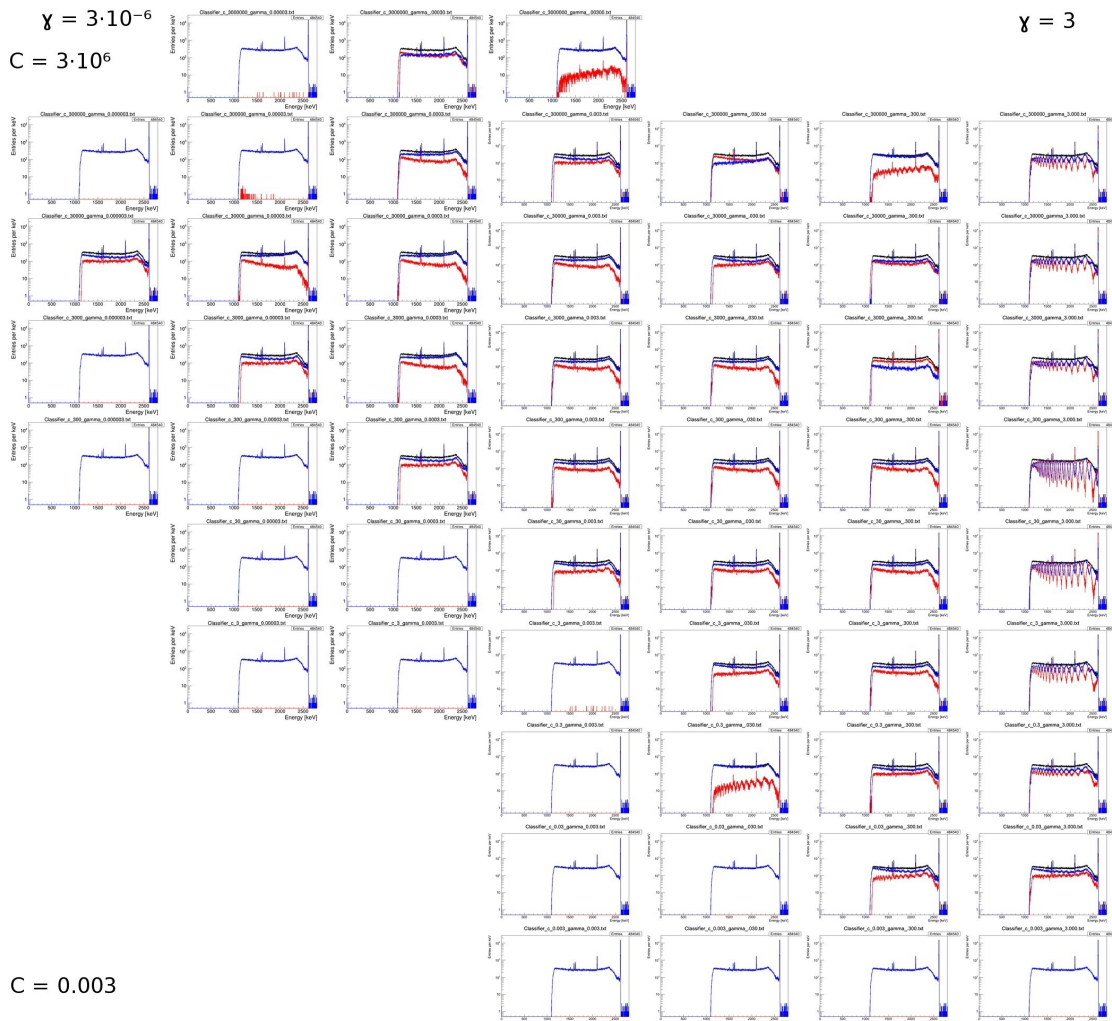


**Figure 5.6:** Overview of spectra obtained with the rough parameter scan. Each diagram shows counts on the y axis and energy on the x axis. Full spectra are shown in black, SSE spectra in red and MSE spectra in blue. The value of the parameter  $\gamma$  is increasing by one order of magnitude each column. The value of  $C$  is decreasing by one order of magnitude each line. For high values of  $\gamma$ , oscillation due to overfitting are observable. Several parameter sets resulted in all events being classified as MSE (no red spectrum visible). The parameter space providing reasonable classification is a closed area surrounded by clearly unphysical spectra. Spectra from the fine scans are not shown (see text).

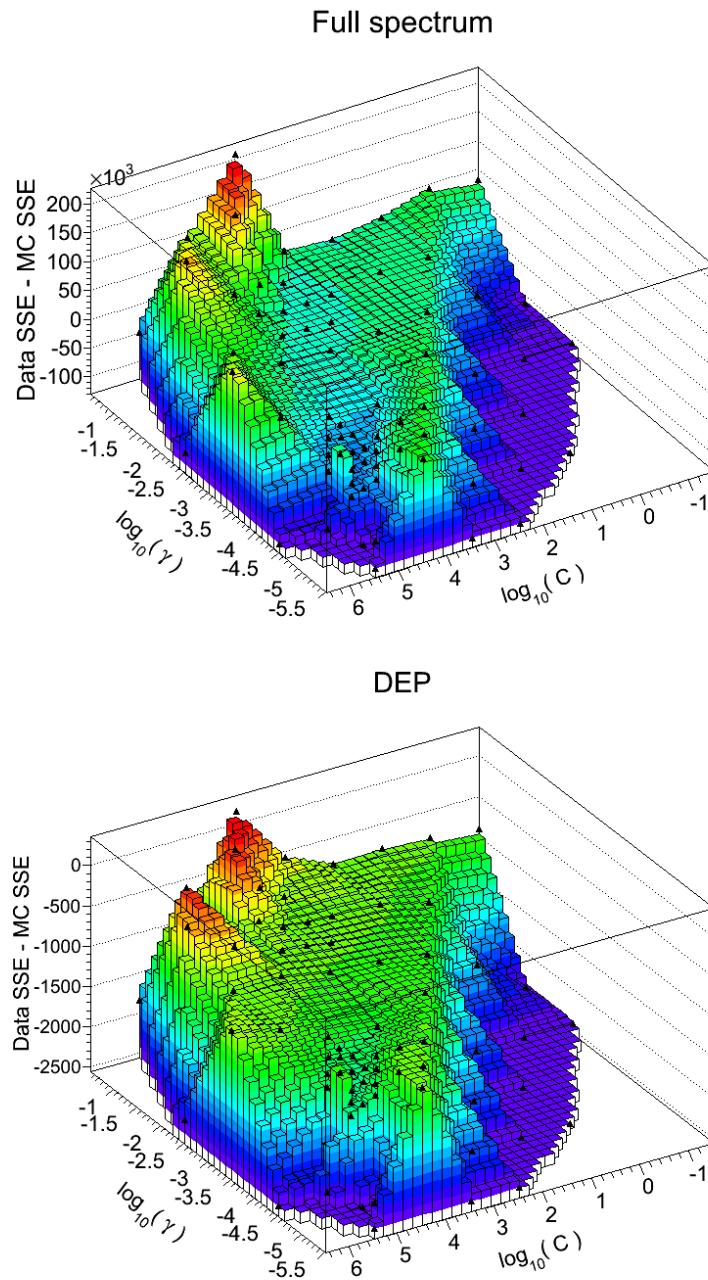


**Figure 5.7:** Difference between SSE spectra obtained from measurement and simulation for different values of  $C$  and  $\gamma$ . The lowest (violet) region in the figure corresponds to no events classified as SSE in the measurement. The black triangles show the computed points. The simulated reference spectrum was obtained by a cut threshold of 0.04 mm. Top: integrated difference in the energy range (1200–2800) keV. Bottom: difference in the DEP ( $1592.5 \pm 3$ ) keV.

a present signal without any visible signature. A false acceptance results in a higher background and thus lower sensitivity. Parameter values close to a drop are therefore considered to be more critical than those close to a rise. The plateau has a minimum in the region of  $\log_{10}(C) = 4.5$  and  $\log_{10}(\gamma) = -4$ . A fine scan was performed around this minimum, with the step size reduced to a factor of  $10^{1/4}$ .

The number of SSEs in the DEP only was additionally compared. The difference spectrum is therefore integrated in the energy range of  $(1592.5 \pm 3)$  keV. This is shown in the bottom plot of Figure 5.7. The shape of the resulting surface is similar to the one for the total spectrum. The number of events in the DEP is however systematically too low in the data. SSE spectra for the maxima in the DEP parameter scan show a similar acceptance for the DEP and FEP. These can hence not be the valid parameter sets. The optimal set is therefore at a location which is low in the upper plot and high in the lower plot. It should also not be close to a drop off. A region fulfilling these criteria is around the parameter pair of  $C = 3000$  and  $\gamma = 0.03$ . This region was therefore scanned with a smaller step size of a factor of  $\sqrt[4]{10}$ . The parameter pair in the centre (in log scale) of this fine scan results in the best trade off between minimum in the difference of the full spectrum and maximum in the difference of the DEP. A larger weight was given to the difference of the full spectrum to possibly reduce the influence of the inhomogeneous distribution of the DEP. The parameter set  $C = 3000$  and  $\gamma = 0.03$  is additionally far from a drop off and was chosen as the optimum. The resulting spectra for the long calibration are shown in the top plot of Figure 5.8. The difference between data and MC simulation is shown in the bottom plot. A good agreement is achieved for the Compton continuum. Too many events are however accepted in the single escape peak of the 2614.5 keV line and above its Compton edge, including the FEP. The number of events in the DEP is too low, as already observed before. The differences are for the full spectrum 26 events, single site 4862 events, multi site -4836 and in the DEP -814 events. The difference of 26 in the full spectrum originates from rounding of the scaling factor.

The classifier of all events in the training dataset is shown in the left plot of Figure 5.9. The right plot shows it for all events in the long calibration. A negative value corresponds to events classified as multi site and a positive value to events classified as single site. The distribution has a clear change in shape at a value of  $\sim -0.4$ , which might have a physical reason. The value  $-0.4$  is thus considered as an alternative cut threshold in the following. The thresholds are illustrated in the right plot of Figure 5.9.

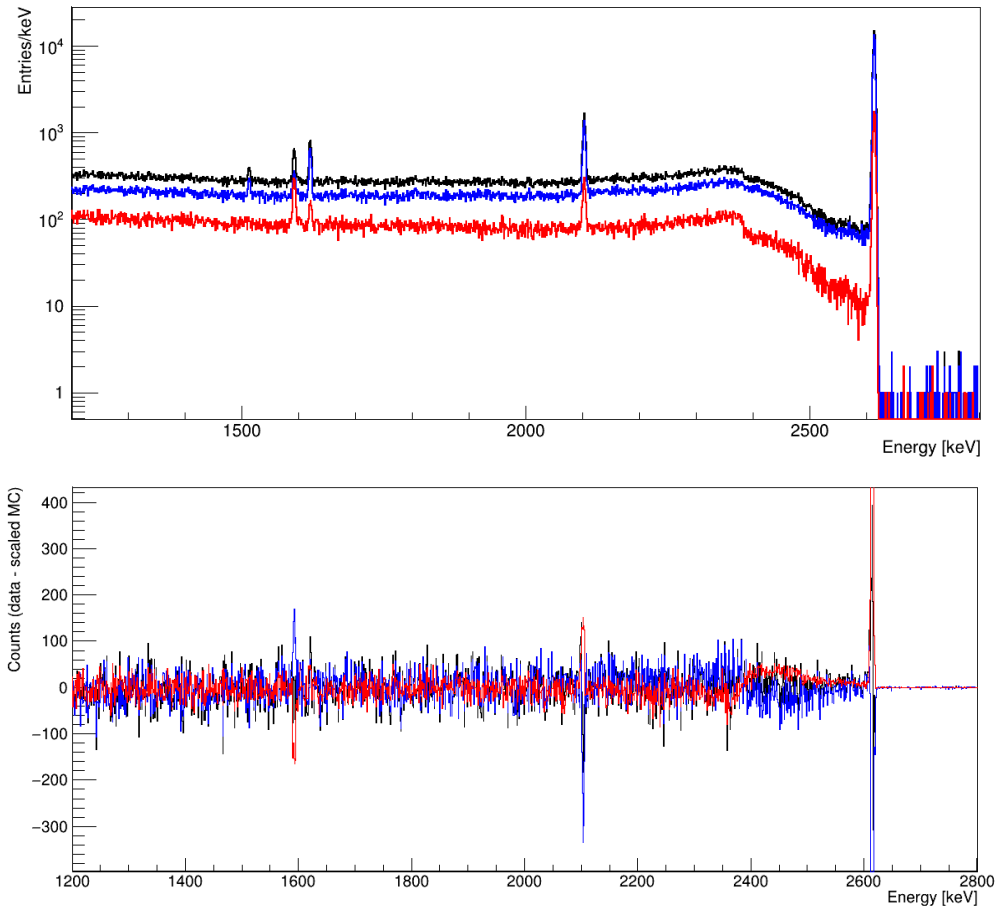


**Figure 5.8:** Comparison of the event classification between measurement and simulation. Top: spectrum of all events in the long calibration measurement (black) and of events classified as single (red) and multi (blue) site. The classification was performed employing the optimal parameter set of  $C = 3000$  and  $\gamma = 0.03$ . Bottom: difference between the measured and the scaled simulated spectra (same colour code). The classification in the simulation is performed based on a threshold of the centre of energy at 0.04 mm.

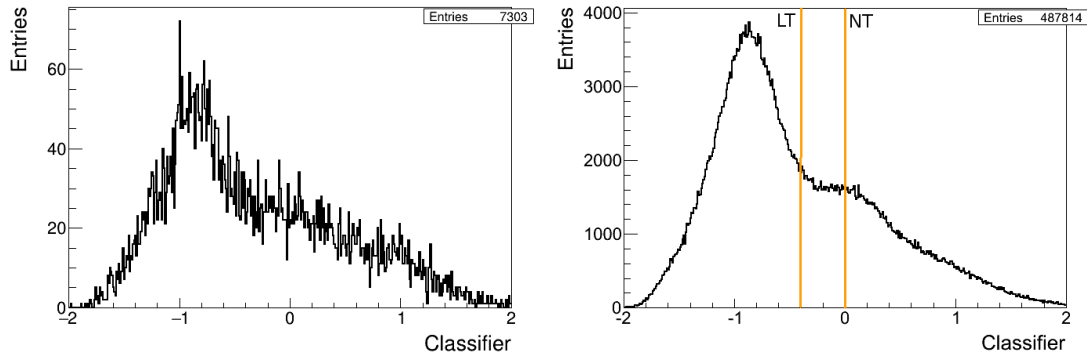


**Figure 5.9:** Classifier as obtained by the SVM for the long calibration measurement. The SVM has been trained employing the 1593 keV DEP and 1621 keV FEP. Values of the parameters correspond to the optimal set of  $C = 3000$  and  $\gamma = 0.03$ . Left: classifier for the DEP and FEP only. Right: classifier for the full spectrum. The normal (NT) and low cut threshold (LT) are illustrated by orange lines.

## 5.4 Application to GERDA Phase I Data

The model obtained from training the SVM on the long calibration measurement can not be applied directly to Phase I data. The reason are different parameter settings in the energy reconstruction algorithm. The Phase I settings result in a larger value of the uncalibrated energy and hence smaller values of the scaled traces (= input to the SVM). The optimal parameter set is nevertheless expected to be the same. It is hence employed to train the SVM on an early calibration measurement of Phase I (calibration 20111219). The obtained model was then applied to this calibration and a calibration shortly before inserting additionally 5 BEGe detectors (calibration 20120630). The resulting spectra are shown in Figure 5.10 in the top plots. Some electronics was changed together with the insertion of the detectors. An application of this model to calibrations acquired later results in a much larger fraction of events being classified as single site. The Phase I data was therefore split into a period before and after the insertion of BEGe detectors. Such a change has also been observed by other PSD methods [60].

Another calibration (20111121) was acquired in the first period before the calibration employed for training. The supply voltage of two other detectors were changed in between these two measurements. The model obtained with the later calibration was also applied to calibration 20111121. The resulting SSE spectrum fits well to the expectations, hence such voltage changes have a small influence on the PSD of the ANG2 detector. The effect of other high voltage changes are thus not investigated separately. A model for the second period was obtained training the SVM on an early calibration of this period (20120723). This model was then

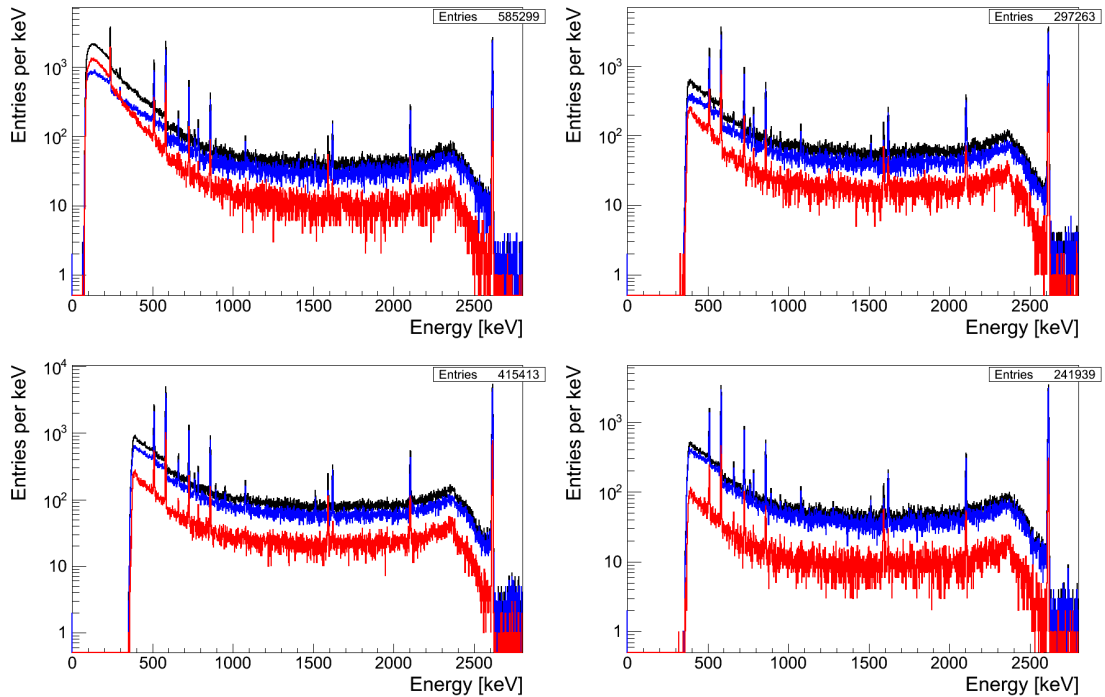


**Figure 5.10:** Classified calibration spectra during Phase I. Full spectrum in black, SSE in red and MSE in blue. All methods for the optimal parameter set of  $C = 3000$  and  $\gamma = 0.03$ . Top left: first calibration after change of parameters in the energy reconstruction algorithm. This calibration was employed to train the SVM for the first period. The SSE spectrum fits well to the expectation. Top right: last calibration in the first period, classified with the model obtained from the first calibration in this period. A significant difference compared to the calibration at the beginning of this period is not visible by eye. Bottom left: first calibration after insertion of BEGe detectors. This calibration was employed to train the SVM for the second period. The SSE spectrum fits well to the expectation. Bottom right: last calibration in the second period, classified with the model obtained from the first calibration in this period. A significant difference compared to the calibration at the beginning of this period is not visible by eye.

applied to a late calibration in this period (20130520). The spectra for these two calibrations are shown in Figure 5.10 in the bottom plots. The resulting spectra fit well to the expectations. A quantitative comparison is provided in Table 5.1 and discussed below in this section. The presented cross checks with three calibrations provide a test of the validity to apply the two obtained models to the physics data of the respective period. The change in shape of the distribution of the classifier at value of  $-0.4$  as discussed in Section 5.3.2 is also observed for the four calibrations shown in Figure 5.10.

The physics data set employed in the following is the same as for the official Phase I results published in [61]. In both cases several cuts were applied to obtain the final data set. These are data quality cuts, a cut of events with an energy deposition in more than one detector, a cut on events in coincidence with a muon tagged by the water Cherenkov or plastic scintillator veto, a cut on pile-up events and a cut of events from an electronic test pulser periodically fed to the preamplifier input. These cuts result in 131038 events remaining in the dataset for the full period of Phase I in the detector ANG2. A cut on coincident decays in the  $^{214}\text{Bi}$  to  $^{214}\text{Po}$  decay chain was additionally applied for the official Phase I results and not in the present work, however it cuts only 5 additional events in this detector.

The physics dataset was split into the same two periods, before and after the insertion of BEGe detectors. The two models obtained from training on calibration data were then applied to classify events from the respective period. The resulting energy spectra are shown in Figure 5.11 in the top left and right plot for the first and second period, respectively. The spectra of the respective event class are similar for the two periods. A difference can be observed in the classification for events near the detector threshold. This is not an issue as the low energy region is not relevant for the search of the neutrinoless double beta decay. The summed spectrum of the full Phase I data from ANG2 is shown in the bottom plot of this figure. All plots in this figure were obtained for a classifier threshold of 0. The total expose of this detector is 3.81 kg.yr.

The physics data spectrum contains several features. The peaks at an energy of 511 keV, 1461 keV and 1525 keV originate from positron annihilation,  $^{40}\text{K}$  and  $^{42}\text{K}$ , respectively. The low energy part is dominated by beta decays from  $^{39}\text{Ar}$ . In the energy range of ( $\sim 520 - -1400$ ) keV it is dominated by the two neutrino double beta decay [59]. The decomposition of the spectrum performed in [59] employs the summed data set of all coaxial detectors. The spectrum shown therein does not contain the first 30 days after insertion of the BEGe detectors because of a higher background rate in that time period. The exact fraction of two neutrino double beta decay events in this energy range can thus not be given for ANG2. It is nevertheless expected to contain more SSE than MSE. The classification as shown in Figure 5.11 is however not as expected.

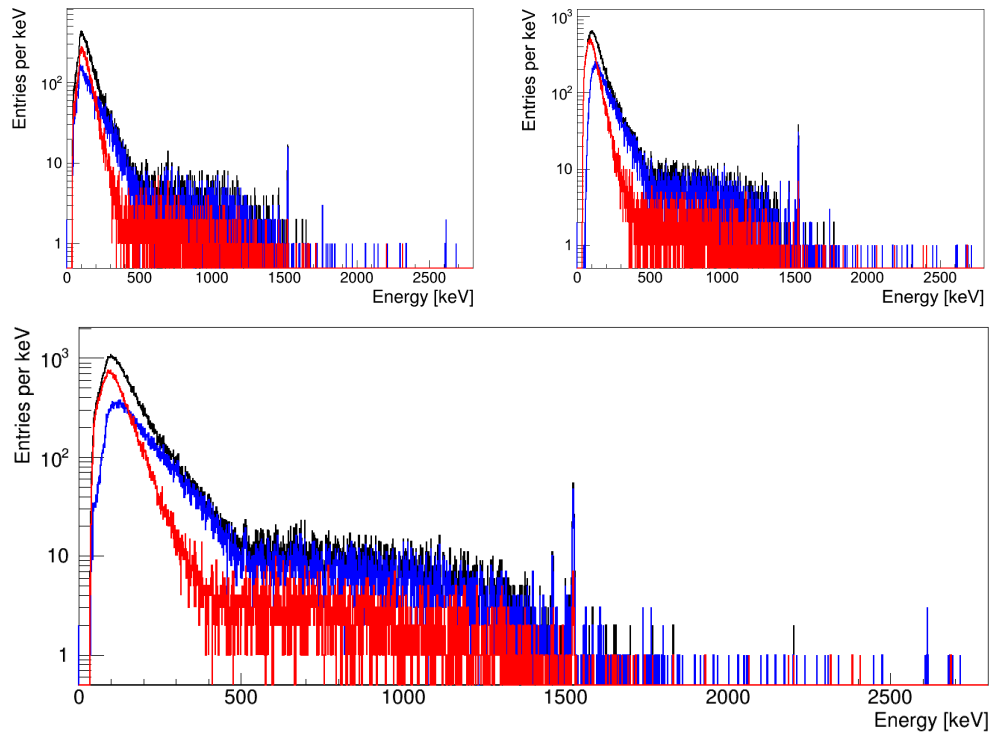


**Figure 5.11:** Energy spectrum acquired by ANG2 during GERDA Phase I (black). The event classification in SSE (red) and MSE (blue) was performed employing the optimal parameter set of  $C = 3000$  and  $\gamma = 0.03$ . The cut threshold on the classifier is 0. Top left: first period. Top right: second period. Bottom: combined spectrum of the complete Phase I.

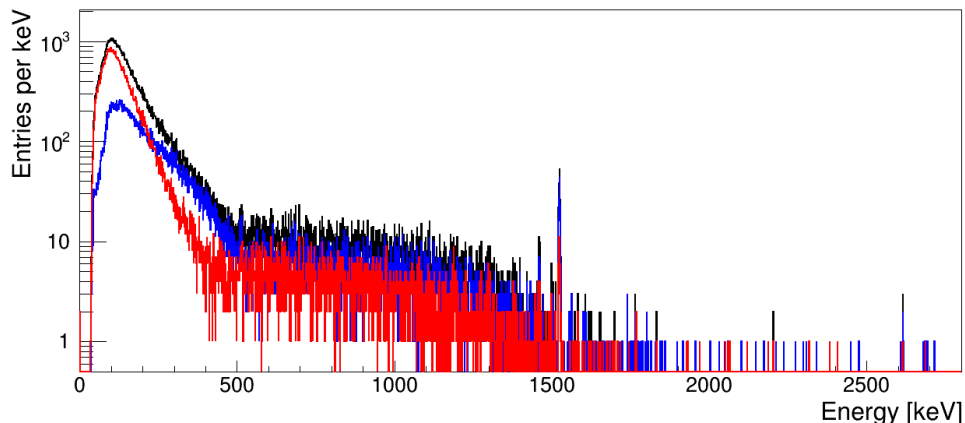


**Figure 5.12:** Energy spectrum acquired by ANG2 during GERDA Phase I (black). The event classification in SSE (red) and MSE (blue) was performed employing the optimal parameter set of  $C = 3000$  and  $\gamma = 0.03$ . The cut threshold on the classifier is  $-0.4$ .

Applying the low cut threshold of  $-0.4$  (discussed in Section 5.3.2) to the classifier of the same dataset results in the energy spectrum shown in Figure 5.12. The acceptance of the two neutrino double beta decay region is increased compared to the normal cut threshold. The number of events classified as multi site is however still larger than the number classified as single site.

Energy regions dominated by the respective event class are selected for a quantitative comparison of the acceptance. The regions are the DEP of  $^{208}\text{Tl}$  at 1592.5 keV, the FEP of  $^{212}\text{Bi}$  at 1620.7 keV, the single escape peak (SEP) of  $^{208}\text{Tl}$  at 2103.5 keV, the high energy part of the two neutrino double beta decay range (1000–1400) keV, the  $^{42}\text{K}$  FEP at 1524.7 keV and the ROI. The latter is approximated by the energy range of  $(2039 \pm 130)$  keV. The low energy part of the two neutrino double beta decay dominated region is not considered as it is more likely affected by electronic noise. The energy window for peaks is the peak energy  $\pm 3$  keV. The acceptances for those regions are listed in Table 5.1 for both classifier cut thresholds and periods. The acceptance was calculated dividing the number of events in the SSE spectrum by the number of events in the full spectrum for the respective energy range. A range of acceptances is provided for calibration measurements. The first value corresponds to the calibration which has been employed for training and the second to the validation calibration at the end of the respective period. The table provides also acceptances obtained from the MC simulation of the long calibration. The number of real SSEs in a given energy range does depend on the source positions relative to the detector. Those were different for the different calibration measurements. The values from the simulation are

CHAPTER 5. PULSE SHAPE DISCRIMINATION FOR SEMI-COAXIAL  
DETECTORS EMPLOYING A SUPPORT VECTOR MACHINE

---

Method	Period calib.	DEP calib .	FEP calib.	SEP calib.	$2\nu\beta\beta$ data	$^{42}\text{K}$ data	ROI data
Class		SSE	MSE	MSE	SSE	MSE	MSE
MC	long	0.63	0.18	0.08			
SVM, NT	long	0.45	0.22	0.20			
	1	0.45 – 0.45	0.15 – 0.19	0.16 – 0.20	0.24	0.08	0/6
SVM, LT	2	0.42 – 0.37	0.17 – 0.11	0.21 – 0.15	0.26	0.15	2/9
	1	0.60 – 0.58	0.25 – 0.30	0.29 – 0.33	0.36	0.18	4/6
ANN, no Compt.	2	0.56 – 0.50	0.27 – 0.19	0.35 – 0.27	0.37	0.22	3/9
	1	0.9		0.33	0.74	0.30	2/4
Likelihood, no Compt.	2	0.9		0.47	0.73	0.4	6/8
	1	0.8		0.47	0.61	0.35	1/3
Asymmetry, no Compt.	2	0.8		0.50	0.57	0.37	4/10
	1	0.69		0.32	0.52	0.28	1/5
	2	0.70		0.40	0.50	0.33	4/6

**Table 5.1:** Fraction of events classified as SSE for different periods, methods and energy regions. All values are provided for the detector ANG2. The respective energy regions are specified in the text. They vary slightly for the different methods. The row “Class” indicates the dominating class of events in the respective energy region. “long” stands for the long calibration, NT and LT for cut thresholds on the classifier of 0 and  $-0.4$  respectively. Values for the artificial neural network (ANN), likelihood method and asymmetry based cut are taken from [60]. For these methods underlying Compton distributions were subtracted for the calculation of acceptance. The ANN does not include the first four weeks after the insertion of the BEGe detectors.

hence valid only for the long calibration and should be considered as an estimate for other calibrations.

The acceptance of the SVM is higher for all SSE samples compared to all MSE enriched samples. This is valid for both calibration and physics data. The SVM is hence capable to distinguish SSE from MSE events. The acceptance of events in the DEP is however significantly higher compared to the two neutrino double beta decay region. The latter contains  $\sim 25\%$  Compton events [59], which are dominantly MSE. The remaining fraction in this energy range is expected to have a SSE content higher than the DEP peak. There is hence a discrepancy between the acceptance of the DEP and the two neutrino double beta decay region. DEP events are more likely to occur in the corners of detectors, which is caused by a higher escape probability for the two 511 keV gamma rays at those locations. Two neutrino double beta decay events are however distributed uniformly inside the

detectors. The observed discrepancy in the acceptance for this two type of events is hence likely caused by an additional volume selection of the SVM. The obtained models thus seem to perform a combination of SSE and volume cut. Applying a lower cut threshold of  $-0.4$  instead of  $0$  to the classifier increases the acceptance for all energy regions. Besides this, the same observations are valid also for the low cut threshold.

The largest statistical uncertainty in the calculations of the acceptances is given by the number of events classified as SSE. Amongst the different energy regions, the  $^{42}\text{K}$  peak has the smallest count rate. Its statistical uncertainty on the number SSEs is in the range of  $(18-41)\%$ . For all other energy regions it is in the range of  $(2.5-9)\%$ . The acceptance changes on average by  $0.042$  for the normal threshold and  $0.065$  for the low threshold between the calibrations employed for training and validation. The changes are larger than the statistical uncertainty and hence, are not caused by statistical fluctuations. Similar variations were observed applying other PSD methods [60] to the same data. The variations are hence likely dominated by the data rather than the analysis methods. The reasons are most likely changing noise conditions and a contribution by changes in the pulse shape due to drifts in the read out electronics. The effect of the latter is expected to be reduced retraining the SVM whenever a change in the electronic read out chain is observed. Those can be detected e.g. by changes in the position of the electronic test pulser. The improvement is expected to be on the order of a few percent.

An estimate of the effect of the SVM PSA on the background index of ANG2 can be calculated employing the number of events in the previously defined ROI. The background index for the GERDA Phase I results was calculated in the energy range  $(1930 - 2190)\text{keV}$  excluding a  $\pm 5\text{keV}$  energy window around  $Q_{\beta\beta}$  ( $2039\text{keV}$ ) and two known background peaks at  $2104\text{keV}$  and  $2119\text{keV}$ . The background peaks were included in the present calculation to reduce the large statistical uncertainty caused by the small number of events in this energy region.  $Q_{\beta\beta}$  was included because of the observed absence of a neutrinoless double beta decay peak [61]. The calculated background index of ANG2 in Phase I is  $(1.5 \pm 0.4) \cdot 10^{-2}\text{cts}/(\text{keV}\cdot\text{kg}\cdot\text{yr})$  before PSA and  $(0.20 \pm 0.14) \cdot 10^{-2}\text{cts}/(\text{keV}\cdot\text{kg}\cdot\text{yr})$  or  $(0.71 \pm 0.27) \cdot 10^{-2}\text{cts}/(\text{keV}\cdot\text{kg}\cdot\text{yr})$  after application of the SVM with the normal and low threshold respectively. The normal threshold did hence reduce the BI of this detector by a factor of  $7.5 \pm 4.9$  and the low threshold by a factor of  $2.1 \pm 0.6$ . The uncertainties are statistical only. The uncertainties on the number of events in the ROI before and after application of the PSD are not independent. This must be considered for the calculation of the uncertainties on the reduction factor. The statistical uncertainties on the number of events classified as single site and the number classified as multi site were employed instead. The number of events before the cut is given by the sum of SSE and MSE.

### 5.4.1 Comparison to Other Pulse Shape Discrimination Methods

Acceptances for other PSD methods [60] which were applied to the Phase I data are also listed in Table 5.1. The calculations of the acceptances were performed in a slightly different way for those methods. Events from the Compton continuum are subtracted in the respective energy regions before the calculation. This is performed both for the SSE spectra and full spectra. The effect on the acceptances is qualitatively discussed in the following. Comparing the SSE and MSE spectra obtained from MC (Figure 5.5) one can conclude the following. The DEP and two neutrino double beta decay region do contain more SSE than the Compton continuum, while FEPs do contain more MSE than the Compton continuum. This is valid for all energy ranges employed in Table 5.1. The acceptances listed for the other methods for SSE samples would hence be smaller if the Compton continuum would be included, while the acceptances for MSE samples would be larger. The exact value depends on the Compton content as well as on the energy range.

This knowledge is sufficient to derive the following statements from Table 5.1. All other methods do accept significantly more events in the MSE regions compared to the SVM, including the ROI. However, they do also have a higher acceptance for SSEs at  $Q_{\beta\beta}$ . The acceptance for two neutrino double beta decay events by the other methods is also reduced compared to expectations from the DEP. This suggests a combined selection of SSEs and volume also for those methods. However, the volume effect for SVM seems larger than for the other methods. The presence of such an effect is also confirmed in [59] for the pulse asymmetry based method and as a small effect also for the ANN. There is no statement made for the likelihood method. Amongst all methods, the ANN seems to have the smallest volume effect. It is also the primary PSD method employed for the GERDA Phase I results. A volume selection was also reported by an earlier work performing a different ANN pulse shape analysis [147], which is not the ANN method applied to the GERDA Phase I data. The volume selection was therein found employing simulated pulse shapes.

## 5.5 Conclusions and Outlook

A pulse shape discrimination method to distinguish single site events (SSEs) from multi site events (MSEs) has been developed employing the semi-coaxial detector ANG2. The method is a multivariate analysis performed by a Support Vector Machine (SVM). A Gaussian kernel function with the free parameter  $\gamma$  was chosen. The second parameter  $C$  is related to the penalty for misclassified events during training. The parameter space has been scanned applying the SVM to a  $^{228}\text{Th}$

calibration measurement. The optimal parameter set was determined comparing the classified calibration spectrum to simulation. It was found to be  $C = 3000$  and  $\gamma = 0.03$  and was employed to train the SVM on calibration data of GERDA Phase I. The obtained models were applied to the physics data of Phase I. The sensitivity to SSEs by the SVM was confirmed comparing the acceptances of events in specific energy ranges. It was however discovered that the SVM is performing a combination of SSE and detector volume selection. A similar effect has also been observed for other PSD methods [59], however on a smaller level. It is most likely driven by an inhomogeneous distribution of the SSE sample employed for training. The SVM can be employed as a cross check for other PSD methods in its current state. For an application as primary PSD method one has to reduce the volume selection first. There are several potential ways to perform this task.

One way would be, employing training datasets in which SSEs and MSEs have a similar geometrical distribution. Such a dataset is however only available by the two neutrino double beta decay events. A cross check would have to be performed employing the inhomogeneously distributed DEP from calibration data. Acquiring SSEs e.g. by performing a single Compton scattering experiment outside of GERDA would result in different readout electronics conditions. The differences of the pulse shapes in such a dataset compared to GERDA would result in a model not applicable to GERDA data.

Another possibility would be to employ a different set of input variables. This set would have to contain less information on the event location but still sufficient information about the event topology. It is unclear if such a data set can be found. A cleaner SSE set could be obtained selecting events with a 511 keV  $\gamma$  in coincidence in another detector. This would require a much larger initial dataset, which might be available combining all calibration measurements. However, it is not clear if this would reduce the volume cut. If these studies yield an improvement, the acceptance at the Q-value of the neutrinoless double beta decay would have to be studied.

## Chapter 6

# Electronic Noise Reduction Employing Wavelet Transformations

BEGe-type germanium detectors possess significantly higher pulse discrimination capabilities than semi-coaxial detectors. A single-variable-based cut method is sufficient to suppress most background-like events. The method is explained in Section 6.1. In Phase II this detector type will provide  $\sim 20$  kg of in total  $\sim 35$  kg enriched detector mass. This type is also a very likely candidate for future germanium-based neutrinoless double beta decay experiments. The reason for the enhanced PSD capabilities have been described in Section 2.3. The rejection efficiency of the BEGe PSD depends on the level of electronic noise. A digital filter was therefore implemented to reduce the noise of recorded germanium pulses. The filter employs one dimensional wavelet transformations.

### 6.1 Pulse Shape Discrimination Principle with BEGe-Type Detectors

The pulse shape discrimination with BEGe-type detectors is based on the amplitude of the current pulse  $A$  normalised by the energy  $E$ . The latter corresponds to the amplitude of the charge pulse. The ratio  $A/E$  is constant for events with a single energy deposition in the detector bulk. The charge and current pulse of such an event are illustrated in the top left plot of Figure 6.1. Events with an energy deposition at several locations in the detector possess a pulse shape corresponding to the superposition of SSE pulses. The pulse of such a MSE is illustrated in the top right plot. It possesses a smaller  $A/E$  value than SSEs. Events occurring on the surface of the p+ readout contact, such as surface alpha contaminations, result

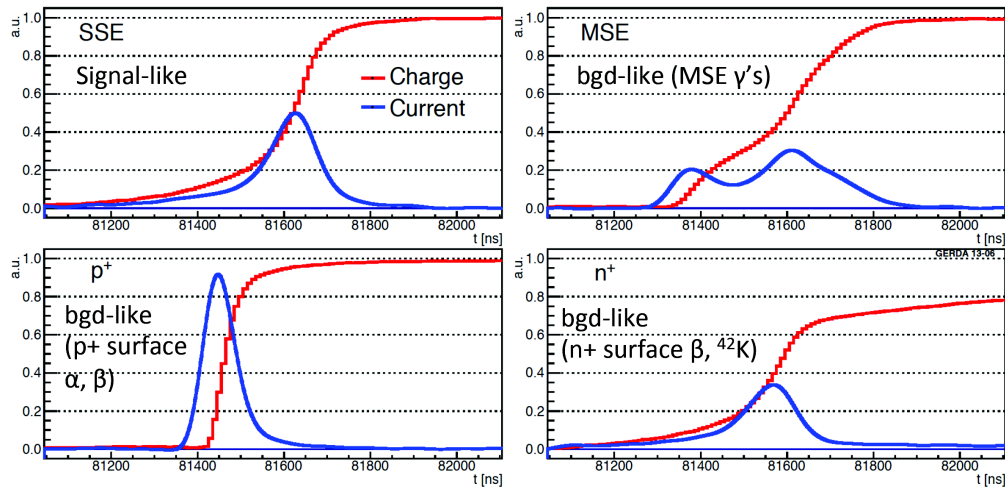


**Figure 6.1:** Illustration of the principle of the PSD with BEGe detectors. Top left: SSE in the detector bulk. The amplitude of the current pulse  $A$  has a fixed value relative to the amplitude of the charge pulse  $E$ . Top right: event with an energy deposition at two locations.  $A$  is reduced relative to  $E$ . Bottom left: energy deposition close to the p+ readout contact. These event have a high  $A/E$ . Bottom right: energy deposition close to the outer n+ high voltage electrode. These events have a reduced  $A/E$ . Figure from [60].

in a step rise in the charge pulse due to the large electric field in this region. The ratio of  $A/E$  is hence larger than for SSEs. A pulse of such an event is illustrated in the bottom left plot of Figure 6.1. Events with an energy deposition at the outer n+ high voltage contact, like beta decays of  $^{42}\text{K}$ , result in a current pulse with a small amplitude. This is caused by the low electric field strength in those regions. Further details about PSD in BEGe-type detectors are available in [60, 63, 148–151].

The  $A/E$  parameter is calculated by a module of the GERDA analysis software GELATIO [144]. For a  $^{228}\text{Th}$  calibration measurement it is shown in Figure 6.2 as function of the energy. The measurement was taken in a vacuum cryostat and not in GERDA. No noise filtering was applied before the calculation. Vertical bands are gamma peaks. The horizontal band at an  $A/E$  value of  $\sim 0.019$  corresponds to the SSE band. The sensitivity of the  $A/E$  parameter to SSEs is demonstrated by the DEP at 1593 keV. It has a negligible fraction of events below the SSE band. The tail of this peak towards higher energies and lower  $A/E$  values originates from Compton scattered 511 keV gammas. The mean  $A/E$  value of this SSE band is slightly oscillating with the energy. The amplitude of this oscillation is on the order of 1% of its mean value.

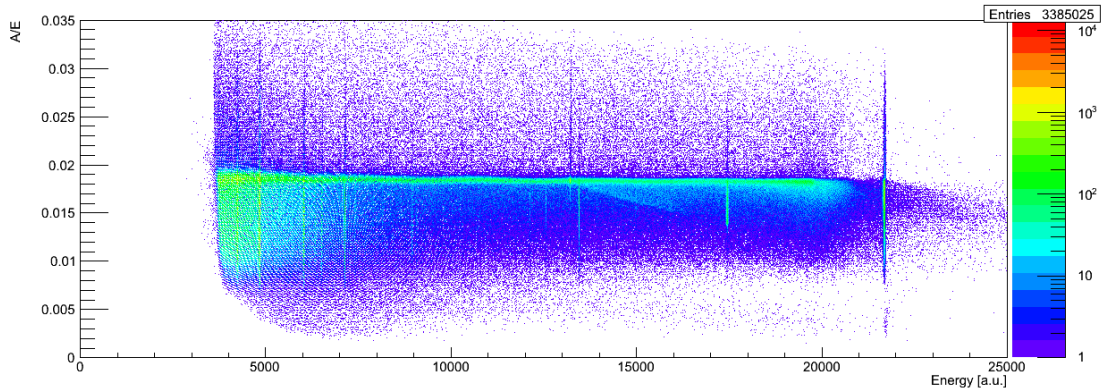


**Figure 6.2:** The A/E pulse shape discrimination parameter as function of the energy for a  $^{228}\text{Th}$  calibration measurement. Vertical lines are gamma peaks. The band at an A/E value of  $\sim 0.019$  corresponds to SSE. Events above this band originate from the p+ readout contact, below this band from MSEs and n+ surface events. No denoising was applied to produce this plot.

## 6.2 Introduction to Wavelet Transformations

A wavelet transformation is a multi resolution decomposition. In the work at hand, it is applied to traces from germanium detectors. This decomposition is performed by the convolution of a wavelet and a scaling function and with the waveform. The respective function is moved along the trace on order to obtain one transformed trace in each case, which contains the local amplitude of the wavelet or scaling function, respectively. The former selects the high frequency component of the original trace and the latter the low frequency component. In case of discrete (digitised) signals, the wavelet and scaling functions are replaced by discrete values called wavelet and scaling coefficients. The number of coefficients (support) depends on the employed wavelet. One wavelet transform coefficient is then calculated by the sum of the respective trace samples multiplied by the wavelet coefficients. The next wavelet transform coefficient in time is calculated moving the wavelet by two samples. This is continued  $n/2$  times, with  $n$  the number of samples in the trace. The support typically exceeds the end of the waveform for the last samples. The waveform must thus be continued e.g. by periodisation. This means that the beginning of the trace gets attached to its end. The same procedure is performed to calculate the scaling (transform) coefficients. Note the similar naming of the scaling coefficients describing the scaling functions and the scaling (transform) coefficients describing the low frequencies content of the original trace. The result are two sets of coefficients, each with half the length of the original trace, which is sufficient to fully describe the original trace. The

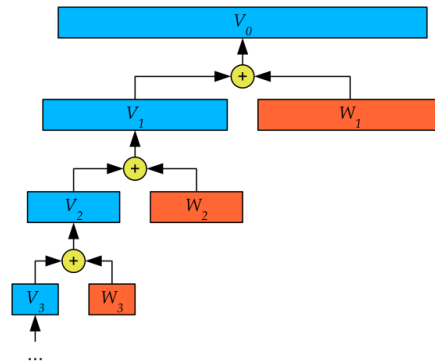


**Figure 6.3:** Illustration of the decomposition of a waveform  $V_0$  into wavelet coefficients. Figure from [152].

set of scaling coefficients is then decomposed identically on the so-called next scale. The decomposition is repeated until one scaling coefficient is left. Together with the sets of wavelet coefficients it forms a complete description of the original waveform. Such a decomposition is depicted in Figure 6.3.

The set of wavelet coefficients of a scale (decomposition level) corresponds to the information of the original trace within a specific frequency range. An advantage over the Fourier transformation is the additional time information. A cut on the sets of wavelet coefficients does correspond to a time-resolved frequency cut. This is important if the frequency range of noise is potentially overlapping with the frequency range of the signal, but might be shifted in time. Further information about wavelet transformations can be found in [153, 154].

The type of wavelets employed in this Chapter are called Daubechies wavelets. These form an orthogonal basis for square integrable functions [155], i.e. they can fully describe any digitised signal. Four different scaling and wavelet functions of this class of wavelets are shown in Figure 6.4.

### 6.3 Implementation into the GERDA Analysis Software

Two modules were written for the GERDA analysis software GELATIO to implement the wavelet-based denoising. The first module takes a waveform as input and provides the transformed waveform as output. It employs the MGDO [157] library to perform the transformation. The continuation of the signal is realised by periodisation. An example of a decomposed waveform of an event in the GERDA physics data of Phase I is shown in Figure 6.5. A Daubechies 6 wavelet was employed for the decomposition. The top left plot corresponds to the first scale or

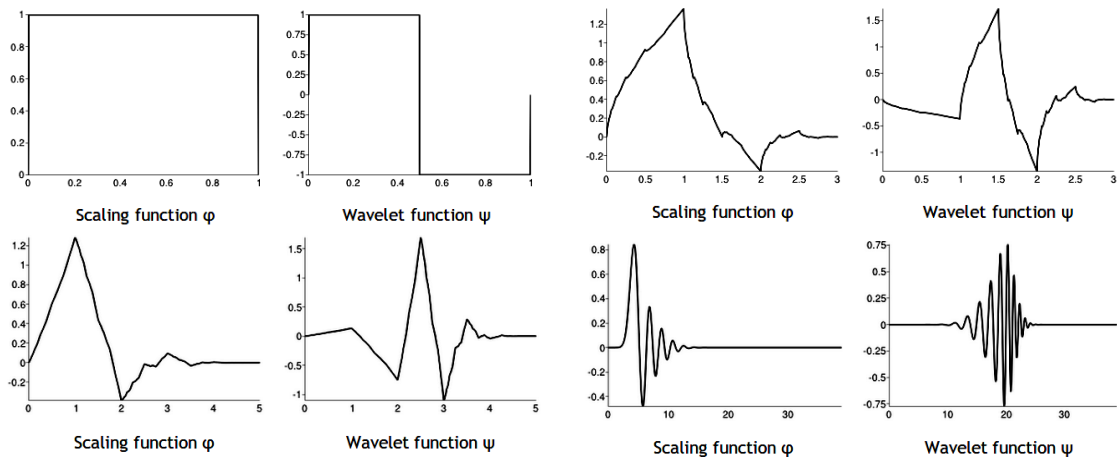


**Figure 6.4:** Different scaling and wavelet functions. Top left: Daubechies 2. Top right: Daubechies 4. Bottom left: Daubechies 6. Bottom right: Daubechies 20. Plots are from [156] and have been optically modified.

iteration (highest frequency range), the bottom right- to the last wavelet and the last scaling coefficient. These are valid for the full time window each and are shown within one trace for practical reasons only. The actual event signal in the centre of each set of wavelet coefficients is clearly visible. The signal-to-noise ratio is clearly increasing with the scale. The first scale is almost completely dominated by noise. The large coefficients at the end of the trace are caused by the periodisation of the traces, which results in a sharp step. These coefficients are off scale in the first four plots.

A second GELATIO module was written to perform the actual denoising. It takes as the input a transformed waveform and provides the denoised waveform as the output. Advanced cutting options were implemented to perform this task. The cuts are applied to the transformed waveform which is then transformed back to a regular waveform. The back transformation is utilising the MGDO library.

The cut is applied to the transformed wavelet coefficients based on their value. Two options are available for the height of the cut threshold. Either a fixed value provided by the user or an event-by-event calculation. The former case was only implemented to allow an application to traces with insufficient signal-free regions. In the latter case, the module calculates the mean and standard deviation ( $\sigma$ ) of noise individually for each scale. An iterative algorithm has been implemented to automatically exclude signals from this calculation, without requiring to set time ranges. It is realised by recalculating the mean and  $\sigma$ , excluding samples which deviate more than a certain, settable number of  $\sigma$  from the mean. The calculation of the mean and  $\sigma$  is then repeated a third time employing the mean and  $\sigma$  of

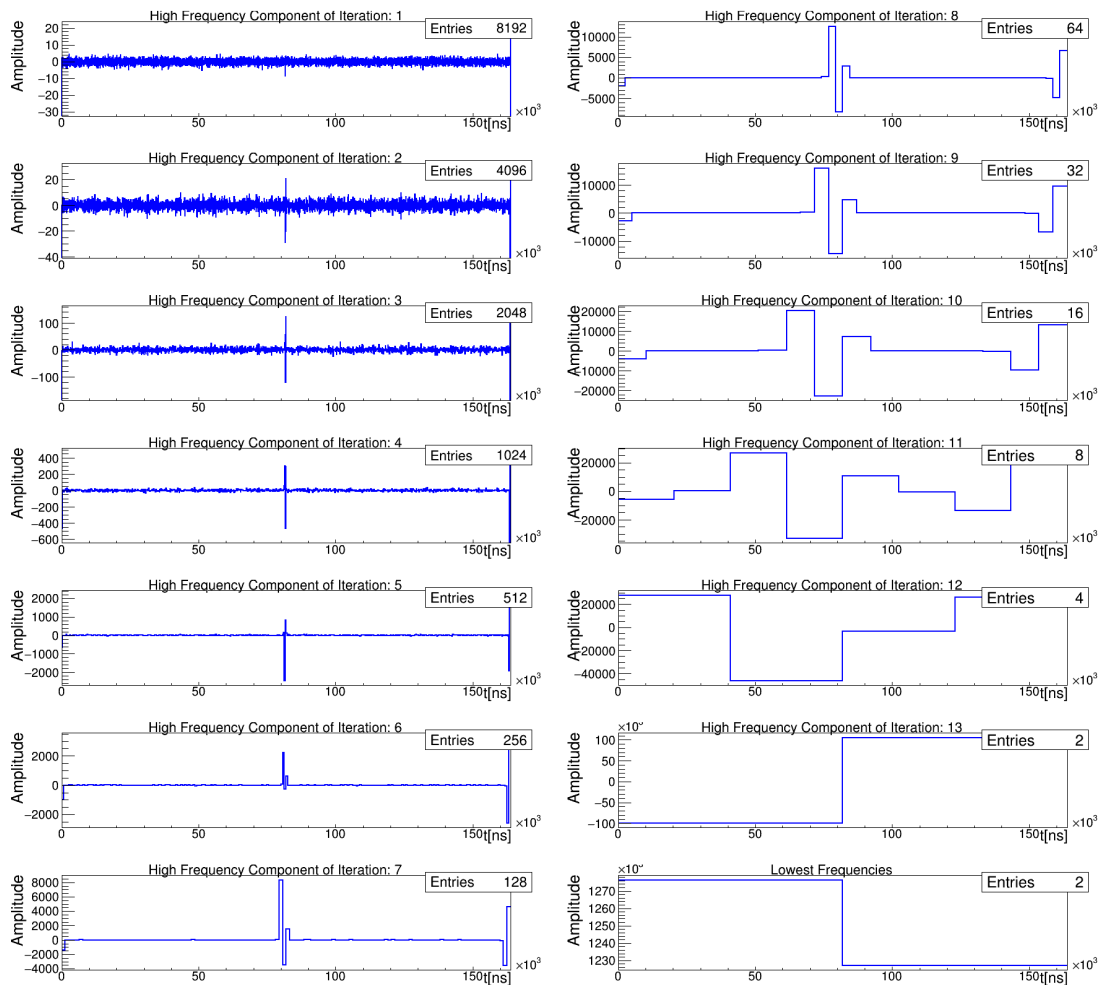


**Figure 6.5:** Example of a transformed (decomposed) waveform employing Daubechies 6 wavelets. The last sample(s) for the four highest frequency components are off scale. Those plots were zoomed in order to show the presence of the signal.

the second iteration for the exclusion. The default value of  $1.5 \sigma$  is employed for all cases presented in this Chapter. This value was found comparing the rejected samples in the transformed waveform with the expectation by eye. The algorithm is tailored to keep the influence of signals small and not to accurately calculate the actual standard deviation of the noise. The last calculated mean and  $\sigma$  are employed for the denoising cut threshold. This cut is applied to all samples which deviate more than a number of  $\sigma$  from the mean are cut. This number of  $\sigma$  can be chosen independently from the number of  $\sigma$  for the calculation of the noise level.

The cut can be applied employing either a soft or a smooth threshold. In the former case, wavelet coefficients below threshold are set to 0 while coefficients above the threshold get subtracted by the threshold. Subtraction of the threshold results in a softer transition from the cut to the remained samples. It does however result in a larger influence on signals compared to no subtraction. If a smooth threshold is selected, the wavelet coefficients after the cut  $c_{cut}$  are calculated from the original coefficients  $c_{orig}$  in the following way:

$$c_{cut} = c_{orig} \cdot \operatorname{erf} \left( c_{orig} / (t \cdot \sqrt{2}) \right), \quad (6.1)$$

where  $\operatorname{erf}()$  stands for the (Gaussian) error function and  $t$  for the value of the threshold. This results in a more smooth transition between strongly cutting low values and not cutting high values. It does not change the value of large coefficients and hence has less influence on the signal than the soft threshold. For both types of cutting it is possible to select the number of scales (frequency range) to cut on.

An additional option is to select a scale-dependent reduction of the cut threshold. This is realised introducing the “level dependence” parameter  $l$ . The threshold  $t(s)_{appl}$  to be applied is calculated dividing the threshold for each scale  $t(s)$  by the scale  $s$  to the power of the level dependence:

$$t(s)_{appl} = \frac{t(s)}{s^l}. \quad (6.2)$$

The threshold for the highest frequency range does hence get divided by  $1^l = 1$ , the second highest by  $2^l$  and so on. Choosing  $l = 0$  is identical to no scale-dependent reduction.

Summarising, the following options are available: the type of Daubechies wavelet, a fixed threshold or a threshold relative to the noise level in the respective event, a soft threshold or a smooth threshold, a selection of the number of scales to cut on and a parameter to yield a scale-dependent reduction of the threshold. The two described modules have been approved and were integrated into the standard version of the official GERDA analysis software GELATIO. The wavelet transformation was implemented in a separate module in order to provide more flexibility. This opens the possibility to employ the transformed waveform by other modules, possibly developed in the future.

## 6.4 Demonstration of the Effects of Different Cutting Options

The effect of different options is shown in Figure 6.6 for the same event as in Figure 6.5. An event-by-event calculated threshold is employed in all cases. For (a), denoising has been performed employing Daubechies 6 wavelets cutting with a soft threshold of  $10\sigma$  on the 7 highest frequencies. This yields a good description of the waveform and a significant noise reduction. For each of the three other sets of plots only one option is chosen differently compared to (a). (b) shows the effect when setting the level dependence to 0. Cutting on 10 scales instead of 7 results in the plot (c). Employing a Daubechies 2, instead of a Daubechies 6 wavelet results in (d). The latter has an unsteady description of the exponential decay of the charge signal.

These demonstrations show that each option is required to obtain a good description of the signal, while efficiently removing noise. They also demonstrate that each types of wavelet is differently suitable to describe certain features, such as the exponential decay.

## 6.5 Application to the Pulse Shape Discrimination with BEGe-Type Detectors

The effect of electronic noise on the resolution of A/E is dominated by the resolution of A. Noise reduction is hence applied to the trace before calculation of A. The rising edge a germanium (charge) pulse contains the full information about the event. It has a width of approximately 600 ns. Neighbouring samples in the original waveform have a time difference of 10 ns. This time information is contained in the wavelet transform coefficients of the first scale. The seventh scale contains the information of samples with a distance of  $10\text{ ns} \cdot 2^6 = 640\text{ ns}$ . Noise on this time scale is not expected to have an influence on the A/E parameter. Cuts were therefore applied to the first 6 scales (1–6).

The improvement of denoising by wavelets can be quantified employing calibration measurements. In particular the DEP at 1593 keV as SSE proxy and the FEP of  $^{212}\text{Bi}$  at 1621 keV as MSE proxy (see also Section 5.2). The peak counts are determined in an energy interval of  $\pm 2.5\sigma$  around the peak energy, with  $\sigma$  the standard deviation of the respective peak. The Compton continuum is statistically subtracted in all cases.

GERDA data is acquired with a sampling rate of 10 ns/sample. For physics data these traces have a length of 16384 samples. In calibration measurements, a trace with only 400 samples is stored at this rate. A full length trace (same

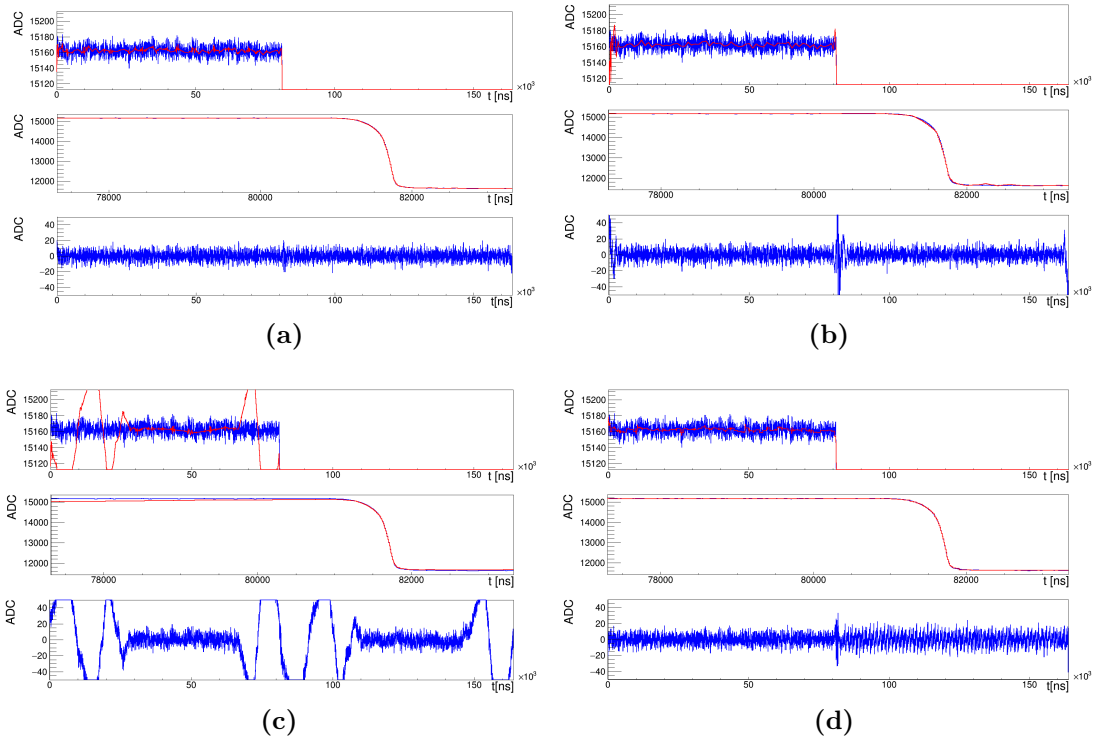


**Figure 6.6:** Effect of four different denoising options demonstrated by an application to the same waveform in all four cases. Three plots are shown for each option. A zoom into the baseline, a zoom into the signal step and the difference between the original and denoised waveform. The denoised waveform is superimposed in red. A soft threshold calculated event-by-event is employed in all four cases. (a): Daubechies 6 wavelet with a cut threshold of  $10\sigma$  on the 7 highest frequency ranges and a level dependence of 1. (b): Daubechies 6 wavelet with a cut threshold of  $10\sigma$  on the 7 highest frequency ranges and a level dependence of 0. (c): Daubechies 6 wavelet with a cut threshold of  $10\sigma$  on the 10 highest frequency ranges and a level dependence of 1. (d): Daubechies 2 wavelet with a cut threshold of  $10\sigma$  on the 7 highest frequency ranges and a level dependence of 1.

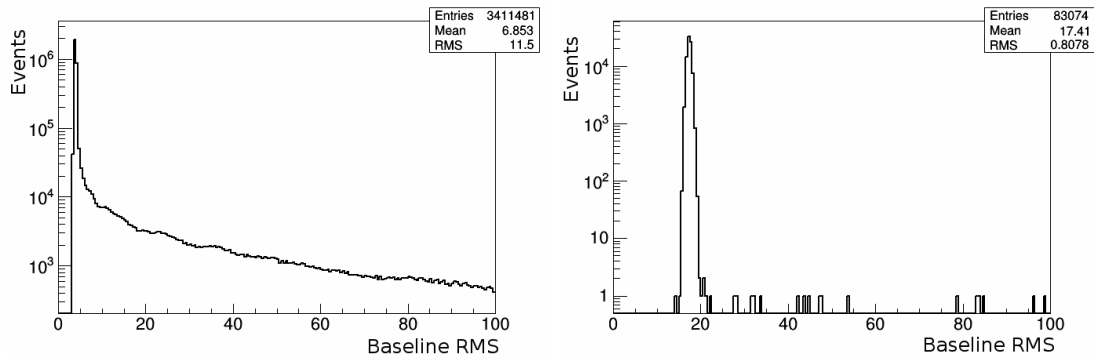


**Figure 6.7:** Standard deviation of the baseline. Left: for the calibration taken in the vacuum cryostat. The tail towards larger values originates from pile-up events. Right: the noise level in GERDA is significantly higher.

length in time) is stored at a reduced rate of 40 ns/sample. The baseline in the high frequency calibration trace is too short to determine the noise  $\sigma$  for the first six scales. Visual inspection of denoised traces show that they do not properly describe the signals. A specific calibration measurement in a vacuum cryostat was therefore performed with a trace length of 4096 samples and a sampling rate of 10 ns/sample. This length is sufficient to perform an event-based noise level calculation. A calibration in GERDA with long high frequency traces is planned to be taken in Phase II.

The standard deviation of the (untransformed) baseline in this measurement and in a GERDA calibration measurement are shown in Figure 6.7 on the left and right, respectively. The long tail towards larger values in the left plot is caused by pile up events. The most probable value of the noise distribution is at  $\sim 4$  ADC counts in the vacuum cryostat and  $\sim 17$  ADC counts in GERDA data. The margin of improvement is hence much larger for GERDA data compared to the data acquired in the vacuum cryostat, which should be considered for the interpretation of the following results.

Many of the analysis modules in GELATIO require to set time ranges. These have to be adjusted in order to apply the standard analysis procedure to the calibration taken in the vacuum cryostat. The A/E spectrum obtained this way, without previous moving window average was shown in Figure 6.2. Small oscillations of A/E as a function of energy can be observed therein. The amplitude is on the order of 1%. The oscillations are probably caused by an energy dependence of waveform position. It can be removed applying a moving window average before calculating A.

Denoising the waveform beforehand with Daubechies 6 wavelets, a soft threshold at  $10 \sigma$  on the first 6 scales and a level dependence of 0.9 results in the A/E

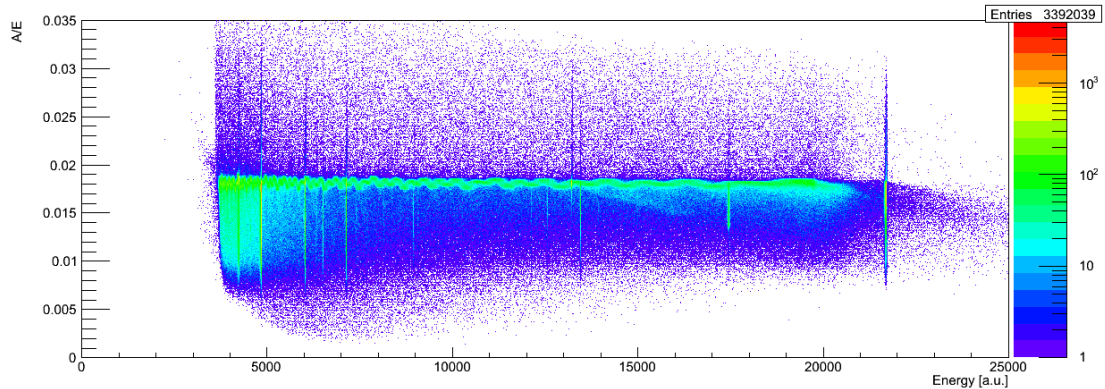


**Figure 6.8:** A/E as a function of energy employing Daubechies 6 wavelets for denoising. Applied was a soft threshold at  $10 \sigma$  on the first 6 scales and a level dependence of 0.9.

spectrum shown in Figure 6.8. Here the oscillations are much larger and increase further when applying stronger cuts. Applying a smooth threshold instead of a soft threshold reduces the oscillations. The result is shown in Figure 6.9. All other cut parameters are identical to Figure 6.8. The smooth threshold was thus employed for the following optimisation. Applying the cut to 5 instead of 6 scales does not yield an improvement. Cutting on 6 scales is therefore kept as standard.

Daubechies 2, 4, 6, 8, 10 and 20 were then employed to perform a scan of different values of the threshold and level dependence. All parameter sets which resulted in oscillations larger than 1% are rejected. Amongst the scanned wavelet types, Daubechies 20 and 2 tend to show the smallest oscillations. A possible reason why Daubechies 2 wavelets perform better could be the similarity in the shape (step function) to the underlying charge deposition. For Daubechies 20 wavelets this could be their similarity to noise pulses.

The acceptance of the 1621 keV FEP taken as a measure for the improvement achieved by the denoising. The acceptance in this peak is calculated for a cut on the A/E parameter resulting in an acceptance of 90% of the events in the DEP. The A/E value has to be corrected for a small energy dependence [148, 151] beforehand. The correction is performed by a fit with a linear function. The calculations of the acceptance and correction of the energy dependence was performed by a script written in the framework of the PhD thesis of Hen-Ye Liao [158].

The FEP acceptance without prior denoising is 12.1% for the calibration in the vacuum cryostat. Denoising with Daubechies 4, 6, 8 and 10 wavelets resulted in a higher acceptance (worse rejection of MSEs). This can be caused by two reasons. Cutting on wavelet transform coefficients obtained with those wavelets do either

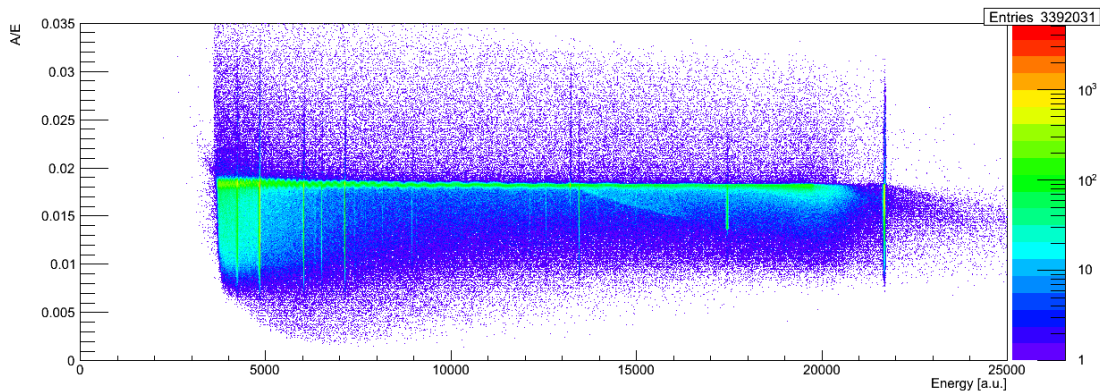


**Figure 6.9:** A/E as a function of energy employing Daubechies 6 wavelets for denoising. Applied was a smooth threshold of  $10 \sigma$  on the first 6 scales and a level dependence of 0.9.

remove relevant features or introduce disturbing features. Employing Daubechies 2 wavelets does not cause any difference in the acceptance. The reason might be that they are not similar to noise signals and hence not sensitive to those.

The MSE acceptance for the scanned parameter range with Daubechies 20 wavelets is shown in Figure 6.10. The lowest acceptance of 11.6% was observed for a cut threshold of  $15 \sigma$  in a range of the level dependence of 7–12. This is an improvement of 4% compared to the acceptance without denoising. Remember that the improvement is expected to be larger for GERDA data, which has a higher noise level. The acceptance is almost constant for different parameter values in this region. This is pointing to fact that stable results are obtained for the chosen parameter values. The white region in Figure 6.10 corresponds to a parameter range resulting in oscillations of A/E with an amplitude larger than 1%.

The best result was hence obtained employing Daubechies 20 wavelets. A cut has been applied to the first 6 scales with a smooth threshold of  $15 \sigma$  and a level dependence of  $\sim 10$ . The result is stable to small variations in the parameter values. The A/E as function of energy calculated employing such a denoising is shown in Figure 6.11.

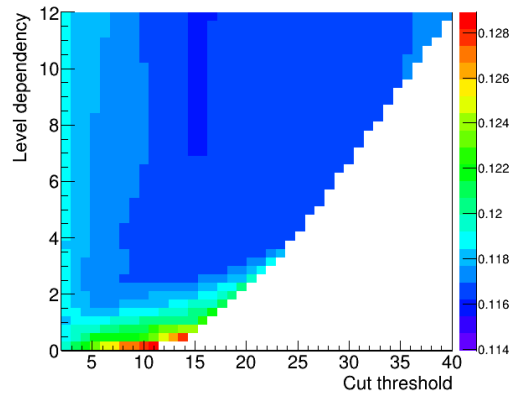


**Figure 6.10:** Acceptance of events in the 1621 keV FEP peak after denoising with Daubechies 20 wavelets for different cut thresholds and values of the level dependence. A smooth threshold was applied to the first 6 scales in all cases.

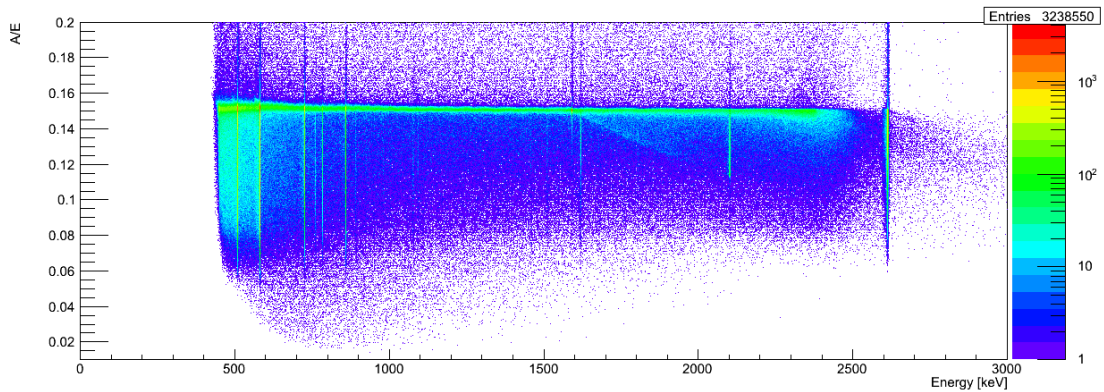


**Figure 6.11:** A/E as function of energy after denoising with the optimal parameter combination. The decomposition was performed employing a Daubechies 20 wavelet. A cut threshold of  $15\sigma$  was applied to the first 6 scales with a level dependence of 7 employing a smooth threshold.

## 6.6 Conclusions and Outlook

Two new modules have been implemented in the official release of the GERDA analysis software GELATIO. One module is performing a wavelet transformation employing Daubechies wavelets. It is utilising the MGDO library to perform this task. The second module filters electronic noise by the application of cuts to the transformed waveform. An advanced set of options was implemented to perform this task. The effect of different options and parameter values has been demonstrated.

The denoising has been applied to a  $^{228}\text{Th}$  calibration measurement acquired with a BEGe detector in a vacuum cryostat. This calibration was employed instead of a GERDA calibration because of an insufficient trace length in the latter case. The MSE acceptance improved therein from 12.1% to 11.6%. This improvement was achieved employing Daubechies 20 wavelets, a smooth cut threshold of  $15\sigma$  applied to the first 6 scales  $s$  with a scale dependent reduction of the threshold of  $1/s^7$ . The electronic noise level in GERDA is  $\sim 4$  times higher. A larger improvement is thus expected therein.

The method might be improved by an alignment of the traces with a sub-sample precision before denoising. The 50% pulse height position is probably a good candidate for such an alignment. This might also reduce energy-dependent oscillations in A/E, observed if strong cut are applied. A further improvement might be achievable if the denoising would be applied to the current instead of the charge pulse. This was however not possible with the version of GELATIO available at the time of the presented studies.

The implemented tools have a wide range of applications. The energy resolution obtained with the current algorithms might be improved by a prior denoising employing wavelets. The advantage is the possibility to apply a time-dependent cut. An improvement of the energy resolution is similarly important as a reduction of the background. This can be seen e.g. in Equation 2.6. Denoising might also be particularly helpful if studies are performed which include low energy events. It might furthermore lead to an improved performance of pulse shape discrimination methods with semi-coaxial detectors.

# Chapter 7

## The GERDA Phase II Calibration System

The GERDA germanium detectors are calibrated employing three  $^{232}\text{Th}$  sources, which are lowered into the GERDA cryostat using a custom built source insertion system (SIS) for each source. A schematic of this system is shown in Figure 7.1. Each source is contained in a capsule of type VZ3474 which is screwed into a tantalum absorber hanging on a longitudinally perforated steel band. The holes in the steel band are counted by an optical sensor and translated into an absolute position by an incremental encoder. This is the primary positioning system with a resolution of 1 mm. A secondary system uses an absolute encoder measuring position and turns of the drive shaft with a resolution of 8 bit per turn ( $\approx 0.6$  mm). The displayed position is relative to the parking position on top of the GERDA lock system. The secondary system is used to cross-check the position of the primary system and in case of failure of the primary system. It remembers the current position also when the system is powered off. The parking position for both systems is initialized by an end switch which is activated by a pin located at the source holder. The drive shaft is coupled to an electrical engine through a friction clutch to avoid over-forcing. The system was designed, built and tested for Phase I in the framework of the PhD thesis of Michal Tarka and Francis Froborg and is described in detail in [32, 56, 57]. It is controlled by a LabVIEW [159] program.

### 7.1 Modification of the End Switch Activation Pin

During Phase I, calibrations were taken on average every 1.5 weeks. The SIS was switched off during physics runs and the positioning system reinitialised after

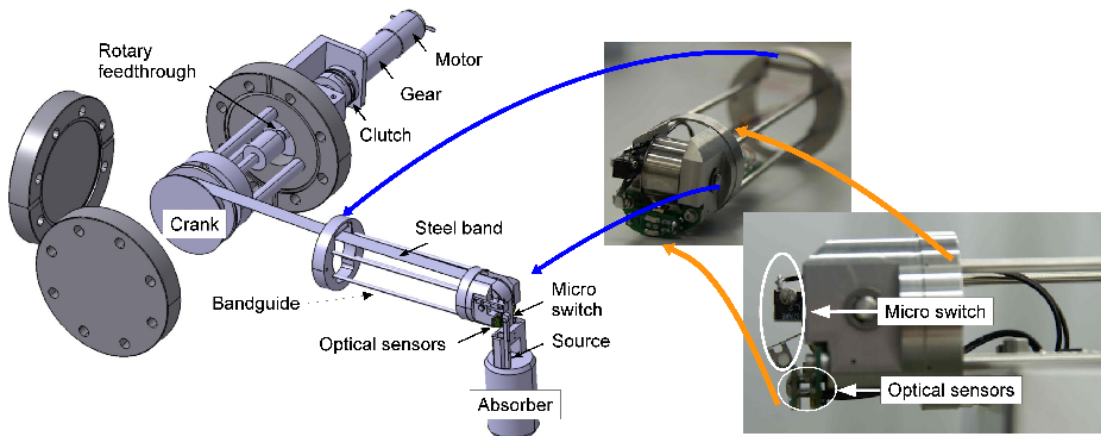


**Figure 7.1:** Schematic view of the GERDA calibration system including also the optical sensors of the incremental encoder. Not shown is the absolute encoder which is connected to the drive shaft. Figure from [32], original drawing from [56].

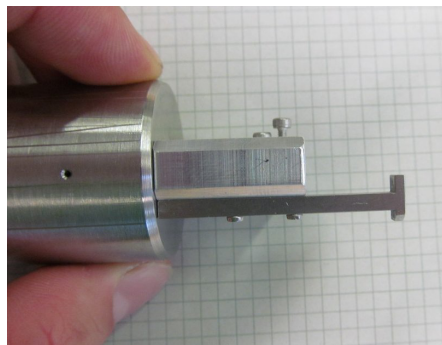


**Figure 7.2:** Dummy stainless steel absorber and holder with the new T-shaped pin for activation of the end switch.

switching on. The initialisation is realised moving the source upwards until a pin is activating an end switch. The pin is attached to the source holder. During the 1.5 years of operation the initialization failed twice. The origin of the failures was identified to be the pin missing the end switch. A new T-shaped pin, which is shown in Figure 7.2 was therefore designed. Tests with this new pin were undertaken and confirmed a reliable activation of the end switch even under exaggerated unfavourable conditions, such as turning the absorber by hand or very angled positions of the full system. The pin was in all cases activating the end switch and never got stuck on any system components. All straight pins were therefore replaced by the new T-shaped pin.

## 7.2 Configuration and Calibration of the Absolute Encoder

In Phase II the calibration system is mounted  $\sim 3$  m higher compared to Phase I due to a new lock system for the GERDA cryostat. The old  $\sim 7$  m long steel bands had to be replaced for this reason by 10 m long steel bands which required a new calibration of the absolute encoder as well as resetting its zero position. This was done similarly to the initial installation in Phase I as described in [32]. The steps undertaken for this operation are mentioned below, an exact description of each individual step can be found in [32] and is not repeated here. The installation and calibration were first applied to a spare system at the University of Zurich, which was used for further tests before installation of the other three systems in GERDA.

The control box stops a source movement if the discrepancy between the absolute and incremental encoder position is more than 20 mm. This feature was disabled for the following operations and the box was run in debug mode, displaying additional raw values, such as the number of turns of the absolute encoder. Driving the system to the point where the steel band is completely unrolled or beyond would damage the band at its fixation. This is therefore prevented in two ways. First, the band length is written into the control box by a LabVIEW program. Second, the control box prevents moving below the zero position of the absolute encoder, which has its largest value in the parking position on the top of the GERDA Phase II lock system. The first step is setting the band length in the control box to 9.5 m, this allows for a range by far sufficient for GERDA Phase II while simultaneously maintaining a large safety margin before reaching the end of the steel band.

The next step is to reset the zero position of the absolute encoder. This is performed disconnecting the absolute encoder mechanically from the drive shaft while the source is in the parking position. It is subsequently turned until reaching a value of at least 60 turns, which is sufficient to go to the end of the new steel bands. The encoder is then reconnected to the drive shaft. In a next step the system is driven to 9.5 m. Moving below this point is possible only by over stressing the friction clutch, which is done to lower the source until the steel band is covering only 1/4 of the crank wheel, which can be seen through a view port at each system. The absolute encoder is reset to zero at this position by bridging two pins in the control box. The source is then moved back to the parking position, completing the first full cycle of the system.

The actual calibration is performed based on the position information provided by the incremental encoder. It is realised writing a correction table containing the discrepancy between the two position measurement systems for each full turn of the absolute encoder to a memory in the SIS control box. The discrepancy values are

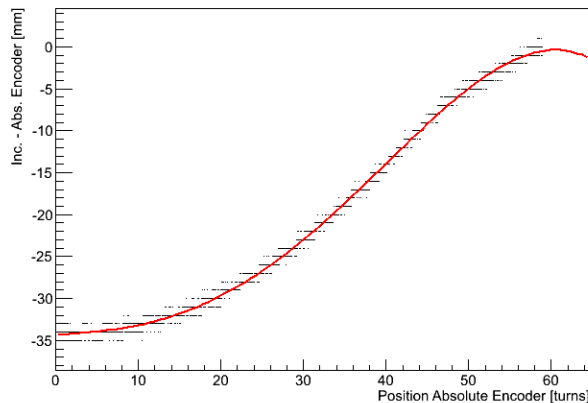


**Figure 7.3:** Discrepancy between the absolute and incremental encoder (black dots) before calibrating the absolute encoder superimposed by a fit of a fourth order polynomial used to create the calibration table for the absolute encoder. Zero turns of the absolute encoder corresponds to lowest possible source position.

continuously written to a text file by the main LabVIEW control program whenever the sources are moved. The first step is to reset the current table to 0. The source is then moved to 9.5 m and back to the parking position in order to obtain stable conditions. After reinitialisation to 0 mm of both position measurement systems the source is moved to 9.5 m. The discrepancy from this movement is then employed to write the calibration table into a text file. This is performed by a program written to plot this discrepancy and fit it with a fourth order polynomial using the ROOT framework. The result is shown in Figure 7.3 for the spare system. The program also writes the five parameters of the polynomial in the same file as the correction table. The system is then moved back to the parking position and the calibration is written by a LabVIEW program to the control box. This is the last step of the procedure and the control box is then set back to the normal operation mode. The system is now ready for operation.

### 7.3 Position Measurement Validation with a 10 m Long Steel Band

The first validation of the systems was, investigating the time stability of the position determination over multiple cycles without intermediate reinitialisation of the parking position. The system was therefore cycled two times between 0 and 9.5 m, then 4 times between 0 and 4 m and then eighteen times between 0 and 9.5 m. The discrepancy was fit with a fourth order polynomial for each full

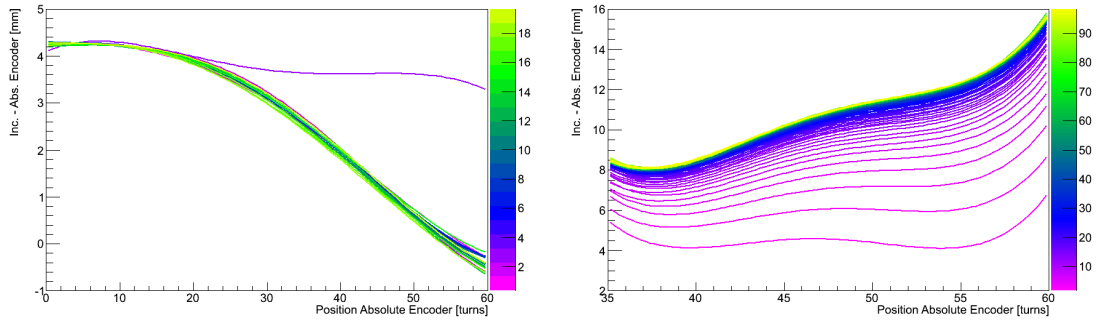


**Figure 7.4:** Fits with fourth order polynomials to the discrepancy between the absolute and incremental encoder for full cycles. Left: 20 cycles going to 9.5 m intermittent by 4 cycles to 4 m (not shown) between cycle 2 and 3. Right: 100 cycles going to 4 m showing a converging drift.

cycle. The fit results are shown in Figure 7.4 (left) for the 20 cycles to 9.5 m. The discrepancy for moving down in the first cycle taken after the four cycles to 4 m and hence also the fit to the full cycle, shows a different shape while the discrepancy between any other two cycles is at most 0.5 mm and without any trend. This behaviour was further investigated cycling the system 100 times between 0 and 4 m ( $\sim 36$  absolute encoder turns). The fits to the discrepancies in these cycles are shown in Figure 7.4 (right). A drift in discrepancy can be observed converging to a maximal difference between the first and last cycle of 10 mm at the parking position. The origin of this drift is likely tightening of the remaining steel on the roll when the system stops and starts at 4 m. Afterwards, the system was cycled three times to 9.5 m showing an exact same behaviour as in Figure 7.4 (left).

The discrepancy between the position measurement systems showed to be dependent on the history of the source position, caused most likely by different tightening of the remaining steel band and hence a wrong value calculated from the position of the absolute encoder and crank wheel diameter. The maximum observed discrepancy is 16 mm which could be reduced to 8 mm by intermediate reinitialisation of the parking position. This discrepancy is acceptable especially as it is caused by the secondary absolute encoder and hence not influencing the displayed position, which is confirmed by the validations presented in the next paragraph.

The position measurement of the incremental encoder was cross-checked with a laser distance measuring device of type PD4 from Hilti [160]. The displayed position is corrected for thermal contraction of the part of the steel band which would be in liquid argon in GERDA (thermal correction coefficient 1.002735). The displayed incremental encoder position, the inverse corrected position (which cor-

Displayed	W/o thermal correction	Laser
0	0	0
150	150	150
6150	6161.9	6162
9500	9521.1	9522

**Table 7.1:** Position in mm as measured by the incremental encoder including and excluding a thermal correction for GERDA as well as measured with a laser. The latter agree within the resolution of the incremental encoder of 1 mm.

responds to the real position at room temperature) and the position measured with the laser are given Table 7.3. The liquid level was set to 1800 mm during this validation. Each position was measured once. The obtained values agree within the resolution of the incremental encoder of 1 mm, proving the accuracy of this position measurement system. The agreement is better than the uncertainty of the laser, as stated by the producer to be  $\pm 2$  mm.

During other operations with the spare system it was observed that the incremental encoder sometimes misses a hole in the steel band if the system is not well levelled. Special care must therefore be taken on the levelling, when mounting the systems for GERDA.

## 7.4 Source Absorber Oscillation Tests at 9.5 m

The source absorber is expected to oscillate when moving in GERDA, particularly large oscillations are expected when it enters liquid argon. The amplitude and time of oscillations have to be known in order to define the minimum required distance to the source path. This is estimated with the spare system and a lead dummy absorber lowered into liquid nitrogen at 9.5 m. The restoring force is minimal at this length and the oscillation amplitude is respectively maximal. Lead is used instead of tantalum because of lower material costs.

The absorber was  $\sim 20$  cm above the liquid level and oscillating by less than  $\pm 2.5$  mm before it was moved into liquid  $N_2$  at 9.5 m. The difference between the time when the bottom of the absorber touches the liquid and the liquid stops to boil is the boiling time  $t_B$  and when the oscillations become less than  $\sim \pm 2.5$  mm, is the oscillation time  $t_O$ . The maximal transversal amplitude  $A$  was measured with a ruler, subtracting the maximum position in one direction from the maximum position in the opposite direction and dividing this value by two. The angular oscillation is roughly estimated by eye. A picture of the set-up is provided in Figure 7.5. The measurements were repeated six times. The liquid nitrogen level was decreasing between the beginning of the first and the end of the last measurement



**Figure 7.5:** Arrangement to measure the oscillation time and amplitude of a source absorber caused by boiling when lowered into liquid nitrogen at 9.5 m.

from 6 cm above the top of the holder to 1.5 cm. The two most relevant parameters are the oscillation amplitude and time. The former was on average  $(15 \pm 3)$  mm and the latter  $(240 \pm 40)$  s. The oscillation amplitude when moving out of the liquid was measured 4 times. The average value is with  $(5 \pm 2)$  mm sufficiently small. Two more measurements were performed with 24 cm of liquid nitrogen above the holder in order to investigate the effect of a deeper immersion. The oscillation time is similar, the amplitude increased however by  $\sim 9$  mm. The measurements are summarised in Table 7.4.

The presented results need to be scaled as they were obtained with a lead dummy absorber in liquid nitrogen in contrary to tantalum in liquid argon. The boiling and oscillation time are dependent on the materials and are converted employing a simplified model:

$$t_B \propto \frac{mc}{\lambda}, \quad (7.1)$$

here  $m$  is the mass of the absorber,  $c$  is the specific heat capacity of tantalum and  $\lambda$  is the heat conductivity of tantalum which results in a 1.45 times longer boiling time of  $\sim 3:20$  min for tantalum compared to lead. The cooling power of liquid argon and nitrogen is assumed to be similar as it is expected to be dominated by the movement of the liquid, which is expected to be comparable in both cases. An anti-proportional relation between the time needed to damp the oscillations and the density of the liquid is assumed, resulting in a reduction of the damping time by a factor of 0.58. Using these approximations one obtains the oscillation time of tantalum in liquid Ar of

$$t_O = 2:18 \text{ min} \cdot 1.45 + 1:42 \text{ min} \cdot 0.58 = 4:19 \text{ min}. \quad (7.2)$$

Earlier measurements with 2 m band length which had been performed for Phase I

	$A$ [mm]	$A$ [°]	$t_B$ [min:s]	$t_O$ [min:s]
6 cm in liquid	15	45		04:00
6 – 1.5 cm in liquid	13	50	02:15	03:50
6 – 1.5 cm in liquid	17	45	02:16	03:30
6 – 1.5 cm in liquid	17	35	02:25	03:30
6 – 1.5 cm in liquid	18	50	02:20	05:20
1.5 cm in liquid	10	25	02:15	03:50
average	15	42	02:18	04:00
standard deviation	3	10	00:04	00:40
24 cm in liquid	25	45	02:10	03:00
24 cm in liquid	23	45	02:30	04:30

**Table 7.2:** Oscillation amplitude  $A$  transversal and rotational as well as the boiling  $t_B$  and oscillation time  $t_O$  after immersion of a lead dummy absorber in liquid nitrogen at 9.5 m.

resulted in a boiling time of 3 min and oscillation time of 4 min [56]. These are similar to the times obtained from the presented measurements. The definition of oscillation time therein is “time of enhanced oscillation”, which is not further specified and might hence differ slightly from the definition used in this work.

Based on these results, the following recommendations are made for GERDA Phase II. The source should be stopped for 5 min after immersion in liquid argon in order to certainly stop oscillations. This waiting is automatically performed by the the lab view program. Any object which should not get in contact with the source holder (because of possible damage or risk of getting stuck on the initialisation pin) should be more than 10 mm away from the path of the source holder. If a closer object has to be passed, it is recommended to stop for 1 min right before passing it.

## 7.5 Installations at LNGS for GERDA Phase II

All three source insertion systems were leak checked and mounted at LNGS between the 25<sup>th</sup> of July and 1<sup>st</sup> of August 2014. The absolute encoder of SIS 1 and 3 were configured according to the description in Section 7.2. The calibration was similarly performed from the downward movement after one cycle to a 1/4 turn of the crank wheel before the end of the band and one cycle to 9.5 m. SIS 2 could not be calibrated at that date due to cables of the Ge detectors positioned temporarily in the path of source 2. Its calibration was performed on the 26<sup>nd</sup> of February 2015. The determined calibration curves for the three systems are shown in Figure 7.6.

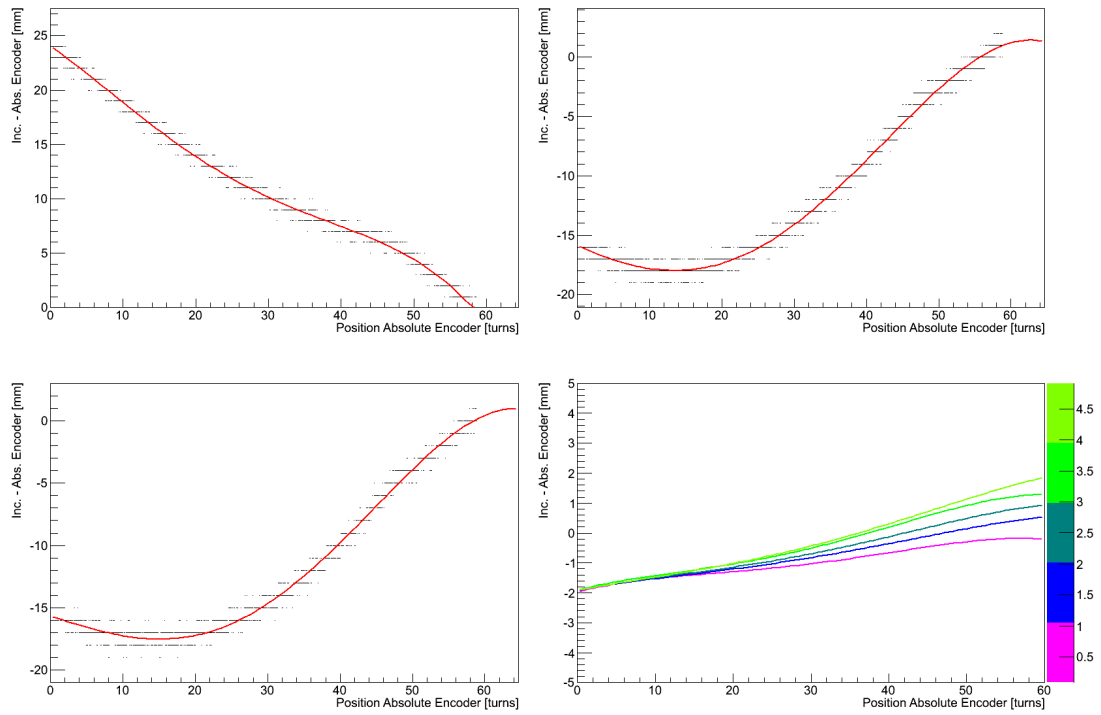


**Figure 7.6:** Calibration curves of the absolute encoder for GERDA Phase II SIS 1 (top left), 2 (top right) and 3 (bottom left) as well as the discrepancy between the two encoders occurring in subsequent five full cycles to 9.5 m (bottom right).

After the calibration, SIS 1 and 3 were cycled 5 times between 0 and 9500 mm, without initialisation of the parking position between the cycles, to test their stability. The discrepancy between the two position measurement systems was observed to be practically identical for both SISs. It is shown by one line for each full cycle for SIS 1 in Figure 7.6 (bottom right). The largest drift of up to 2 mm has been observed at the parking position. This is within the requirements but suggests that a recalibration might be necessary in at some point in Phase II. All three systems are now readily installed and can be used normally.

## 7.6 Shutter Alarm and Parking Indicator System

The three SISs are mounted on top of the GERDA lock. Each can be separated from the lock by a manual shutter. Closing the shutter of a system while the source is not parked results in serious damage of the perforated steel band and shutter. In the worst case the steel band gets cut and the tantalum absorber will fall into the cryostat with a high chance to damage further detector components, such as the Ge diodes, pre-amplifier or liquid argon veto PMTs. In order to prevent this, a parking position indicator and shutter alarm system was developed, in the following referred to as “alarm system”.

The alarm system consists of one box for each shutter indicating if the respective source is in the parking position and housing a buzzer for an alarm. It is installed directly on top of the handle for closing the respective shutter and connected to a central I/O box. This is based on a RedLab 1024LS from Meilhaus Electronic [161] and additionally connected to each shutter, which are equipped with two switches, one indicating “shutter fully closed” and the other “shutter fully opened”. The I/O box is connected to a PC by a USB cable transmitting the shutter status to the main SIS control program written in LabVIEW. The existing program was extended to control the LEDs of the shutter indicator and the alarm signal. The hardware of the system is shown in Figure 7.7. It is powered via the USB interface.

All channels of the I/O box are set as input after power on. In this default state the alarm buzzer is emitting a constant tone, the “not parked” LED is on and the “parked” LED is off. The SIS control program is then establishing the connection to the I/O box and initialising the respective ports as output which are initialised with a logic “low”. This means that the indicators and alarm remain in the same state. The connection and initialisation are maintained until the LabVIEW program is stopped. During operation the status is set as following. The SIS control program has a general flag for a system error. If this flag indicates



**Figure 7.7:** Shutter alarm and parking indicator system with the central I/O box and one box for each SIS shutter housing an LED indicating the parking position and an alarm buzzer.

no error and the source position is  $\leq 2$  mm, the program writes a “high” to the respective output buffer which results in the green “parked” LED to turn on and the red “not parked” LED to turn off. The output buffer will also be set to (or stay) “low”. The alarm buzzer is switched off if the “shutter fully opened” switch is high and the “shutter fully closed” switch is low or if the source “parked” is high. Otherwise it will emit an intermittent tone and the red “not parked” LED will be blinking. It is possible to switch off all shutter monitoring and alarms in the SIS control program, e.g. for test operations. If it is switched off, it is assumed that there is no shutter alarm system present and the control program will not try to connect to the I/O box. An additional output at the I/O box supplies a TTL “high” signal if all sources are in the “parked” state. This will be connected to the PLC controller for the GERDA lock system and prohibit closing of the main shutter if any one of the sources is not parked.

### 7.6.1 Exception Handling

The system is designed to handle exceptions in a safe way. Several cases of exceptions are discussed below.

**Signal Interruption** An interruption of any signal, e.g. due to a malfunctioning connection, results in a safe indication, namely “source not parked” or “buzzer on” or both, depending on which signal failed.

**Stopping the SIS Control Program** The default state (“source not parked“ and buzzer with a continuous tone) is restored when stopping the control program by the ”stop“ button. Closing LabVIEW without previously stopping the SIS control program should never be done as this does not call the stop function. In this case the alarm system stays in the last state as long as the USB is providing power and turns off otherwise. The sources can still be moved using the SIS main control box directly instead of the control program but the alarm system is not updating, as it is controlled by the SIS control program and can not check if the LabVIEW program is still running. This scenario can potentially lead to an unsafe state but does not occur performing normal operations. There is no known reasonable solution for this case.

**Switching the SIS Control Box off** Switching the SIS control box off results in a communication error in the control program and an interruption of it. The alarm box remains in the current state. A source movement is not possible with a powered off control box. Hence sources stay in the current position which is indicated correctly. If the source is not parked and the red ”Not Parked, Don’t Close The Shutter!“ LED is ignored, closing the respective shutter will not trigger an alarm as the control program is interrupted. The latter sub case is however considered very unlikely as the control box is usually powered on and the LED warning next to the handle must be ignored additionally. It should be possible to safely handle this sub case by changing the exception handling of the main SIS control program.

## 7.7 Conclusions and Outlook

The end switch activation pin has been exchanged by a reliable T-shaped pin. All three calibration systems are installed for Phase II and calibrated with new 10 m long steel bands. Stability studies of the secondary position measurement system (absolute encoder) revealed a small drift, possibly requiring a recalibration of the system during Phase II. This will not effect the main experiment operations.

Movements of the absorber caused by entering liquid argon were investigated resulting in a recommended waiting time of 5 min after entering the liquid and a safety distance of 10 mm to any components which should not get in contact with the source holder.

An indication and alarm system for the three SIS shutters was designed and installed providing additionally an ”all sources parked“ signal for the main lock system, reducing the risk of operation mistakes.



# Chapter 8

## Final Conclusions and Outlook

An extremely low background is required in GERDA, which searches for the neutrinoless double beta decay of  $^{76}\text{Ge}$ . GERDA achieved a background index of  $10^{-2}$  cts/(keV kg yr) in Phase I and is aiming to reduce it by one order of magnitude in Phase II. This is the main purpose of the current upgrade besides increasing the detector mass. The background reduction is achieved with approximately similar contributions from enhanced pulse shape discrimination, the installation of a liquid argon veto and the elimination of known background sources, such as  $^{228}\text{Th}$  and  $^{214}\text{Bi}$  in the detector holders. Working on this reduction was the main focus of this thesis.

Wavelength-shifting reflector foils were developed by applying several coatings to VM2000 and Tetratex. These were investigated on their mechanical and cryogenic stability to ensure a reliable functioning in Phase II. The production technique of dip-coating was selected to permit an efficient coating of meter-scale reflector foils. The light yield was measured under conditions very similar to the final application. A setup allowing continuous operation in liquid and gaseous argon was especially developed for this purpose. Light yield measurements were performed for different purities and computed relative to that of an uncoated VM2000 foil. This technique was conducted to cancel out the purity dependence of the light yield of argon. Tetratex dip-coated with pure TPB proved to be the superior coated reflector foil in several aspects. It has a light yield in liquid argon  $3.15 \pm 0.16$  times higher than uncoated VM2000 and was proved to be insensitive to long-term operation in liquid argon and to air exposure. Its mechanical stability and radioactive trace contaminants were found to be within the specifications for GERDA. Based on these positive results it was installed in GERDA as part of the liquid argon veto system. An installation method by stitching was developed, minimising the amount of material, avoiding the introduction of radioactive contaminations. The TPB coated Tetratex is expected to maintain its light yield and stability at least for the full period of Phase II. It is also a top candidate for other

experiments employing liquid argon as a scintillator. The results of this work were published in [94].

Several additional results were obtained in the context of the described measurements. Amongst the coatings which are transparent and stable, 80 % Makrolon and 20 % TPB resulted in the highest light yield. Applied to VM2000,  $2.3 \pm 0.16$  times higher than for uncoated VM2000. Such a coating is a top candidate for applications which require transparency to visible light. The light yield of coated nylon cylinders (another component of the liquid argon veto) was additionally measured. The content of TPB in its coating was increased based on those results. PMTs of type R11065-10 were intended to be installed in GERDA. Employing this PMT for the argon setup yielded a valuable cross check for issues observed with this PMT by others in the collaboration. The setup is available for further measurements and is currently employed to characterise new silicon PMs at liquid xenon temperature ( $\sim 165$  K). A characterisation of a new PMT, designed for operation in liquid argon will also be conducted in this setup.

A system to measure rates of emanating gases and their chemical composition was designed, built and commissioned at the University of Zurich. It is a valuable tool to identify components which potentially spoil the liquid argon purity, before their deployment. The key component of this setup is a mass spectrometer with a range of 1–200 amu/q. Measurement techniques were developed together with the master project of Michael Miloradovic [135] for samples with emanation rates down to  $10^{-13}$  mbar l/s, with  $\sim 10$  % uncertainty. A sample of TPB-coated Tetratex from the same production as for the liquid argon veto was measured with this setup. The emanation rates of the dominant components  $\text{CO}_2$ ,  $\text{N}_2+\text{CO}$ ,  $\text{H}_2\text{O}$  and the solvent dichloromethane were found to be  $( < 317, < 47, 11.1, 12) \cdot 10^{-12}$  mbar l/s, respectively, after pumping for  $\sim 1300$  min. These are excellent rates and well suitable for deployment in GERDA. The system is furthermore capable to measure trace concentrations in gas samples with a maximum sensitivity below 1 ppm. The purpose of this setup goes beyond the presented measurements and the hardware and software are ready to be employed for further developments also in the context of other experiments.

A multivariate analysis was developed to distinguish single site events (SSEs) from multi site events (MSEs) in semi-coaxial detectors. This classification is performed by a Support Vector Machine (SVM) with a Gaussian kernel function. The two primary parameters, the kernel parameter  $\gamma$  and the training related parameter  $C$  were optimised applying the SVM to a specific  $^{228}\text{Th}$  calibration measurement and comparing the results to simulation. The optimal values were found to be  $C = 3000$  and  $\gamma = 0.03$ . The SVM was trained with this parameter set on calibration data of GERDA Phase I and applied to the physics data of Phase I. The acceptances of single and multi site enriched data samples in calibration and

physics data were compared. This revealed that the SVM is performing a combination of SSE and detector volume selection. A very low acceptance for MSE samples was found, namely  $\sim 18\%$  for the single escape peak of  $^{208}\text{Tl}$  at 2103.5 keV in calibration measurements and  $\sim 12\%$  for the  $^{42}\text{K}$  full energy peak at 1524.7 keV in physics data. Other pulse shape discrimination methods for semi-coaxial detectors also observed a volume selection, however less pronounced [59]. It is most likely driven by an inhomogeneous distribution of the SSE sample employed for training.

The method can not be applied as primary pulse shape discrimination method in its current state, but is beneficial for cross checks of other techniques. There are several possibilities which might reduce the volume selection bias. One possibility is to employ a training dataset in which SSEs and MSEs have a similar geometrical distribution. Such a dataset is available by the two neutrino double beta decay events, however, it limits the possibilities for cross checks. An improvement could also be achieved if a set of input variables could be found which contains less information on the event location but sufficient information about the event topology. Several further possibilities were discussed which might yield minor improvements.

The pulse shape discrimination power is related to the level of electronic noise. Two new modules were developed and implemented in the official release of the GERDA analysis software GELATIO for advanced digital filtering. One module is performing a wavelet transformation employing Daubechies wavelets and the second module filters electronic noise by the application of cuts to transformed waveforms. The module contains an advanced set of cutting options which includes the computation of an estimate on the noise levels at different frequencies. This is performed on an event-by-event basis. The denoising was optimised on the pulse shape discrimination power with a BEGe-type detector. GERDA is acquiring calibration data with approximately 40 times shorter high-frequency trace than background data. A special calibration measurement with a longer high-frequency trace was acquired to apply the noise filtering. This enhanced the MSE acceptance from 12.1 % to 11.6 %. The enhancement is expected to be larger in GERDA because of a  $\sim 4$  times higher noise level. The method might be improved by an alignment of the traces with a sub-sample precision before denoising. The denoising is currently applied to the recorded charge traces, which are then employed to calculate the amplitude of the current pulse. The latter is the parameter relevant for the pulse shape analysis with BEGe-type detectors. Applying the denoising to the current instead of the charge pulse would probably yield a further improvement. It might also be first applied to the charge and then again to the current pulse. This was not studied in the current work, but would be useful to study in the future.

These tools possess applications beyond the pulse shape analysis of BEGe-type

detectors. For example, they might improve pulse shape discrimination methods with semi-coaxial detectors. An enhancement of the energy resolution might as well be achievable by a denoising with wavelets prior to the application of the energy reconstruction algorithm. The advantage is the possibility to apply a time-dependent cut. An improvement of the energy resolution is similarly important as a background reduction. Denoising might be particularly helpful for studies which include low energy events, such as the double beta decay to excited states, further background studies and studies of the detector dead layers.

An upgrade of the three calibration source insertion systems was also performed in the context of upgrading from GERDA Phase I to Phase II. This includes modifying the end switch activation pins to a reliable T-shape, the installation of longer stainless steel bands and a recalibration of the positioning systems. A new indication and alarm system for the three SIS shutters was designed and installed, reducing the risk of operational mistakes. It also provides an interlock signal to the main shutter control if a source is not in the parking position.

In summary, significant contributions were made to several upgrades of GERDA, in particular to the background reduction by one order of magnitude. This includes an upgrade of the calibration source insertion system and studies on an alternative pulse shape discrimination method for coaxial detectors. A new tool for the reduction of electronic noise was implemented into the official analysis software. It proved to enhance the pulse shape discrimination with BEGe-type detectors and has a significant potential to yield further improvements. A wavelength-shifting reflector foil has been developed and installed in the liquid argon veto. It is a key component of this system, strongly influencing its performance. An emanation rate measurement system was built in this context and is available as a valuable tool for further developments.

GERDA is about to start running Phase II with an order of magnitude less background. Furthermore, the mass of enriched germanium increased by additional BEGe-type detectors from 18 kg to 35 kg. Achieving the envisioned sensitivity of  $T_{1/2} \approx 1.4 \cdot 10^{26}$  yr will also be feasible due to the developments presented in this thesis.

# Chapter 9

## Acknowledgements

I would like to thank Prof. Dr. Laura Baudis for the opportunity to perform my PhD thesis in her research group at the University of Zurich and to participate in a world leading neutrino experiment. I would also like to thank for her guidance while leaving space for developing my own ideas.

I would like to thank the current and former members of the research group for the kindly atmosphere and helpful discussions; in particular Prof. Dr. Marc Schumann, also for being available for my doctorate committee, Dr. Alexander Kish, whom I would also like to thank for proof reading my thesis, Dr. Aaron Manalaysay, Dr. Teresa Marrodan Undagoitia, Giovanni Benato, Andreas James, Francesco Piastra, who measured the activity of the coated Tetratex with Gator, Michael Miloradovic, for successfully working together on the emanation measurement system and last but not least Gaudenz Kessler for many helpful discussions and his friendship.

Special thanks also to Prof. Dr. Ueli Straumann for being available for my doctorate committee and the electronics and mechanics workshops of the Physik-Institut of the University of Zurich for technical support and advices. In particular to Daniel Florin, Achim Vollhardt, Kurt Bösiger and Reto Maier. I would furthermore like to thank Dr. Roland Bernet for always helping me with any computer related issue, the secretaries of the Physik-Institute for the help with various bureaucratic issues, the group of Hans-Werner Fink for the kind possibility to use their optical microscope and Dr. Yargo Bonetti for the possibility to coat the reflector foils for GERDA in the clean room facility “First Lab” at the ETH Zurich.

I very much enjoyed the friendly and motivating atmosphere of the GERDA collaboration. Special thanks in the context of the developments of wavelength-shifting reflector foils to Dr. Mark Heisel, Prof. Dr. Anatoly Smolnikov and Anne Wegmann from the Max Planck Institut für Kernphysik in Heidelberg for their technical support and fruitful discussions, Dr. Hardy Simgen for performing the radon emanation measurement and Maria Laura Di Vacri and Stefano Nisi from

the LNGS chemistry laboratory for the IPC-MS measurements. Many thanks as well for the kind possibility to employ the fluorescence spectrometer at Max Planck Institut für Kernphysik in Heidelberg. Furthermore I would like to thank Dr. Rugard Dressler and Dr. Ilya Usoltsev from the Paul Scherrer Institute for the production of the cryogenic alpha source employed in the liquid argon setup.

Thanks to my family and friends for the support and counterbalance which are indispensable for the success of a PhD thesis.

# Bibliography

- [1] C. L. Cowan, F. Reines, F. B. Harrison, H. W. Kruse, and A. D. McGuire, “Detection of the free neutrino: A Confirmation,” *Science*, vol. 124, pp. 103–104, 1956.
- [2] E. Fermi, “Tentativo di una teoria dei raggi  $\beta$ ,” *La Ricerca Scientifica*, vol. 2, no. 12, 1933.
- [3] M. Gell-Mann, “A Schematic Model of Baryons and Mesons,” *Phys.Lett.*, vol. 8, pp. 214–215, 1964.
- [4] G. Zweig, “An SU(3) model for strong interaction symmetry and its breaking. Version 2,” pp. 22–101, 1964.
- [5] M. Breidenbach, J. I. Friedman, H. W. Kendall, E. D. Bloom, D. Coward *et al.*, “Observed Behavior of Highly Inelastic electron-Proton Scattering,” *Phys.Rev.Lett.*, vol. 23, pp. 935–939, 1969.
- [6] S. Glashow, “Partial Symmetries of Weak Interactions,” *Nucl.Phys.*, vol. 22, pp. 579–588, 1961.
- [7] A. Salam, “Weak and Electromagnetic Interactions,” *Conf.Proc.*, vol. C680519, pp. 367–377, 1968.
- [8] S. Weinberg, “A Model of Leptons,” *Phys.Rev.Lett.*, vol. 19, pp. 1264–1266, 1967.
- [9] R. Davis, “Attempt to detect the antineutrinos from a nuclear reactor by the  $\text{cl}^{37}(\bar{\nu}, e^-)\text{a}^{37}$  reaction,” *Phys. Rev.*, vol. 97, pp. 766–769, Feb 1955. [Online]. Available: <http://link.aps.org/doi/10.1103/PhysRev.97.766>
- [10] M. Goldhaber, L. Grodzins, and A. W. Sunyar, “Helicity of Neutrinos,” *Phys. Rev.*, vol. 109, pp. 1015–1017, 1958.

## BIBLIOGRAPHY

---

- [11] G. Danby, J.-M. Gaillard, K. Goulianos, L. M. Lederman, N. Mistry, M. Schwartz, and J. Steinberger, “Observation of high-energy neutrino reactions and the existence of two kinds of neutrinos,” *Phys. Rev. Lett.*, vol. 9, pp. 36–44, Jul 1962. [Online]. Available: <http://link.aps.org/doi/10.1103/PhysRevLett.9.36>
- [12] B. T. Cleveland, T. Daily, J. Raymond Davis, J. R. Distel, K. Lande, C. K. Lee, P. S. Wildenhain, and J. Ullman, “Measurement of the solar electron neutrino flux with the homestake chlorine detector,” *The Astrophysical Journal*, vol. 496, no. 1, p. 505, 1998. [Online]. Available: <http://stacks.iop.org/0004-637X/496/i=1/a=505>
- [13] W. Hampel *et al.*, “GALLEX solar neutrino observations: Results for GALLEX IV,” *Phys. Lett.*, vol. B447, pp. 127–133, 1999.
- [14] J. N. Abdurashitov *et al.*, “Solar neutrino flux measurements by the Soviet-American Gallium Experiment (SAGE) for half the 22 year solar cycle,” *J. Exp. Theor. Phys.*, vol. 95, pp. 181–193, 2002, [Zh. Eksp. Teor. Fiz.122,211(2002)].
- [15] Y. Fukuda *et al.*, “Solar neutrino data covering solar cycle 22,” *Phys. Rev. Lett.*, vol. 77, pp. 1683–1686, 1996.
- [16] Q. R. Ahmad *et al.*, “Direct evidence for neutrino flavor transformation from neutral current interactions in the Sudbury Neutrino Observatory,” *Phys. Rev. Lett.*, vol. 89, p. 011301, 2002.
- [17] B. Pontecorvo, “Mesonium and anti-mesonium,” *Sov. Phys. JETP*, vol. 6, p. 429, 1957, [Zh. Eksp. Teor. Fiz.33,549(1957)].
- [18] B. Pontecorvo, “Neutrino Experiments and the Problem of Conservation of Leptonic Charge,” *Sov. Phys. JETP*, vol. 26, pp. 984–988, 1968, [Zh. Eksp. Teor. Fiz.53,1717(1967)].
- [19] Z. Maki, M. Nakagawa, and S. Sakata, “Remarks on the unified model of elementary particles,” *Prog. Theor. Phys.*, vol. 28, pp. 870–880, 1962.
- [20] V. N. Gribov and B. Pontecorvo, “Neutrino astronomy and lepton charge,” *Phys. Lett.*, vol. B28, p. 493, 1969.
- [21] P. A. Dirac, “The quantum theory of the electron,” in *Proceedings of the Royal Society of London A: Mathematical, Physical and Engineering Sciences*, vol. 117, no. 778. The Royal Society, 1928, pp. 610–624.

## BIBLIOGRAPHY

---

- [22] K. A. Olive *et al.*, “Review of Particle Physics,” *Chin. Phys.*, vol. C38, p. 090001, 2014.
- [23] E. Majorana, “Teoria simmetrica dell’elettrone e del positrone,” *Il Nuovo Cimento Series 10*, vol. 14, 04 1937.
- [24] M. Fukugita and T. Yanagida, “Baryogenesis Without Grand Unification,” *Phys. Lett.*, vol. B174, p. 45, 1986.
- [25] V. A. Kuzmin, V. A. Rubakov, and M. E. Shaposhnikov, “On the Anomalous Electroweak Baryon Number Nonconservation in the Early Universe,” *Phys. Lett.*, vol. B155, p. 36, 1985.
- [26] J. Schechter and J. W. F. Valle, “Neutrino masses in  $SU(2) \otimes U(1)$  theories,” *Phys. Rev. D*, vol. 22, pp. 2227–2235, Nov 1980. [Online]. Available: <http://link.aps.org/doi/10.1103/PhysRevD.22.2227>
- [27] S. M. Bilenky, J. Hosek, and S. T. Petcov, “On Oscillations of Neutrinos with Dirac and Majorana Masses,” *Phys. Lett.*, vol. B94, p. 495, 1980.
- [28] S. M. Bilenky and S. T. Petcov, “Massive neutrinos and neutrino oscillations,” *Rev. Mod. Phys.*, vol. 59, pp. 671–754, Jul 1987. [Online]. Available: <http://link.aps.org/doi/10.1103/RevModPhys.59.671>
- [29] Z.-z. Xing and Y.-L. Zhou, “Majorana  $cp$ -violating phases in neutrino-antineutrino oscillations and other lepton-number-violating processes,” *Phys. Rev. D*, vol. 88, p. 033002, Aug 2013. [Online]. Available: <http://link.aps.org/doi/10.1103/PhysRevD.88.033002>
- [30] M. Goeppert-Mayer, “Double beta-disintegration,” *Phys. Rev.*, vol. 48, pp. 512–516, 1935.
- [31] M. Agostini *et al.*, “Results on  $\beta\beta$  decay with emission of two neutrinos or Majorons in  $^{76}\text{Ge}$  from GERDA Phase I,” 2015.
- [32] M. Tarka, “Studies of Neutron Flux Suppression from a  $\gamma$ -ray Source and The GERDA Calibration System,” Ph.D. dissertation, Universität Zürich, 2012. [Online]. Available: [http://www.physik.uzh.ch/groups/groupbaudis/darkmatter/theses/gerda/PHD\\_Tarka.pdf](http://www.physik.uzh.ch/groups/groupbaudis/darkmatter/theses/gerda/PHD_Tarka.pdf)
- [33] W. Rodejohann, “Neutrino-less Double Beta Decay and Particle Physics,” *Int. J. Mod. Phys.*, vol. E20, pp. 1833–1930, 2011.

## BIBLIOGRAPHY

---

- [34] W. H. Furry, “On transition probabilities in double beta-disintegration,” *Phys. Rev.*, vol. 56, pp. 1184–1193, Dec 1939. [Online]. Available: <http://link.aps.org/doi/10.1103/PhysRev.56.1184>
- [35] O. Chkvorets, “Search for double beta decay with HPGe detectors at the Gran Sasso underground laboratory,” Ph.D. dissertation, Heidelberg U., 2008. [Online]. Available: <https://inspirehep.net/record/804442/files/arXiv:0812.1206.pdf>
- [36] C. Arnaboldi *et al.*, “CUORE: A Cryogenic underground observatory for rare events,” *Nucl. Instrum. Meth.*, vol. A518, pp. 775–798, 2004.
- [37] R. Ardito *et al.*, “CUORE: A Cryogenic underground observatory for rare events,” 2005.
- [38] M. Redshaw, B. J. Mount, E. G. Myers, and F. T. Avignone, III, “Masses of Te-130 and Xe-130 and Double-beta-Decay Q Value of Te-130,” *Phys. Rev. Lett.*, vol. 102, p. 212502, 2009.
- [39] K. Alfonso *et al.*, “Search for Neutrinoless Double-Beta Decay of  $^{130}\text{Te}$  with CUORE-0,” 2015.
- [40] E. Andreotti *et al.*, “ $^{130}\text{Te}$  Neutrinoless Double-Beta Decay with CUORICINO,” *Astropart. Phys.*, vol. 34, pp. 822–831, 2011.
- [41] E.-. Collaboration, “Search for majorana neutrinos with the first two years of exo-200 data,” *Nature*, vol. 510, no. 7504, pp. 229–234, Jun 2014, article. [Online]. Available: <http://dx.doi.org/10.1038/nature13432>
- [42] N. Moggi *et al.*, “Neutrinoless double-beta decay search with CUORE and CUORE-0 experiments,” *EPJ Web Conf.*, vol. 90, p. 03004, 2015.
- [43] M. Redshaw, E. Wingfield, J. McDaniel, and E. G. Myers, “Mass and double-beta-decay  $q$  value of  $^{136}\text{Xe}$ ,” *Phys. Rev. Lett.*, vol. 98, p. 053003, Feb 2007. [Online]. Available: <http://link.aps.org/doi/10.1103/PhysRevLett.98.053003>
- [44] A. Gando *et al.*, “Limit on Neutrinoless  $\beta\beta$  Decay of  $^{136}\text{Xe}$  from the First Phase of KamLAND-Zen and Comparison with the Positive Claim in  $^{76}\text{Ge}$ ,” *Phys.Rev.Lett.*, vol. 110, no. 6, p. 062502, 2013.
- [45] —, “Limits on Majoron-emitting double-beta decays of Xe-136 in the KamLAND-Zen experiment,” *Phys. Rev.*, vol. C86, p. 021601, 2012.

## BIBLIOGRAPHY

---

- [46] K. Asakura *et al.*, “Results from KamLAND-Zen,” *AIP Conf. Proc.*, vol. 1666, p. 170003, 2015.
- [47] M. Auger *et al.*, “The EXO-200 detector, part I: Detector design and construction,” *JINST*, vol. 7, p. P05010, 2012.
- [48] M. G. Marino, “Results from EXO-200,” *AIP Conf. Proc.*, vol. 1666, p. 170004, 2015.
- [49] B. J. Mount, M. Redshaw, and E. G. Myers, “Double-beta-decay Q values of Se-74 and Ge-76,” *Phys.Rev.*, vol. C81, p. 032501, 2010.
- [50] C. Cuesta *et al.*, “Status of the MAJORANA DEMONSTRATOR,” 2015.
- [51] A. Bettini, “The World underground scientific facilities: A Compendium,” 2007.
- [52] “Laboratori nazionali del gran sasso of istituto nazionale di fisica nucleare, via g. acitelli, 22 67100 assergi l’aquila, italy.” [Online]. Available: <http://www.lngs.infn.it/>
- [53] C. Aalseth *et al.*, “The IGEX Ge-76 neutrinoless double beta decay experiment: Prospects for next generation experiments,” *Phys.Rev.*, vol. D65, p. 092007, 2002.
- [54] H. Klapdor-Kleingrothaus, A. Dietz, L. Baudis, G. Heusser, I. Krivosheina *et al.*, “Latest results from the Heidelberg-Moscow double beta decay experiment,” *Eur.Phys.J.*, vol. A12, pp. 147–154, 2001.
- [55] M. Balata, L. Cadonati, M. Laubenstein, G. Heusser, M. Giammarchi *et al.*, “The water purification system for the low background counting test facility of the Borexino experiment at Gran Sasso,” *Nucl.Instrum.Meth.*, vol. A370, pp. 605–608, 1996.
- [56] F. Froberg, “Calibration of Phase I of the GERDA Double Beta Decay Experiment,” Ph.D. dissertation, Universität Zürich, 2012. [Online]. Available: [http://www.physik.uzh.ch/groups/groupbaudis/darkmatter/theses/gerda/Thesis\\_Froberg.pdf](http://www.physik.uzh.ch/groups/groupbaudis/darkmatter/theses/gerda/Thesis_Froberg.pdf)
- [57] L. Baudis, A. Ferella, F. Froberg, and M. Tarka, “Monte Carlo studies and optimization for the calibration system of the GERDA experiment,” *Nucl.Instrum.Meth.*, vol. A729, pp. 557–564, 2013.
- [58] K. Ackermann *et al.*, “The GERDA experiment for the search of  $0\nu\beta\beta$  decay in  $^{76}\text{Ge}$ ,” *Eur.Phys.J.*, vol. C73, no. 3, p. 2330, 2013.

## BIBLIOGRAPHY

---

- [59] M. Agostini *et al.*, “The background in the  $0\nu\beta\beta$  experiment GERDA,” *Eur.Phys.J.*, vol. C74, no. 4, p. 2764, 2014.
- [60] M. Agostini, M. Allardt, E. Andreotti, A. Bakalyarov, M. Balata *et al.*, “Pulse shape discrimination for GERDA Phase I data,” *Eur.Phys.J.*, vol. C73, no. 10, p. 2583, 2013.
- [61] M. Agostini *et al.*, “Results on Neutrinoless Double- $\beta$  Decay of  $^{76}\text{Ge}$  from Phase I of the GERDA Experiment,” *Phys.Rev.Lett.*, vol. 111, no. 12, p. 122503, 2013.
- [62] M. Agostini, “The GERDA experiment for the search of neutrinoless double beta decay: status and perspectives,” *25th Rencontres de Blois, conference talk*, 2013.
- [63] M. Agostini, “Signal and background studies for the search of neutrinoless double beta decay in GERDA,” Ph.D. dissertation, Technische Universität München, 2013. [Online]. Available: [http://www.mpi-hd.mpg.de/gerda/public/2013/phd2013\\_matteoAgostini.pdf](http://www.mpi-hd.mpg.de/gerda/public/2013/phd2013_matteoAgostini.pdf)
- [64] H. Klapdor-Kleingrothaus, I. Krivosheina, A. Dietz, and O. Chkvorets, “Search for neutrinoless double beta decay with enriched Ge-76 in Gran Sasso 1990-2003,” *Phys.Lett.*, vol. B586, pp. 198–212, 2004.
- [65] M. Agostini *et al.*, “Upgrade of the gerda experiment,” *PoS*, vol. TIPP2014, p. 109, 2014.
- [66] “Joint Stock Company "Production Association Electrochemical Plant", Pervaya Promyshlennaya 1, 663690 Zelenogorsk, Russia.” [Online]. Available: <http://www.ecp.ru/indexen.shtml>
- [67] “PPM Pure Metals GmbH, Am Bahnhof 1, 38685 Langelsheim, Germany.” [Online]. Available: <http://www.pppuremetals.de/>
- [68] “Canberra Industries Inc., 107 Union Valley Rd, Oak Ridge, TN, USA.” [Online]. Available: <http://www.canberra.com/>
- [69] “Canberra Semiconductor N.V., Lammerdries 25, 2250 Olen, Belgium.” [Online]. Available: <http://www.canberra.com/>
- [70] M. Agostini, M. Allardt, E. Andreotti, A. Bakalyarov, M. Balata *et al.*, “Production, characterization and operation of  $^{76}\text{Ge}$  enriched BEGe detectors in GERDA,” 2014.

## BIBLIOGRAPHY

---

- [71] “Hamamatsu Photonics K.K., 325-6, Sunayama-cho, Naka-ku, Hamamatsu City, Shizuoka Pref., 430-8587, Japan.” [Online]. Available: <http://www.hamamatsu.com>
- [72] K. Ackermann *et al.*, “The GERDA experiment for the search of  $0\nu\beta\beta$  decay in  $^{76}\text{Ge}$ ,” *Eur.Phys.J.*, vol. C73, no. 3, p. 2330, 2013.
- [73] A. Badertscher, F. Bay, N. Bourgeois, C. Cantini, A. Curioni *et al.*, “ArDM: first results from underground commissioning,” *JINST*, vol. 8, p. C09005, 2013.
- [74] P. Agnes *et al.*, “First Results from the DarkSide-50 Dark Matter Experiment at Laboratori Nazionali del Gran Sasso,” *arXiv:1410.0653 [astro-ph.CO]*.
- [75] P.-A. Amaudruz *et al.*, “DEAP-3600 Dark Matter Search,” *arXiv:1410.7673 [physics.ins-det]*, 2014.
- [76] S. Amerio *et al.*, “Design, construction and tests of the ICARUS T600 detector,” *Nucl.Instrum.Meth.*, vol. A527, pp. 329–410, 2004.
- [77] M. Heisel, “LArGe – A liquid argon scintillation veto for Gerda,” Ph.D. dissertation, Ruperto-Carola University of Heidelberg, 2011. [Online]. Available: [http://www.mpi-hd.mpg.de/gerda/public/2011/phd2011\\_MarkHeisel.pdf](http://www.mpi-hd.mpg.de/gerda/public/2011/phd2011_MarkHeisel.pdf)
- [78] M. Agostini, M. Barnabe-Heider, D. Budjas, C. Cattadori, A. Gangapshev *et al.*, “LArGe - Active background suppression using argon scintillation for the GERDA  $0\nu\beta\beta$ -experiment,” 2015.
- [79] “3M Corporation, St. Paul, Minnesota, USA (Vikuiti<sup>TM</sup> ESR can be found on their homepage but not VM2000).” [Online]. Available: <http://www.3m.com/>
- [80] “Donaldson Company Inc., 1400 West 94th Street, Bloomington, Minnesota, USA .” [Online]. Available: [www.donaldson.com/](http://www.donaldson.com/)
- [81] M. Janecek, “Reflectivity spectra for commonly used reflectors,” *IEEE TRANSACTIONS ON NUCLEAR SCIENCE*, vol. 59, 2012.
- [82] W. Buck and R. Swank, “Preparation and performance of efficient plastic scintillator.” *Nucleonics*, vol. 11, 1953.
- [83] F. Krenz, “Energy transfer in polystyrene-anthracene.” *trans. Farady Soc.*, vol. 51, 1955.

## BIBLIOGRAPHY

---

- [84] P. Pfeiffer, “Liquid argon as active shielding and coolant for bare germanium detectors: A novel background suppression method for the Gerda  $0\nu\beta\beta$  experiment,” Ph.D. dissertation, Universität Heidelberg, 2007. [Online]. Available: <http://www.mpi-hd.mpg.de/gerda/public/2007/phd2007-peiffer.pdf>
- [85] The ArDM Collaboration, “Development of wavelength shifter coated reflectors for the ArDM argon dark matter detector,” *JINST*, vol. 4, p. P06001, 2009. [Online]. Available: <http://iopscience.iop.org/1748-0221/4/06/P06001>
- [86] R. Francini, R. Montereali, E. Nichelatti, M. Vincenti, N. Canci *et al.*, “Tetraphenyl-butadiene films: VUV-Vis optical characterization from room to liquid argon temperature,” *JINST*, vol. 1309, p. C09010, 2013.
- [87] “Varian Inc., now part of Agilent Technologies, 5301 Stevens Creek Blvd. Santa Clara, California, USA.” [Online]. Available: [www.agilent.com/chem](http://www.agilent.com/chem)
- [88] M. Suzuki, J.-z. Ruan(Gen), and S. Kubota, “Time dependence of the recombination luminescence from high-pressure argon, krypton and xenon excited by alpha particles,” *Nucl. Instr. Meth.*, vol. 192, pp. 565–574, 1982.
- [89] C. Amsler, V. Boccone, A. Buchler, R. Chandrasekharan, C. Regenfus *et al.*, “Luminescence quenching of the triplet excimer state by air traces in gaseous argon,” *JINST*, vol. 3, p. P02001, 2008.
- [90] W. Lippincott, K. Coakley, D. Gastler, A. Hime, E. Kearns *et al.*, “Scintillation time dependence and pulse shape discrimination in liquid argon,” *Phys.Rev.*, vol. C78, p. 035801, 2008.
- [91] J. W. Keto, R. E. Gleason, and G. K. Walters, “Production mechanisms and radiative lifetimes of argon and xenon molecules emitting in the ultraviolet,” *Phys. Rev. Lett.*, vol. 33, pp. 1365–1368, Dec 1974. [Online]. Available: <http://link.aps.org/doi/10.1103/PhysRevLett.33.1365>
- [92] R. Acciarri, M. Antonello, B. Baibussinov, M. Baldo-Ceolin, P. Benetti *et al.*, “Effects of Nitrogen and Oxygen contamination in liquid Argon,” *Nucl.Phys.Proc.Suppl.*, vol. 197, pp. 70–73, 2009.
- [93] “Paul Scherrer Institut, 5232 Villigen PSI, Switzerland.” [Online]. Available: <http://www.psi.ch/>

## BIBLIOGRAPHY

---

- [94] L. Baudis, G. Benato, R. Dressler, F. Piastra, I. Usoltsev, and M. Walter, “Enhancement of Light Yield and Stability of Radio-Pure Tetraphenyl-Butadiene Based Coatings for VUV Light Detection in Cryogenic Environments,” *JINST (forthcoming, accepted)*, 2015.
- [95] “CAEN S.p.A., Via Vetraia 11, 55049 Viareggio (LU), Italy.” [Online]. Available: <http://www.caen.it/>
- [96] “Swagelok, Solon, Ohio, USA.” [Online]. Available: <http://swagelok.com/>
- [97] “Newport Electronics GmbH, Daimlerstrasse 26,75392 Deckenpfromm, Germany.” [Online]. Available: <http://www.omega.de>
- [98] “EMKO Elektronik A.S., DOSAB Karanfil St. No. TR 16369, Bursa, Turkey.” [Online]. Available: [www.emkoelektronik.com.tr](http://www.emkoelektronik.com.tr)
- [99] R. L. Amey and R. H. Cole, “Dielectric constants of liquefied noble gases and methane,” *The Journal of Chemical Physics*, vol. 40, no. 1, pp. 146–148, 1964. [Online]. Available: <http://scitation.aip.org/content/aip/journal/jcp/40/1/10.1063/1.1724850>
- [100] “Smartec BV, Delpratsingel 26, 4811 AP Breda, The Netherlands.” [Online]. Available: <http://www.smartec.nl/>
- [101] R. Brun and F. Rademakers, “{ROOT} – an object oriented data analysis framework,” *Nuclear Instruments and Methods in Physics Research Section A: Accelerators, Spectrometers, Detectors and Associated Equipment*, vol. 389, no. 1–2, pp. 81 – 86, 1997, new Computing Techniques in Physics Research V. [Online]. Available: <http://www.sciencedirect.com/science/article/pii/S016890029700048X>
- [102] J. D. Hunter, “Matplotlib: A 2d graphics environment,” *Computing In Science & Engineering*, vol. 9, no. 3, pp. 90–95, 2007.
- [103] N. Sofer, “Nirsoft.” [Online]. Available: <http://www.nirsoft.net>
- [104] A. Hitachi, T. Takahashi, N. Funayama, K. Masuda, J. Kikuchi *et al.*, “Effect of ionization density on the time dependence of luminescence from liquid argon and xenon,” *Phys.Rev.*, vol. B27, pp. 5279–5285, 1983.
- [105] W. Viehmann, A. G. Eubanks, G. F. Pieper, and J. H. Bredekamp, “Photomultiplier window materials under electron irradiation: fluorescence and phosphorescence,” *Applied Optics*, vol. 14, 1975. [Online]. Available: <http://gen.lib.rus.ec/scimag/index.php?s=10.1364/AO.14.002104>

## BIBLIOGRAPHY

---

- [106] G. Mavromanolakis, “Quartz fiber calorimetry and calorimeters,” 2004.
- [107] T. Heindl, T. Dandl, M. Hofmann, R. Krucken, L. Oberauer *et al.*, “The scintillation of liquid argon,” *Europhys.Lett.*, vol. 91, p. 62002, 2010.
- [108] “Hamamatsu Photonics K.K., private communication.” [Online]. Available: <http://www.hamamatsu.com>
- [109] A. Behrens, “Light Detectors for the XENON100 and XENON1T Dark Matter Search Experiments,” Ph.D. dissertation, Universität Zürich, 2014. [Online]. Available: [http://www.physik.uzh.ch/groups/groupbaudis/darkmatter/theses/xenon/thesis\\_behrens.pdf](http://www.physik.uzh.ch/groups/groupbaudis/darkmatter/theses/xenon/thesis_behrens.pdf)
- [110] Hamamatsu, “Photomultiplier Tubes, Basics and Applications.” [Online]. Available: [https://www.hamamatsu.com/resources/pdf/etd/PMT\\_handbook\\_v3aE.pdf](https://www.hamamatsu.com/resources/pdf/etd/PMT_handbook_v3aE.pdf)
- [111] G. A. Morton, H. M. Smith, and R. Wasserman, “Afterpulses in photomultipliers,” *IEEE Transactions on Nuclear Science*, vol. 14, 1967. [Online]. Available: <http://gen.lib.rus.ec/scimag/index.php?s=10.1109/tns.1967.4324452>
- [112] H. Loosli, “A dating method with  $^{39}\text{Ar}$ ,” *Earth and Planetary Science Letters*, vol. 63, no. 1, pp. 51 – 62, 1983. [Online]. Available: <http://www.sciencedirect.com/science/article/pii/0012821X83900213>
- [113] P. Benetti *et al.*, “Measurement of the specific activity of  $^{39}\text{Ar}$  in natural argon,” *Nuclear Instruments and Methods in Physics Research Section A: Accelerators, Spectrometers, Detectors and Associated Equipment*, vol. 574, no. 1, pp. 83 – 88, 2007. [Online]. Available: <http://www.sciencedirect.com/science/article/pii/S0168900207001672>
- [114] K. Lung, K. Arisaka, A. Bargetzi, P. Beltrame, A. Cahill *et al.*, “Characterization of the Hamamatsu R11410-10 3-Inch Photomultiplier Tube for Liquid Xenon Dark Matter Direct Detection Experiments,” *Nucl.Instrum.Meth.*, vol. A696, pp. 32–39, 2012.
- [115] L. Baudis, A. Behrens, A. Ferella, A. Kish, T. Marrodan Undagoitia *et al.*, “Performance of the Hamamatsu R11410 Photomultiplier Tube in cryogenic Xenon Environments,” *JINST*, vol. 8, p. P04026, 2013.
- [116] R. Acciarri *et al.*, “Oxygen contamination in liquid Argon: Combined effects on ionization electron charge and scintillation light,” *JINST*, vol. 5, p. P05003, 2010.

## BIBLIOGRAPHY

---

- [117] —, “Effects of Nitrogen contamination in liquid Argon,” *JINST*, vol. 5, p. P06003, 2010.
- [118] W. Creus, Y. Allkofer, C. Amsler, A. Ferella, J. Rochet *et al.*, “Scintillation efficiency of liquid argon in low energy neutron-argon scattering,” 2015.
- [119] D. Gastler, E. Kearns, A. Hime, L. Stonehill, S. Seibert *et al.*, “Measurement of scintillation efficiency for nuclear recoils in liquid argon,” *Phys.Rev.*, vol. C85, p. 065811, 2012.
- [120] H. Cao *et al.*, “Measurement of Scintillation and Ionization Yield and Scintillation Pulse Shape from Nuclear Recoils in Liquid Argon,” 2014.
- [121] R. Brunetti *et al.*, “Warp liquid argon detector for dark matter survey,” *New Astron.Rev.*, vol. 49, pp. 265–269, 2005.
- [122] D.-M. Mei, Z.-B. Yin, L. Stonehill, and A. Hime, “A Model of Nuclear Recoil Scintillation Efficiency in Noble Liquids,” *Astropart.Phys.*, vol. 30, pp. 12–17, 2008.
- [123] M. Szydagis and *et. al.*, “Noble element simulation technique, a model of scintillation and electroluminescence in noble elements,” 2012. [Online]. Available: [http://nest.physics.ucdavis.edu/data/LBL\\_NEST\\_2012.pdf](http://nest.physics.ucdavis.edu/data/LBL_NEST_2012.pdf)
- [124] T. Doke, A. Hitachi, J. Kikuchi, K. Masuda, H. Okada, and E. Shibamura, “Absolute Scintillation Yields in Liquid Argon and Xenon for Various Particles,” *Jpn. J. Appl. Phys.*, vol. 41, no. 3A, pp. 1538–1545, 2002.
- [125] “Comsol Multiphysics 4.3.” [Online]. Available: <http://www.comsol.com/>
- [126] E. Segreto, “Evidence of delayed light emission of TetraPhenyl Butadiene excited by liquid Argon scintillation light,” *Phys.Rev.*, vol. C91, no. 3, p. 035503, 2015.
- [127] L. Baudis, A. Ferella, A. Askin, J. Angle, E. Aprile *et al.*, “Gator: a low-background counting facility at the Gran Sasso Underground Laboratory,” *JINST*, vol. 6, p. P08010, 2011.
- [128] S. Agostinelli *et al.*, “Geant4-a simulation toolkit,” *Nuclear Instruments and Methods in Physics Research Section A: Accelerators, Spectrometers, Detectors and Associated Equipment*, vol. 506, no. 3, pp. 250 – 303, 2003. [Online]. Available: <http://www.sciencedirect.com/science/article/pii/S0168900203013688>

## BIBLIOGRAPHY

---

- [129] S. Hauf, M. Kuster, M. Batic, Z. W. Bell, D. H. H. Hoffmann *et al.*, “Radioactive Decays in Geant4,” *IEEE Trans.Nucl.Sci.*, vol. 60, no. 4, pp. 2966–2983, 2013.
- [130] W. Rau and G. Heusser, “ $^{222}\text{Rn}$  emanation measurements at extremely low activities,” *Applied Radiation and Isotopes*, vol. 53, no. 1–2, pp. 371 – 375, 2000. [Online]. Available: <http://www.sciencedirect.com/science/article/pii/S096980430000155X>
- [131] J. Benziger, L. Cadonati, F. Calaprice, E. de Haas, R. Fernholz *et al.*, “The Nylon Scintillator Containment Vessels for the Borexino Solar Neutrino Experiment,” *Nucl.Instrum.Meth.*, vol. A582, pp. 509–534, 2007.
- [132] “Extorr Inc., 307 Columbia Road, New Kensington, PA 15068, USA.” [Online]. Available: [www.extorr.com](http://www.extorr.com)
- [133] E. Aprile *et al.*, “The XENON100 Dark Matter Experiment,” *Astropart.Phys.*, vol. 35, pp. 573–590, 2012.
- [134] L. Baudis, “DARWIN: dark matter WIMP search with noble liquids,” *J. Phys. Conf. Ser.*, vol. 375, p. 012028, 2012.
- [135] M. Miloradovic, “Emanation Measurement System and GERDA Phase II Calibration,” forthcoming 2015.
- [136] “Hositrad - Holland B.V., De Wel 44, 3871 MV Hoevelaken.” [Online]. Available: [www.hositrad.com](http://www.hositrad.com)
- [137] “MKS Instruments, Granville-Phillips Devison, 2 Tech Drive, Suite 201, Andover, Massachusetts 01810, USA.” [Online]. Available: <http://www.mksinst.com/Granville-Phillips>
- [138] F. Nakao, “Determination of the ionization gauge sensitivity using the relative ionization cross-section,” *Vacuum*, vol. 25, 1975. [Online]. Available: [http://gen.lib.rus.ec/scimag/index.php?s=10.1016/0042-207x\(75\)90491-1](http://gen.lib.rus.ec/scimag/index.php?s=10.1016/0042-207x(75)90491-1)
- [139] E. P. Linstrom, N. I. o. S. W.G. Mallard, and . Technology, Gaithersburg MD, “NIST Mass Spec Data Center, S.E. Stein, director, "Mass Spectra" in NIST Chemistry WebBook.” [Online]. Available: <http://webbook.nist.gov>
- [140] MKS instruments, Inc., 2 Tech Drive, Suite 201, Andover, MA 01810, USA, “RGA Application Bulletin #208, Spectra Reference, Note #03/02.” [Online]. Available: <http://www.mksinst.com/>

## BIBLIOGRAPHY

---

- [141] A. Ben-Hur and J. Weston, “A users guide to support vector machines.” [Online]. Available: [http://cau.ac.kr/~mhhgtx/courses/AdaptiveFilters/References/SVM\\_UsersGuide.pdf](http://cau.ac.kr/~mhhgtx/courses/AdaptiveFilters/References/SVM_UsersGuide.pdf)
- [142] T. Joachims, “Making large-scale SVM learning practical,” in *Advances in Kernel Methods - Support Vector Learning*, B. Schölkopf, C. Burges, and A. Smola, Eds. Cambridge, MA: MIT Press, 1999, ch. 11, pp. 169–184.
- [143] M. Agostini, L. Pandola, and P. Zavarise, “Off-line data processing and analysis for the gerda experiment,” *Journal of Physics: Conference Series*, vol. 368, no. 1, p. 012047, 2012. [Online]. Available: <http://stacks.iop.org/1742-6596/368/i=1/a=012047>
- [144] M. Agostini, L. Pandola, P. Zavarise, and O. Volynets, “GELATIO: A General framework for modular digital analysis of high-purity Ge detector signals,” *JINST*, vol. 6, p. P08013, 2011.
- [145] M. Boswell *et al.*, “MaGe-a Geant4-based Monte Carlo Application Framework for Low-background Germanium Experiments,” *IEEE Trans. Nucl. Sci.*, vol. 58, pp. 1212–1220, 2011.
- [146] A. Kirsch, “Search for the neutrinoless double  $\beta$ -decay in GERDA Phase I using a Pulse Shape Discrimination technique,” Ph.D. dissertation, MPI-K/U.Heidelberg, 2014. [Online]. Available: [http://www.mpi-hd.mpg.de/gerda/public/2014/phd2014\\_andreaKirsch.pdf](http://www.mpi-hd.mpg.de/gerda/public/2014/phd2014_andreaKirsch.pdf)
- [147] I. Abt, A. Caldwell, F. Cossavella, B. Majorovits, D. Palioselitis, and O. Volynets, “Signal recognition efficiencies of artificial neural-network pulse-shape discrimination in HPGe  $0\nu\beta\beta$ -decay searches,” 2014.
- [148] D. Budjas, M. Barnabe Heider, O. Chkvorets, N. Khanbekov, and S. Schonert, “Pulse shape discrimination studies with a Broad-Energy Germanium detector for signal identification and background suppression in the GERDA double beta decay experiment,” *JINST*, vol. 4, p. P10007, 2009.
- [149] M. Agostini, C. A. Ur, D. Budjas, E. Bellotti, R. Brugnera, C. M. Cattadori, A. di Vacri, A. Garfagnini, L. Pandola, and S. Schonert, “Signal modeling of high-purity Ge detectors with a small read-out electrode and application to neutrinoless double beta decay search in Ge-76,” *JINST*, vol. 6, p. P03005, 2011.
- [150] A. Lazzaro, “Studies of high-purity Ge detector signals,” Ph.D. dissertation, Technische Universität München, 2012.

## BIBLIOGRAPHY

---

- [151] D. Budjas, “Germanium detector studies in the framework of the GERDA experiment,” Ph.D. dissertation, University of Heidelberg, 2009.
- [152] O. Schulz, “Exploration of new data acquisition and background reduction techniques for the COBRA experiment,” Ph.D. dissertation, Technischen Universität Dortmund, 2011. [Online]. Available: <https://eldorado.tu-dortmund.de/handle/2003/29108>
- [153] I. Daubechies, *Ten lectures on wavelets*. Philadelphia, PA: Society for Industrial and Applied Mathematics, 2006, 1992.
- [154] “A Really Friendly Guide To Wavelets.” [Online]. Available: <http://www.polyvalens.com/blog/wavelets/theory/>
- [155] I. Daubechies, “Orthonormal bases of compactly supported wavelets,” *Comm. Pure Appl. Math.*, vol. 41, 1988.
- [156] “<http://www.pybytes.com/pywavelets>.”
- [157] M. Agostini *et al.*, “The MGDO software library for data analysis in Ge neutrinoless double-beta decay experiments,” *J. Phys. Conf. Ser.*, vol. 375, p. 042027, 2012.
- [158] H.-Y. Liao, “Investigation of pulse shape discrimination efficiencies with HPGe detectors,” Ph.D. dissertation, Ludwig–Maximilians–Universität München, forthcoming.
- [159] “LabVIEW, National Instruments Corporation, 11500 Mopac Expwy, Austin, TX 78759-3504, USA.” [Online]. Available: <http://www.ni.com/labview/>
- [160] “Hilti Corporation, Feldkircherstrasse 100, 9494 Schaan, Liechtenstein.” [Online]. Available: [www.hilti.com](http://www.hilti.com)
- [161] “Meilhaus Electronic GmbH, Am Sonnenlicht 2, D-82239 Alling bei München.” [Online]. Available: <http://www.meilhaus.de/>